Reconstruction of the Paratethys-Mediterranean Climatic System during the Upper Miocene

Dissertation

zur Erlangung des Doktorgrades

der Naturwissenschaften

vorgelegt beim Fachbereich 11

der Johann Wolfgang Goethe –Universität

in Frankfurt am Main

von

Geanina-Adriana Butiseacă

aus Roșioru (Buzău)

Frankfurt am Main, Mai 2022

Vom Fachbereich 11 der Johann Wolfgang Goethe – Universität als Dissertation angenommen.

Dekan: Prof. Dr. Georg Rümpker

Gutachter: **Prof. Dr. Andreas Mulch**

Senckenberg Biodiversität und Klima Forschungszentrum,

Senckenberganlage 25, 60325 Frankfurt (Main), Deutschland

und

Institut für Geowissenschaften, Johann Wolfgang Goethe Universität,

Altenhöferallee 1, 60438 Frankfurt (Main), Deutschland

Datum der Disputation: 26 Oktober 2022

To my grandfather.

TABLE OF CONTENTS

List of figures Page

Chapter 9 − Appendices

List of tables Page

Abreviations

AEFA	Alfeo-Etna Fault System
Ag	Silver (*Argentium*)
Al	Aluminium
AM	Agios Myron
APTS	Astronomically tuned polarity time scale
Bg	Bulgaria
BIT index	Branched and Isoprenoid Tetraethers index
BL	Belenyenice
BL N	Belenyenice nodule
br	branched
C	Carbon
CAL	Cretan Ash Layer
CBT	Cyclization of Branched Tetraethers
°C	Celsius degree
Ce	Cephalonia Fault
Cm	centimeter
CM	Central Mediterranean
Cu	Copper (*Cuprum*)
CyR	Cyrenaica Ridge
δ	delta
D (1)	Dry (1)
DaB	Darnah Basin
DCM	Dichloromethane
DFG	Deutsche Forschungsgemeinschaft (German Research Fundation)
DOI	Digital Object Identifier
DSDP	Deep Sea Drilling Program

E	East
ε	isotopic fractionation
EF	Efes Fault
e.g	*exempli gratia*
E. huxleyi	*Emiliania huxleyi*
EM	Eastern Mediterranean
Era	Eratosthenes
Et	Ethyl
et al.	*et alia*
etc.	*et cetera*
f	fraction
Fe	Iron (*Ferrum*)
Fig.	Figure
FO	First Occurrence
GC-MS	Gas Chromatography-Mass Spectrometry
GDGTs	Glycerol dialkyl glycerol tetraethers
G. obliquus	*Globigerinoides obliquus*
GPTS	Global Polarity Time Scale
gr	grams
h	hour
H	Hydrogen
HCl	Clorhidric Acid
HEX	Hexane
HLL	High Lake Level
HPLC	High-performance liquid chromatography/er
HSL	High Sea Level
i.e.	*id est*

IFS	Ionian Fault System
IFV	Ice Free Volume
IME	Intra-Maeotian Event
IPA	Isopropanol
irMS	isotope-ratio mass spectrometry/er
iso	isoprenoidal
JAA	Jabal Al Akhdar
Jef	Jeffara Basin
KAL	Kalamaki
Konk.	Konkian
Kyr	kilo year (thousand years)
La2004	Laskar 2004
LAT	Latitude
Le	Lebanon
LLL	Low Lake Level
LO	Last Occurrence
LSL	Low Sea Level
m	meter
Ma	*Mega Annum*
MaB	Marmarica Basin
MAT	Mean Annual Temperature
M.bulgarica	*Mactra bulgarica*
MBT	Methylation of Branched Tetraethers
MDC	Monte dei Corvi
Me	Methyl
Me	Maeotian
MeOH	Methanol

MF	Manisa Fault
M.fabreana	*Mactra fabreana*
µg	microgram
ml	milliliter
µm	micrometer
MN zones	Mammal Neogene zones
MSC	Messinian Salinity Crisis
Myr	Million years (duration)
N	North
N_2	Nitrogen
NBS	National Bureau of Standards
n.d.	not defined
NE	North East
NW	North West
NWO	Nederlandse Organisatie voor Wetenschappelijk Onderzoek (Netherlands Organisation for Scientific Research)
NIOZ	Royal Netherlands Institute for Sea Research
O	Oxygen
Obs	Observed
ODP	Ocean Drilling Program
OFZ	Orhaneli Fault Zone
O.G.	Organic Geochemistry
ORCID	Open Researcher Contributor Identification
P (2)	Point (2)
Pa	Palmyra Through
pCO_2	paleo CO_2
pH	potential of Hydrogen

PhD	Doctor of Philosophy (*doctor philosophiae*)
R or r	Radius
rhs	relative humidity at the surface
rRNA	Ribosomal ribonucleic acid
S	Salinity/South
S 2A	Slănic 2A
Sarm.	Sarmatian
SBiK-F	Senckenberg Biodiversity and Climate Research Centre
SE	South East
S.fig.	Supplementary figure
Si	Silicium
s.l.	*sensu lato*
SMOW	Standard Mean Ocean Water
sp.	species
spp.	several species
s.s.	*sensu stricto*
SST	Sea Surface Temperature
SST^H	Sea Surface Temperature High
SST^L	Sea Surface Temperature Low
SSS	Sea Surface Salinity
S.tab.	Supplementary table
STDEV	Standard Deviation
sw	sea water/surface water
SW	South West
T	Temperature
Tab.	Table
TC	Termal Conversion

TEX_{86}	TetraEther indeX of tetraethers consisting of 86 carbon atoms
TLE	Total Lipid Extract
T. multiloba	Turborotalia multiloba
TP	Taman Panagia
ULFC	Ultra-Fast Liquid Chromatography/er
$U^{K'}_{37}$	Alkenone (C_{37}) unsaturation ratio
VP	Putna Valley (Valea Putnei)
VPDB	Vienna Pee Dee Belemnite
VSMOW	Vienna Standard Mean Ocean Water
W	West
WM	Western Mediterranean
Wv	water vapor
Yr	years
‰	per mil
%	percentage

Chapter 1

General introduction

Upper Miocene represents the onset of the world as we know it today. It is a period with extreme changes in topography, precipitation patterns (changes in the Asian monsoon), flora (onset of savanna type vegetation in southern and central Eurasia) and faunal characteristics and distribution, ecological changes which led to extinctions, dwarfism, but also to the emergence of new mammal lines like baleen whales, primates and later − hominines. All these elements are making the Miocene a quite exquisite time period, with huge implications in the understanding of our present Earth.

The combined effects of global climate change and drastic modifications in the distribution and connectivity of large basin systems strongly affected the Upper Miocene climate patterns, especially areas like epicontinental seas/lake systems, such as Paratethys and Mediterranean. The impact of tectonics and climate over these large water masses is still uncertain and remains an important question when discussing links and feedbacks between climate and tectonics and their impact over biota. These feedbacks and consequences over the Miocene life have been explored mainly by paleontology and mostly in an old fashion manner.

1.1 Scope of this thesis

This dissertation purpose is to contribute to the overall understanding of the interactions between climate, tectonics and biosphere during the Upper Miocene, focusing on the Paratethys and Mediterranean domains (Afro-Eurasia). My efforts are directed towards a better understanding of this area in a global context, what are the implications of climatic changes over the environment in the time interval between 12.7 and 6.5 Ma, how climate can became a major factor into the evolution and adaptation of vegetation and fauna, and what is happening when major aquatic systems are decoupled from the planetary ocean and reshaped by tectonics.

1.2 Objectives

The objectives of this work are: (1) building valid paleo-temperatures records for both basins based on biomarkers, (2) reconstruct the hydrology during the selected time interval, (3) identify vegetation patterns and changes, (4) identify paleo-fires in the late Miocene savanna and (5) identify the biotic response to the overall climate and tectonic changes.

In this aspect I have analyzed biomarkers (*n*-alkanes, alkenones iso- and branched GDGTs) and stable isotopes (such as δ^2H, $\delta^{13}C$ and $\delta^{18}O$) for 2 sections from Russia (Taman peninsula, Panagia section) and Greece (Crete Island, Agios Myron section). In order to further explore the response of vegetation to the Paratethys continentalisation, I subsequently analyzed the fire regime in Taman based on the paleo-charcoal found in sediments. From biomarker point of view, the main focus was obtaining paleo-temperatures, sea surface temperatures (SST) and mean annual temperatures (MAT), but also pH data and organic matter sources (BIT Index). The combined SST and $\delta^{18}O$ on planktonic foraminifera from Agios Myron section was also used to further reconstruct sea surface salinities (SSS).

1.3 Thesis outline

The thesis is structured into 10 chapters, 3 main ones based on publications and 7 additional ones presenting details about general geology aspects, methodology, as well as a series of preliminary data from other sections. The chapters are preceded by a list of figures, tables and used abbreviations. At the end of the thesis is presented the list of appendices corresponding to each chapter, the curriculum vitae of the author, followed by the conclusions and outlook of this work, in both English and German languages.

1.3.1 Chapter 1

The introduction chapter describes the context, scope and objectives of the PhD thesis, including general information about the studied sections and used methods, as well as the structure of the thesis.

1.3.2 Chapter 2

The second chapter explains the state of the art of research for the Mid-Upper Miocene in Eurasia and focuses two main domains, the Paratethys and the Mediterranean, the two water

bodies that regulated the continental climate during this time interval. The chapter contains information about the tectonic evolution of the two aquatic systems, connectivity or lack of it, sedimentology, fauna, flora, as well as general information about the Miocene and global climatic trends.

1.3.3 Chapter 3

This chapter focuses on the two main sections analyzed in the thesis: Panagia (Taman Peninsula, Russia, Paratethys domain) and Agios Myron (Crete, Greece, Mediterranean). The chapter covers information about previous work and general aspects about location, lithology, paleontology, geological background and their importance in regional and global context.

1.3.4 Chapter 4

The fourth chapter explains the laboratory procedures and used methods. The chapter is structured in 3 parts, each having its own subchapters. The first part is focused on biomarkers and comprises information about sampling, preparation, lipid extraction, fractionation and measurements of the main biomarker categories, *n*-alkanes, alkenones and GDGTs. The second part is focused on stable isotopes and presents the samples preparation and measurements for hydrogen isotopes ($\delta^{2}H$), carbon ($\delta^{13}C$) and oxygen ($\delta^{18}O$) on organic compounds and bulk sedimentary rocks. The last part of this chapter details the sampling, preparation, identification and quantification methods for charcoal and the importance of fossil charcoal for fire regimes and paleoclimate reconstructions.

1.3.5 Chapter 5

The chapter titled "S**evere late Miocene droughts affected Western Eurasia**" is written by Geanina-Adriana Butiseacă, Iuliana Vasiliev, Marcel T.J. van der Meer, Wout Krijgsman, Dan V. Palcu, Angelica Feurdean, Eva M. Niedermeyer and Andreas Mulch and is published in **Global and Planetary Change (2021).** The paper focuses on the Panagia section (Russia) and covers the interval between 12.7 and 7.65 Ma. Here are used biomarker analyses coupled to compound-specific hydrogen and carbon isotope data and charcoal, to track changes in sea surface and mean annual temperatures, hydrological budget and vegetation, to reconstruct the long-term climate conditions in Eurasia and their impact over existing biota. The chapter

provides new insights into the late Miocene environmental conditions surrounding the Eastern Paratethys and quantifies for the first time the amplitude of major draughts that affected the continent, the scale of East Paratethys aridisation, and correlates the droughts with continental scale faunal turnovers and C_4 plants expansion. The chapter also supports major changes in the hydrology of the basin and explains endemic marine mammals' evolution and extinction as response to isolation and changes in water temperature and circulation.

1.3.6 Chapter 6

The chapter "**Hypersalinity accompanies tectonic restriction in the early Messinian Eastern Mediterranean**" by George Kontakiotis*, Geanina-Adriana Butiseacă*, Assimina Antonarakou, Konstantina Agiadi, Stergios D. Zarkogiannis, Emilija Krsnik, Evangelia Besiou, Jan-Willem Zachariasse, Lucas Lourens, Danae Thivaiou, Efterpi Koskeridou, Pierre Moisette, Andreas Mulch, Vasileios Karakitzios and Iuliana Vasiliev was published in **Palaegeography, Palaeoclimatology, Palaeoecology (2022)**.The paper focuses on the hydroclimatic evolution of the Mediterranean region during the Early Messinian stage (7.2−6.5 Ma) based on the analysis of Agios Myron section (Crete Island, Greece). The study presents sea surface temperatures and salinity reconstructions based on a combined analysis of biomarkers and oxygen isotopes on planktonic foraminifera proposing a paleogeographic evolution in three steps, reflecting the progressive restriction of the Mediterranean during the Early Messinian, as consequence of the Atlantic cutoff and global cooling. The first two authors have equal contribution to this publication.

1.3.7 Chapter 7

The chapter titled "**Multiple crises before the big crisis: Early Messinian Eastern Mediterranean paleoclimate reconstruction inferred from biomarkers and stabile isotopes**" by Geanina-Adriana Butiseacă, Marcel T.J. van der Meer, George Kontakiotis, Konstantina Agiadi, Danae Thivaiou, Evangelia Besiou, Assimina Antonarakou, Andreas Mulch and Iuliana Vasiliev was submitted to Global and Planetary Change and is currently being under review. The paper focuses on the interplay between tectonics and climate, the continental response to global climatic changes, vegetation, organic matter sources, and the sea-land interactions in the Eastern Mediterranean between 7.2−6.5 Ma. The paper targets the same section as chapter 6 and

represents a follow up. The paper confirms a series of drastic environmental and ecological changes, indicating several highly evaporitic events accompanied by shifts in vegetation, documenting for the first time the aridification of the Mediterranean-North African domain during early Messinian, as well as the onset of C_4 plants in the region. The paper also shows a decoupling of marine and continental systems due to the Atlantic gateway(s) obstruction and local tectonics. The overall results support an ongoing restriction and aridisation of the Mediterranean and surrounding areas after 7 Ma, with multiple phases progressing in intensity until the final Messinian Salinity Crisis event.

1.3.8 Chapter 8

The chapter named "**Preliminary results other sites**" comprises of preliminary results from other key sections from the Paratethys−Mediterranean area. It is divided in three subchapters, first for Turkey, second for Bulgaria and third for Romania. The first subchapter focuses on Belenyenice section from Turkey, preliminary dated as middle-late Miocene. In this chapter are included general data about sampling, geology and tectonics, but also about depositional systems and the sedimentary evolution of the basin. The focuses on this section are $\delta^{13}C$ and $\delta^{13}O$ stable isotopes and lithology, which depict important changes in humidity, connectivity and depositional systems, in relationship with tectonics.

The second subchapter covers preliminary biomarker data, stratigraphy and lithology for three sections in NE Bulgaria (Bolata, Kamen Briag and Kavarna). The sections in discussion are the approximate equivalent of Panagia section (Taman, chapter 5), but deposited in a carbonate system and highly influenced by local tectonics.

The third subchapter comprises of preliminary biomarker data for two sections in Romania (Putna and Slănic), part of the Central Paratethys. All sets of data are the first of this type in their region and will be incorporated in future research and publications.

1.3.9 Chapter 9

The chapter "**Summary and outlook**" provides a synopsis of the main findings and discussions in this PhD work, as well as future directions, in English.

1.3.10 Chapter 10

The chapter "**Zusammenfassung und Ausblick**" provides the translation in German language of the main findings and outlook of this thesis.

Chapter 2

State of the art of the Mid-Upper Miocene Eurasia

2.1 Paratethys system

2.1.1 Origins and geography

Paratethys is an extinct large epicontinental sea that formed during the Paleogene (Eocene-Oligocene) as a consequence of the tectonic closure of the Eocene Peri−Tethys Ocean induced by the Eurasia−Afro−Arabia collision that shaped the Alpine-Himalayan belt (Rögl, 1999; Popov et al., 2006). Initially defined by Laskarev a century ago (Laskarev, 1924), Paratethys giant covered a large part of Eurasia, stretching from France (to west) to China (in the east) (Figure 2.1).

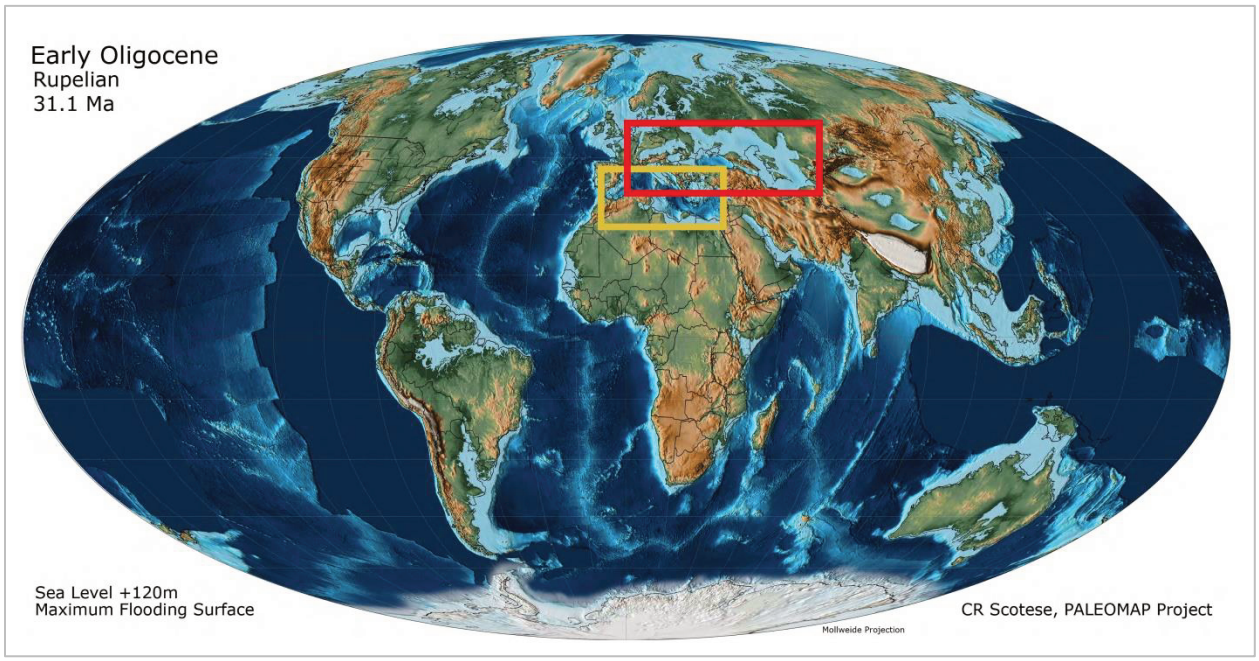

Figure 2.1 Early Oligocene paleogeographic map (maximum extension of Paratethys). With red is marked the Paratethys Sea, while with yellow the Mediterranean Sea (Scotese, 2021).

Paratethys is not special only by its size, but also by its geography. Particular to Paratethys is its non-unitary configuration, being a puzzle of smaller basins connected in between intermittently through short-lived or sustained gateways (e.g. Bârlad, Kerch, etc.). Poor

connectivity led in time to complete restriction, followed by protracted biotic endemism. The partial or complete isolation led to intense stratification, poorly oxygenated waters and finally anoxia. These anoxic waters remained locked in deep depressions such as the Euxinic (Black Sea) and Caspian basins. Shallower basins, with limited anoxia, bordered the deeper basins and recorded mixed influences from seas and rivers that drained a large surface of central Eurasia (Palcu, 2018).

Based on geography, Paratethys was divided into three sectors: western, central and eastern Paratethys. The western Paratethys covered parts of France, Switzerland, South Germany and Upper Austria (Seneš, 1961) and was controlled early on by the orogenic belts developed in the area. Central Paratethys overlaps most of modern day Central Europe, from Austria to Romania (Papp et al., 1978), while eastern Paratethys covered the rest. The Black Sea, Caspian Sea and Aral Lake are the only modern survivors after the demise of Paratethys.

Overall, the continentalisation of Paratethys is the result of multiple factors, such as southern Eurasia orogenic belts rising, eustatic changes, isolation and climate (Clauzon et al., 2005; Harzhauser and Piller, 2007; Palcu et al., 2021, Butiseacă et al., 2021).

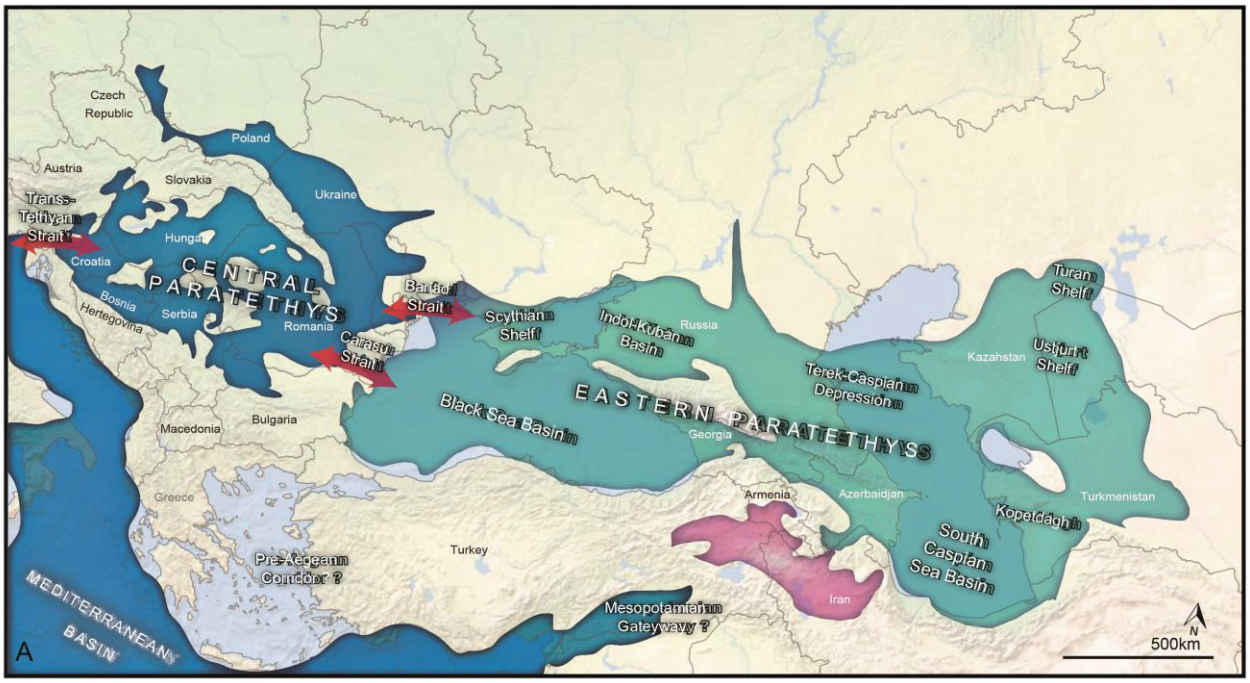

Figure 2.2 The Central and Eastern Paratethys domains with their major divisions, as suggested by the distribution of middle Miocene sediments (Palcu et al., 2016). With red are represented the active marine gateways.

Fragmentation and isolation of Paratethys (i.e. local diachronic events) could not follow correlations to the Geological Time Scale and led to the establishment of regional stages (e.g. Bessarabian, Volhynian, etc.). The influence of Paratethys over the global climate is still unknown, but the impact over the Eurasian climate and biota was significant (e.g. Böhme et al., 2021; Butiseacă et al., 2021− Chapter 5).

2.1.2 Timeline

2.1.2.1 Oligocene-Early Miocene

By the early Oligocene, the collision between the Arabian Peninsula and the Iranian Terrane was almost complete, but during highstands (late Oligocene to early Miocene), the Paratethys was still connected with the Mediterranean. During the late Oligocene and early Miocene, the Western Paratethys was connected with the Mediterranean via the North Alpine Foreland Basin and the Rhône Valley (Berger et al., 2005). A significant retreat is diachronically recorded ~17.6−17.2 Ma, when the before mentioned gateway closes due to the alpine tectonic uplift as the frontal part of the Eastern Alps thrusted over the European Platform (Grad et al., 2009). As a result, the Paratethys turned gradually into a system of brackish basins with endemic fauna (Harzhauser and Piller, 2007). Opposite to the western side, Central Paratethys (i.e. Carpathian-Pannonian domains) witnesses a transgression at ~17.0 Ma (Zuschin et al., 2014). A direct connection to the Mediterranean is established through the Transtethyan corridor (Kováč et al., 2007, Mandic et al., 2012), following the Mid-Hungarian Line (Géczy, 1973), the pull-apart area caused by the rotation of Alcapa and Tisza-Dacia mega-units (Magyar et al., 1999; Márton et al., 2007). The Black Sea basin (Eastern Paratethys) though, does not record any evidence of open marine conditions for early Miocene (Popov et al., 2006).

2.1.2.2 Mid-Late Miocene

The Transtethyan gateway was the main gateway until ~12.6 Ma (Bartol et al., 2014). In the meantime, other gateways opened towards the east (i.e. Carasu and Barlad straits, Palcu et al., 2015, 2017), facilitating the connection between the Dacian basin and Black Sea/Kuban basin and linking the Central and Eastern Paratethys. These active connections were closed by the end of Bessarabian (~12–9.65 Ma) (Sant et al., 2017; Palcu et al., 2017), completely isolating the central and eastern sides.

In the absence of gateways and protracted tectonics and continentalisation, the paratethyan basins started to be filled with sediments eroded from the new rising orogenies. The tectonic uplift and recurrent isolation changed the character of Paratethys from marine to brackish, and ultimately lacustrine or anoxic. At the end of Miocene, Paratethys was the largest megalake in the Eurasian geological record (Palcu et al., 2021), tectonically-trapped and disconnected from the global ocean.

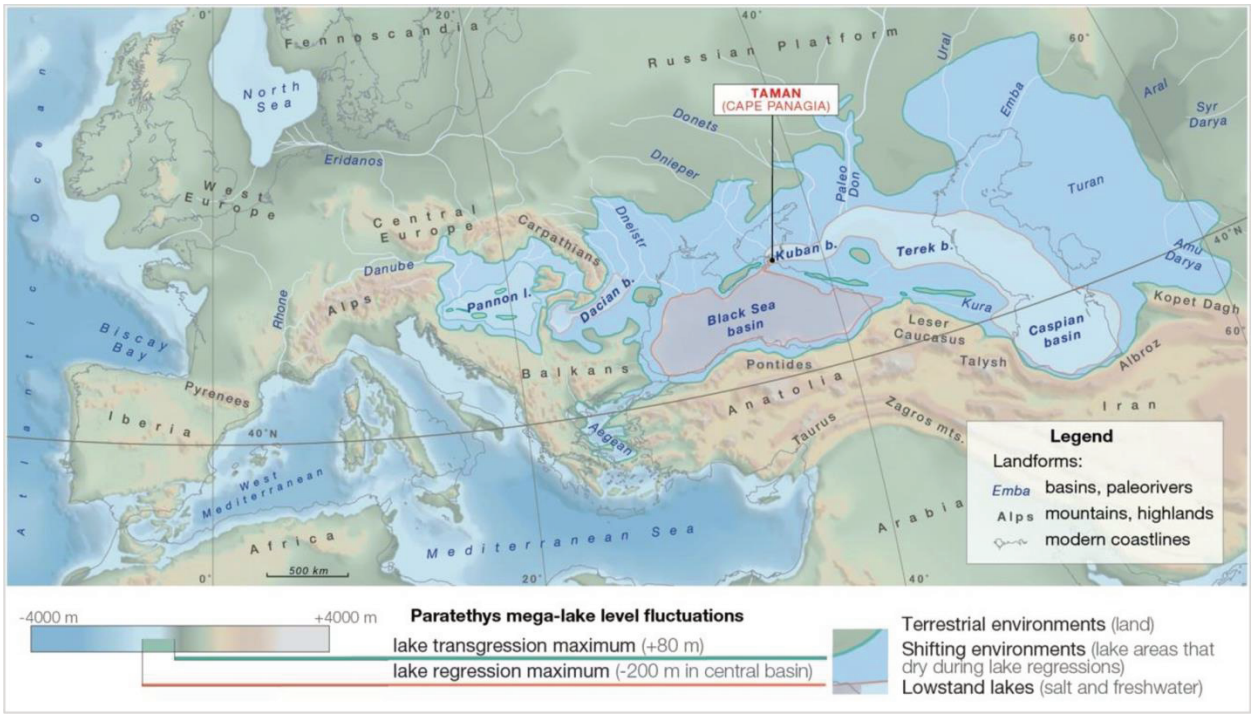

Figure 2.3 Paleogeographic reconstruction of late Miocene Paratethys fluctuations, with central saltier Black Sea (red) and peripheral basins that periodically refilled and became fresher (light blue) (Palcu et al., 2021).

2.1.3 Black Sea in the Paratethys context

The Black Sea is the deepest and largest modern remnant of the Paratethys, but its history starts in the Early Cretaceous with the closing of Vardar oceanic branch of Tethys (Finetti et al., 1998; Okay et al., 1994). Black Sea facilitated in the past the connection with Central Paratethys and Indian Ocean (Rögl, 1999), and since Holocene with the Marmara/Aegean system through the Bosporus Strait (Gökaşan et al., 1997). The basin is formed by two distinct sub-basins, delimitated by a high elevated block called the Andrusov Ridge (Andrusov, 1890). The Western Black Sea was influenced over time by the tectonic movements in the Carpathian foreland,

Balkans and North Anatolian Fault (e.g. Tari et al., 2009; Yilmaz et.al, 1997), while the Eastern Black Sea basin was affected mainly by the Caucasus uplift (e.g. Popov et al., 2006). The late Miocene strong compression in the Caucasus area had a high impact over the architecture of North Black Sea, Crimea (Stovba et al., 2020), Indol-Kubanian and Terek-Caspian foredeeps. As consequence, extensive shallow and swampy environments started to develop during the late Miocene (Popov et al., 2016). Panagia section (Chapter 5) captures the transition from deeper to shallow water settings. At present, the stratigraphic sequence is tectonically uplifted and overturned, exposing the entire Miocene sequence along the north shore of the Black Sea, Taman Peninsula.

2.2 Mediterranean system

2.2.1 Origins and geography

The Mediterranean geological history goes back to Triassic, when Neotethys ocean was active (Robertson et al., 1991). At that time several branches were opened (e.g. Sakarya, Pelagonian, east Tauride, Menderes–Tauride, etc.). During the late Cretaceous the convergence between Eurasia, Arabia and the African plate began, causing the active spreading ridges to collapse (Robertson and Dixon, 1984). From the late Cretaceous to Paleogene several subduction zones developed. The progressive convergence resulted in a protracted and complex terrain accretion, closing the northern branches of the Neotethyan ocean, only the southernmost strand remaining active (Aksu et al., 2005). This southern branch was reshaped by subduction during Neogene into what we know as the Mediterranean basin.

The present-day tectonic Mediterranean domain is divided into several microplates (Apulia-Adriatic, West Mediterranean, Levantine-Sinai and Aegean) and is controlled by active subduction planes and lateral escapement (Figure 2.4). The complex Mediterranean also acts like a buffer between the African and Eurasian plates, making it instrumental for the development of numerous geological principles and geodynamic concepts on mountain building and collapse, as well as their relationship with subduction evolution (van Hinsbergen et al., 2020).

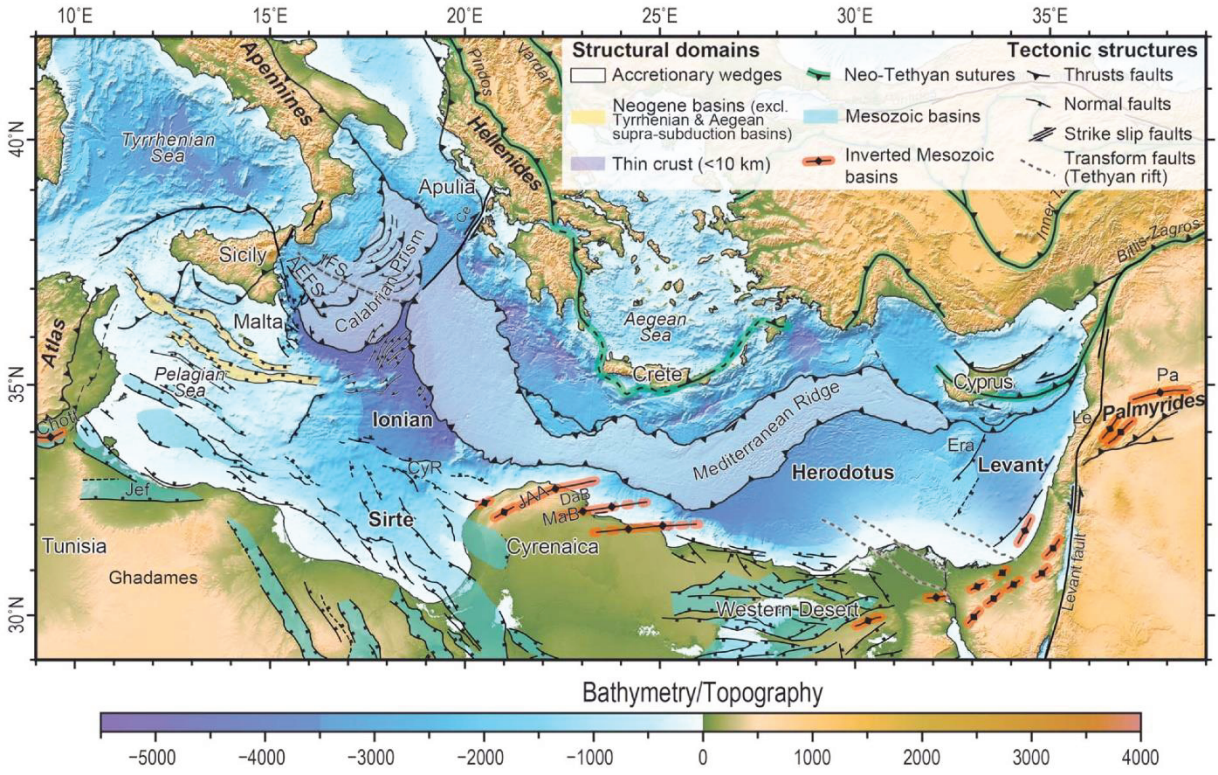

Figure 2.4 Simplified structural map of the eastern Mediterranean Basins. AEFA: Alfeo-Etna Fault system; Ce: Cephalonia Fault; CyR: Cyrenaica Ridge; DaB: Darnah Basin; Era: Eratosthenes; IFS: Ionian Fault System; JAA: Jabal Al Akhdar; Jef: Jeffara Basin; Le: Lebanon; MaB: Marmarica Basin; Pa: Palmyra through (Tugel et al., 2019 and references therein).

2.2.2 Timeline

2.2.2.1 Triassic-Middle Miocene

Until Late Cretaceous the proto-Mediterranean area was dominated by an extensional regime, which changed into compressional once Africa-Eurasia entered in collision. The tectonically driven Cenozoic closure of the Tethys Ocean invoked a significant reorganization of oceanic circulation and climate patterns on a global scale (Torfstein and Steinberg, 2020). The Paleogene sedimentation was dominated by shallow carbonate platforms (e.g. Carnevale et al., 2011; Reuter et al., 2013), concentrated on the shelf. These platforms reached the maximum extension after the Eocene Thermal optimum, when large areas were flooded. These environments prevailed until the late Miocene, when global cooling started. Significant cooling occurred around 15–12 Ma, after the Middle Miocene Climatic Optimum (Zachos et al., 2001), which intensified ~7 Ma, with the onset of the Greenland glaciation (Capella et al., 2019).

Prior to the late Miocene, the Mediterranean had open connectivity to the Atlantic and Indian Oceans, and temporary with the Paratethys. The Indian gateway (via Red Sea) had closed completely by the late Miocene (Rögl, 1999), as well as paratethyan gateways. The only open gateway remaining was with the Atlantic.

2.2.2.2 Late Miocene-Pliocene

During the Tortonian (~11.6 to 7.2 Ma), several marine gateways through southern Spain, northern Morocco and potentially Gibraltar, connected the Mediterranean with the Atlantic (Krijgsman et al., 2018), the Betic being already restricted since early Tortonian (Martín et al., 2014). As the collision Africa-Iberia and tectonic uplift in Northern Morocco advanced (Cappella et al., 2018), the two Atlantic gateways (Betic and Rifian corridors) closed.

The final closure of the gateways and sea level fall due to the growth of the Antarctic ice cap isolated the Mediterranean from the global ocean. This isolation resulted in a dramatic drop down and onset of evaporitic precipitation in marginal basins (Krijgsman et al., 1999; Roveri and Manzi, 2006), leading to a basinal catastrophe between 5.97 and 5.33 Ma., called the Messinian Salinity Crisis (MSC; Manzi et al., 2013) (Figure 2.5).

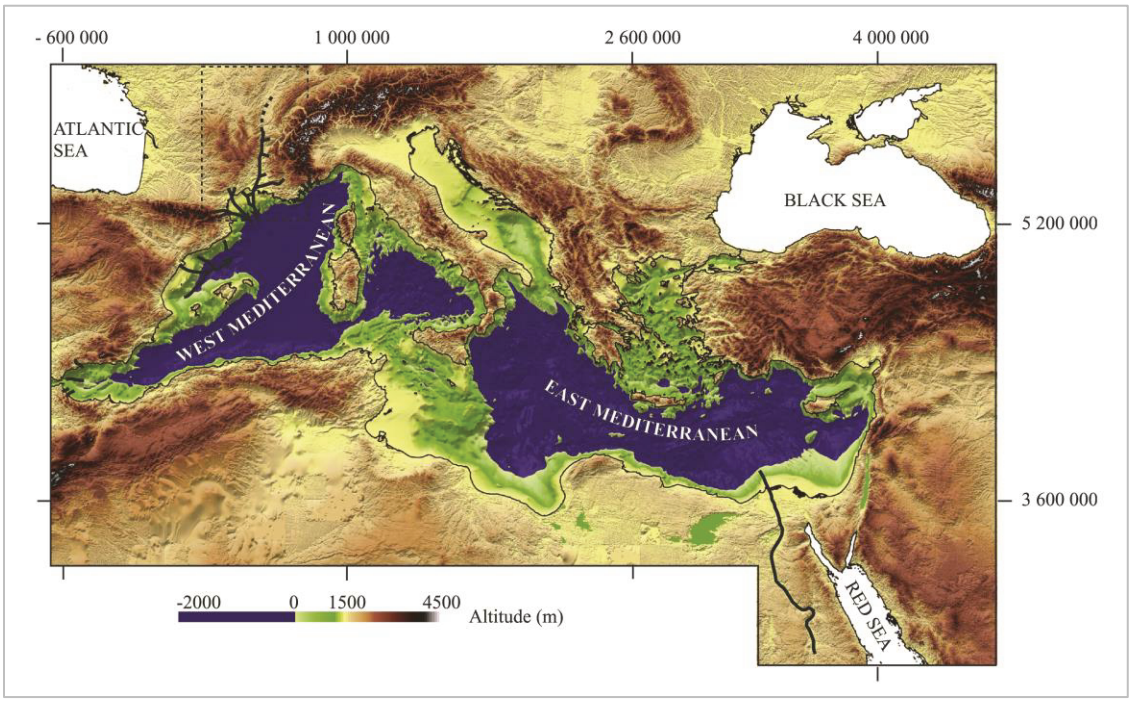

Figure 2.5 Digital elevation model of the Mediterranean region during the Messinian Salinity Crisis (GTOPO30 and ETOPO2, Mercator projection in meters; Loget et al., 2006).

Throughout the MSC the Mediterranean evolved as an enclosed system, cut off from the oceanic domain. The only water input was possible through riverine discharge from the catchments around it and from the Paratethys, especially for the interval between 5.55 and 5.33 Ma, during the so-called Lago Mare.

During the early Pliocene, the Gibraltar strait opened (Hsü et al., 1973a), reestablishing the connection with the Atlantic. The reconnection was initially small (possibly a narrow and elongated channel (Krijgsman et al., 2018), but enlarged over time through erosion, as water from the Atlantic was cascading into the Mediterranean until full connection was established.

2.2.3 Relationships with Paratethys: connectivity vs. isolation

The Paratethys and the Mediterranean water bodies governed the Cenozoic Eurasia's paleogeography and paleoclimate and were connected directly from the late Oligocene until early Miocene (Berger et al., 2005). After the uplift of the Alpine foreland, this connection was terminated. During the Miocene Climatic Optimum (early Badenian in the Paratethys stage nomenclature), transgressions from the Mediterranean toward the Central Paratethys via the Transtethyan Corridor (Slovenia and northern Croatia; Kováč et al., 2007) flooded the Pannonian Basin (Central Paratethys) and further the Carpathian Foredeep, bringing with it newcomers, like planktonic foraminifera *Orbulina suturalis* (Ćorić et al., 2008).

The connection between Paratethys and Mediterranean is interrupted until Messinian (7.27−5.33 Ma) when a new gateway opens in the northern Aegean (6.9−6.1 Ma; Krijgsman et al., 2020). The first persisting marine conditions in the Egemar basin (proto- Marmara and North Aegean), alternating with brackish Paratethyan environments, appear during this time period, with multiple marine influxes (Krijgsman et al., 2020). The termination of marine conditions is very well documented by a marked paleoenvironmental change to the brackish water environments that correlate to the Maeotian/Pontian local stages boundary (6.1 Ma) in Eastern Paratethys.

A major flood is also documented at ~6.8 Ma from the Mediterranean into Paratethys during the Intra-Maeotian Event (IME), resulting in a sudden water level drop for the Mediterranean (6.8−6.1 Ma; Palcu, 2018). At 6.1 Ma the entire Eastern Paratethys region is reconnected with Lake Pannon and the Mediterranean, as suggested by the faunal exchange and

migration (6.1–5.6 Ma in Russia; 6.1–4.8 Ma in Romania) (Krijgsman et al., 2010; Van Baak et al., 2017).

Once the connection with the Atlantic was restored (5.33 Ma) through the new born Gibraltar corridor, the Mediterranean was flooded by Atlantic waters (Garcia-Castellanos et al., 2009) causing the Zanclean flood, the refilling of the Mediterranean. Paratethys fauna from Spain (Stoica et al., 2016) and Italy (Cosentino et al., 2012) suggest that Paratethys influxes in the Mediterranean occurred during the latest MSC and opportunistic migrators took advantage of the brackish conditions from the Mediterranean during Lago-Mare phase (5.55−5.33 Ma).

As late Miocene Paratethys and Mediterranean changes in connectivity affected profoundly the stratigraphy of the two basins, a revised chronology has been developed as well, mainly based on the integration of ostracod biostratigraphy and magnetostratigraphy (Figure 2.6).

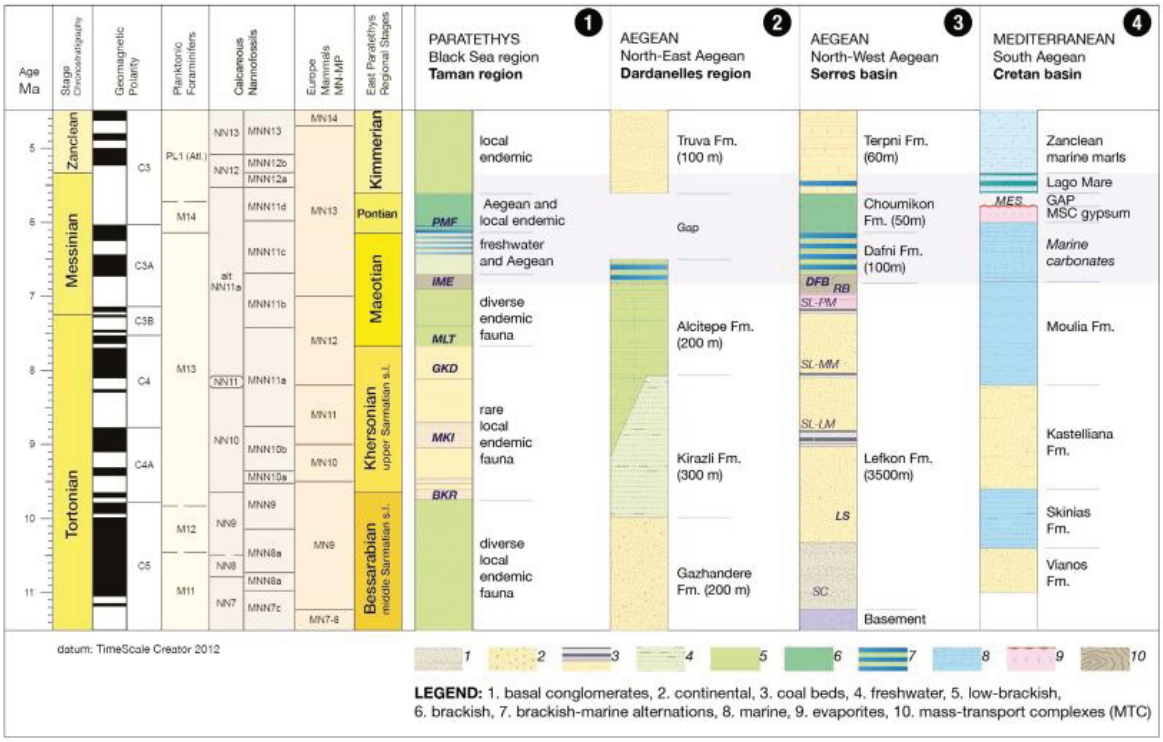

Figure 2.6 Synthetic chronostratigraphic and biostratigraphic table for the Paratethys-Mediterranean systems (Krijgsman et al., 2020 and references therein).

Episodic or sustained marine connectivity affected drastically the two systems, both in terms of hydrology and faunal exchange. Lack of connectivity and isolation also had a major

impact over the two systems. The Paratethys was first fragmented, then sub-basins became semi- or completely isolated. A series of severe draughts caused by negative water budgets are registered in the Eastern Paratethys (Popov et al., 2006; Vasiliev et al., 2017; 2020; Palcu et al., 2019; 2021; Butiseacă et al., 2021− Chapter 5), as the basin is cut off from the rest of the open marine domain.

The reduced Paratethys water surface meant not only isolation of different sub-basins, but also of the organisms populating it. The restriction led either to extinction (i.e. the paratethyan whales), or to speciation (i.e. mollusks and planktonic taxa; terrestrial mammals). The lack of connectivity between the Paratethys and the Mediterranean basins reshaped Eurasian faunal composition and migration routes (Koufos et al., 2005) (e.g. Vallesian and Turolian mammal turnovers), and promoted the spreading of grasslands (e.g. Uno et al., 2016; Butiseacă et al., 2021) in Eurasia. It created new land bridges and finally, it led to first hominines in Europe at ~7.2 Ma (Böhme et al., 2017).

References

Aksu, A.E., Calon, T.J., Hall, J., Yaşar, D. 2005. Origin and evolution of the Neogene Iskenderun Basin, northeastern Mediterranean Sea. Marine Geology 221 (1−4), 161−187.

Andrusov, N.L., 1890. Need for deep-water investigations in the Black Sea: Izv. Russk. Geogr. Obshch., 26, 171−185.

Bartol, M., et al., 2014. Paleontological evidence of communication between the Central Paratethys and the Mediterranean in the late Badenian/early Serravallian." Palaeogeography, Palaeoclimatology, Palaeoecology 394, 144−157.

Berger, J.−P., Reichenbacher, B., Becker, D., Grimm, M., Grimm, K., Picot, L., Storni, A., Pirkenseer, C., Derer, C., Scaefer, A., 2005. Paleogeography of the Upper Rhine Graben (URG) and the Swiss Molasse Basin (SMB) from Eocene to Pliocene. International Journal of Earth Sciences 94, 697−710.

Böhme, M., Spassov, N., Ebner, M., Geraads, D., Hristova, L., Kirscher, U., Kötter, S., Linnemann, U., Prieto, J., Roussiakis, S., Theodorou, G., Uhlig, G., Winklhofer, M., 2017. Messinian age and savannah environment of the possible hominin Graecopithecus from Europe. Plos one.

Böhme, M., Spassov, N., Majidifard, M.R., Gärtner, A., Kirscher, Marks, M., Dietzel, C.U., Uhlig, G., El Atfy, H., Begun, D.R., Winklhofer, M., 2021. Neogene hyperaridity in Arabia drove the directions of mammalian dispersal between Africa and Eurasia, Nature Communication Earth and Environment, 2, 85, https://doi.org/10.1038/s43247-021-00158-y.

Butiseacă, G.A., Vasiliev, I., van der Meer, M.T.J., Krijgsman, W., Palcu, D.V., Feurdean, A., Niedermeyer, E.M., Mulch., A., 2021. Severe late Miocene droughts affected Eurasia. Global and Planetary Change. https://doi.org/10.1016/j.gloplacha.2021.103644.

Capella, W., Barhoun, N., Flecker, R., Hilgen, F.J., Kouwenhoven, T.E., Mațenco, L., Sierro, F.J., Tulbure, M., Zousfi, Z., Krijgsman, W., 2018. Palaeogeographic evolution of the Late Miocene Rifian Corridor (Morocco): reconstructions from surface and subsurface data Earth-Sci. Rev., 180, 37−59.

Capella, W., Flecker, R., Hernandez-Molina, F.J., Simon, D., Meijer, P.T., Rogerson, M., Sierro, F.J., Krijgsman, W., 2019. Mediterranean isolation preconditioning the Earth System for late Miocene cooling. Scientific reports 9, 3785.

Carnevale, G., Patacca E., Scandone P. R.C.M.N.S. Interim Coll; Scontrone, Italy, 2011. Field guide to the post-conference excursions (Scontrone, Palena and Montagna della Majella). 1–98.

Clauzon, G., Suc, J.−P., Popescu, S.−M., Mărunțeanu, M., Rubino, J.-L., Marinescu, F., Melinte, M.C., 2005. Influence of Mediterranean sea-level changes on the Dacic Basin (Eastern Paratethys) during the late Neogene: the Mediterranean Lago Mare facies deciphered. Basin Res. 17, 437–462.

Ćorić, S., Pavelić, D., Mandic, O., Vrabac, S., Rögl, f., Vranjkovic, A., 2008. The initial marine flooding of the Southern Pannonian Basin System: the North Croatian Basin transgression correlates with the Middle Miocene. Geophysical Research Abstracts, 10, EGU2008-A-06497, SRef-ID: 1607-7962/gra/EGU2008-A-06497.

Cosentino, D., Bertini, A., Cipollari, P., Florindo, F., Gliozzi, E., Grossi, F., Mastro, L., Sprovieri, M., 2012. Orbitally forced paleoenvironmental and paleoclimate changes in the late postevaporitic Messinian of the central Mediterranean Basin. Geol. Soc. Am. Bull., 124 (3-4), 499−516, 10.1130/B30462.1

Finetti, I., Bricchi, G., Del Ben, A., Pipan, M., Xuan, Z., 1988. Geophysical study of the Black Sea area. Bullettino di Geofi sica Teorica ed Applicata 30, 197–324.

Garcia-Castellanos, D., Estrada., E., Jimćnez-Munt, I., Gorini, C., Fernàndez., M., Vergés, J., De Vicente, R., 2009. Catastrophic flood of the Mediterranean after the Messinian salinity crisis. Nature, 462, 778−781, 10.1038/nature08555.

Géczy, B., 1973. Plate tectonics and paleogeography in the East-Mediterranean Mesozoic. Acta Geol. Acad. Sci. Hung., 17, 421−428.

Gökaşan, E., Demirbag., E., Oktay, F.Y., Ecevitog, B., Şimşek, M., Yüce, H., 1997. On the origin of the Bosphorus. Marine Geology 140 (1−2), 183−199.

Grad M., Brückl E., Majdánski M., Behm M., Guterch A. & CELEBRATION 2000 & ALP 2002 Working Groups, 2009: Crustal structure of the Eastern Alps and their foreland: seismic model beneath the CEL10/Alp04 profile and tectonic implications. Geophys. J. Internat. 177, 279–295. doi:10.1111/j.1365-246X.2008.04074.x.

Harzhauser, M., and Piller, W.E., 2007. Benchmark data of a changing sea − Palaeogeography, Palaeobiogeography and events in the Central Paratethys during the Miocene:

Palaeogeography, Palaeoclimatology, Palaeoecology, 253 (1–2), 8–3. doi:10.1016/j.palaeo.2007.03.031.

Hilgen, F.J., Lourens, L.J., Van Dam, J.A., 2012. The Neogene Period, in Gradstein, F.M., Ogg, J.G., Schmitz, M.D., and Ogg, G.M. eds., The Geological Time Scale 2012, Elsevier B.V., Amsterdam, 947–1002.

Hsü, K.J., Ryan.,W.B.F., Cita, M.B.,1973. Late Miocene desiccation of the Mediterranean Nature, 242 (5395), 240−244.

Koufos, G.D., Kostopoulos, D., Vlachou, T.D., 2005. Neogene/Quaternary mammalian migrations in Eastern Mediterranean. Belgian Journal of Zoology, 135 (2), 181−190.

Kováč, M., Andreyeva-Grigorovich, A., Bajraktarević, Z., Brzobohatý, R., Filipescu, S., Fodor, L., Harzhauser, M., Nagymarosy, A., Oszczypko, N., Pavelić, D., Rögl, F., Saftić, B., Sliva, U., Studencka, B., et al., 2007. Badenian evolution of the Central Paratethys Sea : paleogeography, climate and eustatic sea-level changes: Cour. Forsch.-Inst. Senckenberg, 58, December, 579–606.

Krijgsman, W., Hilgen, F.J., Raffi, I., Sierro, F.J., Wilsonk, D.S., 1999. Chronology, causes and progression of the Messinian salinity crisis. Nature, 400, 652−655.

Krijgsman, W., Stoica, M., Vasiliev., I., Popov, S.V., 2010. Rise and fall of the Paratethys Sea during the Messinian Salinity Crisis. Earth Planet. Sci. Lett., 290, 183−191, 10.1016/j.epsl.2009.12.020

Krijgsman, W., Capella, W., Simon., D., Hilgen, F.J., Kouwenhoven, T.J., Meijer, P.T., Sierro, F.J., Tulbure., M.A., van der Berg, B.C.J., van der Schee, M., Flecker, R., 2018. The Gibraltar Corridor: Watergate of the Messinian Salinity Crisis. Marine Geology 403, 238–246. https://doi.org/10.1016/j.margeo.2018.06.008

Krijgsman, W., Palcu., D.V., Andreetto, F., Stoica, M., Mandic, O., 2020. Changing seas in the Late Miocene Northern Aegean: a Paratethyan approach to Mediterranean basin evolution. Earth-Science Reviews, 210. https://doi.org/10.1016/j.earscirev.2020.103386

Krijgsman, W., Stoica, M., Hoyle, T.M., Jorissen, E., Lazarev, L.S., Rausch, L., Bista, D., Alçiçek, M.C., Ilgar, A., van den Hoek, L.W., Mayda, S., Raffi., I., Flecker., R., Mandic, O., Neubauer, T.A., Wesselinh, F.P., 2020.The myth of the Messinian Dardanelles: Late Miocene stratigraphy and palaeogeography of the ancient Aegean-Black Sea gateway. Palaeogeogr. Palaeoclimatol. Palaeoecol. 10.1016/j.palaeo.2020.110033.

Laskarev, V., 1924. Sur les équivalents du Sarmatien supérieur en Serbie. Recueil de travaux offert à M. Jovan Cvijic par ses amis et collaborateurs, 73–85.

Loget, N., Davy., P., Van Den Driessche, J., 2006. Mesoscale fluvial erosion parameters deduced from modeling the Mediterranean sea level drop during the Messinian (Late Miocene). Journal of Geophysical Research, 111, F03005. doi:10.1029/2005JF000387.

Magyar, I., Geary, D.H. and Müller, P., 1999. Paleogeographic evolution of the Late Miocene Lake Pannon in Central Europe. Palaeogeography, Palaeoclimatology, Palaeoecology , 147(3-4), 151−167.

Mandic, O., Leeuw, A. De, Bulic, J., Kuiper, K.F., Krijgsman, W., and Jurisic-Polsak, Z., 2012. Paleogeographic evolution of the Southern Pannonian Basin: 40Ar/39Ar age constraints on the Miocene continental series of Northern Croatia: International Journal of Earth Sciences, 101 (4), 1033–1046, doi: 10.1007/s00531-011-0695-6.

Manzi, V., Gennari, R., Hilgen, F., Krijgsman,W., Lugli, S., Roveri, M., Sierro, F.J., 2013. Age refinement of the Messinian salinity crisis onset in the Mediterranean. Terra Nova, 25 (4), 315−322.

Martín, J.M., Puga-Bernabéu, Á., Aguirre, J., Braga J.C., 2014. Miocene Atlantic-Mediterranean seaways in the Betic Cordillera (Southern Spain), Rev. Soc. Geol. Esp., 27 (1), 175−186.

Márton, E., Tischler, M., Csontos, L., Fügenschuh, B., and Schmid, S.M., 2007. The contact zone between the ALCAPA and Tisza-Dacia mega-tectonic units of Northern Romania in the light of new paleomagnetic data: Swiss Journal of Geosciences, 100 (1), 109–124. doi: 10.1007/ s00015-007-1205-5.

Okay, A.I., Sengör, A.M.C., Görür, N., 1994. Kinematic history of the opening of the Black Sea and its effect on the surrounding regions. Geology 22, 267–270.

Palcu, D.V, Tulbure, M., Bartol, M., Kouwenhoven, T.J., and Krijgsman, W., 2015. The Badenian – Sarmatian Extinction Event in the Carpathian foredeep basin of Romania: Paleogeographic changes in the Paratethys domain: Global and Planetary Change, 133, 346–358, doi: 10.1016/j.gloplacha.2015.08.014.

Palcu D.V., Golovina L.A., Vernyhorova Y.V., Popov S.V., Krijgsman W., 2017. Middle Miocene paleoenvironmental crises in Central Eurasia caused by changes in marine gateway configuration. Global and Planetary Change, 158, 57–71. https://doi.org/10.1016/j.gloplacha.2017.09.013

Palcu, D.V., 2018. The Dire Straits of Paratethys. Dating, matching and modeling connectivity between the Miocene seas of Eurasia. PhD thesis. Utrecht, The Netherlands.

Palcu, D.V., Vasiliev, I., Stoica, M., Krijgsman, W., 2019. The end of the Great Khersonian Drying of Eurasia: Magnetostratigraphic dating of the Maeotian transgression in the Eastern Paratethys. Basin Research, 31, 33–58.

Palcu, D.V., Patina, I.S., Şandric, I., Lazarev, S., Vasiliev, I., Stoica, M., Krijgsman, W., 2021. Late Miocene megalake regressions in Eurasia. Scientific reports, 11, 11471. doi.org/10.1038/s41598-021-91001-z.

Papp, A., and Cicha, I., 1978. Definition der Zeiteinheit M - Badenian, in Chronostratigraphie und Neostratotypen, 47–48.

Popov, S.V., Shcherba, I.G., Iluina, L.B., Nevesskaya, L.A., Paramonova, N.P., Khondkarian, S.O., Magyar, I., 2006. Late Miocene paleogeography of the Paratethys and its relation to the Mediterranean. Palaeogeography, Palaeoclimatology, Palaeoecology, 238, 91–106.

Popov, S.V., Rostovtseva, Y.V., Gillipova, N.Y., Golovina, L.A., Radionova, E.P., Goncharova, I.A, Vernyhorova, Y.V., Dykan, N.I., Pinchuk, T.N., Iljina, L.B., Koromyslova, A.V., Kocyrenko, T.M., Nikolaeva, I.A., Viskova, L.A., 2016. Paleontology and Stratigraphy of the Middle-Upper Miocene of the Taman Peninsula. Paleontological Journal, 50, 10, 1–168.

Reuter, M., Piller, W.E., Brandano, M., Harzhauser, M., 2013. Global and Planetary Changes 111, 226−236. doi: 10.1016/j.gloplacha.2013.09.018

Robertson, A.H.F., Dixon, J.E., 1984. Introduction: aspects of the geological evolution of the Eastern Mediterranean. In: Dixon, J.E., Robertson, A.H.F. (Eds.), The Geological Evolution of the Eastern Mediterranean, Geological Society Special Publication. 17, 1 – 74.

Robertson, A.H.F., Clift, P.D., Degnan, P., Jones, G., 1991. Paleogeographic and paleotectonic evolution of the Eastern Mediterranean Neotethys. Palaeogeography, Palaeoclimatology, Palaeoecology, 87, 289 – 344.

Rögl, F., 1999. Mediterranean and paratethys. Facts and hypotheses of an Oligocene to Miocene Paleogeography (short overview): Geologica Carpathica, 50 (4), 339–349.

Roveri, M., Manzi, V., The Messinian Salinity Crisis: looking for a new paradigm? Palaeogeography, Palaeoclimatology, Palaeoecology, 238 (1), 386−398.

Sant, K., Palcu, D.V., Mandic, O., Krijgsman, W., 2017. Changing seas in the Early-Middle Miocene of Central Europe. Terra Nova. http://dx.doi.org/10.1111/ter.12273.

Scotese, C.R., 2021. An Atlas of Phanerozoic Paleogeographic Maps: The seas come in and the seas go out. Annual Review of Earth and Planetary Sciences 49, 679−728.

Seneš, J., 1961. "Paläogeographie des Westkarpatischen Raumes in Beziehung zur übrigen Paratethys im Miozän." Geologické Práce, 60, 1−56.

Strovba, S.M., Papadyuk, I.V., Fenota, P.O., Khriachtchevskaia, O.I., 2021. Geological structure and tectonic evolution of the Ukrainian sector of the Black Sea. Geofizicheskiy zhurnal, 42(5), 53–106. DOI: https://doi.org/10.24028/gzh.0203-3100.v42i5.2020.215072.

Stoica, M., Krijgsman, W., Fortuin, A., Gliozzi, E., 2016. Paratethyan ostracods in the Spanish Lago-Mare: More evidence for interbasinal exchange at high Mediterranean sea level. Palaeogeography, Palaeoclimatology, Palaeoecology 441 (4), 854−870.

Tari, G., Davies, J., Dellmour, R., Larratt, E., Novotny, B. & Kozhuharov, E. 2009. Play types and hydrocarbon potential of the deepwater Black Sea, NE Bulgaria. The Leading Edge 28, 1076–1081.

Torfstein, A., Steinberg, J., 2020. The Oligo-Miocene closure of the Tethys Ocean and evolution of the Proto-Mediterranean Sea. Sci. Rep. 10(1):13817. doi: 10.1038/s41598-020-70652-4

Tugend, J., Chamot-Rooke, N., Arsenikos, S., Blanpied, C., Frizon de Lamotte, D., 2019. Geology of the Ionian Basin and Margins: A Key to the East Mediterranean Geodynamics. Tectonics, American Geophysical Union (AGU), 38 (8).2668-2702. ff10.1029/2018TC005472ff. ffhal-02324095f

Van Baak, C.G.C., Krijgsman, W., Magyar, I., Sztanó, O., Golovina, L.A., Grothe, A., Hoyle, T.M., Mandic, O., Patina, I.S., Popov, S.V., Radionova, E.P., Stoica, M., Vasiliev, I., 2017. Paratethys response to the Messinian salinity crisis. Earth-Science Reviews 172, 193−223.

Van Hinsbergen, D.J.J., Torsvik., T.H., Schmid, S.M., Maţenco, L.C., Maffione, M., Vissers, R.L.M., Gürer, D., Spakman, W., 2020. Gondwana Research, 81, 79–229.

Vasiliev, I., Mezger, E. M., Lugli, S., Reichart, G. J, Manzi, V., Roveri, M., 2017. How dry was the Mediterranean during the Messinian Salinity Crisis? Palaeogeography, Palaeoclimatology, Palaeoecology, *471,* 120–133. https://doi.org/10.1016/j.palaeo.2017.01.032

Vasiliev, I., Feurdean, A., Reichart, G.J., Mulch, A., 2020. Late Miocene intensification of continentality in the Black Sea Region. International Journal of Earth Sciences, 109, 831–846.

Uno, K. T., Polissar, P. J., Jackson, K. E., deMenocal, P.B., 2016. Neogene biomarker record of vegetation change in eastern Africa. Proceedings of the National Academy of Sciences, 113(23), 6355–6363. https://doi.org/10.1073/pnas.1521267113.

Yilmaz, Y., Tuysuz, O., Yigitbas, E., Çan Genç, S., Sengör, A.M.C., 1997. Geology and Tectonic evolution of the Pontides. In: A.G. Robinson (Ed.), Regional and Petroleum Geology of the Black Sea and Surrounding Regions: AAPG Memoir 68, p. 183-226, Tulsa, OK.

Zachos, J., Pagani, H., Sloan, L., Thomas, E., Billups, K., 2001. Trends, rhythms, and aberrations in global climate 65 Ma to present. Science 292, 686–693.

Zuschin, M., Harzhaauser, M., Hengst, B., Mandic, O., Roetzel, R., 2014. Long-term ecosystem stability in an Early Miocene estuary. Geology 42 (1), 7−10.

Chapter 3

Study sites

3.1 Panagia Section (Taman Peninsula), Russia – East Paratethys Basin

Panagia section was the first site approached for this thesis and the summarized data are discussed extensively in Chapter 5. Panagia (45°09' N, 36°38' E) is located on the southern continental margin of Taman Peninsula (south Russia), which delimitates the present day Azov Sea from the Black Sea basin (Figure 3.1).

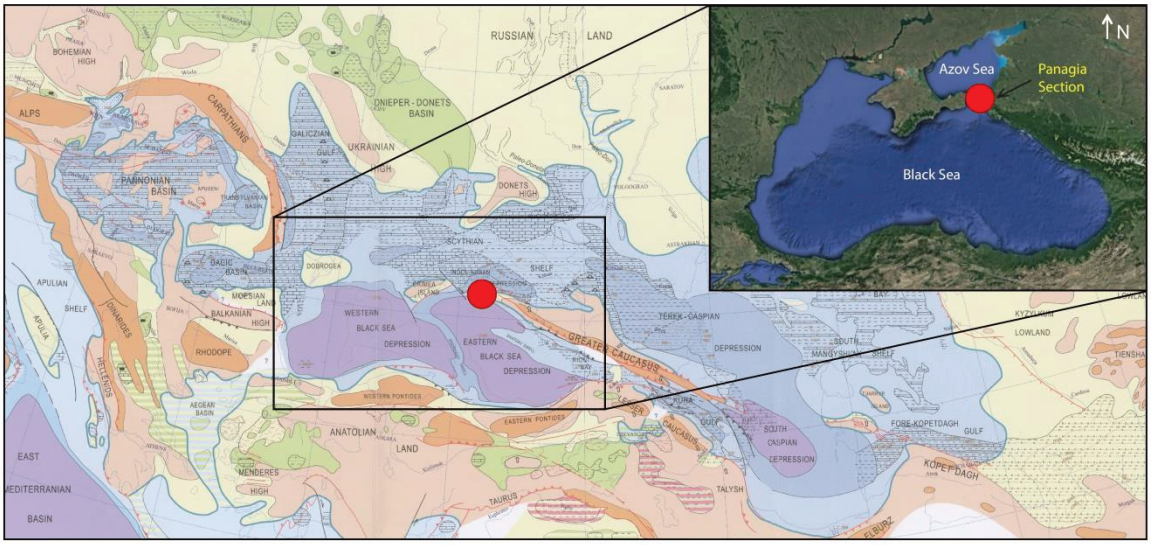

Figure 3.1 Location of Panagia Section. Location on paleogeographical map (Popov et al., 2006) within the Paratethys system during Late Miocene. Inset represents the present day location.

The section is situated in the central part of the eastern Paratethys and represents a quasi-continuous outer shelf depositional facies (Palcu et al., 2017), for a period of ~ 5 Myr (12.7−7.65 Ma, Middle−Late Miocene), which makes it a reference section for the entire eastern Paratethys. The stratigraphic succession was sampled during two fieldwork campaigns (2006, 2008) by a Dutch−Russian−Romanian team, including the necessary samples for this study. The samples were deposited at the Paleomagnetic Laboratory from Utrecht University until 2018, when subsamples from each stratigraphic level were transported to Frankfurt for organic geochemistry laboratory analyses. Presently, a large part of the section is covered by a newly built harbor, thus the access to the complete succession is not possible anymore.

Stratigraphically, Panagia section is 638 m thick and covers the entire Upper Miocene and the lower part of the Pliocene, which are disclosed in natural outcrops on the Black Sea coast and Kerch Strait (Popov et al., 2016). The Upper Miocene covers several regional stages: Volhynian, Bessarabian and Khersonian (Popov et al., 2016; Palcu et al., 2021).

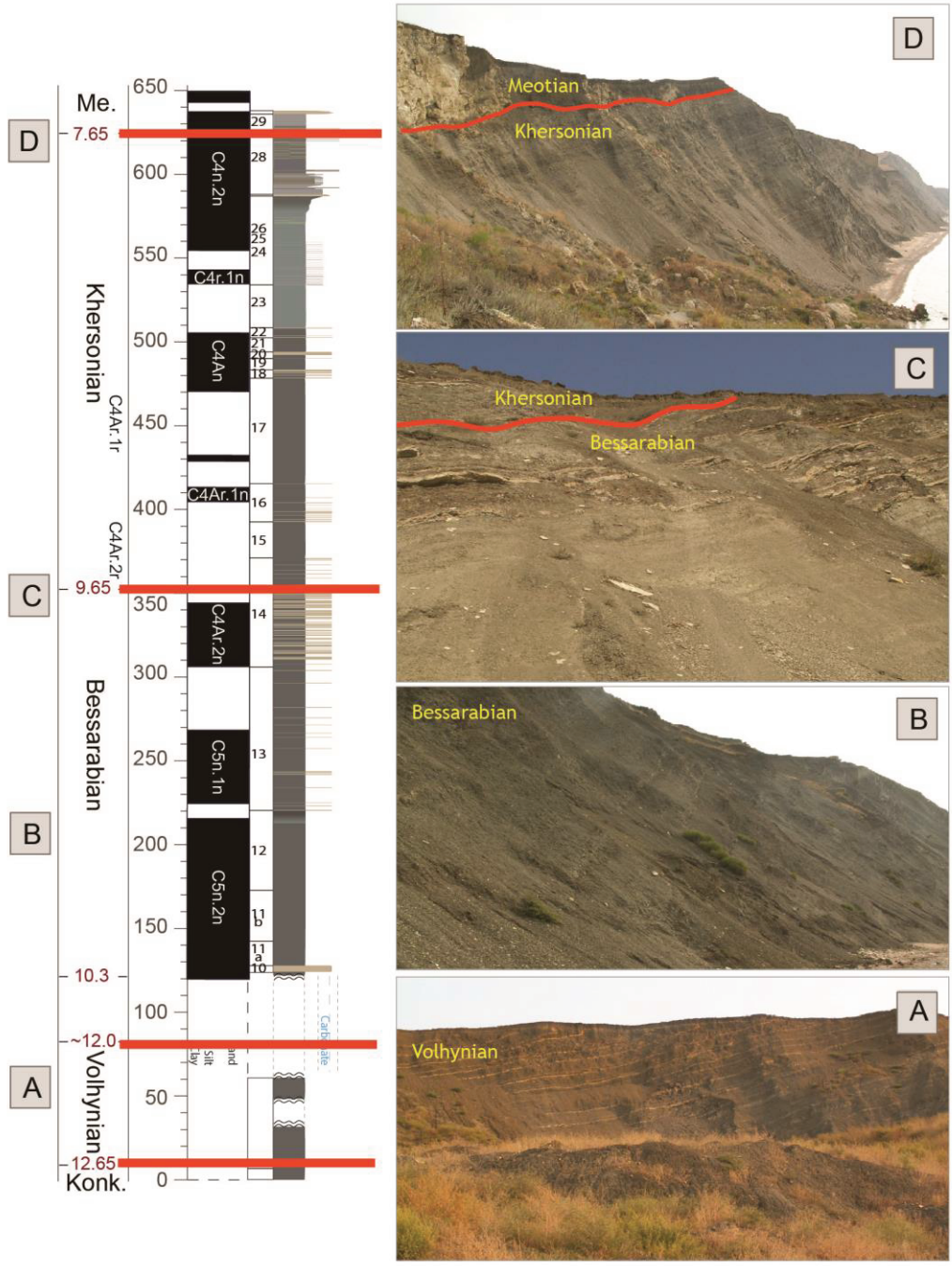

Figure 3.2 Main lithology of Panagia section. With red bars are marked the stratigraphic limits. Photos by: Iuliana Vasiliev, Wout Krijgsman and Marius Stoica.

The sediments are mainly siliciclastic, with shales and clays being dominant (Figure 3.2). Thin carbonate layers intercalations appear in Bessarabian and Khersonian. The carbonate layers were interpreted to correspond to highly evaporitic periods in the basin (Palcu et al., 2021).

Previous studies (Popov et al., 2006; Popov et al., 2016; Palcu et al., 2017; Palcu et al., 2021; Razumkova, 2012) have provided complex information about stratigraphy, paleontology, paleogeography, paleobathymetry and pollen from Panagia and other sections in Taman Peninsula. The data included in this thesis (biomarkers, stable isotopes, charcoal; Chapter 5) provide information not only about the regional paleoclimate, but about the entire eastern Paratethys region and inner-Eurasia. Vasiliev et al. (2013, 2015, 2019) and Feurdean and Vasiliev (2019) previously used similar proxy records, principally for sequences younger than ~8.5 Ma (overlapping to the terminal Khersonian until the Miocene – Pliocene boundary). The work presented in this thesis significantly extends these records back in time to 12.7 Ma, identifying major environmental changes in the eastern Paratethys and its surroundings that affect large parts of Eurasia and the biota populating it.

3.2 Agios Myron Section (Crete Island), Greece – Eastern Mediterranean Basin

The Agios Myron section is the second site investigated in this thesis with main results discussed in Chapters 6 and 7. The section (N 35°23′, E 25°12′) is located on Crete Island (Greece; Figure 3.3) in the Heraklion basin, next to the village with the homonym name. Stratigraphically, it registers a ~25 m thick very well exposed sedimentary record and covers the lower half of the Messinian (~7.2−6.5 Ma). Due to its tectonic position at the margin of the African plate (Fassoulas, 2001) it preserves a continuous reflection of the sedimentological record (Figure 3.4). The lowest 7 m of the section consist of silty marls without any identifiable evidence for cyclic deposition, while the rest of the record (8−25 m) shows clear expression of cyclic alternation of marls and laminated marls, with various thicknesses (from 7 to 80 cm).

The Agios Myron sedimentary succession is rich in macrofauna, with bivalves being the most abundant (e.g. pycnodonts, cardiids, lucinids, veneriids, pectinids), followed by gastropods (e.g. buccinidae), bryozoans, fish and sporadic plant remains. The section is also important from micropaleontological point of view, with abundant and well preserved foraminifera, ostracods,

microgastropods and fish otoliths. $\delta^{18}O$ benthic foraminifera are described and interpreted in Chapter 6 of this thesis.

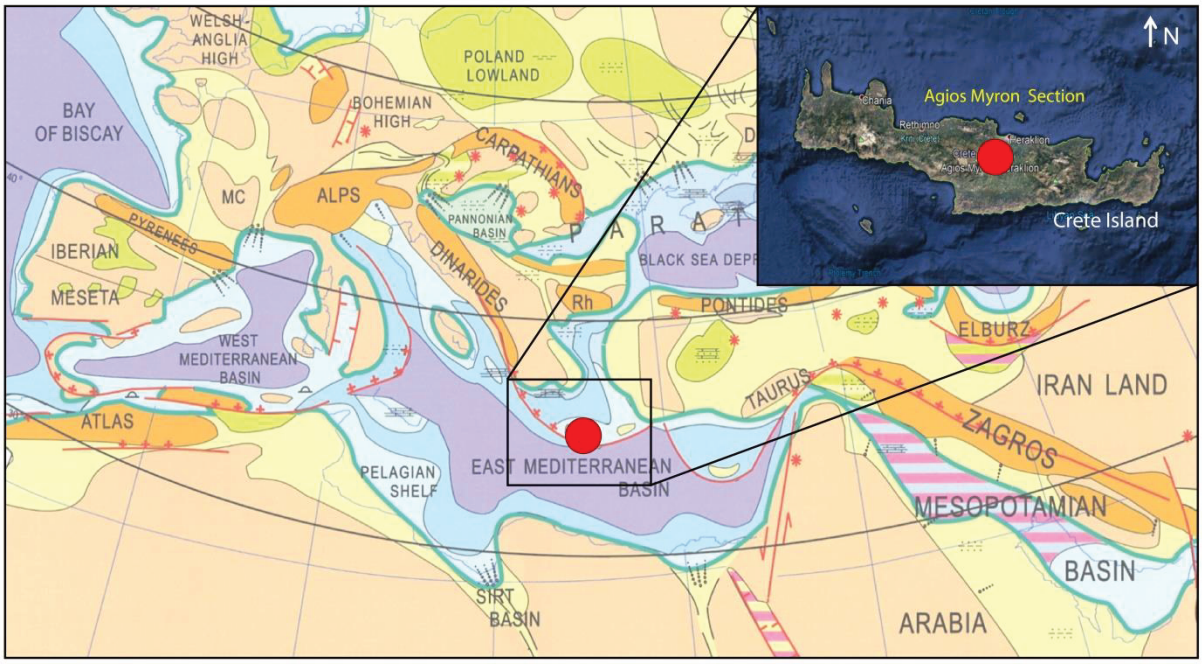

Figure 3.3 Location of Agios Myron Section on the paleogeographical map (Popov et al., 2006) within Mediterranean system during latest Miocene. Inset represents the geographical location within Crete Island.

The chronology of Agios Myron section was established by Zachariasse et al. (2021) who provided an astronomically-tuned age model based on detailed bio-cyclo-stratigraphic correlations with the nearby Metochia section (Gavdos Island, SE of Crete). The Agios Myron section covers the 7.16−6.54 Ma time interval and the age model is based on the combination of astronomically calibrated planktonic foraminiferal bioevents, tephra layers and the midpoints of the laminated marls (sapropels).

Agios Myron section is offering a glimpse of the environmental conditions in the early half of the Messinian Mediterranean and the combined proxy analysis presented in chapters six and seven will turn it into a reference section for the eastern Mediterranean paleoclimate and paleoenvironment. Here are covered a large array of proxies for both marine (Tex_{86} SST, U^{k}_{37} SST, SSS, $\delta^{18}O$ on planktonic foraminifera, $\delta^{2}H$ on alkenones, BIT, $\delta^{18}O$ and $\delta^{13}C$ on bulk carbonates) and continental domains ($\delta^{13}C$ on *n*-alkanes, MAT, pH), to better constrain the climatic evolution of the Mediterranean for the given time, as well as its response to tectonics and global factors.

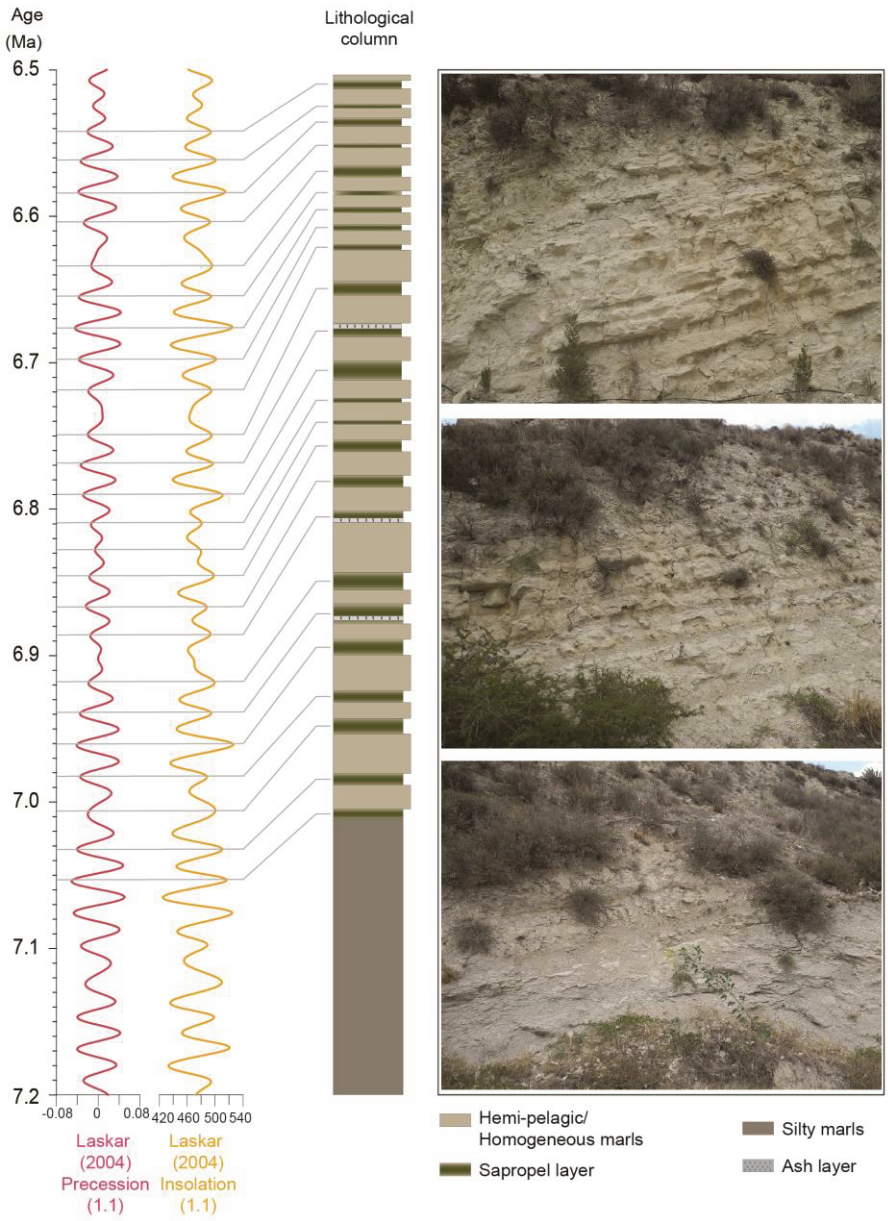

Figure 3.4 Main lithology of Agios Myron section. With red and orange are depicted the precession and insolation curves respectively. Photos by: Geanina Butiseacă and Iuliana Vasiliev.

References

Fassoulas, C., 2001. The tectonic development of a Neogene basin at the leading edge of the active European margin: the Heraklion basin, Crete, Greece. Journal of Geodynamics, 31, 49−70.

Feurdean, A. and Vasiliev, I., 2019. The contribution of fire to the late Miocene spread of grasslands in eastern Eurasia (Black Sea region). Scientific reports, 9:6950.

Palcu, D.V., Golovina, L.A., Vernyhorova, Y.V., Popov, S.V., Krijgsman, W., 2017. Middle Miocene paleoenvironmental crises in Central Eurasia caused by changes in marine gateway configuration. Global and Planetary Change, 158, 57–71.

Palcu, D.V., Patina, I.S., Şandric, I., Lazarev, S., Vasiliev, I., Stoica, M., Krijgsman, W., 2021. Late Miocene megalake regressions in Eurasia. Scientific reports, 11, 11471. doi.org/10.1038/s41598-021-91001-z.

Popov, S.V., Shcherba, I.G., Ilina, L.B., Nevesskaya, L.A., Paramonova, N.P., Khondkarian, S.O., Magyar, I., 2006. Late Miocene paleogeography of the Paratethys and its relation to the Mediterranean. Palaeogeography, Palaeoclimatology, Palaeoecology, 238, 91–106.

Popov, S.V., Rostovtseva, Y.V., Gillipova, N.Y., Golovina, L.A., Radionova, E.P., Goncharova, I.A, Vernyhorova, Y.V., Dykan, N.I., Pinchuk, T.N., Iljina, L.B., Koromyslova, A.V., Kocyrenko, T.M., Nikolaeva, I.A., Viskova, L.A., 2016. Paleontology and Stratigraphy of the Middle-Upper Miocene of the Taman Peninsula. Paleontological Journal, 50, 10, 1–168.

Razumkova, E.S., 2012. Palynological Characterization of the Sarmatian Deposits of the Eastern Paratethys (Section Zelenskii Mountain–Panagiya, Taman Peninsula). Stratigraphy and Geological Correlation, 20, 1, 97–108.

Vasiliev, I., Reichart, G.J., Krijgsman, W., 2013. Impact of the Messinian Salinity Crisis on Black Sea hydrology-Insights from hydrogen isotopes analysis on biomarkers. Earth and Planetary Science Letters 362, 272–282.

Vasiliev, I., Reichart, G.J., Grothe, A., Sinninghe Damsté, J., Krijgsman, W., Sangiorgi, F., Weijers, J.W.H., van Roij, L., 2015. Recurrent phases of drought in the upper Miocene of the Black Sea region. Palaeogeography, Palaeoclimatology, Palaeoecology 423, 18–31.

Vasiliev, I., Reichart, G.J., Krijgsman, W., Mulch, A., 2019. Black Sea rivers capture drastic change in catchment-wide mean annual temperature and soil pH during the Miocene-to-Pliocene transition, Global and Planetary Change, 172, 428–439.

Zachariasse, W.J., Kontakiotis, G., Lourens, L.J., Antonarakou, A., 2021. The Messinian of Agios Myron (Crete, Greece): A key to better understanding diatomite formation on Gavdos (south of Crete). Palaeogeography, Palaeoclimatology, Palaeoecology, 581. https://doi.org/10.1016/j.palaeo.2021.110633

Chapter 4

Laboratory work

The records produced during this PhD used a very diverse array of proxies. The core of the laboratory work is represented by organic geochemistry-based biomarker proxies coupled to compound specific stable isotopes. The thesis was further substantiated by isotope geochemistry on carbonates (foraminifera tests, bulk rocks and carbonate nodules), paleosalinity and ultimately charcoal analysis.

4.1 Biomarkers

4.1.1 Long chain *n*-alkanes

4.1.1.1 Source

Plant waxes are found primarily in the cuticles of vascular plants (Eglington and Hamilton, 1967) and their main role is to prevent and regulate water loss. The cuticle is a biopolymer (Koch and Ensikat, 2008) on the surface of leaves that protects them against external damages and allows the plant to control the exchange with the environment (water intake/transpiration and CO_2/O_2 exchange) (Figure 4.1).

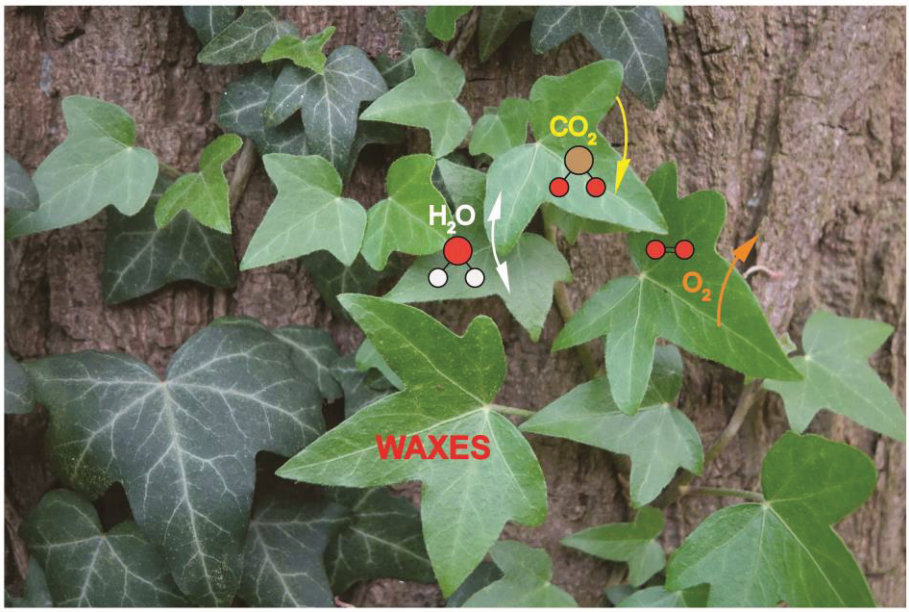

Figure 4.1 Leaf waxes in modern plants (e.g. *Hedera helix*). With yellow is marked the CO_2 intake, with white the water exchange and with orange the O_2 release.

The exterior layer of the cuticle is covered with wax crystals, a mixture of lipids (fatty acids, ketones, alcohols, etc.) resistant to biodegradation (Duan and He, 2011) that remain preserved in sediments and sedimentary rocks for a long time after plants' death. Plant waxes are used as paleo-biomarkers to reconstruct continental climate in the past (Eglington and Eglington, 2008).

4.1.1.2 Extraction and fractionation

Depending on the sample type (plant parts, soils, rocks), there are several extraction protocols that involve an apolar solvent (e.g. *n*-hexane) or a semi-polar mixture of solvents such as dichloromethane (DCM) and methanol (MeOH). Extraction can be conducted manually or involving a semi-/automatic device such as ultrasonication, Soxhlet extractors, or controlled temperature and pressure solvent extraction (Speed Extractor). For the samples included in the main chapters of this thesis I have used only the Soxhlet extraction because the initial target included further compound specific stable isotope measurements, that require overconcentration. An additional factor in using Soxhlets extractors was the presence of elemental sulphur that could harm the Speed Extractor units. Soxhlet extraction is a popular technique for extraction of analytes from solid materials since its discovery in 1879 (Zygler et al., 2012). Soxhlet apparatus is a distilling device incorporating a stove, a soxhlet glass, boiling flask, a condenser and a running water source (Figure 4.2B). Usually more soxhlets are running in parallel (up to six).
Samples are dehydrated, ground, weighted and placed in pre-extracted cellulose thimbles and further positioned in the Soxhlet apparatus (Figure 4.2A, B). A mixture of solvents is added (DCM:MeOH). The stove is turned on and continuous extraction takes place by condensing and refluxing the solvent. Once the extraction chamber is filled, the solvent mixture containing the total lipid extract (TLE) is refluxed into the boiling flask. The process is repeated for at least five times, typically for ca. 12 h. After extraction samples are concentrated and the total lipids extract is obtained (Figure 4.2C), further used for the remaining laboratory procedures.

The TLE is further evaporated to near dryness under N2 flow using a TurboVap LV. Subsequently elemental sulphur is removed from the TLE using Cu shreds. Cu is activated using 10% HCl, the acid is then removed and the activated Cu rinsed with demineralized water until a neutral pH is achieved.

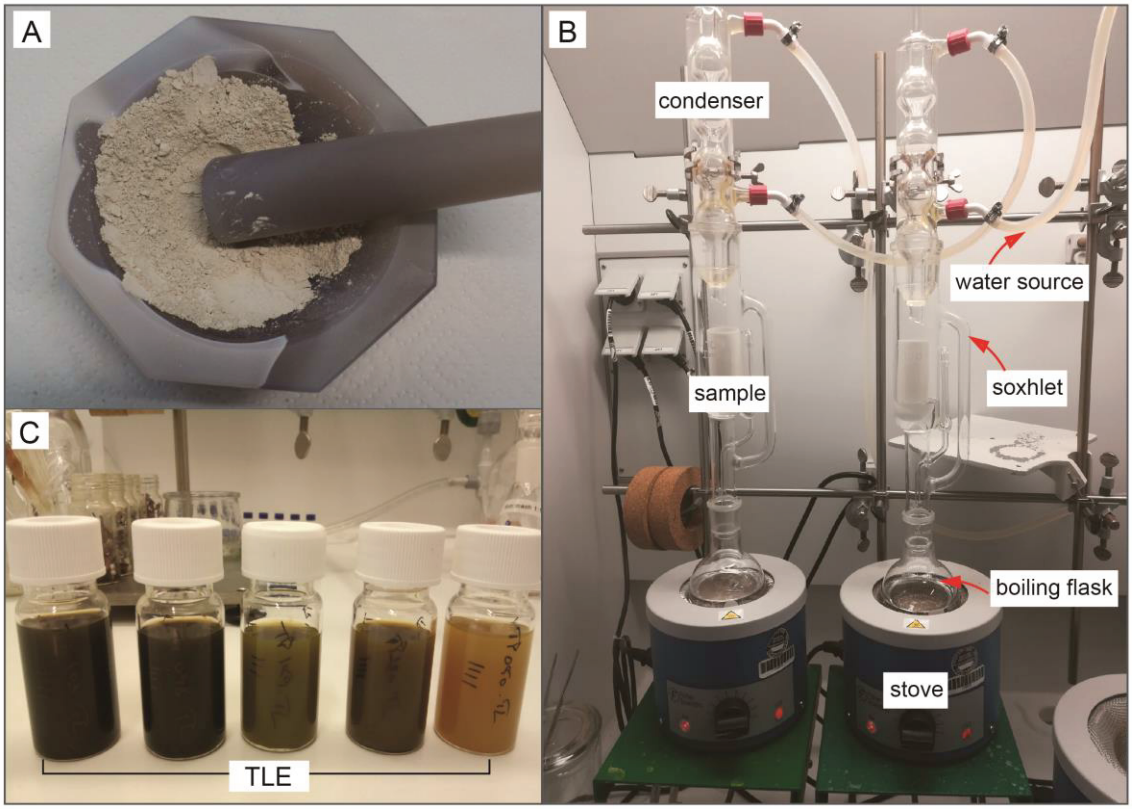

Figure 4.2 Samples preparation and extraction simplified cycle. A) Ground sample from Agios Myron section; B) Soxhlet extraction device and components; C) TLE prepared for fractionation (from Panagia section).

Cu is further cleaned using MeOH and DCM. The vials containing TLE dissolved in DCM, activated Cu and magnetic rods are placed on a rotary table for >16 hours. After each desulphurization TLEs dissolved in DCM are filtered over an anhydrous Na_2SO_4 column to filter from Cu fragments and possible water. The desulphurization step is repeated until no reaction with the Cu is observed.

Part of the TLE is archived. The work TLE is then separated into fractions (specific compounds with increased polarity) using Al_2O_3 column chromatography: apolar (e.g. *n*-alkanes) using *n*-HEX:DCM (*v:v*/9:1), ketones (e.g. alkenones) using DCM, polar (e.g. GDGTs) with DCM:MeOH (*v:v*/1:1) and a rest containing most polar lipids with MeOH only. Prior to separation into fractions, the Al_2O_3 is combusted for two hours at 150 °C and left in a desiccator for at least 30 minutes. The apolar fraction containing n-alkanes is further purified using AgNO3 covered silica-gel column chromatography. This fraction is further separate in two sub-fractions, one eluted with *n*-hexane (the saturated) and the second with DCM (the unsaturated). The saturated part is further purified using urea adduction, resulting in the isolating of strait chain *n*-

alkanes. After urea adduction, the adduct part (clean and well separated *n*-alkanes, Figure 4.3) are used for compound specific stable isotope measurements. All samples in this work were extracted and prepared following the protocol from Vasiliev (2020) laboratory notebook. Purified samples were injected using an auto sampler onto the GC−MS using *n*-hexane.

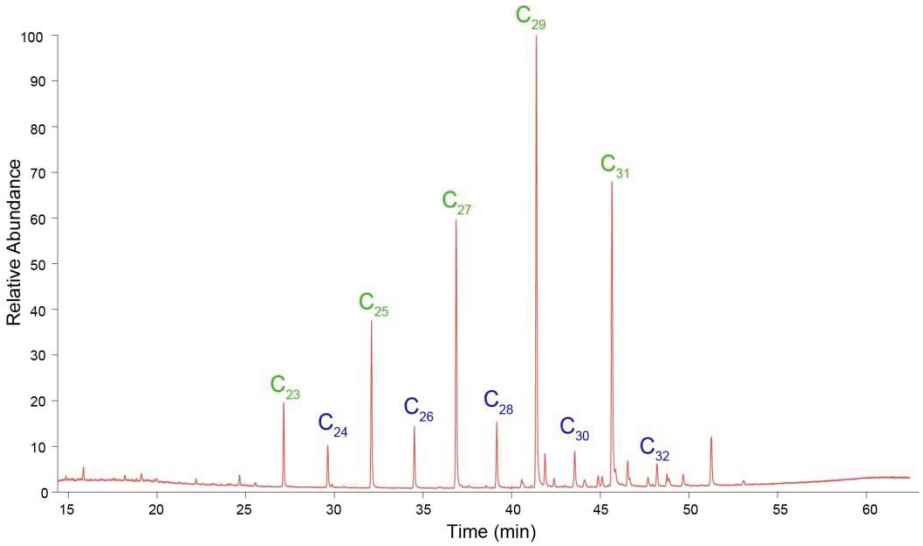

Figure 4.3 Example of clean chromatogram after urea adduction (TP 263- Panagia Section)

4.1.1.3 Application as proxy for paleo-vegetation

N-alkanes are acyclic saturated hydrocarbon compounds with a general formula of $C_nH_{2n}+2$. C_{14}−C_{20} are considered short chain *n*-alkanes, while C_{20}−C_{40} long chain ones. Plant derived n-alkanes show an odd-over-even predominance in the chain lengths as a result of a dominance of the biosynthetic pathway leading to odd numbered n-alkanes over the one leading to even numbered *n*-alkanes (Zhou et al., 2010). Due to their increased resistance against microbial decomposition in comparison with lipidic precursor compounds like fatty acids and alcohols (Kästner, 2000), *n*-alkanes are usually very well preserved in sediments. The chain length of *n*-alkanes indicate their provenance, odd carbon numbered long-chained (>C_{25}) alkanes being produced by higher plants (Eglinton et al., 1967), while odd carbon numbered short-chained (<C_{21}) alkanes derive from microbial organisms (Dinel et al., 1990). Therefore, *n*-alkanes reflect the sources of organic biomass in sediments (Peters et al., 2005) and the vegetation type contributors.

4.1.2 Alkenones

4.1.2.1 Source

Alkenones are long-chained organic molecules (C_{35}–C_{40}) produced by haptophyte algae (Herbert, 2003). Present day alkenone producers belong mostly to the Isochrysidales clade, which includes the calcifying haptophytes (coccolithophores) *Emiliania huxleyi* and the closely related *Gephyrocapsa oceanica* (both being open marine taxa), and noncalcifying elements like *Isocrysis galbana* (coastal) (Marlowe et al., 1984), but recently was shown that these are not the only producers. Other species of Isochrysadales produce alkenones too (Kaiser et al., 2019; Wang et al., 2021) and populate a wide series of environments. Other haptophyte algae have produced alkenones in the past and C_{37}–C_{38} alkenones can be abundant in marine sediments.

The production of alkenones is linked to the growth temperature (Marlowe et al., 1984; Prahl and Wakeham, 1987; Figure 4.4), but was also associated with productivity (Epstein et al., 1998). Studies on modern organisms (Schulz et al., 2000; Bendle et al., 2009) have shown that alkenones production is also linked to physiological stress induced by low salinity waters; however, the exact role of producing alkenones is not known.

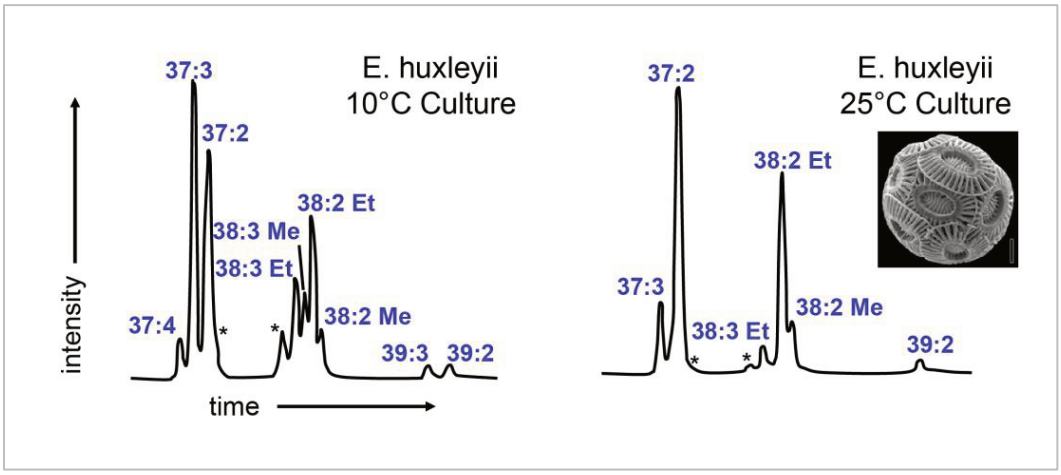

Figure 4.4 Partial gas chromatograms of the long-chain (C_{37} and C_{38}) unsaturated alkenone compositions measured in cultures of *E. huxleyii* grown isothermally in batch cultures at two different temperatures (Prahl and Wakeham, 1987).

Alkenones are the result of algae blooms. Major blooms occur as a consequence of eutrophication, the enrichment in minerals and nutrients, which takes place when sediments or fertilizers supply increase. Most blooms are seasonal, but they can also persist all year around due to the increased resilience and high competitional advantage. Alkenones and other molecule

compounds are then incorporated in sediments and stored over long periods of time. Their preservation varies with the sediments/rocks preserving conditions, water pH and diagenetic processes.

4.1.2.2 Fractionation and measurement

Alkenones (contained by the ketone and aromatic fraction) are separated from the TLE extract using DCM and measured on the GC−MS with *n*-hexane. When alkenone fraction contains many other compounds, alkenones are purified using $AgNO_3$ covered silica-gel column chromatography and eluted using ethyl acetate (EtAc), then further quantified.

4.1.2.3 Application as paleo-proxy for sea surface temperature

The frequent abundance of alkenones in sedimentary records and their production being related to changes in water temperature has made them ideal for paleoecological/paleoenvironmental reconstructions. The organisms that produce alkenones live in the upper photic zone, thus they are indicators of near-/surface water thermal conditions of large water bodies and indirectly a salinity indicator (Herbert, 2016), as they depend also on the salinity of the water they live in (Schouten et al., 2006).

Based on the relative abundance of $C_{37:2}$ and $C_{37:3}$ unsaturated ketones, an empirical function to the sea surface temperature (SST) was developed (Brassel, 1986; Prahl and Wakeham, 1987; Muller et al., 1998), called unsaturation index.

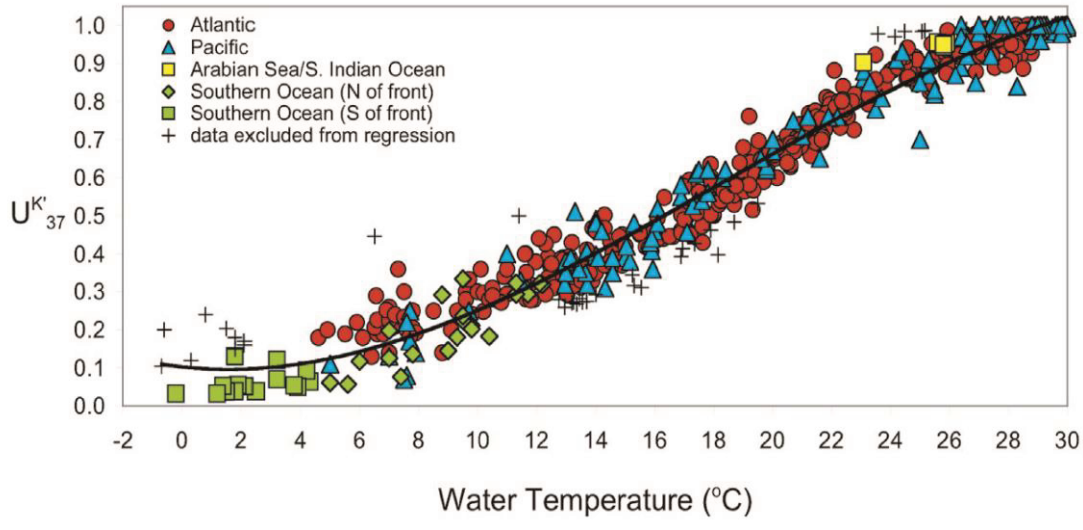

Figure 4.5 Modern global data of $U^{K}_{37}{}'$ versus measured water temperature for surface mixed layer (0 – 30 m) (Conte et al., 2006).

The unsaturation index ($U^{K}_{37}{}'$) allows us to calculate the SST and is defined as:

$$UK37' = \frac{C37:2}{C37:2 + C37:3}$$

where $C_{37:2}$ and $C_{37:3}$ are the concentrations of the di- and tri- unsaturated C_{37} alkenones. $U^{K}_{37}{}'$ values vary with sea water temperature (Figure 4.5).

4.1.3 GDGTs

4.1.3.1 Source

GDGTs (glycerol dialkyl glycerol tetraethers) are complex membrane lipids produced mainly by kingdoms Crenarchaeota and Euryarcheota, which populate various environments (Schouten et al., 2013; Pancost et al., 2001), both aquatic and terrestrial. Initially supposed to belong entirely to extremophilic Archaea, modern phylogenetic analysis proved that GDGTs are synthetized by other Archaea groups too (Figure 4.6), but also by some bacteria (Acidobacteria group, Sinninghe Damsté et al., 2007).

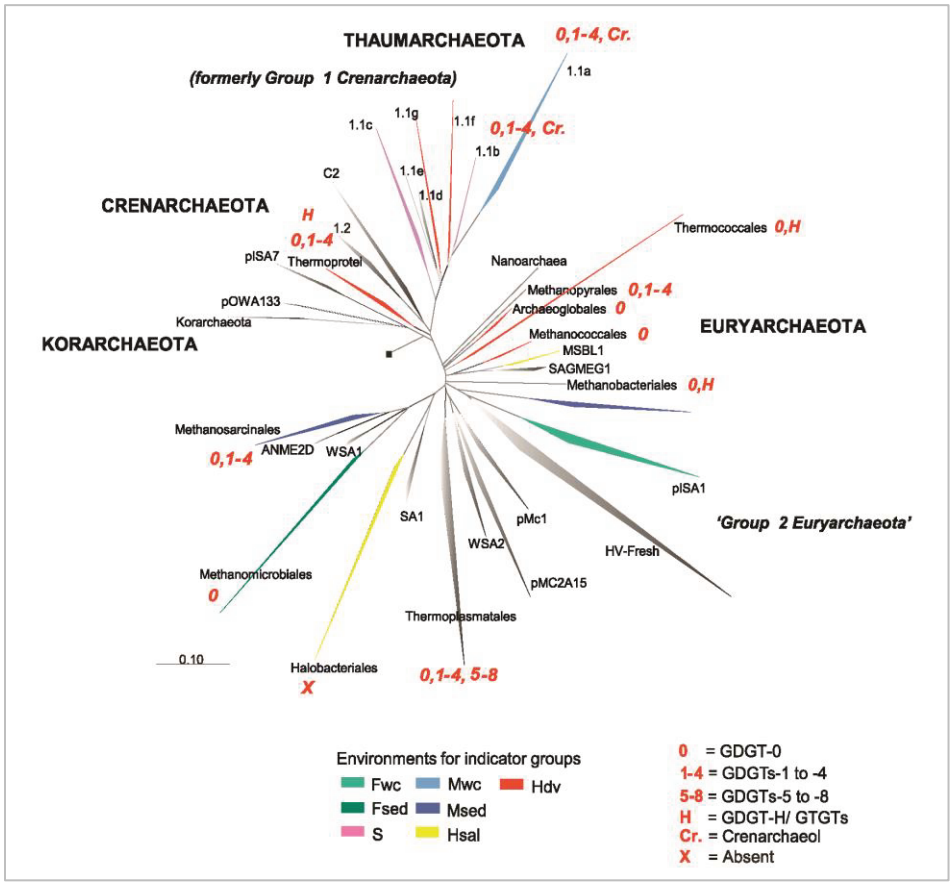

(capture next page)

Figure 4.6 Phylogeny of Archaea based on 16s rRNA gene analysis (from Schouten et al., 2013, adapted from Auguet et al., 2008). The presence of isoprenoid GDGTs in cultivated relatives within the different phylogenetic clusters is indicated. Colours indicate where the particulate phylogenetic clusters dominantly occur. Fwc, freshwater column; Fsed, freshwater sediment; S, soil; Mwc, marine water column; Msed, marine sediment; Hsal, hypersaline and Hdv, hydrothermal vent.

GDGTs are divided into two main classes according to differences in the structure of the long apolar groups connecting the two glycerol polar heads. The first class is isoprenoidal GDGTs (isoGDGTs) (Figure 4.7), which display an isoprenoid carbon skeleton (~32 carbons) which can contain from 0 (GDGT-0) to 8 (GDGT-8) cyclopentyl units and up to 1 cyclohexyl unit (Schouten et al., 2013). IsoGDGTs are abundant in marine, lacustrine and wetland environments (Schouten et al., 2000) and their production has been associated with various groups of archaea living in the water column (e.g. Thaumarchaeota, Crenarchaeota).

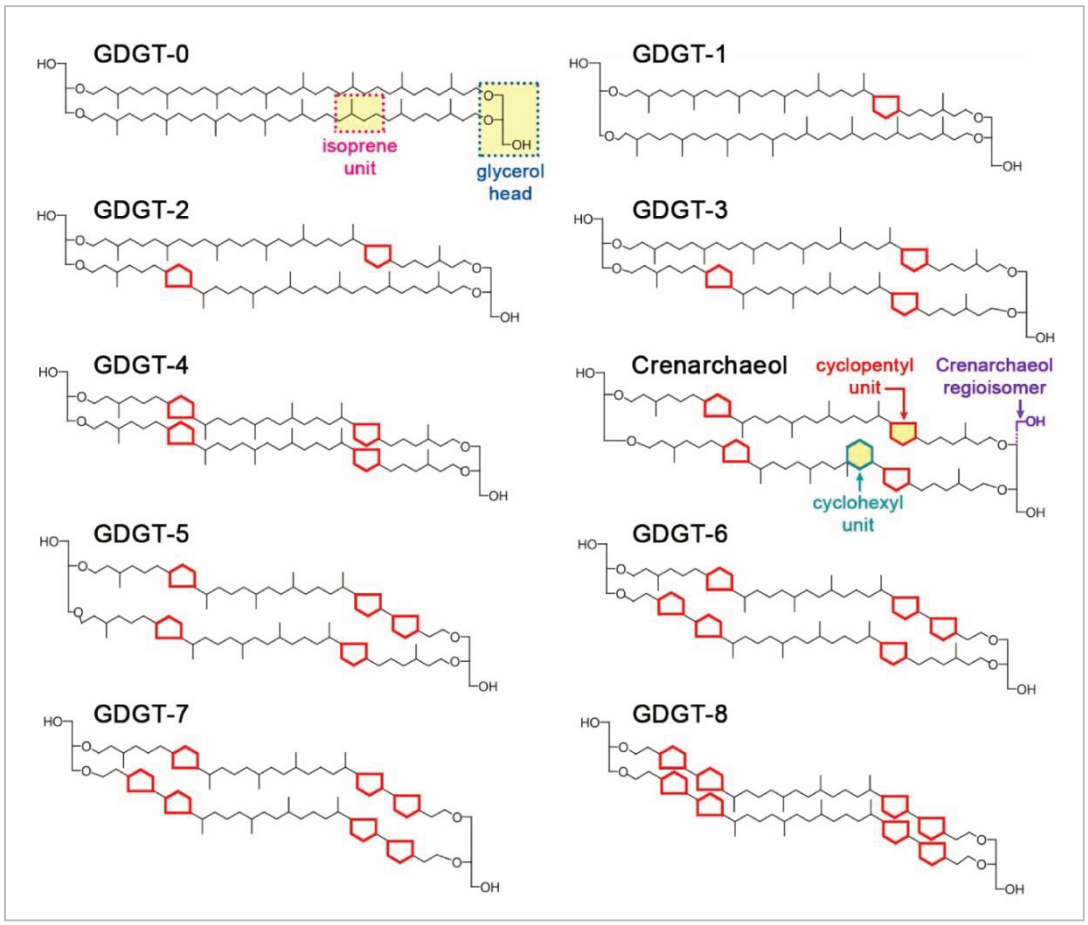

Figure 4.7 Main isoprenoidal GDGTs structures (from Ardengi, 2019; redrawn after Schouten et al., 2013). IsoGDGTs including from 0 to 3 cyclopentyl units (in red) and crenarchaeol regio-isomer (in purple) are used in TEX_{86} calibrations.

The second big class of GDGTs are branched GDGTs (brGDGTs) (Figure 4.8), in which case the glycerol polar heads are connected by two C_{28} *n*-alkyl chains containing from 4 (GDGT-I) to 6 (GDGT-III) methyl groups (di-, tri-, and tetramethyloctacosane) (Schouten et al., 2013). BrGDGTs have been recovered from soils, peats, lacustrine and deltaic sediments, indicating a terrestrial origin (e.g. Sinninghe Damsté et al., 2000; Hopmans et al., 2004).

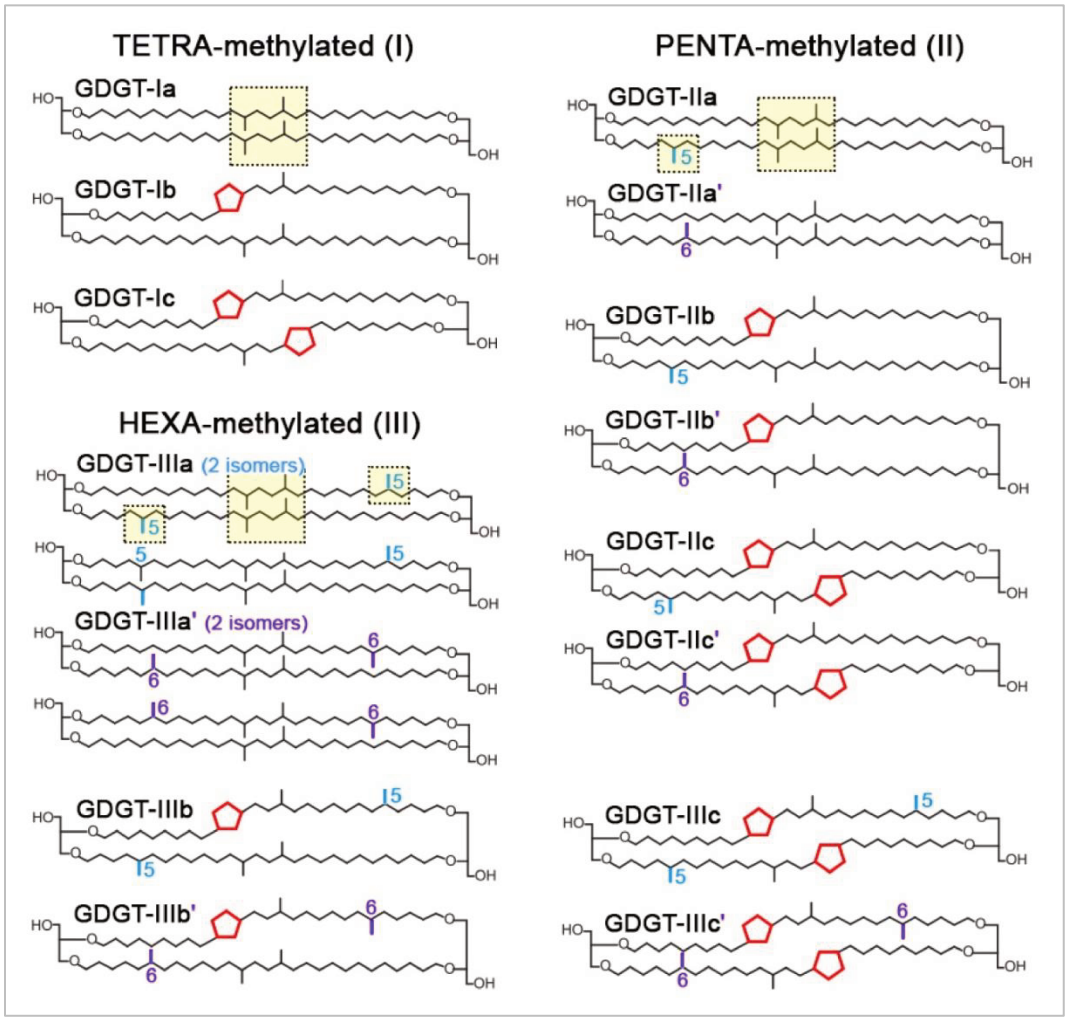

Figure 4.8 Main branched GDGTs structures (from Ardengi, 2019; redrawn after De Jonge et al., 2014). Roman numerals indicate the degree of methylation (I, II, III = tetra-, penta-, hexa-methylated), while normal letters indicate the degree of cyclisation (a, b, c = 0, 1, 2 methyl groups substituted by an equal number of cyclopentyl units, indicated in red). The position of the two additional methyl groups in II and III can be either at the 5th (blue) or 6th (purple) carbon of the tetradecane (C_{14}) moieties of the octacosane chains (C_{28}).

4.1.3.2 Fractionation and measurement

After extraction and fractionation, the polar fraction containing GDGTs is separated with DCM/MeOH (1:1, *v:v*), dried, dissolved in a 1 ml mixture of *n*-hexane (*n*-hex)/isopropanol (IPA)-(99:1, *v:v*) and filtered over a 0.45 mm PTFE filter using a 1 ml syringe, to remove part of the components like chlorophyll and excess of organic matter other than GDGTs. After filtering, the samples are concentrated and further measured on the HPLC. The acquisition of both isoprenoid and branched GDGTs is performed within a single run for each sample, or separately (depending on the interest). For this thesis, the acquisition was combined, followed by the quantification of GDGTs using Analyst software, manually integrating the picks for each sample.

4.1.3.3 Application as proxy for temperatures

As *n*-alkanes and alkenones, GDGTs are preserved in sediments over long periods of time. Due to their large distribution and colonization of different environments on the planet, GDGTs contain information about environmental parameters such as soil organic matter input (Hopmans et al., 2004), sea water temperature (Schouten et al., 2002), soil pH and mean air temperature (Weijers et al., 2007a), being used successfully as proxies for paleoclimatic reconstructions.

The SST is usually calculated by using TEX_{86} (TetraEther indeX of tetraethers consisting of 86 carbon atoms), method based on the relative abundance of isoGDGT lipids (Schouten et al., 2002). For this work TEX_{86} values were calculated as:

TEX_{86}= [(GDGT-1) + (GDGT-2) + (Crearchaeol)] /

[(GDGT-0) + (GDGT-1) + (GDGT-2) + (Crearchaeol)]

where GDGT-0, GDGT-1, GDGT-2 and Crenarchaeol are isoprenoid GDGTs.

Several calibrations have been defined for different environments, with an overall −3 to 30 °C range and error varying from less than 2 °C to 4 °C (Castañeda and Schouten, 2011 and references therein). For this thesis TEX_{86} values were converted into SST using the calibration and recommendation of Kim et al. (2010) to apply the TEX_{86}^{H} above 15 °C (i.e. outside the polar and subpolar domains):

$SST^{H} = 68.4 \times TEX_{86}^{H} + 38.6$

Here TEX_{86}^{L} is = log ((GDGT-2) / GDGT-1 + GDGT-2 + GDGT-3))

$TEX_{86}^{H} = \log (TEX_{86})$

$SST^{L} = 67.5 \times TEX_{86}^{L} + 46.9$

The distribution of brGDGTs, expressed as the Methylation index of Branched Tetraethers (MBT), correlating positively primarily to temperature, and the Cyclisation ratio of Branched Tetraethers (CBT), correlating negatively mainly to pH, were calculated using the calibration of Weijers et al. (2007a). The initial definition of MAT and pH proxies was subject to subsequent recalibration and refinement (e.g. Peterse et al., 2012; De Jonge et al., 2014). From the multiple existing calibrations, we rely on Peterse et al. (2012) as a more conservative choice given that the expected environmental changes for the more than 5 Myr duration of the studied intervals are large (12.5 to 7.6 Ma in the Black Sea domain and 7.2 to 6.4 Ma in the Mediterranean Sea). Therefore, mean annual air temperature (MAT) and pH were estimated as follows (Peterse et al., 2012):

$$MAT' = 0.81 - 5.67 \times CBT + 31 \times MBT'$$

$$pH = 7.90 - 1.97 \times CBT$$

MBT' and CBT are expressed as:

$$MBT' = [(GDGT\ Ia + GDGT\ Ib + GDGT\ Ic)] / [(GDGT\ Ia + GDGT\ Ib + GDGT\ Ic) + (GDGT\ IIa + GDGT\ IIb + GDGT\ IIIb) + (GDGT\ IIIa)]$$

$$CBT = -\log (GDGT\ Ib + GDGT\ IIb) / (GDGT\ Ia + GDGT\ IIa)$$

where *GDGT I* - *GDGT III* are branched GDGTs.

The BIT (Branched and Isoprenoid Tetraethers) index is further applied, a function that defines the terrigenous versus aquatic components of organic input into a basin. The BIT index is a ratio of the three major brGDGTs (mostly terrigenous) to isoGDGT crenarchaeol (aquatic) (Hopmans et al., 2004):

$$BIT = [(GDGT\text{-}I) + (GDGT\text{-}II) + (GDGT\text{-}III)] / [(Crenarchaeol) + (GDGT\text{-}I) + (GDGT\text{-}II) + (GDGT\text{-}III)]$$

The application of both continental and marine biomarkers on the two main study sites allowed the reconstruction of the relationship between the continental and aquatic domains in time and asses the changes in the basins' catchments and sources.

4.2 Stable isotopes

4.2.1 Compounds specific isotopes on hydrogen (δ^2H)

4.2.1.1 δ^2H on n-alkanes

N-alkanes are one of the most abundant lipid molecules biosynthesized by plants. Hydrogen is also an essential element of organic matter (Chikaraishi and Naraoka, 2003), as plants extract it from the water they receive from the environment they live in. The basic source for the deuterium (^2H, the heavy stable isotope of hydrogen) in a plant comes from the soil water (Sachse et al., 2012; Figure 4.9), which in turn depends on the concentration in the precipitation water. The δ^2H value (metabolic hydrogen) on plant materials grown under controlled conditions was correlated with pathways of photosynthetic carbon metabolism (Ziegler et al., 1976), showing major differences between C_3 and C_4 plant groups, with C_4 15% more D (^2H)-enriched (Sachse et al., 2012).

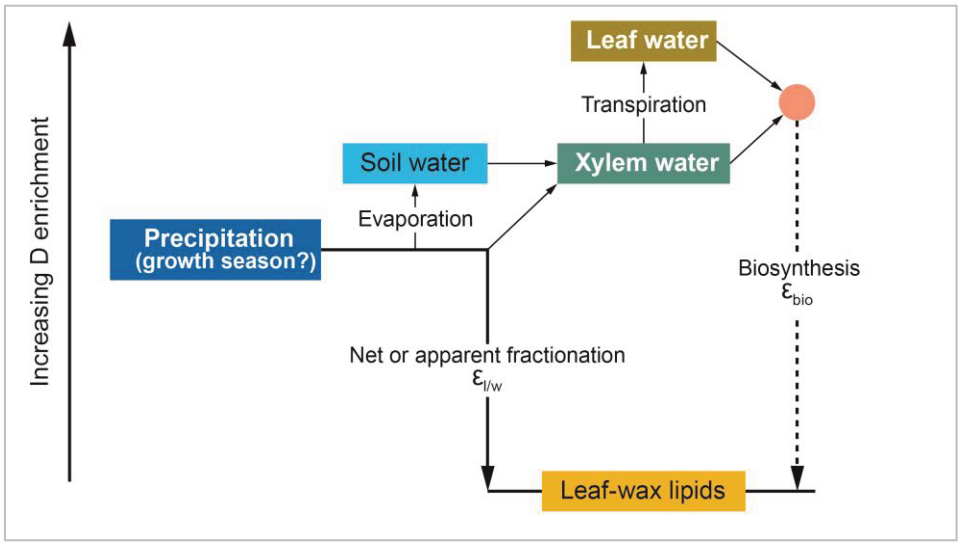

Figure 4.9 Conceptual diagram describing the hydrogen-isotopic relationships between precipitation and leaf-wax *n*-alkanes from terrestrial plants (not to scale). The red dot illustrates a hypothetical biosynthetic water pool, i.e. a potential mixture of different water pools within the leaf and the ultimate hydrogen source for lipid biosynthesis. From Sachse et al., 2012; modified after Sachse et al., 2006 and Smith & Freeman, 2006. Abbreviations: ε_{bio}, biosynthetic hydrogen-isotopic fractionation; $\varepsilon_{l/w}$, isotopic fractionation between lipids and source water.

Besides isotopic fractionation during biosynthesis, hydrogen isotopic composition of organic matter is related to hydrologic variables such as seawater mass and humidity (Chikaraishi and Naraoka, 2003), reflecting thus the evaporation and aridity. This property make is extremely useful to reconstruct past hydroclimate variability using sedimentary leaf wax δ^2H values

(Pagani et al., 2006; Sachs et al., 2009). Subsequent studies investigating lipid δ^2H (δD) values from living organisms and/or plants have revealed that additional environmental and physiological variables can also influence isotopic fractionation between hydrogen in environmental water and in terrestrial and aquatic lipids (Sachse et al., 2012; Figure 4.10A, B). The relative effects of these processes are not yet completely understood, though.

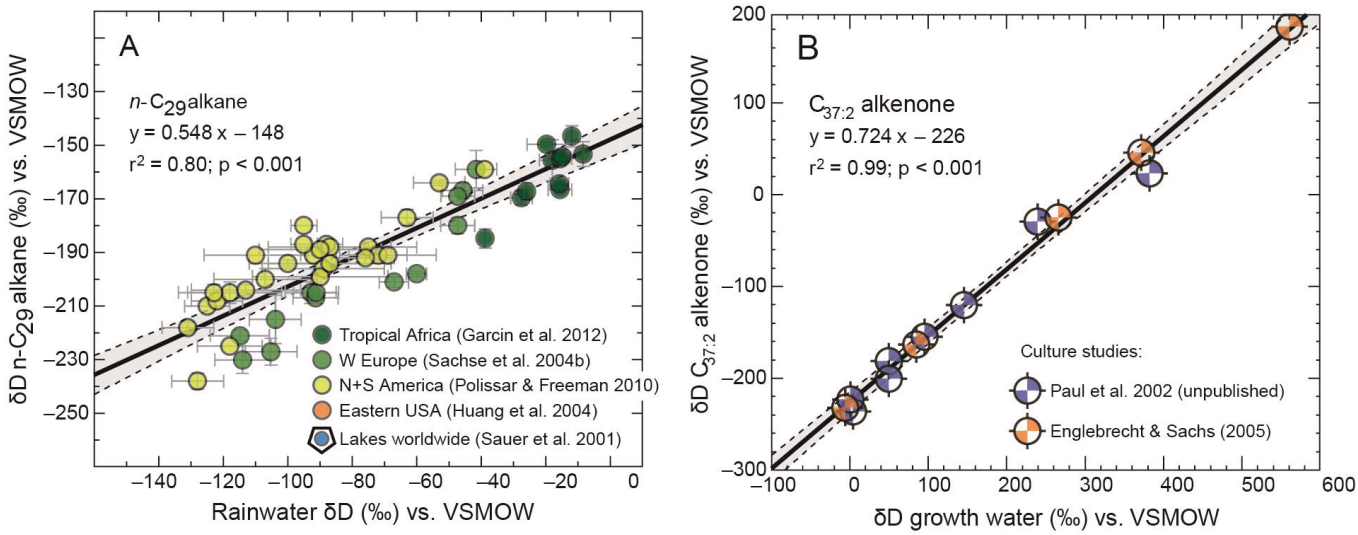

Figure 4.10 Relationships between source-water δ^2H (referred in the initial figure as δD) and lipid biomarker δ^2H values: *n*-alkanes (A) and alkenones (B) (Sachse et al., 2012).

4.2.1.2 δ^2H on alkenones

Algae record information about the water they grow in. This information is preserved in the organic compounds and can be elucidated by measuring the stable hydrogen isotope composition of these molecules (Weiss et al., 2020). Algal and cyanobacterial lipid δ^2H values are being used to infer changes in rainfall, runoff, salinity and climate (Sachs et al., 2009; Smittenberg et al., 2011; van der Meer et al., 2007, 2008). δ^2H of long chain alkenones directly reflect the conditions in which the haptophyte algae lived, as these organisms depend mainly on the δ^2H of the water, salinity (Figure 4.9B) and growth rate (Schouten et al., 2006; van der Meer et al., 2008). The hydrogen isotope fractionation of alkenones synthesized by *E. huxleyi* in the last 3000 yrs in the Black Sea (van der Meer et al., 2008), had shown a strong dependence on the salinity of the growth medium and only to a small extent on growth rate. In both analyzed sections were present C_{37}, C_{38} and C_{39} alkenones, indicating multiple producer groups.

4.2.2 Compounds specific isotopes on carbon ($\delta^{13}C$)

4.2.2.1 $\delta^{13}C$ on n-alkanes

Plants take carbon from the environmental water and atmospheric CO_2. For this reason, the stable C (^{12}C and ^{13}C, referred to as $\delta^{13}C$) isotopic composition of *n*-alkanes reflects the environmental water and CO_2 at the time of plant growth, making the isotopic analysis of *n*-alkanes a potential proxy for various mechanisms regulating $\delta^{13}C$ in the environment. Because this exchange is not a direct one, the paleo-interpretation of *n*-alkanes $\delta^{13}C$ ideally has to be complemented by other proxies (e.g. temperature, vegetation composition; Chapters 5 and 7).

Plants use different mechanisms of compartmentalization and diffusion of CO_2, therefore the $\delta^{13}C$ values of C_3 and C_4 plants are very different, fluctuating from –33‰ for C_3 plants (e.g. trees, shrubs and most of the out of tropics grasses), up to –21.7‰ for C_4 plants (e.g. tropical grasses, desert plants, succulents, halophytes) (O'Leary, 1988; Kohn, 2010; Figure 4.11).

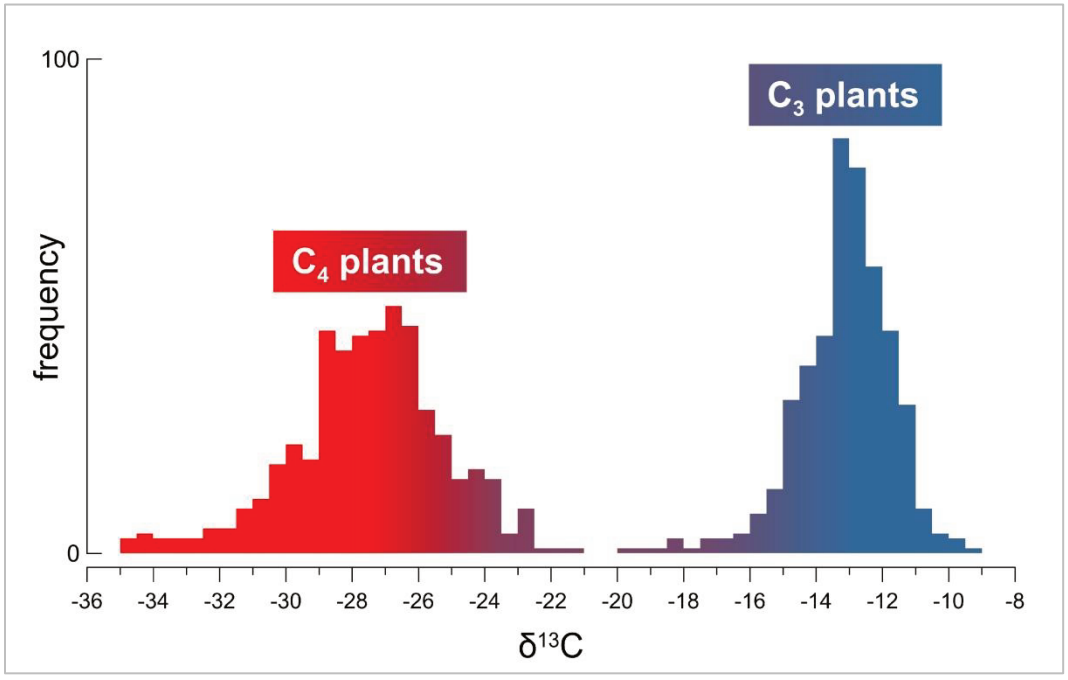

Figure 4.11 Carbon stable isotopic composition ($\delta^{13}C$) of bulk plant material of C_3 and C_4 plant species (O'Leary, 1988).

As C_4 plants are better adapted to arid conditions than C_3 plants, $\delta^{13}C$ shifts between the two ranges allow inferring changes in the original plant community, most likely related to shifts in paleo-aridity (Schefuß et al., 2003). Plants also react to water stress (for example during droughts

they lack water, temperatures too high), by varying their stomatal conductance to contain water loss from their tissues. This physical reaction is being registered by plants, thus $\delta^{13}C$ on *n*-alkanes provides data on arid events. Together with the other proxies, both terrestrial and aquatic (Figure 4.12), we are able to reconstruct now the climatic conditions on vast areas and expand our knowledge further back in time.

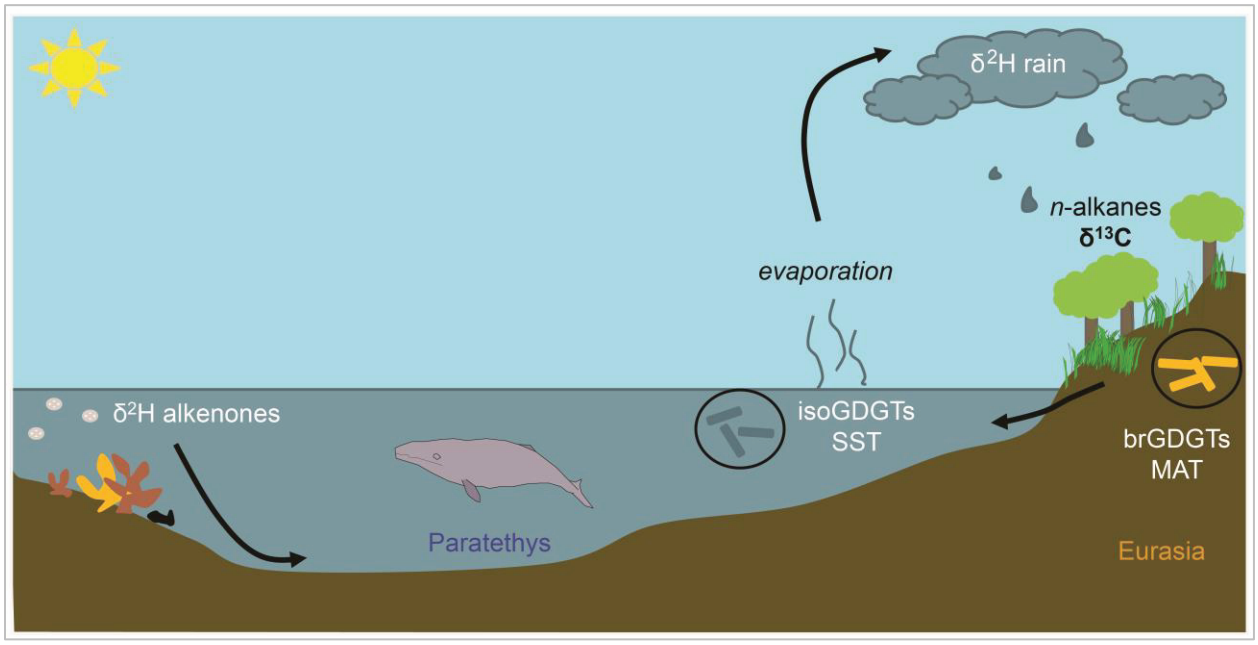

Figure 4.12 Schematic drawing of proxy sources in a basin and the interaction between them. Study case: Paratethys.

4.2.2.2 $\delta^{13}C$ on alkenones

The oceanic and marine environments play a crucial role for carbon intake. By studying the ratio of stable carbon isotopes in the organic matter from marine sediments, it is possible now to estimate the dissolved CO_2 concentrations in surface waters in deep time (Andersen et al., 1999; Pagani et al., 2011). Alkenones, organic compounds produced by algae, are extremely important because carbon demand depends mainly on the algal growth rate, thus $\delta^{13}C$ on alkenones can be successfully used to infer productivity in the aquatic environments (Bidigare et al., 1997).

Similar to land plants (Farquhar et al., 1989), marine algae are also more likely to assimilate the lighter carbon isotope ^{12}C over the heavier ^{13}C, and the carbon isotopic composition of their biomolecules ($\delta^{13}C_{phyto}$) is therefore ~10−25‰ lower than the $\delta^{13}C$ of

dissolved CO_2 in surface seawater (Rau et al., 1982). CO_2 is processed through photosynthesis similar with land plants, so the degree to which algae discriminate against ^{13}C, commonly expressed as ε_p (Freeman and Hayes, 1992), depends on the concentration of their aqueous carbon source. As a result, the more carbon is available, the more selective the algae can be lowering the $\delta^{13}C_{phyto}$ (Figure 4.13).

$$\varepsilon_p = \varepsilon_f - b/[CO_2]$$

where ε_p is the carbon isotope fractionation between aqueous CO_2 and $\delta^{13}C_{phyto}$ ($\varepsilon_p \approx \delta^{13}C_{CO2} - \delta^{13}C_{phyto}$), and ε_f is the carbon isotope fractionation associated with enzymatic carbon fixation typically assumed to be constant at 25‰.

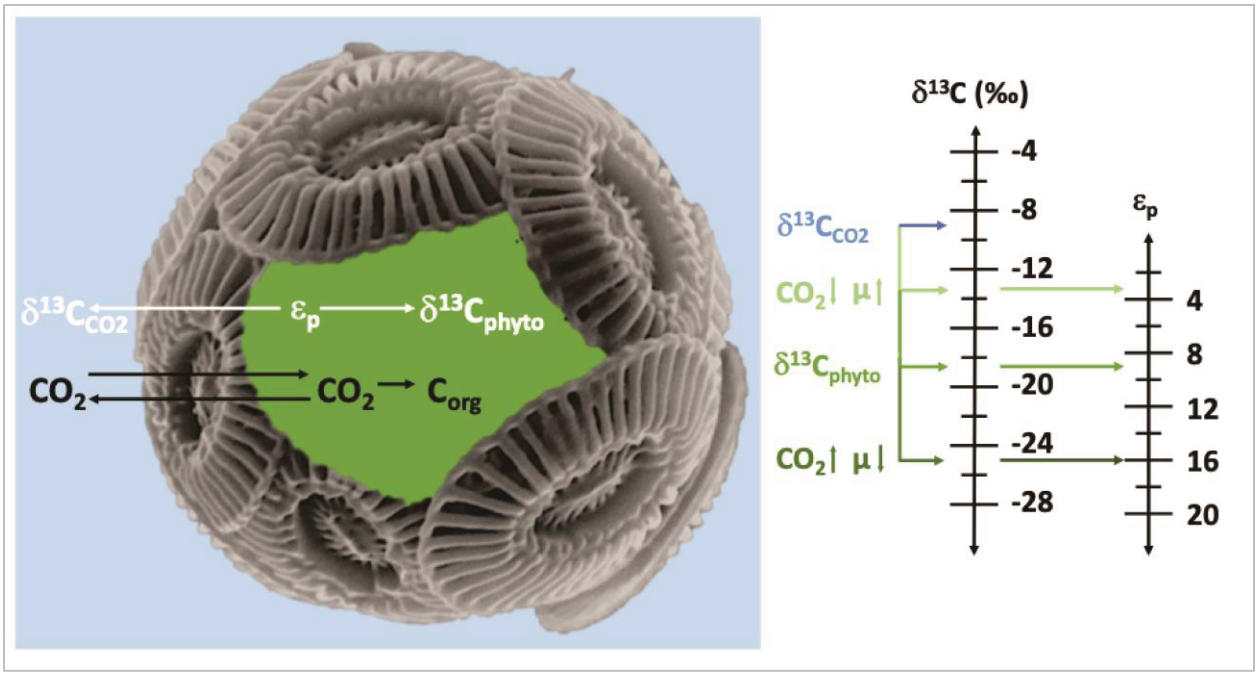

Figure 4.13 Exchange of $\delta^{13}C$. The $\delta^{13}C$ of algae biomarkers relates to the $\delta^{13}C$ of the aqueous carbon source for photosynthesis. This relationship is summarized in ε_p, the carbon isotope fractionation associated with photosynthetic carbon fixation. ε_p increases when aqueous carbon supply (i.e. CO_2) is high, but also when algae growth rates (μ) are slow (Polissar et al., paleo-CO_2.org).

4.2.2.3 $\delta^{13}C$ on bulk sedimentary rocks

The organic carbon in marine sediments is a mix of autochthonous and continental carbon, with the autochthonous usually dominant. The land-sourced signal is related to climate, erosion and transport of bulk land minerals to the sea (Leventhal, 2004) and changes over time. $\delta^{13}C$ values

are also considered to reflect changes in productivity (Li and Ku, 1997), which means that a lot of organisms that produce carbonate are growing and dying in that basin. Thus, an increase in $\delta^{13}C$ suggests an increase in basinal productivity. When the available resources are dropping, more competitive species become dominant, becoming the main carbonate producers.

Existing dissolved carbonate can precipitate from water too, due to changes in water chemistry, temperature or salinity. A very interesting situation happens in the Mediterranean during Messinian, when cyclic carbonates and sapropels formed as a consequence of restriction and orbital forcing. Chapter 7 of the thesis is detailing the results from Agios Myron section (Crete Island, Greece), which covers the interval between 7.2 and 6.5 Ma.

4.2.3 Compounds specific isotopes on oxygen ($\delta^{18}O$)

4.2.3.1 $\delta^{18}O$ on bulk

Evaporation is a key process in the water cycle. When water evaporates, enrichment in $\delta^{18}O$ takes place, thus $\delta^{18}O$ is considered a proxy for the evaporation in a basin. High $\delta^{18}O$ is induced by increased evaporation, while depletions by fresh water intake. $\delta^{18}O$ is also recycled by rain, being carried over the continents (Figure 4.14).

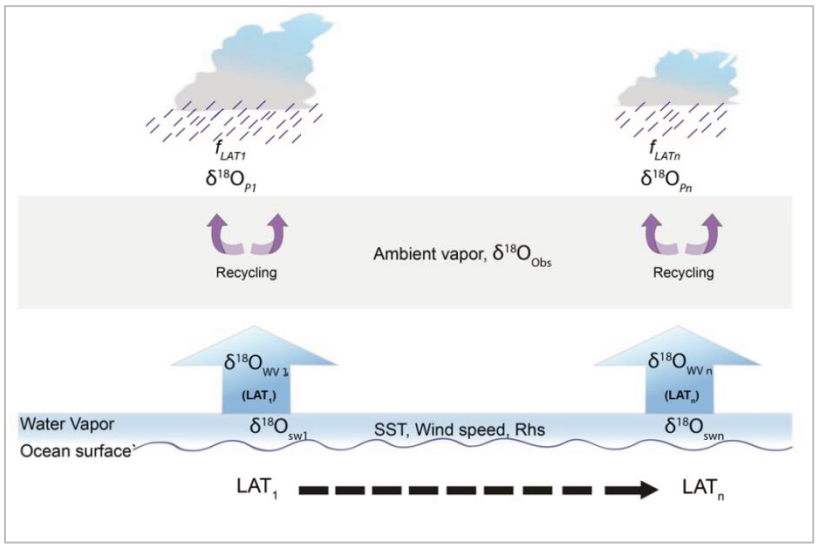

Figure 4.14 Model of $\delta^{18}O$ recycling in the Indian Ocean over different latitudes. Observed values of SST, wind speed, rhs, $\delta^{18}O$ in sea water [$\delta^{18}O_{sw}$] over different latitudes are used as the initial condition for the water vapor isotopic composition of surface evaporative flux [$\delta^{18}O_{wv}$]. The rainout fraction [f] is used to calculate the rainwater isotopic composition and the remnant water vapor. The ambient vapor is the vapor collected during sampling [$\delta^{18}O_{Obs}$] which includes the evaporated, transported and recycled components (Rahul et al., 2018).

Unlike the $\delta^{16}O$ who is lighter and evaporates faster, $\delta^{18}O$ is heavier and is incorporated in precipitations, but also in geologic archives (i.e. sediments and rocks). Due to this extraordinary

property, $\delta^{18}O$ is used in reconstructing past precipitations and evaporative events. When compared against $\delta^{13}C$, the graphic obtained gives information about the open or enclosed character of a basin (e.g. Leng and Marshall, 2004; Meijers et al., 2020).

4.2.3.2 $\delta^{18}O$ on planktonic foraminifera

Foraminifera are microscopic organisms living in open marine and oceanic environments. They live both in the water column and on the bottom, with a rate of speciation extremely high. Due to their short lives and environmental sensitivity, their tests are widely used for paleo-reconstruction proxies. $\delta^{18}O$ records are a function of temperature and the ambient $\delta^{18}O$ composition of seawater ($\delta^{18}O_{SW}$) in which the shell precipitated, which in turn depends on global ice volume and salinity, turning them into excellent salinity records (LeGrande and Schmidt, 2006). In chapter 6 is described the approach used to calculate SSTs in the Mediterranean based on the $\delta^{18}O$ on *Orbulina universa* species, for the interval between 7.2 and 6.5 Ma, during the lower half of the Messinian. All $\delta^{2}H$ and $\delta^{13}C$ compounds specific isotopes were measured at the Royal Netherlands Institute for Sea Research (NIOZ) and joined laboratory facilities of Senckenberg Biodiversity and Climate Research Centre and Goethe University (detailed in chapters 5−7).

4.3 Charcoal

4.3.1 Source

Charcoal is produced when a fire incompletely combusts organic matter (Whitlock and Larsen, 2001). When vegetation burns, a part of the burnt material is stored in the sediment archive. While most (macro)charcoal usually stays close to the fire source (primary charcoal), wind and rivers transport charcoal particles (secondary charcoal), both small and large (Verardo and Ruddiman, 1996). As rivers discharge into a basin, the sediment record of that basin will register the fire signal in the catchment over time. This tool was applied on Panagia section, covering the time period between 12.7 to 7.5 Ma.

4.3.2 Samples preparation and quantification

To evaluate past burning biomass in the east Paratethys region, charcoal particles had to be extracted from rocks. From each sample, 2 cm^3 were dissolved in water, and then bleached with

NaOCl for 24 h, to detach unburnt organic matter. After bleaching, samples were further wet-sieved under continuous water flow and divided into 90 µm, 120 µm and 180 µm fractions. Each fraction was stored in a beaker, and then transferred to a Petri dish and further examined under microscope. For this purpose an Olympus SZX7 stereomicroscope was used, at 30 x to 60 x magnification (Figure 4.15). Sedimentary charcoal particles were counted and subdivided into three categories: poaceae (grasses), forbs (other herbaceous plants) and wood (ligneous material), morphotypes following the methodology used by Feurdean and Vasiliev (2019). The charcoal counts of each morphotype were further transformed into percentages of the total charcoal counts and plot against stratigraphic level and age, in order to correlate and track the changes in charcoal/vegetation with other proxies.

Figure 4.15 Short protocol exposition of charcoal extraction and identification. A) Samples dissolved in water and chlorinated; B) Wet-sieving; C) Quantification under microscope; D) Identification of charcoal morphologies.

4.3.3 Application as tool for paleo-fires

Charcoal analysis from sediments allows the identification of the burnt vegetation and the subsequent quantification helps estimating the intensity of fires. Together with pollen and phytolith analyses, it provides a direct evidence of vegetation disturbances, while accumulation of charred particles provides details about the sedimentation rate. Based on the dimension and shape of particles, the distance and intensity of fires can be identified. Further details and results interpretation from Taman peninsula are presented in chapter 5 of this thesis.

References

Andersen, N., Muller, P.J., Kirst, G., Schneider, R.R., 1999. Alkenone $\delta^{13}C$ as a Proxy for Past pCO_2 in surface waters: Results from the Late Quaternary Angola Current. In Fischer, G. Wefer, G. (eds), 1999, Use of Proxies in Paleoceanography: Examples from the South Atlantic. Springer-Verlag Berlin Heidelberg, 469–488.

Araie, H., Nakamura, H., Toney, J.L., Haig, H.A., Plancq, J., Takashi, S., Leavitt, P.R., Seki, O., Ishida, K.I., Sawada, K., Suzuki, I., Shirawa, Y., 2018. Novel alkenone-producing strains of the genus Isochrysis (Haptophyta) isolated from Canadian saline lakes show temperature sensitivity of alkenones and alkenoates. Organic Geochemistry, 121, 80–103. https://doi.org/10.1016/j.orggeochem.2018.04.008.

Ardengi, N., 2019. Climatic reconstruction of Marine Isotope Stages 11–10 in the Eastern Mediterranean through the interpretation of plant and bacterial derived biomarkers from a Greek wetland (Tenaghi Philippon). PhD thesis.

Auguet, J.C., Casamayor, E.O., 2008. A hotspot for cold Crenarchaeota in the neuston of high mountain lakes. Environ Microbiol 10: 1080–1086.

Bendle, J.A.P., Rosell-Melé, A., Cox, N.J., Shennan, I., 2009. Alkenones, alkenoates, and organic matter in coastal environments of NW Scotland: Assessment of potential application for sea level reconstruction. Geochemistry, Geophysics, Geosystems 10 (12), https://doi.org/10.1029/2009GC002603.

Bidigare, R.R., Fluege, A., Freeman, K.H., Hanson, K.L., Hayes, J.M., Hollander, D., Jasper, J.P., King, L.L., Laws, E.A., Milder, J., Millero, F.J., Pancost, R., Popp, B.N., Steinberg, P.A., Wakeham, S.G., 1997. Consistent fractionation of ^{13}C in nature and the laboratory: Grouth-rate effects in some haptophyte algae. Global Biogeochemical Cycles 13:251.

Brassell, S.C., Eglinton, G., Marlowe, I.T., Pflaumann, U., Sarnthein, M., 1986. Molecular stratigraphy: A new tool for climatic assessment. Nature, 320, 129–133. https://doi.org/10.1038/320129a0.

Castañeda, I.S., Schouten, S., 2011. A review of molecular organic proxies for examining modern and ancient lacustrine environments. Quaternary Science Reviews 30, 2851–2891. doi:10.1016/j.quascirev.2011.07.009

Chikaraishi, Y., Naraoka, H., 2003. Compound-specific δD–δ^{13}C analyses of *n*-alkanes extracted from terrestrial and aquatic plants. Phytochemistry 63 (3), 361–371. https://doi.org/10.1016/S0031-9422(02)00749-5

Conte, M.H., Sicre, M.-A., Rühlemann, C., Weber, J. C., Schulte, S., Schulz-Bull, D., Blanz T., 2006. Global temperature calibration of the alkenone unsaturation index ($U^{K'}_{37}$) in surface waters and comparison with surface sediments, Geochem. Geophys. Geosyst., 7, Q02005, doi:10.1029/2005GC001054.

De Jonge, C., Hopmans, E.C., Zell, C.I., Kim, J.-H., Schouten, S., and Sinninghe Damsté, J.S., 2014. Occurrence and abundance of 6-methyl branched glycerol dialkyl glycerol tetraethers in soils: Implications for palaeoclimate reconstruction. Geochimica et Cosmochimica Acta, 141, 97–112.

Dinel, H., Schnitzer, M., Mehuys, G.R., 1990. Soil lipids: origin, nature, contents, decomposition and effect on soil physical properties. In: Bollag, J.M., Stotzky, G. (Eds.), Soil Biochemistry. Marcel Dekker, New York, 397–427.

Druffel, E.R.M., Williams, P.M., Bauer, J.E., Ertel, J.R., 1992. Cycling of dissolved and particulate organic matter in the open ocean. J. Geophys. Res., [Oceans], 97:15639–15659.

Duan, Y., He, J., 2011. Distribution and isotopic composition of *n*-alkanes from grass, reed and tree leaves along a latitudinal gradient in China. Geochemical Journal, 45, 199−207.

Eglinton, G., Hamilton, R.J., 1967. Leaf epicuticuular waxes. Science 156, 1322−1335.

Eglinton, T.I., Eglinton, G., 2008. Molecular proxies for paleoclimatology. Earth and Planetary Science Letters 275, 1–16. doi:10.1016/j.epsl.2008.07.012

Epstein, B., D'Hondt, S., Quinn, J.G., Zhang, J., Hargraves, P.E., 1998. An effect of dissolved nutrient concentrations on alkenone-based temperature estimates. Paleoceanography, 13, 122−126.

Farkuhar, G.D., Ehleringer, J.R., Hubick, K.T., 1989. Carbon Isotope Discrimination and Photosynthesis. Annual Review of Plant Physiology and Plant Molecular Biology. 40, 503−537. https://doi.org/10.1146/annurev.pp.40.060189.002443

Feakins S.J., Sessions, A.L., 2010a. Controls on the D/H ratios of plant leaf waxes in an arid ecosystem. Geochimica et Cosmochimica Acta, 74:2128–41

Feurdean, A. and Vasiliev, I., 2019. The contribution of fire to the late Miocene spread of grasslands in eastern Eurasia (Black Sea region). Scientific reports, 9:6950.992.

Freeman, K.H., Hayes, J.M., 1992. Fractionation of carbon isotopes by phytoplankton and estimates of ancient CO_2 levels. Global Biogeochemical Cycles 6 (2), 185−198.

Herbert, T., 2003. Treatise of Geochemistry. ISBN 978-0-08-043751-4. Chp. 6: The Oceans and Marine Geochemistry. Alkenone Paleotemperature determinations, 391−432.

Herbert, T.D., Lawrence, K.T., Tzanova, A., Peterson, L. C., Caballero-Gill, R., Kelly, C.S., 2016. Late Miocene global cooling and the rise of modern ecosystems. Nature Geoscience, 825 9, 843–847. http://dx.doi.org/10.1038/NGEO2813.

Hopmans, E.C., Weijers, J.W.H., Schefuss, E., Herfort, L., Sinninghe Damsté, J.S., Schouten, S., 2004. A novel proxy for terrestrial organic matter in sediments from agricultural soil. Applied and Environmental Microbiology 77, 8635-8647.

Kaiser, J., Wang, K.J., Rott, D., Li, G., Zheng, Y., Amaral-Zettler, L., Arz, H.W., Huang, Y., 2019. Changes in long chain alkenone distributions and Isochrysidales groups along the Baltic Sea salinity gradient. Organic Geochemistry, 127, 92–103. https://doi.org/10.1016/j. orggeochem.2018.11.012

Kästner, M., 2000. Degradation of Aromatic and Polyaromatic Compounds. In: Rehm, H.J., Reed, G., Pühler, A., Stadler, P. (Eds.), Biotechnologie. Wiley-VCH, Weinheim, 211–239.

Koch, K., Ensikat, H.-J., 2008. The hydrophobic coatings of plant surfaces: epicuticular wax crystals and their morphologies, cristallinty and molecular self-assembly. Micron. 39 (7), 759–772. doi:http://dx.doi.org/10.1016/j.micron.2007.11.010

Kohn, M.J., 2010. Carbon isotope compositions of terrestrial C3 plants as indicators of (paleo)ecology and (paleo)climate. Proceedings of the National Academy of Sciences of the United States of America 107, 19691–19695.

LeGrande, A.N., Schmidt, G.A., 2006. Global gridded data set of the oxygen isotopic composition in seawater. Geophysics Research Letter, 33, L12604, doi:10.1029/2006GL026011.

Leng, M.J., and Marshall, J.D., 2004. Palaeoclimate interpretation of stable isotope data from lake sediment archives. Quaternary Science Reviews, 23, 811–831. https://doi .org/10.1016/j.quascirev.2003.06.012.

Leventhal, J.S., 2004. Isotopic chemistry of organic carbon in sediments from Leg 184. In Prell, W.L., Wang, P., Blum, P., Rea, D.K., and Clemens, S.C. (Eds.), Proc. ODP, Sci. Results, 184, 1–13.

Li, H.-C., and Ku, T.-L., 1997. $\delta^{13}C$–$\delta^{18}C$ covariance as a paleohydrological indicator for closed-basin lakes. Palaeogeography, Palaeoclimatology, Palaeoecology, 133, 69–80. https://doi.org/10.1016/S0031-0182(96)00153-8

Marlowe, I.T., Brassell, S.C., Eglinton, G., Green, J.C., 1984. Long chain unsaturated ketones and esters in living algae and marine sediments. Org. Geochem. 6, 135–141.

Meijers, M.J.M., Brocard, G.Y., Whitney, D.L., Mulch, A., 2020. Paleoenvironmental conditions and drainage evolution of the Central Anatolian lake system (Turkey) during late Miocene to Pliocene surface uplift. GEOSPHERE, 16 (2), 490-509. https://doi.org/10.1130/GES02135.1

Müller, P., Kirst, G., Ruhland, G., von Storch, I., Rosell-Melé, A., 1998. Calibration of the alkenone palaeotemperature index UK0 37 based on core-tops from the eastern South Atlantic and the global ocean (600 N–600 S). Geochimica et Cosmochimica Acta 62, 1757–1772.

O'Leary, M.H., 1988. Carbon Isotopes in Photosynthesis. BioScience 38, 328–336. doi:10.2307/1310735.

Pagani, M., Pedentchouk, N., Huber, M., Sluijs, A., Schouten, S., et al. 2006. Arctic hydrology during global warming at the Palaeocene/Eocene thermal maximum. Nature 442:671–7.

Pagani, M., Huber, M., Liu, Z., Bohaty, S., Henderinks, J., Sijp, W., Krishnan, S., Deconto, R.M., 2011. Science 334 (6060), 1261–1264. DOI: 10.1126/science.1203909.

Pancost, R.D., Hopmans, E.C., Sinninghe Damsté, J.S., Medinauth Scientific Party, 2001. Archaeal lipids in Mediterranean cold seeps: molecular proxies for anaerobic methane oxidation. Geochimica et Cosmochimica Acta 65, 1611– 1627.

Peters, K.E., Walters, C.C., Moldowan, J.M., 2005. The Biomarker Guide. Cambridge University Press, Cambridge.

Peterse, F., van der Meer, J., Schouten, S., Weijers, J.W.H., Fierer, N., Jacckson, R.B., Kim, J.-H., Sinninghe Damsté, J.S., 2012. Revised calibration of the MBT-CBT paleotemperature proxy based on branched tetraether membrane lipids in surface soils. Geochimica et Cosmochimica Acta, 96, 215–229.

Prahl, F.G., Wakeham, S.G., 1987. Calibration of unsaturation patterns in long-chain ketone compositions for palaeotemperature assessment. Nature, 330(6146), 367. https://doi.org/10.1038/330367a0

Polissar, P., Phelps, S., Zhang, Y., Pearson, A., Hönisch, B., Marine phytoplankton $\delta^{13}C$. paleo-CO_2.org

Rahul, P., Prassana, K., Ghosh, P., Anilkumar, N., Yoshimura, K., 2018. Stable isotopes in water vapor and rainwater over Indian sector of Southern Ocean and estimation of fraction of recycled moisture. Scientific Reports 8:7552. DOI:10.1038/s41598-018-25522-5

Rau, G.H., Sweeney, R.E., Kaplan, I.R., 1982. Plankton ^{13}C: ^{12}C ratio changes with latitude: differences between northern and southern oceans. Deep Sea Research Part A. Oceanographic Research Papers 29 (8), 1035−1039.

Sachs, J.P., Sachse, D., Smittenberg, R.H., Zhang, Z., Battisti, D.S., Golubic, D., 2009. Southward movement of the Pacific intertropical convergence zone AD 1400–1850. Nat. Geosci. 2:519–25.

Sachse, D., Radke, J., Gleixner, G., 2006. δD values of individual n-alkanes from terrestrial plants along a climatic gradient—implications for the sedimentary biomarker record. Org. Geochem. 37:469–83

Sachse, D., Billault, I., Bowen, G.J., Chikaraishi, Y., Dawson, T.E., Feakins, S.J., Freeman, K.H., Magill, C.R., McInerney, F.A., van der Meer, M.T.J., Polissar, P., Robins, R.J., Sachs, J.P., Schmidt, H.-L., Sessions, A.L., White, J.W.C., West, J.B., Kahmen, A., 2012. Molecular Paleohydrology: Interpreting the Hydrogen-Isotopic Composition of Lipid Biomarkers from Photosynthesizing Organisms. Annual Review of Earth and Planetary Sciences. 40, 221–49. 10.1146/annurev-earth-042711-105535

Schefuß, E., Ratmeyer, V., Stuut, J.-.B., W, Jansen, J.H.F., Sinninghe Damsté, J.S., 2003. Stable carbon isotopic analyses of n-alkanes and the calculated C_4 plant-derived fractions in the dust samples. PANGAEA, https://doi.org/10.1594/PANGAEA.141041,

Schouten, S., Hoefs, M.J.L., Sinninghe Damsté, J.S., 2003. A molecular and stable carbon isotopic study of lipids in late Quaternary sediments from the Arabian Sea. Organic Geochemistry, 31 (6), 509−521.

Schouten, S., Hopmans, E.C., Schefuss, E., Sinninghe Damsté, J.S., 2002. Distributional 1016 variations in marine crenarchaeotal membrane lipids: a new tool for reconstructing

ancient sea 1017 water temperatures?. Earth and Planetary Science Letters, 204(1–2), 265–274. 1018. https://doi.org/10.1016/s0012-821x(02)00979-2

Schouten, S., Ossebaar, J., Schreiber, K., Kienhuis, M.V.M., Langer, G., Benthien, A., Bijma, J., 2006. The effect of temperature, salinity and growth rate on the stable hydrogen isotopic composition of long chain alkenones produced by Emiliania huxleyi and Gephyrocapsa oceanica. Biogeosciences 3:113–19.

Schouten, S., Hopmans, H., Sinninghe Damsté, J.S., 2013. The organic geochemistry of glycerol dialkyl glycerol tetraether lipids: A review. Organic Geochemistry 54, 19−61.

Schulz, H.-M., Schöner, A., Emeis, K.-C., 2000. Long-chain alkenone patterns in the Baltic Sea-an ocean-fresh water transition. Geochimica et Cosmochimica Acta 64 (3), 469−477.

Sinninghe Damsté, J.S., Hopmans, E.C., Pancost, R.D., Schouten, S., Geenevasen, J.A.J., 2000. Newly discovered non-isoprenoid dialkyl diglycerol tetraether lipids in sediments. Journal of the Chemical Society, Chemical Communications 23, 1683–1684.

Sinninghe Damsté, J.S., Rijpstra, W.I.C., Hopmans, E.C., Schouten, S., Balk, M., Stams, A.J.M., 2007. Structural characterization of diabolic acid-based tetraester, tetraether and mixed ether/ester, membrane-spanning lipids of bacteria from the order Thermotogales. Archives of Microbiology 188, 629–641.

Smith, F.A., Freeman, K.H., 2006. Influence of physiology and climate on δD of leaf wax n-alkanes from C_3 and C_4 grasses. Geochim. Cosmochim. Acta 70:1172–87.

Smittenberg, R.H., Saenger, C., Dawson, M.N., Sachs, J.P., 2011. Compound-specific D/H ratios of the marine lakes of Palau as proxies for West Pacific Warm Pool hydrologic variability. Quaternary Science Reviews 30: 921–933.

van der Meer, M.T.J, Baas, M., Rijpstra, W.I.C., Marino, G., Rohling., E.J., Sinninghe Damsté, J.S., Schouten, S., 2007. Hydrogen isotopic compositions of long-chain alkenones record freshwater flooding of the Eastern Mediterranean at the onset of sapropel deposition. Earth and Planetary Science Letters, 262 (3–4), 594–600. https://doi.org/10.1016/j.epsl.2007.08.014

van der Meer, M.T.J, Sangiorgi, F., Baas, M., Brinkhuis, H., Damste, J.S.S., Schouten, S., 2008. Molecular isotopic and dinoflagellate evidence for Late Holocene freshening of the Black Sea. Earth Planet. Sci. Lett. 267:426–3

Vasiliev, I., 2020. Laboratory notes. Senckenberg internal use only.

Verardo, D.J., Ruddiman, W., 1996. Late Pleistocene charcoal in tropical Atlantic deep-sea sediments: Climatic and geochemical significance. Geology. DOI:10.1130/0091-7613(1996)024<0855:LPCITA>2.3.CO;2

Wang, K.J., Huang, Y., Majaneva, M., Belt, S.T., Liao, S., Novak, J., Kartzinel, T.R., Herbert, T.D., Richter, N., Cabedo-Sanz, P., 2021. Group 2i Isochrysidales produce characteristic alkenones reflecting sea ice distribution. Nature Communications 12:15.

Weijers, J.W.H., Schouten, S., van Den Donker, J.C., Hopmans, E.C., Sinninghe Damsté, J.S., 2007a. Environmental controls on bacterial tetraether membrane lipid distribution in soils. Geochimica et Cosmochimica Acta 71, 703–713.

Weiss, G.M., Massalska, B., Hennekam, R., Reichart, G.-J., Sinninghe Damsté, J.S., Schouten, S., van der Meer, M.T.J., 2020. Alkenone Distributions and Hydrogen Isotope Ratios Show Changes in Haptophyte Species and Source Water in the Holocene Baltic Sea. Geochemistry, Geophysics, Geosystems, 21, e2019GC008751. https://doi.org/ 10.1029/2019GC008751.

Whitlock, C., Larsen, C., 2001. Charcoal as fire proxy chp. DOI: 10.1007/0-306-47668-1_5 In J. P. Smol, H. J. B. Birks & W. M. Last (eds.), 2001. Tracking Environmental Change Using Lake Sediments. Volume 3: Terrestrial, Algal, and Siliceous Indicators. KluwerAcademic Publishers, Dordrecht, The Netherlands.

Ziegler, H., Osmond, C.B., Stichler, W., Trimborn, P., 1976. Hydrogen isotope discrimination in higher plants: Correlations with photosynthetic pathway and environment. Planta 128, 85–92. https://doi.org/10.1007/BF00397183

Ziegler H., 1989. Hydrogen Isotope Fractionation in Plant Tissues. In: Rundel P.W., Ehleringer J.R., Nagy K.A. (eds) Stable Isotopes in Ecological Research. Ecological Studies (Analysis and Synthesis), vol 68. Springer, New York, NY. https://doi.org/10.1007/978-1-4612-3498-2_8

Zygler, A., Słomińska, M., Namieśnik, J., 2012. Comprehensive Sampling and Sample Preparation. Analytical Techniques for Scientists. 2.04 Soxlet Extraction and New Developments such as Soxtec. 65−103.

Zhou, Y., Grice, K., Stuart-Williams, H., Farquhar, G.D., Hocart, C.H., Lu, H., Liu, W., 2010. Biosynthetic origin of the saw-toothed profile in $\delta^{13}C$ and $\delta^{2}H$ of n-alkanes and systematic isotopic differences between n-, iso- and anteiso-alkanes in leaf waxes of land

plants. Phytochemistry, 71 (4), 388−403. https://doi.org/10.1016/j.phytochem.2009.11.009

Zygler, A., Słomińska, M., Namieśnik, J., 2012. Comprehensive Sampling and Sample Preparation. Analytical Techniques for Scientists. 2.04 Soxlet Extraction and New Developments such as Soxtec. 65−103.

Chapter 5

Severe late Miocene droughts affected Western Eurasia

Geanina A. Butiseacă[1,2,*], Iuliana Vasiliev[1], Marcel T.J. van der Meer[3], Wout Krijgsman[4], Dan V. Palcu[4,5], Angelica Feurdean[6], Eva M. Niedermeyer[1], Andreas Mulch[1,2]

[1]*Senckenberg Biodiversity and Climate Research Centre (SBiK-F), Senckenberganlage 25, D-60325 Frankfurt am Main, Germany*

[2]*Institute of Geosciences, Goethe University Frankfurt, Altenhöferalle 1, 60438 Frankfurt am Main, Germany*

[3]*Royal Netherlands Institute for Sea Research, Department of Marine Microbiology and Biogeochemistry, P.O. Box 59, 1790 AB, Den Burg, Texel, The Netherlands*

[4]*Fort Hoofddijk, Paleomagnetic Laboratory, Utrecht University, Budapestlaan17, 3584 CD, Utrecht, The Netherlands*

[5]*Instituto Oceanográfico da Universida de São Paulo Praça do Oceanográfico, 191, 05508-120, São Paulo-SP, Brasil*

[6]*Department of Physical Geography, Goethe University, Altenhöferallee 1, 60438 Frankfurt am Main, Germany*

This is a pre-copyedited, author-produced version, following peer review, of Butiseacă, G.A., Vasiliev, I., van der Meer, M.T.J., Krijgsman, W., Palcu, D.V., Feurdean, A., Niedermeyer, E.M., Mulch., A., 2021. Severe late Miocene droughts affected Eurasia. Global and Planetary Change, 206: 103644. https://doi.org/10.1016/j.gloplacha.2021.103644

Highlights

- Three droughts peaking at 9.65, 9.4 and 7.9 Ma disturbed circum-Paratethys ecosystem.
- Carbon isotopes indicate increase in C_4 plant contribution during these droughts.
- Increased fire activity during droughts parallel changes towards open vegetation.
- Alleged connection to a proximal basin may trigger the alkenone producers' advent.
- Decoupling of Paratethys from the global climate and hydrology hints its importance.

Graphical abstract

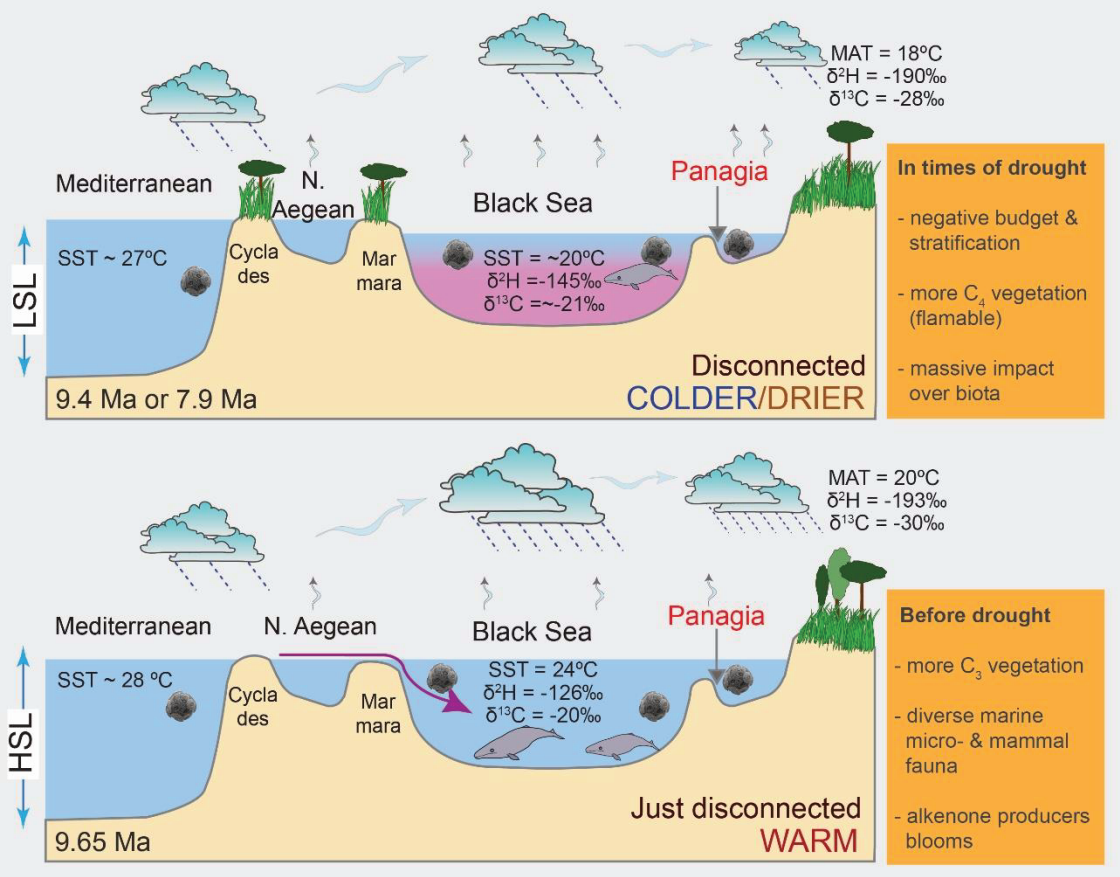

5.1 Abstract

A large and highly dynamic aquatic system called Paratethys governed important elements of the middle and late Miocene (15.97–5.33 Ma) hydrology in western Eurasia. So far, the impact of the vast Paratethys water body on the Eurasian climate, however, is not yet understood. Here we apply biomarker analyses coupled to compound-specific hydrogen and carbon isotope data to track changes in sea surface temperature, mean annual air temperature, hydrological budget and vegetation changes to reconstruct long-term western Eurasian climate conditions between 12.7 and 7.65 Ma in the Black Sea region. Biomarker data from Panagia (Russia) indicate the presence of three exceptionally evaporative intervals peaking at 9.65, 9.4 and 7.9 Ma. These peaks in evaporation relate to aridity, parallel increasing fire activity and are associated with changes in vegetation. Carbon isotope and pollen data support the evidence of an increase in C_4 plants associated with these dry intervals. At 9.66 Ma, alkenone producing algae appear in the basin and thrive for the subsequent two million years. Cumulative fluctuations in both hydrology and surface temperature of Paratethys might have enhanced rainfall seasonality in western Eurasia as a response to changes in evaporation over the Paratethys basin. Our combined data suggest a strong regional imprint on overall climate patterns, dominated by basin dynamics causing Paratethys volume and surface reduction. Collectively, the presented biomarker results provide evidence of severe droughts affecting the late Miocene circum-Paratethys region, leading to a direct impact on the evolution of biota in the basin and its surroundings.

Keywords: Paratethys isolation, late Miocene droughts, vegetation shift, biomarkers, isotope geochemistry

5.2 Introduction

The interplay between tectonics, landscape and climate change influenced the middle and late Miocene development of the Eurasian continental interior (Figure 5.1). As a result, the Paratethys, a large epicontinental water body, became fragmented into smaller basins during the late Miocene (11.6–5.3 Ma), with temporary or no connection to the global oceans (Popov et al., 2006; Figure 5.1). Such semi-isolated water bodies are highly sensitive to changes in their hydrological balance, which is directly reflected in water temperature, salinity, circulation, and

therefore oxygenation of the water column. A general lack of age-diagnostic marine biota characterizes the Paratethyan sub-basins, causing difficulties for reliable biostratigraphic correlation to the marine realm. Furthermore, commonly used geochemical methods in paleoceanography (e.g. stable oxygen and carbon isotopes on foraminifera) are of limited use as the high degree of endemism led to the absence of widespread marine (e.g. planktonic) foraminifera species. As Paratethys water bodies evolved (quasi)disconnected from the global oceans they acquired particular environmental characteristics which can be untangled only through multi-proxy approaches.

Recently established magneto-biostratigraphy provides a reliable geochronological framework for the middle to late Miocene Panagia section of the Eastern Paratethys (Popov et al., 2016; Palcu et al., 2021), a section exposed on the Taman Peninsula (northern Black Sea, Russia; Figure 5.1). Here, we investigate the biomarker record of the Panagia section to reconstruct the climatic conditions between 12.7 and 7.65 Ma (Volhynian to Khersonian local stages), with a special focus on the 9.75 to 7.65 Ma (latest Bessarabian to Khersonian) time interval. We use biomarker analyses coupled to compound-specific hydrogen (δ^2H) and carbon ($\delta^{13}C$) isotopes to track a complex array of environmental changes. We reconstruct: 1) sea surface temperatures (SSTs) using isoprenoidal glycerol dialkyl tetraethers (isoGDGTs), biomarkers synthesized by Archaea group that reflect the near-surface conditions within the water column; 2) mean annual air temperatures (MAT) based on branched (brGDGTs), biomarkers produced primarily by soil bacteria in the circum-Paratethys region. We further analyze changes in the hydrological budget of the Paratethys basin through: 3) δ^2H values from alkenones (produced by coccolithophoriid algae within the uppermost Paratethys water column) and 4) δ^2H measured on long chain *n*-alkanes (produced by higher terrestrial plants recording precipitation changes in the basin catchment). We monitor: 5) changes in basin productivity through $\delta^{13}C$ values of alkenones and reconstruct 6) changes in vegetation surrounding the basin using $\delta^{13}C$ values of *n*-alkanes. Biomarker data are finally supplemented by 7) charcoal analysis and coupled to existing palynological data (Razumkova, 2012) to identify changes in paleo-fire activity and paleo-vegetation.

Similar proxy records previously identified two phases of severe droughts in the Black Sea region (around 8 and 5.8 Ma; Vasiliev et al., 2013; 2015; 2019). The present work

significantly extends these records back in time to 12.7 Ma, identifying major environmental changes in the Eastern Paratethys that affect large parts of Eurasia.

5.3 Stratigraphy of sampled interval and age model

The Panagia section (45°09' N, 36°38' E, Taman Peninsula, Black Sea coast, Russia; Figure 5.1) covers a significant part of the late Miocene in the Eastern Paratethys (Popov et al., 2016).

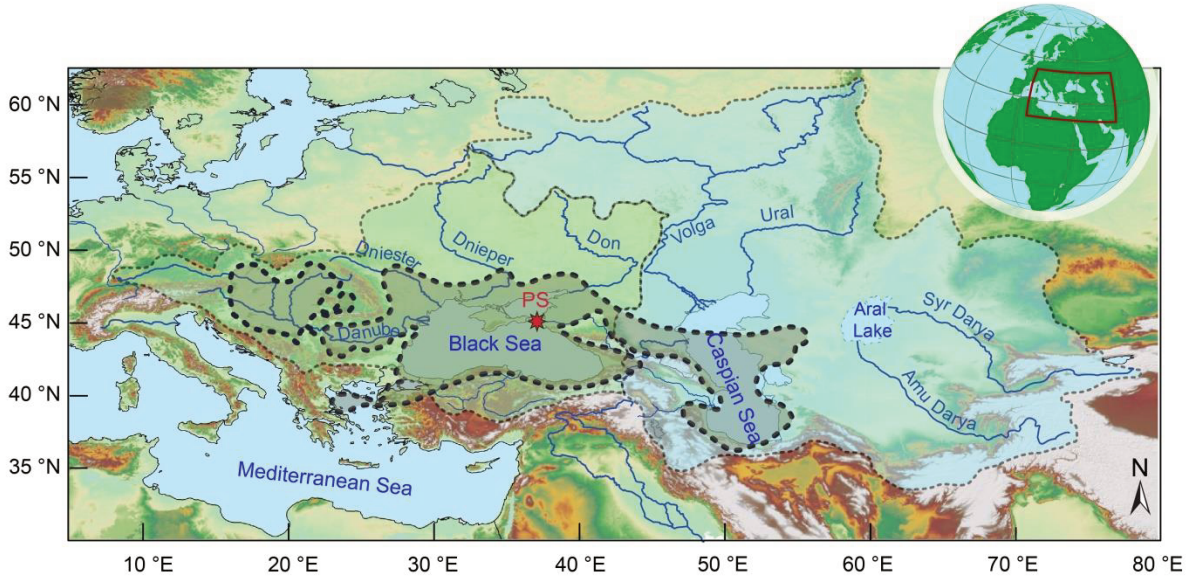

Figure 5.1 Map showing the Late Miocene Paratethys domain extension (black dashed line) overlapped onto the present day geographical configuration. The present-day drainage basins (grey dashed contours) of Black and Caspian Seas hint for the areal extent of the Paratethys drainage basin. The Panagia section (PS) is indicated with a red star.

Because of protracted endemism in the Paratethys basin, we rely on the regional stratigraphy, with the late Miocene successions divided into the Sarmatian *sensu lato (s.l.)* stage with Volhynian, Bessarabian and Khersonian substages and the Maeotian and Pontian stages (Figure 5.2). The 638 m thick Panagia section preserves a fairly complete sedimentary record of the 12.7–7.65 Ma interval with Bessarabian and Khersonian substages being exceptionally well exposed (Popov et al., 2016). Magnetostratigraphic dating of the Panagia section pins the base of the Sarmatian *(s.l.)* at 12.65 Ma (at 2 m; Palcu et al., 2018), the Volhynian−Bessarabian transition at ~12 Ma, the Bessarabian−Khersonian boundary at 9.65 Ma (at 310 m) and the Khersonian−Maeotian boundary at 7.65 Ma (at 625 m; Palcu et al., 2021; Figure 5.2).

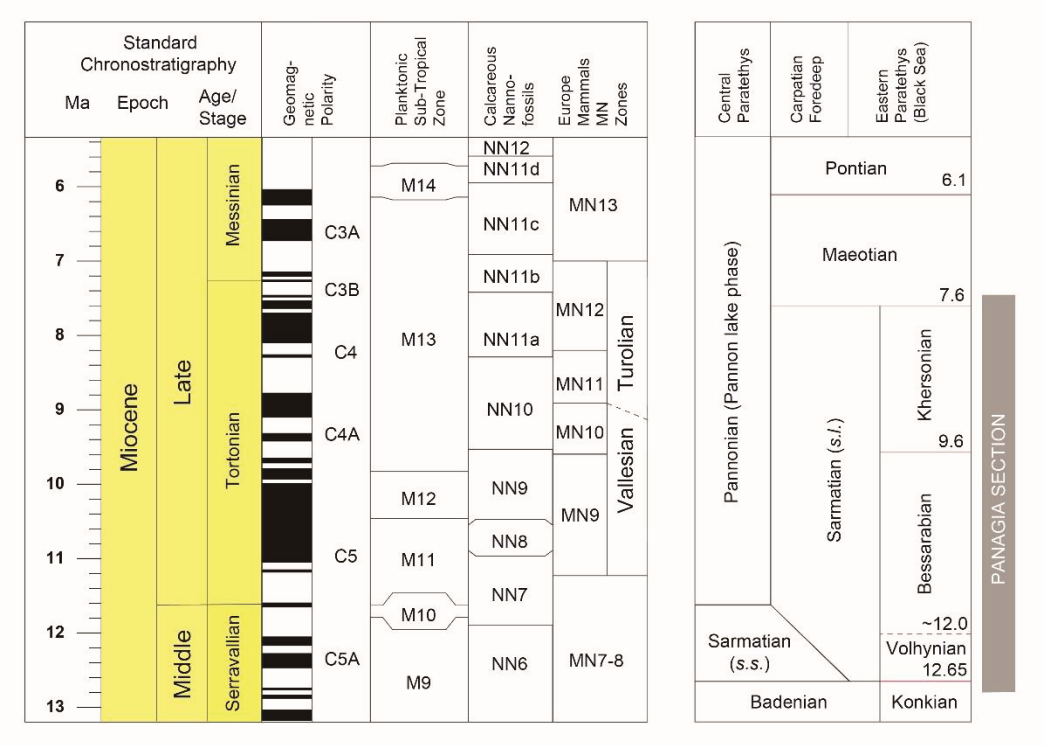

Figure 5.2 Chronostratigraphic correlation of the Middle - Late Miocene (Hilgen et al., 2012) to Paratethys regional substages. Geomagnetic polarity time scale with chron nomenclature and biozones are presented (M for planktonic fauna, NN for calcareous nannofossils and MN for European mammal zonations). The grey bar represents the time interval covered by Panagia section.

The poorly-exposed Volhynian consists of alternations of dark clays with sulphur films and thin carbonate layers, while the Bessarabian comprises clays and marls with increasing carbonate intercalations in its terminal part (Popov et al., 2016). The Khersonian continues with alternations of clays and silty clays, laminated dark shales with yellowish sulphur films, gypsum crystals, pyrite and thin diatomite layers being almost totally devoid of carbonates.

5.4 Material and methods

5.4.1 Organic geochemistry, lipid extraction, fractions separation and analyses

Fifty-seven sedimentary rock samples weighing between 14 and 32 g were analyzed. The complete and detailed workflow for the organic geochemistry is presented in the supplementary material (Appendix 1). In short, the fifty-seven selected samples underwent drying, grinding, total lipid extraction (TLE) and removal of elemental sulphur. Afterwards, a fraction of the TLE was archived. The remainder was then separated using Al_2O_3 column chromatography into apolar, ketone and polar fractions. The apolar fraction containing *n*-alkanes was purified (using

$AgNO_3$ column, or urea adduction, when needed) and later identified using the Gas Chromatography-Mass Spectrometry (GC-MS) at Senckenberg Biodiversity and Climate Research Centre (SBiK-F) in Frankfurt (see Appendix 1). The ketone fraction containing alkenones was occasionally purified using $AgNO_3$ column and subsequently measured on the GC-MS. The polar fraction containing GDGTs, filtered over a 0.45 mm PTFE filter, was analyzed and quantified at the SBiK-F laboratory using a Shimadzu, UFLC performance HPLC mass spectrometer (see Appendix 1).

The SSTs were obtained by using TEX_{86} (TetraEther indeX of tetraethers consisting of 86 carbon atoms) values that were calculated according to the definition of Schouten et al. (2002) and converted into SST using the calibration and recommendation of Kim et al. (2010) to apply the TEX_{86}^{H} above 15 °C (i.e. outside the polar and subpolar domains).

The distribution of brGDGTs, expressed as the Methylation index of Branched Tetraethers (MBT) and the Cyclisation ratio of Branched Tetraethers (CBT), displays a significant linear correlation with modern MAT in the range of 6 to 27ºC (Weijers et al., 2007; Peterse et al., 2012; De Jonge et al., 2014). From the multiple existent calibrations, we chose to use Peterse et al. (2012) as a more conservative choice given that the expected environmental changes for the ~ 5 Myr duration of the studied interval are large. Paleosoil pH estimates use the CBT index based on brGDGTs and follow Peterse et al. (2012).

The δ^2H was determined by GC/Thermal Conversion (TC)/ isotope monitoring MS (irMS) using an Agilent GC coupled to a Thermo Electron DELTA Plus XL mass spectrometer, via a Conflo IV. Alkane and alkenone fractions were injected on column at the Royal Netherlands Institute for Sea Research (NIOZ) (see Appendix 1). The carbon isotope ratios ($\delta^{13}C$) of individual *n*-alkanes and alkenones were measured on the purified and adducted apolar and alkenone fractions on the GC-irMS using similar conditions as for δ^2H measurements at NIOZ.

5.4.2 Charcoal preparation and quantification

To evaluate past biomass burning in the region, charcoal particles were extracted from fifty-eight samples, in compliance with the organic geochemistry sampling (see Appendix 1). From each sample, 2 cm^3 were dissolved in water, bleached, wet-sieved and split into 90 μm, 120 μm and 180 μm fractions. Sedimentary charcoal particles were counted and categorized into: 1) poaceae

(grass), 2) forbs (other herbaceous plants) and 3) wood (ligneous material) morphotypes following the methodology highlighted in Feurdean and Vasiliev (2019). The charcoal counts of each morphotype were transformed into percentages of the total charcoal counts.

5.5 Results

5.5.1 Temperatures

5.5.1.1 SST estimates based on isoGDGTs

The amplitude of calculated SSTs in the Panagia record varies widely with a temperature variation of 17 °C (regardless of the choice of calibration; Figure 5.3A; Appendix 1, Table 5.1). For the lower part of the record (0−360 m, 12.7−9.66 Ma) estimated SSTs average 20°C and vary between 13 and 28 °C (TEX_{86}^{H} calibration of Kim et al., 2010). For a short interval (330 to 360 m) temperatures raise remarkably attaining mean values of 27 °C. At 360 m the TEX_{86}^{H} estimated SSTs drop rapidly and remain comparatively low, with an average value of 16 °C until the top of the investigated section (630 m). When applying TEX_{86}^{L} for <15 °C (i.e. polar and subpolar domains) for calculating SSTs the amplitude is slightly larger than when using TEX_{86}^{H} (Figure 5.3A; Appendix 1, Table 5.1). Notably, the overall trends observed when using TEX_{86}^{H} calibration are mimicked by the TEX_{86}^{L} (Figure 5.3A). Considering the paleogeography of the section we will discuss the data using only the TEX_{86}^{H} and refer to it as SST^{H}.

5.5.1.2 MAT's estimates based on brGDGTs

Measured MAT' values range from 14 to 20 °C with a mean of 17 °C (Figure 5.3B; Appendix 1, table 5.1). Between 120 and 350 m MAT' values increase by ~4 °C when compared to the Volhynian base of the section (0–10 m). From 10 to 120 m temperatures vary between 14 and 18 °C, with a mean value of ~16 °C. From 360 to 540 m MAT' varies between 14 and 19 °C with a mean of 17 °C. For the uppermost part (540–650 m) of the section mean MAT' values increase slightly to ~18 °C. There are root mean square errors on absolute MBT'/CBT-derived MAT reconstructions on the order of 5 °C (Peterse et al., 2012), therefore we postulate that importance should be given to the relative MAT trends.

5.5.2 Compound specific stabile isotope data

5.5.2.1 Compound specific δ^2H and $\delta^{13}C$ data on alkenones

The first significant occurrence of alkenones in the record is at 344.3 m. Until this level alkenones are present in only three samples: at 14.50 m (TP 015), 192.2 m (TP 053) and at 290 m (TP 088). The alkenone concentration in these samples was, however, too low for isotope analysis.

5.5.2.1.1 δ^2H alkenone values

δ^2H values of C_{37} alkenones ($\delta^2H_{C37alkenones}$) range between −126 and −202‰ (Figure 5.3C; Appendix 1, Table 5.2) and follow the same trend as δ^2H values for C_{38} alkenones ($\delta^2H_{C38alkenones}$) showing a very good correlation (R^2 =0.83; Appendix 1, Table 5.2) yet at slightly lower δ^2H values (–125 to –191‰). The $\delta^2H_{C37alkenones}$ record starts with the highest value of –126‰ at 354 m and is followed by a drop to –169‰, increasing again to –145.4‰ at 408.9 m. After 416 m a pronounced negative excursion in $\delta^2H_{C37alkenones}$ occurs with values ranging from –176‰ to –202‰ and a mean of 186‰ (454–560 m). Between 560 and 600 m, $\delta^2H_{C37alkenones}$ and $\delta^2H_{C38alkenones}$ increase again, to values attaining a maximum of –129‰.

After 600 m the $\delta^2H_{C37alkenones}$ decrease sharply from –149‰ to –188‰ and stay at low values until the end of the section, albeit with an accentuated variability (±26‰).

5.5.2.1.2 $\delta^{13}C$ alkenones

$\delta^{13}C$ values of C_{37} alkenones ($\delta^{13}C_{C37alkenones}$) vary between –20.5‰ and –26.1‰ (Figure 5.3D; Appendix 1, Table 5.3) while $\delta^{13}C$ values of C_{38} alkenones ($\delta^{13}C_{C38alkenones}$) fall between –20.2‰ and –26.5‰. Similar to the δ^2H record, $\delta^{13}C_{C38alkenones}$ values follow the same trend as the $\delta^{13}C_{C37alkenones}$ showing a strong correlation (R^2 = 0.89; Appendix 1, Table 5.3). In the 350 m to 416 m interval $\delta^{13}C_{C37alkenones}$ and $\delta^{13}C_{C38alkenones}$ values decrease gradually from –20.5‰ to –23.5‰. Up section, $\delta^{13}C_{C37alkenones}$ values drop to –25.5‰ and remain low with an average of –24.9‰ (except sample TP 183, at 454.95 m).

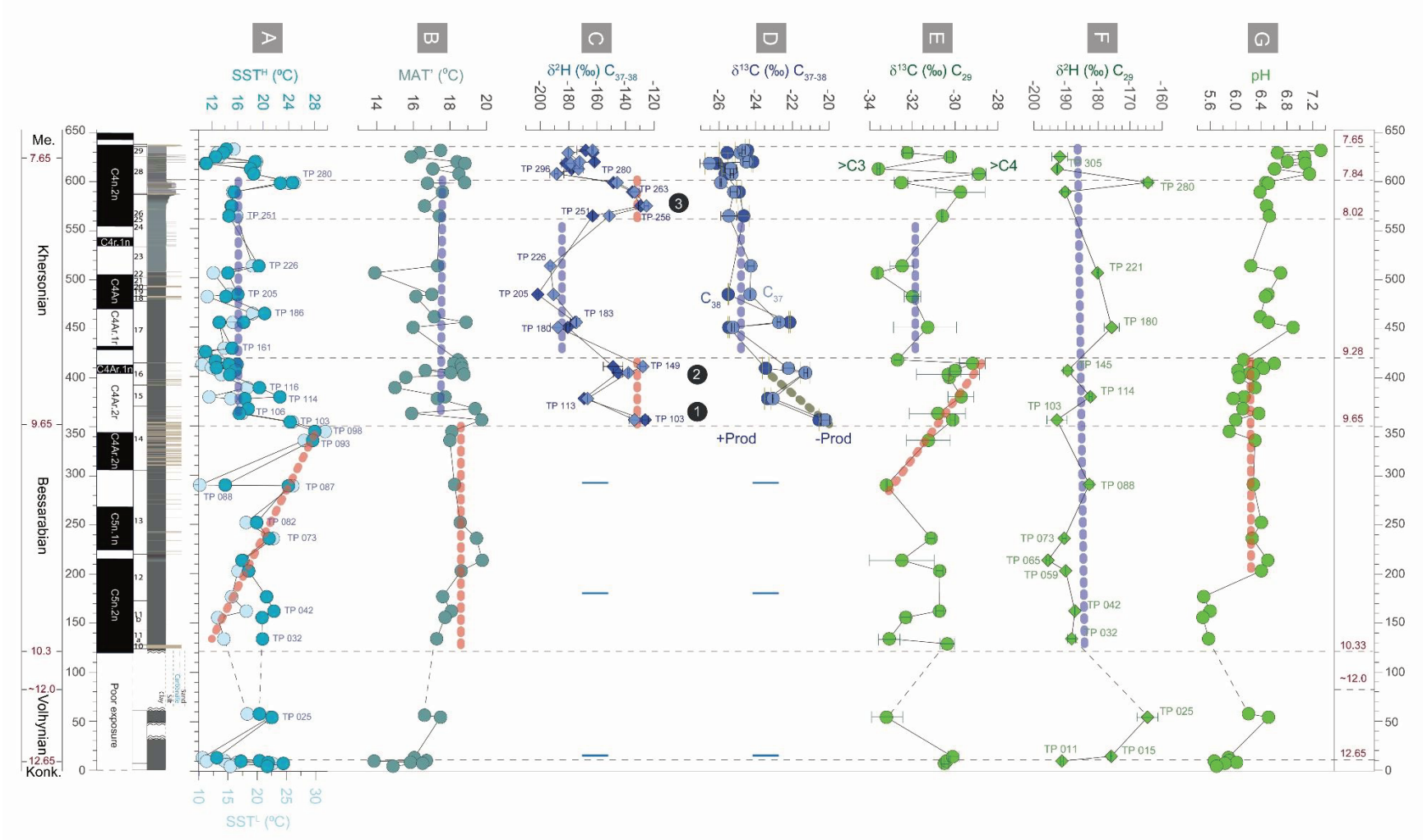

Figure 5.3 Schematic lithologic and magnetostratigraphic logs together with summarized results from GDGTs, alkenones and *n*-alkanes. A) Sea surface temperature (SST^H); B) Mean annual temperature (MAT); C) $\delta^2H_{C37alkenones}$ and $\delta^{13}C_{C38alkenones}$; D) $\delta^{13}C_{C37alkenones}$ and $\delta^{13}C_{C38alkenones}$ No alkenones detected below 350 m except traces in 3 samples (blue lines); E) $\delta^{13}C_{C29n\text{-}alkanes}$ and F) $\delta^2H_{C29n\text{-}alkanes}$; G) Paleo soil pH derived from GDGTs. The stratigraphic levels are in m. The main trends are marked on the figure with dashed lines. Additionally, the drying events are marked (black circles, $\delta^2H_{alkenones}$ plot) and the names of the regional (sub)stages. Error bars are based on the standard deviation of a series of replicate analyses. Dashed colored lines indicate the main values trends.

5.5.2.2 Compound specific $\delta^{13}C$ and $\delta^{2}H$ values of n-alkanes

5.5.2.2.1 $\delta^{2}H$ of long chain n-alkanes

Long chain *n*-alkanes within the Panagia section show a clear odd over even predominance indicating a higher plant wax origin (Eglinton and Hamilton, 1967). $\delta^{13}C$ values of C_{29} *n*-alkanes ($\delta^{13}C_{C29n\text{-alkanes}}$) range between –33.6‰ and –28.9‰ (Figure 5.3E; Appendix 1, Table 5.3). Up to 300 m, $\delta^{13}C_{C29n\text{-alkanes}}$ values fluctuate between –33.2‰ and –30.1‰ attaining a mean of –31.5‰. After 300 m we observe a gradual increase in $\delta^{13}C_{C29n\text{-alkanes}}$ from –33.2 to –29.2‰ at 425.18 m, followed by a rapid and sharp drop to –32.7‰ at 428.70 m (Figure 5.3E). Between 430 and 560 m $\delta^{13}C_{C29n\text{-alkanes}}$ values remain low and range between –30.6 and –33.6‰. Towards the top of the section (560 m to 630 m) $\delta^{13}C_{C29n\text{-alkanes}}$ values are characterized by high variability. With a range of –28.9 to –33.6‰ they cover almost the entire spectrum of $\delta^{13}C_{C29n\text{-alkanes}}$ values recovered over the remainder of the section. In general, $\delta^{13}C_{n\text{-alkanes}}$ values of C_{31} *n*-alkanes ($\delta^{13}C_{C31n\text{-alkanes}}$) parallel the $\delta^{13}C_{C29n\text{-alkanes}}$ record, yet at slightly lower absolute values. $\delta^{13}C_{C29n\text{-alkanes}}$ and $\delta^{13}C_{C31n\text{-alkanes}}$ values co-vary, showing a very good correlation ($R^2 = 0.84$; Appendix 1, Table 5.3).

5.5.2.2.2 $\delta^{13}C$ values of long chain n-alkanes

$\delta^{2}H$ values of C_{29} *n*-alkanes ($\delta^{2}H_{C29n\text{-alkanes}}$) range between –164‰ and –196‰ (Figure 5.3F; Appendix 1, Table 5.2) with an average value of –185‰. Between 0 and 120 m the $\delta^{2}H_{C29n\text{-alkanes}}$ values vary between –165‰ and –191‰ with a gradual increase from of –191‰ at 14.9 m to –165‰ at 120 m. Between 120 m and 630 m $\delta^{2}H_{C29n\text{-alkanes}}$ values fall within a relatively narrow range (–176‰ to –196‰; except one positive excursion to –164‰ at 596 m) attaining a mean $\delta^{2}H_{C29n\text{-alkanes}}$ value of 185‰. The $\delta^{2}H_{C29n\text{-alkanes}}$ values are consistently slightly less negative than their C_{31} counterparts ($\delta^{2}H_{C31n\text{-alkanes}}$; Appendix 1, table 5.2). $\delta^{2}H_{C29n\text{-alkanes}}$ and $\delta^{2}H_{C31n\text{-alkanes}}$ values co-vary, showing a strong correlation ($R^2 = 0.84$; Appendix 1, Table 5.2). $\delta^{2}H$ values of C_{29} *n*-alkanes ($\delta^{2}H_{C29}$) range between –164‰ and –196‰ (Figure 5.3F; Appendix 1, Table 5.2) with an average value of –185‰. Between 0 and 120 m the $\delta^{2}H_{C29}$ values vary between –165‰ and –191‰ with a gradual increase from of –191‰ at 14.9 m to –165 ‰ at 120 m. Between 120 m and 630 m $\delta^{2}H_{C29}$ values fall within a relatively narrow range (–176‰ to –196‰; except one positive excursion to –164‰ at 596 m) attaining a mean $\delta^{2}H_{C29}$ value of 185 ‰. The $\delta^{2}H_{C29}$ values are consistently slightly less negative than their C_{31} counterparts ($\delta^{2}H_{C31n\text{-}}$

$_{alkanes}$; Appendix 1, Table 5.2). δ^2H_{C29} and δ^2H_{C31} values co-vary, showing a strong correlation ($R^2 = 0.84$; Appendix 1, Table 5.2).

5.5.3 Soil pH

Paleo-soil pH values show an overall increasing trend over the course of the section, with pH values increasing from 5.7 (0–20 m) to ca. 7.3 (600–640 m) (Figure 5.3G; Appendix 1, Table 5.1). In the lower part (0–120 m) of the section the pH values fluctuate between 5.6 and 6.5 followed by values typical for more acidic soils (5.5–5.6) at 120–180 m. After 180 m soil pH values increase sharply to 6.4 and maintain within a range of 5.9 to 6.4 until 420 m. Between 420 and 650 m soil pH values increase steadily up to a maximum value of 7.3 at 630.43 m.

5.5.4 Charcoal

The samples show a well-preserved charred material with Poaceae as the most abundant morphotype in the record, followed by herbaceous and wood types (Figure 5.4E; Appendix 1, Table 5.4). The percentage of Poaceae-derived material varies between 0−100%, with the highest abundance (80−100%) at 0–53 m, 200−250 m, 340−490 m and 544 m, and a maximum at 454 m (66 particles/cm^3 representing 85.7% of the total charcoal in the sample).

Herbaceous charcoal morphotypes generally follow the trends of Poaceae. Their abundance varies between 0−100% (0−17 particles/cm^3), with the maximum of charred material at 454 m. Wood morphotypes are less represented in the section and vary between 0 and 67% (0–12 particles /cm^3), with the highest peak at 54 m, accounting for 37.8% of the total charcoal (Figure 5.4E; Appendix 1, Table 5.4). Results from charcoal morphology concentrations and sediment accumulation rates show no significant correlation.

5.6 Discussion: Paleoenvironmental changes between 12.7 and 7.65 Ma

The absolute age constraints for the Panagia section are based on the magnetostratigraphic pattern comprising nine normal and eight reversed polarity intervals with additional seven short-term polarity fluctuations (Palcu et al., 2021) that were correlated to the geomagnetic polarity time scale (GPTS; Hilgen et al., 2012; Ogg et al., 2020). The transition between Konkian and Volhynian dated at 12.65 Ma (Palcu et al., 2017) is located at 2 m in the section. The interval between 2 and 120 m has poor exposure. The outcropping levels pin the 2 to 60 m interval to

Volhynian, while the transition to Bessarabian, at ~12 Ma, must be located in the exposure gap between 60 and 120 m. A straightforward correlation follows. The 120−250 m part of the section covers a long normal polarity interval that correlates to C5n.2n of the GPTS. Upward tuning pins the Bessarabian−Khersonian boundary (at 310 m) at 9.65 Ma. The long dominantly reversed interval between 360−480 m correlates to C4Ar and locates the Khersonian−Maeotian boundary in C4n.1r (625 m) at 7.65 Ma (Palcu et al., 2021). Based on these magnetostratigraphic constraints, the age of each sample was calculated by linear interpolation of the sample levels between the corresponding magnetic chron boundaries. Further, the geochemical proxy results were plotted based on the calculated ages (Figure 5.5).

5.6.1 Sea surface and continental temperature changes

Overall the Panagia SST^H data reveal temperatures higher than the present-day values of 14 °C at the site. SST^H values range from 14 to 28 °C for the interval between 10.3 and 9.68 Ma, a time interval representing most of the Bessarabian substage (Figure 5.5A). After increasing temperatures lasting more than 0.5 Myr, a first rapid increase in SST^H changes marks the end of the Bessarabian substage, at 9.7 Ma, when the SST^H record reaches the highest values of 28 °C, followed by a consecutive warming with SST^H of 24 °C (peaking at 9.57 Ma). This entire warm interval is preceded by an abrupt drop (from 24 to 14 °C) at 9.8 Ma (Figure 5.5A). After 9.66 Ma the record shows low SST^H fluctuations (around 16 °C) until 7.81 Ma. A third prominent SST^H warming peak of ~9 °C is observed in the upper(most) Khersonian (596.47 m) at 7.85 Ma, an interval corresponding to the so-called Great Khersonian Drying (Palcu et al., 2019; 2021). Between 7.85 Ma and 7.66 Ma SST^H values range between 13.8–24.6 °C, with an upward cooling trend. This interval corresponds to the Maeotian transgression, a presumably humid phase (Popov et al., 2016; Palcu et al., 2019) that led to the reconnection with Dacian Basin at 7.65 Ma.

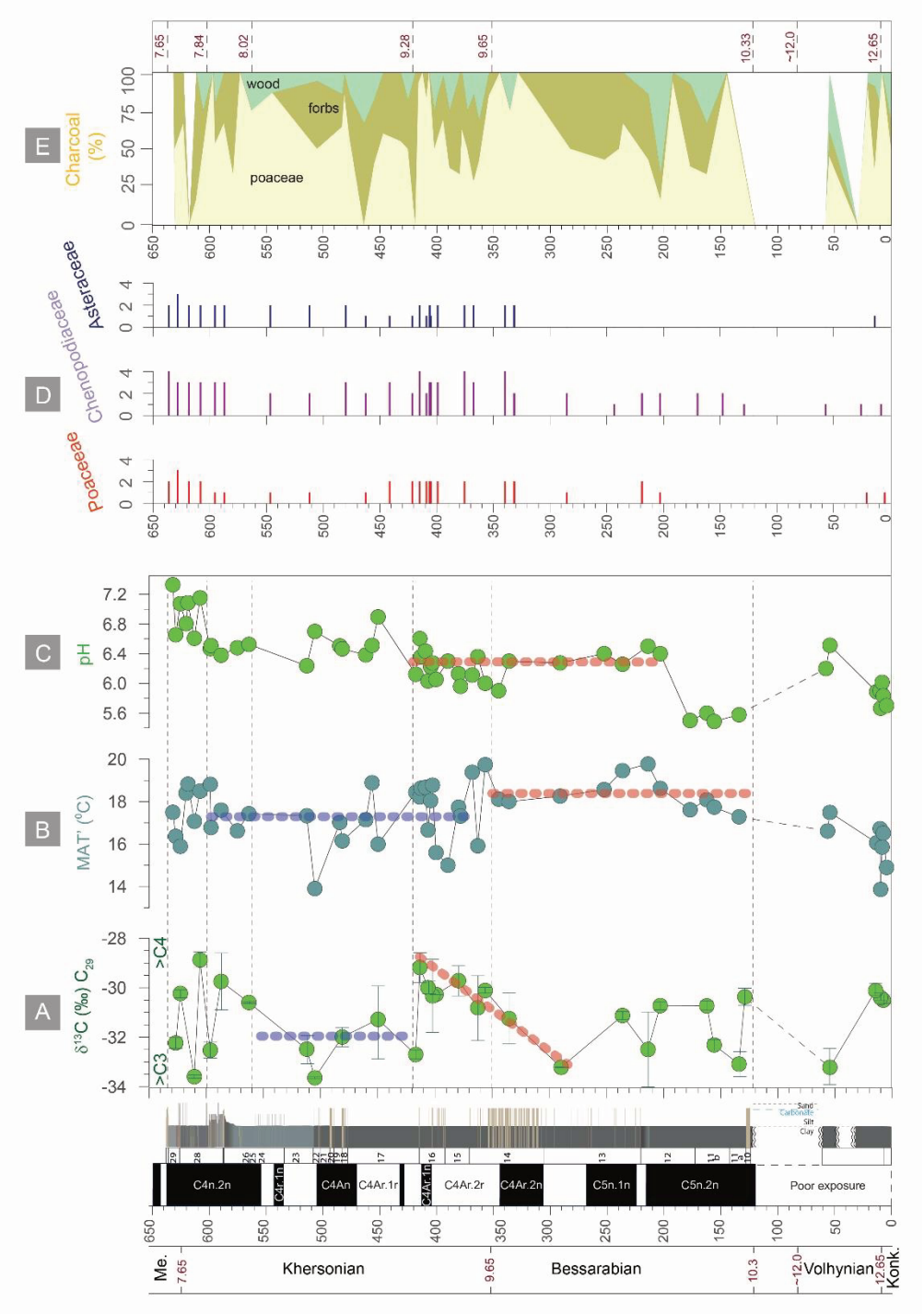

Figure 5.4 Summarized continental signal. A) MAT; B) pH; C) Pollen (Razumkova, 2012) for taxa specific to open land/dry environments (Poaceae, Chenopodiaceae and Asteraceae). The numbers show the relative abundance, where 1 is for present, 2 for rare, 3 for common, and 4 indicates abundant; D) Fire regime reconstruction based on the preserved charcoal. The lithologic and magnetostratigraphic logs, as well as the names of regional substages are presented. Dashed colored lines indicate the main trends.

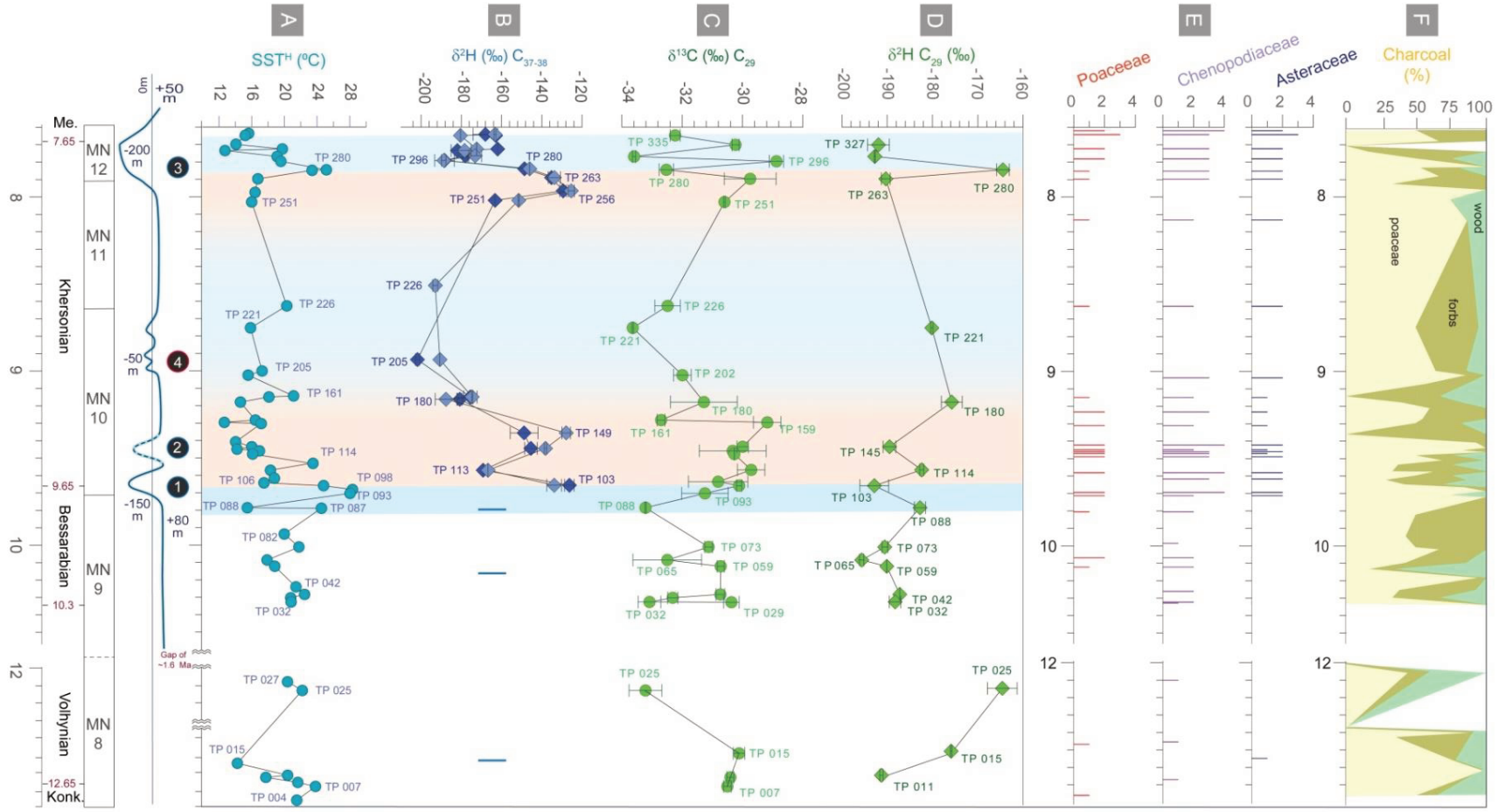

Figure 5.5 Summarized organic geochemistry, pollen and charcoal data. A) SST^{H} derived from GDGTs; B) $\delta^{2}H_{C37alkenones}$; C) $\delta^{13}C_{C29n\text{-}alkanes}$; D) $\delta^{2}H_{C29n\text{-}alkanes}$; E) Selected pollen (Razumkova, 2012) where numbers show the relative abundance, with 1 present, 2 rare, 3 common, and 4 abundant; F) Charcoal. Ages are in million years (Ma). The main environmental changes and their ages are indicated. With orange bars are depicted the main drying periods, while in blue are the wetter periods. The black circles with blue borders represent the observed dry phases (1-3), while red border marks a fourth event cf. Palcu et al. (2021). Blue lines on the $\delta^{2}H_{C37alkenones}$ column mark occasional levels with alkenone occurrence. Dashed lines represent the main trends. The section records a gap of ~1.6 Ma during the Volhynian stage. MN refers to Miocene mammal zones.

The brGDGT-based MAT reconstructions broadly follow the SST record (Figure 5.3B) with MAT values expectedly higher than the present-day values of 11 °C at the site. For the largest part of the Bessarabian (10.3 and 9.79 Ma), a slight increase in temperature (17 to 19 °C) can be observed, while after the onset of the Khersonian, at 9.65 Ma, MAT varies around 17 °C. The only available record in Paratethys, partially overlapping in time with Panagia section, is the DSDP 42B 380 core from central Black Sea (Vasiliev et al., 2020). The interval from the DSDP tentatively correlated to 10 to 8 Ma (Vasiliev et al., 2020) shows values that are slightly lower (14 °C) than those recorded in Panagia (17 °C) specifically for the interval from 9.64 to 7.65 Ma. In the vicinity of the Black Sea, paleobotanical data using coexistence approach estimate similar MAT values of 13.3–17 °C for the Serravallian–Tortonian for sites in Bulgaria and the Ukrainian Carpathians, while lower values of 9–10 °C are depicted for the Ukrainian Plains sites (Ivanov et al., 2011; Syabryaj et al., 2007).

The rapid and large (~14 °C, 9.79−9.68 Ma) SST^H temperature increase prior to the 9.68−9.66 Ma warm interval is remarkable and may have been triggered either by 1) a period of regional warming, 2) a connection to a neighboring warm (marine) basin through a major gateway (Figure 5.6 A–D), or 3) a period of prolonged drought and warming of the Paratethys basin in concert with basin isolation (Figure 5.6 E–H).

1) The absence of large MAT fluctuations coeval to the large SST variation between 9.75 and 9.66 Ma suggests that the warming occurred only in the aquatic domain. Regional transient warming seems to be an unlikely candidate to explain the 14 °C warming of the Paratethys surface waters as age-equivalent brGDGT-based MAT reconstructions indicate that the 9.68–9.66 Ma interval represents the termination of a prolonged time interval (10.3 Ma to 9.66 Ma) of rather constant MAT prior to an overall MAT decrease in concert with SST^H post 9.66 Ma (Figure 5.3).

2) If the rapid SST^H increase between 9.75 and 9.66 Ma was provoked by a connection to a basin supplying a substantial influx of warm waters in <100 kyr, the source must have been a large waterbody since it provoked such a SST change. This interval is marked by the occurrence of *Coccolithus pelagicus* (Popov et al., 2016), an alkenone producer thriving in open marine environments. While alkenones are usually absent from analyzed samples prior to 9.66 Ma, they are continuously reported after this interval. The presence of alkenones could be explained by a model where alkenones producers were introduced by the warm waters derived from a

neighboring (marine) basin. Additionally, the coeval appearance of *Actinoptycus annulatus,* a tropical marine diatom species (Popov et al., 2016), supports the interpretation of an influx of warm marine waters into the Eastern Paratethys. The exact location of the associated marine gateway remains speculative though. During the late Miocene, the Paratethys domain was an active tectonic area with changing connectivity. Previously active Miocene connections through the Transtethyan corridor (in Slovenia; Sant et al., 2017) and Barlad (Romania, Palcu et al., 2017) closed during Bessarabian (~12–9.65 Ma). A gateway between the Black Sea and the Dardanelles existing at ~9 Ma (Krijgsman et al., 2020) may have been too small to generate such important changes in Paratethys SSTs.

3) An alternative explanation for the 9.68−9.66 Ma SST^H warm interval could be a period of prolonged drought and isolation of the Paratethys, leading to a smaller residual water volume in the basin, easier to warm up. Paratethys basin level fluctuated by more than 200 m between the wet and the dry intervals (Palcu et al., 2021). During Paratethys low stands, the area of Panagia switched from deep water to lagoon, coastal swamp and ultimately terrestrial environments (Popov et al., 2006). The high SST^H values could be explained by the installation of shallow water conditions (e.g. lagoonal, coastal). The short-lived warming of the Paratethys basin in the Panagia region however, would not explain the sudden occurrence of alkenone producers and their sustained (post-9.66 Ma) presence in a rather evaporative basin. Continuous drying could have led to increased salinity in the Black Sea/Kuban basin, to values close to normal marine. Possibly, some alkenone producers may have survived previously (as suggested by the TP 015 (12.49 Ma), TP 053 (10.17 Ma) and TP 088 (9.79 Ma) containing traces of alkenones) in ecological niches (e.g. Georgian part of the Black Sea), then expanded in the Paratethys when conditions became suitable.

5.6.2 Hydrological changes: periods of prolonged and intensive droughts

Three periods characterized by extremely high $\delta^2H_{C37alkenones}$ values (corresponding to dry periods) occur within the Panagia record (Figs. 5.3C, 5.5B; Appendix 1, table 5.2): the first one ($\delta^2H_{C37alkenones}$ = −126‰ at 354 m) occurs at the end of the Bessarabian (9.66 Ma), while the second interval (−149‰ at 415.85 m) follows at 9.41 Ma, shortly after the beginning of Khersonian. The third interval, where $\delta^2H_{C37alkenones}$ attains values as high as –129.4‰, occurs at the end of the Khersonian (8.03–7.79 Ma).

Similarly high δ^2H_{C37}values have been reported only from the Mediterranean basin during the Messinian Salinity Crisis (5.97–5.33 Ma), an event characterized by basin-wide massive evaporation ($\delta^2H_{C37alkenones}$ of –140 to –120‰; Vasiliev et al., 2017). In the Black Sea region comparable $\delta^2H_{C37alkenones}$ values (−145‰) were reported in two other sites: Zheleznyi Rog (~10 kilometers east of Panagia section; Vasiliev et al., 2013; 2020) and the deep Black Sea at DSDP 42B site 380 hole (Vasiliev et al., 2015). These sites both document a late Sarmatian (*s.l.*) interval with elevated $\delta^2H_{C37\ alkenones}$. Given the uncertainties on the Zheleznyi Rog and DSDP 42B 380 age models, we tentatively correlate these intervals with the late Khersonian of the Panagia section (562 to 605 m), between 8.02 and 7.79 Ma. Consequently, we interpret the high $\delta^2H_{C37alkenones}$ values as an expression of enhanced evaporation affecting the Paratethys basin. Considering that present-day marine $\delta^2H_{C37alkenones}$ values are rarely higher than −180‰ (e.g. in the warm Sargasso Sea at 31º N; Englebrecht and Sachs 2005; Weiss et al., 2019) evaporative Paratethys water loss must have outpaced rainout and runoff from the basin catchment.

In between the main intervals with high $\delta^2H_{C37alkenone}$ (9.66–9.41 Ma and 8.02–7.79 Ma), MAT and SST^H data indicate a colder climate and δ^2H_{C37} values attain −176 to −202‰. These are found in the present day open marine settings, while the $\delta^2H_{C37alkenones}$ of more restricted Black Sea basin reaches –230‰ (van der Meer et al., 2008). Based on the sedimentological record within the 8.57−9 Ma time period, an additional drying event, of smaller intensity, has been described in Panagia (Palcu et al., 2021). We were unable to identify this event in the organic geochemistry data possibly due to the lower sampling resolution. All warming events observed in the Panagia section are accompanied by carbonate deposition (Palcu et al, 2021), suggesting coeval changes in the chemistry and circulation of the basin.

The $\delta^{13}C_{C37}$ values from Panagia (−26.5‰ to −20.5‰) are close to global upper Miocene values (−25‰ to −21‰) (e.g. Pagani et al., 1999), yet somewhat different to those measured in the recent Black Sea (−26‰ to −29 ‰) (e.g. Freeman and Wakeham, 1992). Important is the 3‰ decrease in $\delta^{13}C_{C37alkenones}$ (Figure 5.3D; Appendix 1, Table 5.3) between 9.66 and 9.28 Ma, that parallels an increase in δ^2H_{C37} up to−126‰, a value typical for evaporative conditions. After 9.28 Ma, until the end of the record, the $\delta^{13}C_{C37alkenones}$ values are stable around −25‰, although between 8.03 and 7.79 Ma the δ^2H_{C37} registers another marked increase up to –129.4‰. While the $\delta^2H_{C37alkenones}$ depends heavily on the hydrological conditions of a basin (e.g. evaporation vs.

precipitation), the $\delta^{13}C_{C37alkenones}$ depends on the magnitude of the carbon isotopic fractionation in the sedimentary record. The latter is a function of various factors, including: 1) the concentration of aqueous CO_2, 2) algal growth rates (Bidigare et al., 1997) and 3) the ratio of cellular carbon content to cell surface area (Popp et al., 1998) during late-stage exponential and stationary growth (Benthien et al., 2007). We can explain the 3‰ decrease between 9.66 and 9.28 Ma in the $\delta^{13}C_{C37alkenones}$ as a consequence of (a combination) of the three factors mentioned above, being enhanced by increasing evaporative conditions (i.e. high $\delta^{2}H_{C37alkenones}$). However, we speculate that the algal growth rate had a major role in determining the carbon isotopic fractionation. No significant changes in the concentration of aqueous CO_2 are known for the time interval to explain alone the 3‰ decrease, although paleo-pCO_2 reconstructions based on $\delta^{13}C_{C37alkenones}$ show an 80 ppm increase at ~9.5 Ma (Pagani et al., 1999), stabilizing afterwards at the preindustrial levels by 9 Ma. The limited number of preserved coccoliths reported in Panagia (Popov et al., 2016) does not allow a reliable assessment of changes in the cell size. The rather constant $\delta^{13}C_{C37alkenones}$ between 8.03 and 7.79 Ma remains difficult to explain without identification of the alkenone producers.

5.6.3 Vegetation changes: expansion of grasslands

The $\delta^{13}C$ values of plant waxes primarily reflect different vegetation types. Leaf wax long chain *n*-alkanes from C_3 plants have a mean $\delta^{13}C$ value of −33.0‰, whereas those from C_4 plants (e.g. grasses, savannah, salt marsh and desert plants) are as high as −21.7‰ (e.g. Castañeda and Schouten, 2011; Feakins et al., 2020).

In the Panagia section, marked trends in $\delta^{13}C_{C29}$ reaching values up to −29‰ are observed between 9.66−9.28 Ma and 8.02−7.77 Ma. The high $\delta^{13}C_{C29n\text{-alkanes}}$ values between 9.66−9.28 Ma coincide with the interval of very high $\delta^{2}H_{C37alkenones}$ values suggesting that (regionally) dry conditions supported the spread of C_4 vegetation in the area surrounding the basin. It is also remarkable that the +2‰ shift in $\delta^{13}C_{C29n\text{-alkanes}}$ (i.e. terrestrial environment) (Figure 5.3E, 5C) is opposite to the –3‰ shift in the alkenone $\delta^{13}C_{C37alkenones}$ (i.e. aquatic environment) data (Figure 5.3D; Appendix 1, Table 5.3). The second interval with high $\delta^{13}C_{C29n\text{-alkanes}}$ values (8.02−7.77 Ma) also exhibits high variability in $\delta^{13}C_{C29}$ values that oscillate between −28.9‰ and −33.6‰. We interpret these fast changes as a consequence of repeated vegetation changes in the area surrounding the basin, from more C_3 plants ($\delta^{13}C_{C29n\text{-alkanes}}$ = −33.6‰) to an

important contribution of C_4 plants ($\delta^{13}C_{C29n\text{-alkanes}}$ = −28.9‰). Phytolith data indicate that C_3 grass-dominated savanna-mosaic vegetation had become widespread in Turkey and surrounding areas by the late Miocene (~9 Ma), while C_4 grasses were of little ecological importance in western Eurasia until at least the latest Miocene (~7 Ma) (e.g. Strömberg et al., 2007; Ivanov et al., 2002). To date, the oldest ecosystem dominated by C_4 grasses in Western Eurasia has been documented for the Pikermi Formation between 7.35−7.14 Ma (Böhme et al., 2017).

The Panagia pollen record (Razumkova, 2012) suggests an important change in the dominant vegetation through the increased abundance of Chenopodiaceae, Asteraceae and Poaceae pollen and of herbaceous charcoal morphologies during the Khersonian, especially during the three main drying events (Figs 5.4D, 5.5E). Our charcoal record further indicates an increase in biomass burning and herbaceous morphotypes, supporting a dryer, more flammable ecosystem (Figure 5.5F). Chenopodiaceae abundance also suggests a dry-saline environment (El-Moslimany, 1990) while the Asteraceae family (*Artemisia* in particular) is a newcomer that expands westwards from China (Wang, 2004). The occurrence and increased abundance of Asteraceae also hints at the expansion of a wider open landscape, favored by a drying Paratethys. Interestingly, the increased dominance of herbaceous charcoal morphologies between 9.66 and 9.28 Ma (Figure 5.5F; Appendix 1, table 5.4) is coeval with the high $\delta^2H_{alkenones}$ (i.e. excess evaporation), high $\delta^{13}C_{n\text{-alkanes}}$ (i.e. more C_4 suggesting dryers conditions), increasing paleo-soil pH (i.e. drier conditions) (Figure 5.3G).

The other time interval with similar data is during late Khersonian, between 8.02 and 7.79 Ma, when increased dominance of herbaceous charcoal morphologies is coeval with higher $\delta^2H_{alkenones}$, high $\delta^{13}C_{n\text{-alkanes}}$, and, in this case, increased paleo-soil pH (up to the highest values, averaging ~ 7), typical for drier conditions and open vegetation. The coeval 2‰ observed increasing trend in $\delta^{13}C_{C29n\text{-alkanes}}$, opposing the decreasing $\delta^{13}C_{C37alkenones}$ by 3‰ is striking. The increase in $\delta^{13}C_{n\text{-alkanes}}$ 9.66 and 9.28 Ma (Figs 5.4E; 5.5C) supports an increase of C_4 plant contribution as the global expansion of C_4 grasslands in the late Miocene has been attributed to a large-scale decrease in atmospheric CO_2 (Cerling et al., 1997). On the other hand, the 3‰ decrease in $\delta^{13}C_{alkenones}$ in Panagia could be explained by a change in haptophytes physiology over time as the depositional environment changed.

Knowledge about vegetation changes has implications for the interpretation of the *n*-alkane δ^2H data because the discrimination against deuterium (^2H) during photosynthesis is

greater in C_3 plants than in C_4 plants (Polissar and Freeman, 2010; Feakins and Sessions, 2010). Despite these physiology-induced limitations $\delta^2H_{n\text{-alkanes}}$ values have been successfully used in reconstructions of δ^2H of paleo precipitation (e.g. Sachse et al., 2004; Pagani et al., 2006; Niedermeyer et al., 2016).

Except for two samples (at 12.13 Ma and at 7.85 Ma) where $\delta^2H_{C29n\text{-alkanes}}$ values increase to ~−164‰, $\delta^2H_{C29n\text{-alkanes}}$ values in the Panagia section average −185 ‰ with rather low (±10 ‰) variability. This low variability in $\delta^2H_{C29n\text{-alkanes}}$ suggests that the hydrogen isotopic composition of precipitation stayed rather constant within the basin catchment during the late Miocene. Particularly important in this context is sample TP 280 at 7.85 Ma (Figure 5.5D). At this level highest $\delta^2H_{C29n\text{-alkanes}}$ values (ca.−164‰) coincide with high $\delta^2H_{C37alkenones}$ values of ca. −130‰, high SST^H of 26 °C, high MAT of 19 °C and high $\delta^{13}C_{C29n\text{-alkanes}}$ values of −29‰. Collectively, these data indicate that exceptionally dry conditions coincided with an exceptionally warm period at 7.85 Ma.

Assuming rather constant rainfall δ^2H values, the positive excursions in $\delta^2H_{C37alkenones}$ values at 9.66, 9.45−9.41 and 7.85−7.87 Ma support the idea that these elevated $\delta^2H_{C37alkenones}$ do not reflect increasing temperature within the basin water column, but are rather a consequence of episodic basin restriction with enhanced evaporation as a consequence of changes in basin hydrology or connectivity to adjacent basins. Such a scenario is supported by the observation that the overall stable $\delta^2H_{C29n\text{-alkanes}}$ values (for exceptions see above) do not mimic the MAT and SST^H temperature records (Figs 4.4; 4.5), indicating that temperature change is not the driver for the drying phases between 9.66−9.41 Ma. Despite the warm SSTs and MATs, the most probable mechanism for basin-wide droughts at the onset of the Khersonian (9.65 Ma) is a change in connectivity resulting in basin isolation and regression.

In contrast, rather low SST^H and low MAT' (at 16–18 °C) combined with increased evaporation (high $\delta^2H_{C37alkenones}$) and low $\delta^2H_{C29n\text{-alkanes}}$ values collectively indicate that the 7.93 Ma Great Khersonian Drying was associated with rather cool conditions, similarly to the increased negative water budget observed for the Mediterranean basin during glacial peaks centered around 5.8 and 5.6 Ma (Vasiliev et al., 2017).

5.6.4 Timing of events in regional and global context

The time-intervals with dryer conditions recorded in Panagia (9.66–9.28 and 8.02–7.84 Ma) coincide with periods of mammal turnover and dispersal in Eurasia suggesting that major environmental changes occurred also in circum-Paratethys region, when periods of prolonged droughts generated biotic crises and animal displacements across the Eurasian continent.

Periods of drought observed in the Panagia record at 9.68–9.66 Ma closely coincide with the MN 9–MN 10 transition, at 9.7 Ma, known as the onset of the Vallesian Crisis (e.g. Fortelius et al., 2014), whose amplitude has been subsequently questioned. Casanovas-Vilar et al. (2014) propose that sampling and preservation bias led to an overrating of extinction rates for the Vallesian Crisis. However, important in the context is the first occurrence of murids in Europe, dispersed from southern Asia, a time-transgressive event connected to the opening of landscapes reaching Eastern Europe between 9.7−9.6 Ma (Van Dam, 1997; Wessels, 2009). The drought in Panagia at 9.68–9.66 Ma also corresponds to a diminishing hydrologic cycle observed between 9.7−9.5 Ma, when an Atlantic driving mechanism was proposed by Böhme et al. (2008) to explain the Europe transition from a washhouse to a dryer climate.

At Panagia, $\delta^{13}C_{C29n\text{-alkane}}$ values indicate an increased contribution of C_4 plants adapted to drier conditions at 9.66 Ma. Similarly high $\delta^{13}C_{C29n\text{-alkane}}$ values continue until 9.4 Ma, when in Western Europe increased seasonality accelerated the demise of the evergreen subtropical woodlands (Mosbrugger et al., 2005; Fortelius et al., 2014). The end of the Bessarabian (9.65 Ma) also corresponds to the maximum in dust mass accumulation rates typical of dry deposition announcing the onset of transient Arabian hyperaridity in the proximity of the Paratethys domain (Böhme et al., 2021). The other marked increased contribution of C_4 plants and excessive drought observed in Panagia between 8.02 and 7.84 Ma appears to be correlated to a second period of Arabian hyperaridity centered at 7.78 Ma (Böhme et al., 2021). Using a 3D paleogeographic model Palcu et al. (2021) calculated a ~ 70% loss of Paratethys surface and a ~33% volume reduction during regressions associated to the 9.66–9.28 and 8.02–7.84 Ma dry phases.

In the aquatic domain, the end of the Bessarabian (9.65 Ma) stands out as the moment when a large number of the endemic paratethyan cetaceans (dominated by baleen whales) become extinct, while the Cetotheriidae family dominated the Khersonian (Gol'din and Startsev, 2017). The Volhynian and Bessarabian whales (Gol'din and Startsev, 2017) partial extinction at

the end of the Bessarabian coincides with an event observed in this contribution at ~9.7 Ma, the so-called bed 14 in Popov et al. (2016). Bed 14 in Panagia section is a peculiar layer containing remains of large baleen whales, small bones and wood fragments (Popov et al, 2016) and coincides with the marked shift in the SST^H between at 9.68 and 9.66 Ma. The Bessarabian–Khersonian transition is also marked by a bivalve turnover in the Eastern Paratethys (Kojumdgieva and Popov, 1988), when assemblages containing *Plicatiforma fittoni* and small-sized *Cardium* bivalves are replaced by *Mactra* genus.

When compared to existing age-equivalent records from the marine Mediterranean (Tzanova et al., 2015), the northern Atlantic and the Indian Ocean (Herbert et al., 2016), the Panagia record shows distinct similarities yet also important differences: 1) Paratethys SST^H values are ~7 °C lower when compared to the Mediterranean Monte dei Corvi section (Italy, Tzanova et al., 2015; Appendix 1, Figure 5.3B), however, the temporal resolution of our record does not allow discriminating the short temperature drops depicted in the Monte dei Corvi SST record; 2) During the upper Khersonian and transition into Maeotian (around 7.7 Ma) we observe a similar cooling trend to the North Atlantic ODP 907 record (Appendix 1, Figure 5.3C); however with significantly warmer (~7 °C) Paratethys waters; 3) For the Bessarabian the overall trend is similar to the Indian Ocean ODP 722 record (Appendix 1, Figure 5.3E) with water temperature only 3 °C higher in the Paratethys.

Collectively these observations support a model in which the Eastern Paratethys evolved as a largely (en)closed system, recording paleoenvironmental signals that are governed by interbasinal connectivity (or lack of it) and regional climate change in the basin catchment. Acting as an important source of humidity for Western and Central Asia, the size and areal extent of the Paratethys water body, however, is likely to have had a major impact on hydroclimate patterns in the Eurasian interior (Ramstein, et al., 1997). The cumulative fluctuations in both hydrology and surface temperature of Paratethys might have increased the aridity and additionally enhanced seasonality, with different partition of moisture over the year. Our combined data suggests a decoupling from the global system (Böhme et al., 2021), dominated by a local regional climate induced by tectonics and Paratethys volume and, more importantly, areal extent reduction.

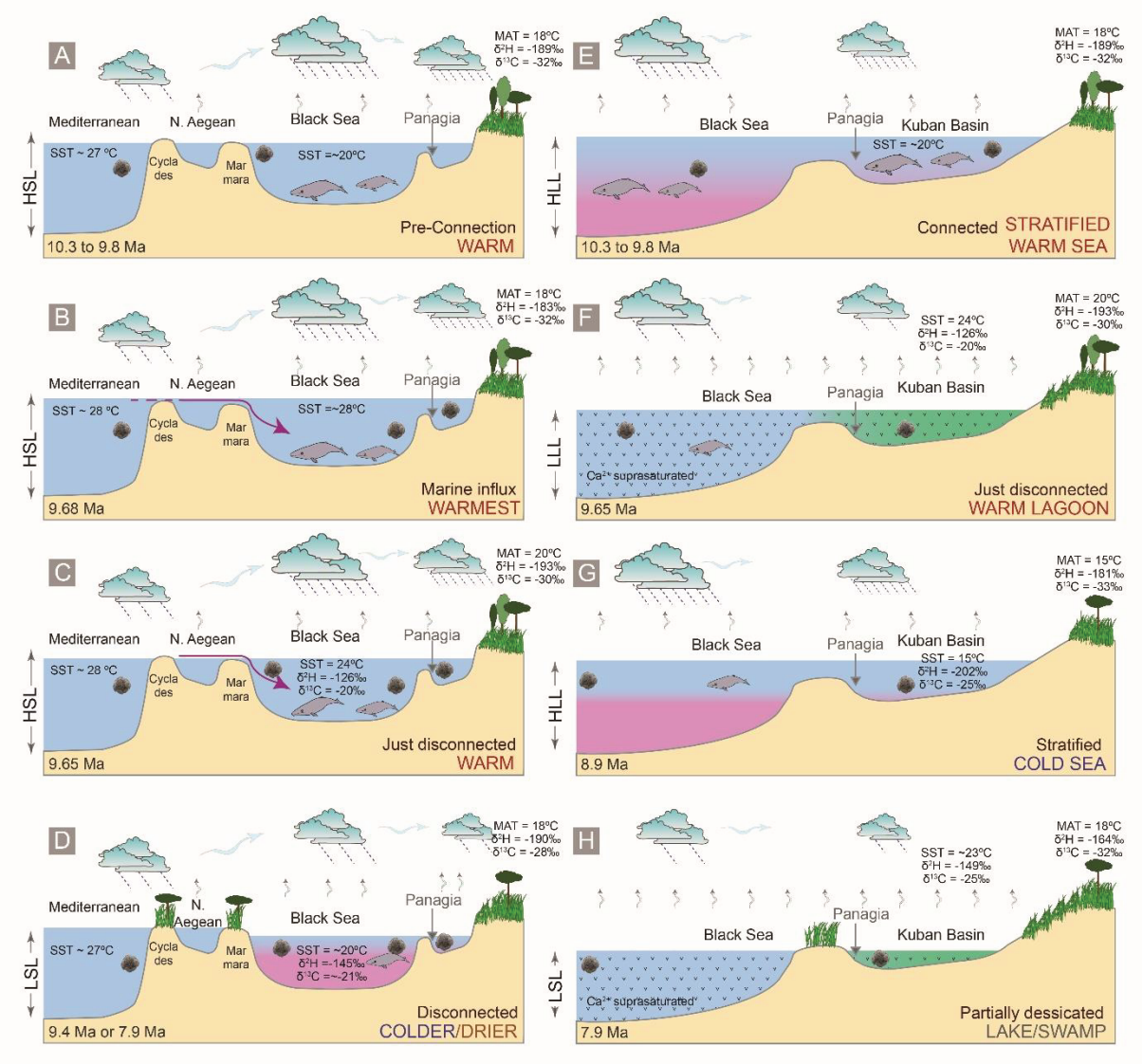

Figure 5.6 Schematic scenarios at different times corresponding with events found in Panagia section. A–D scenarios based on a short connection with another basin at 9.68 Ma followed by complete isolation (Mediterranean SST values from Tzanova et al., 2015), while E–H scenarios assume isolation with no possible connection to another marine basin at 9.68 Ma. A) 10.3−9.8 Ma a warm East Paratethys disconnected from the global ocean; B) At 9.68 Ma, a short connection with a warmer water body is established (possibly the Mediterranean via proto-Aegean); C) At 9.65 Ma the connection is closed; D) At 9.4 and 7.9 Ma the basin becomes isolated again, but in a colder and dyer environment; E) Between 10.3−9.8 Ma the basin becomes stratified due to isolation; F) At ~9.65 Ma the basin experiences a strong regression that transforms marginal realms in poorly connected lagoons or marginal lakes, increase salinity and mineral content in the central basin with negative impacts on the biota; G) After the first crisis the basin experiences a partial recovery during colder and more humid periods; H) The regression trend culminates at ~7.9 Ma when the areas of Panagia become coastal-swamp environments. Please note that the proximity of the Panagia section to terrestrial sources changes greatly throughout the above-mentioned episodes. Abbreviations: HSL−High Sea Level; LSL−Low Sea Level, HLL−High Lake Level, LLL−Low Lake Level.

5.7 Impact of Paratethys over biota*

*Additional chapter not included in the paper

5.7.1 Impact over the aquatic biota

The connection of the Paratethys with the Atlantic Ocean (via the Mediterranean) and the Indian Ocean ended at ~11.6 Ma (Bessarabian; Ter Borgh et al., 2013). Afterwards the Paratethys evolved as a restricted basin inhabited by a highly endemic fauna (Rögl, 1999). Marine mammals trapped inside the Paratethys, in particular whales, adapted and evolved leading to the establishment of the new marine whale family *Cetotheriidae*, lineage that includes the smallest edentulous (toothless) baleen whales in Earth's history (Gol'din, 2018). All paratethyan cetotheriids display a non-pathological condition called pachyostosis (Riabinin 1934; Gol'din et al., 2014), resulting in bones thickening (i.e. mostly vertebras and ribs). When osteosclerosis (increasing bones density) is associated with pachyostosis (Domning and Buffrénil, 1991), it generates a new condition called pachyosteoclerosis, described in plesiosaurs as an ontogenic adaptation to shallower waters (Wiffen et al., 1995). In the case of Paratethys whales, the presence of pachyosteoclerosis and dwarfism did not mean only the adaptation to a shallower environment, but also to an environment restricted in space, as the Paratethys basin fragmentation and shrinking progressed.

The original assemblage of baleen whales (*Zygiocetus nartorum, Cethoterium mayeri, C. klinderi, C. pusillum, C. maicopium, Kurdalagonus mchedlizei*) inhabiting the Eastern Paratethys (Caucasus, Crimea and Taman; Gol'din, 2018) became extinct at around 9.6 Ma (end of Bessarabian). However, other species (*Brandtocetus chongulek, C. riabinini, C. rathkii, Mithridatocetus eichwaldi, M. adygeicus, M.mayeri*) survived in restricted areas until the end of Khersonian (7.65 Ma). In Panagia section, a level containing remains of large baleen whales, small bones and wood fragments (Popov et al., 2016) overlaps with the marked shift in SST^{H} between at 9.68 and 9.66 Ma. We hypothesize that the extinction of these baleen whales might have been the consequence of the short-lived (9.68 to 9.66 Ma) event that brought waters with highly contrasting salinity and sea surface temperature into the Eastern Paratethys (Figs 5.4, 5.5). Most of these animals (both stenohaline and endemic) could not adapt to the abrupt environmental changes and became extinct. Additionally, the highly evaporative conditions between 9.66 and 9.28 Ma possibly allowed the survival of only a limited number of individuals, described mainly from the northern Black Sea region (Gol'din and Startsev, 2017).

Paleontological data also support the appearance of benthic foraminifera (*Nonion, Elphidium*), oceanic planktonic diatoms (*Thalassiosira, Nitzshia, Azpeitia*) and coccolithophoriids (*Coccolithus pelagicus* and *Reticulofenestra sp*.; Popov et al., 2016) at 9.66 Ma. *Coccolithus pelagicus* and *Reticulofenestra sp*. are known as alkenone producers. Their presence reinforces the existence of a possible connection with an adjacent basin, connection that facilitates the transport or migration of new taxa in the Black Sea region. Due to continued restriction and basin stratification alkenone-synthetizing species thrived at Panagia. Over the course of more than 2 Myr (9.7–7.5 Ma) alkenone production in the basin water column was intense indicating massive blooms of alkenone producing algae. Since only isolated calcifying elements were described for the 9.75 Ma event (i.e. *Calcidiscus leptoporus*, *Cocolithus pelagicus*, *Cyclicargolithus floridanus*, *Thoracosphaera* and *Reticulofenestra;* Popov et al., 2016), the dominant alkenone synthesizers were either non-calcifying haptophytes or acidic conditions prevented preservation of tests within the depositional environment.

An abundance of noncalcifying alkenone synthetizers suggests a very important role in the biological pump of Eastern Paratethys as haptophytes have an incredible capacity of adaptation (i.e. *Gephyrocapsa*, Bollman (1997). Studies on modern organisms have shown that alkenone production is also linked to physiological stress induced by low salinity waters (Schulz et al., 2000; Bendle et al., 2009). As a result of basin fragmentation, the Eastern Paratethys sub-basins progressively lost their marine properties and turned into brackish-fresh water bodies fed primarily by riverine input (Figure 5.6C). The resulting conditions must have exerted particular environmental stress for isolated organisms, including haptophytes. It is possible that the high amounts of alkenones identified in the section result from increased environmental stress, especially during early colonization period (9.66 – 9.28 Ma).

5.7.2 Impact over terrestrial biota

Paratethys fragmentation had a great impact also on the terrestrial ecosystems. Coupled $\delta^{13}C_{n\text{-alkanes}}$, $\delta^{2}H_{alkenones}$, pollen (Razumkova, 2012) and charcoal morphology data from the Panagia section indicate an increased presence of C_4 plants in the basin catchment and basinal drought between 9.66 and 9.28 Ma (Bessarabian to Khersonian transition, partly overlapping with the end of the Vallesian) and between 8.02 and 7.84 Ma (latest Khersonian, largely overlapping with the Turolian; Figure 5.5). These two time intervals of dryer conditions recorded in Panagia coincide

with periods of substantial mammal turnover in Eurasia: start of the 9.7 Ma dry phase in Paratethys overlaps with MN 10 (9.7 – 8.0 Ma), while the beginning of 8.02 Ma dry phase overlaps with MN 11 (8 – 7 Ma) early Turolian). Data from Panagia section (Figs. 5.4, 5.5) suggests that major environmental changes occurred at a larger scale (including Central Eurasia) when periods of prolonged droughts dramatically affected animals across the Eurasian continent, generating massive displacements.

The vegetation typical to dryer conditions closely coincides with the onset of the Vallesian Crisis (at 9.7 Ma, with the end of MN 9 mammal zone) when increased seasonality (Mosbrugger et al., 2005) accelerated the demise of the evergreen subtropical woodlands in Western Europe (Fortelius et al., 2014) and is closely linked to major environmental change in the Panagia section at 9.68-9.66 Ma. We hence hypothesize that the environmental change causing the Vallesian Crisis in Western Europe had a coeval, major imprint in the Paratethys domain including the migration of Vallesian taxa in Eastern Europe due to increased continentalisation (Bruch et al., 2011, Vasiliev et al., 2020) and expansion of grasslands from Anatolia to Europe (Syabryaj et al., 2007, Strömberg et al., 2007).

The second increased contribution of C_4 plants and aridity observed between 8.02 and 7.84 Ma (latest Khersonian) also appears to be correlated to the transition between MN 10 to MN 11, at 8 Ma (Hilgen et al., 2012). Apparently, there is a diachrony between the occurrence Vallesian type of fauna in the Western Europe and the one in the Eastern side. However, the lack of direct magnetostratigraphic and radiometric dating for the Eastern European mammal sites render the direct correlation of events in time. Regardless of presence/absence of diachrony between east and west, the migration of Vallesian taxa in Eastern Europe was determined by increased continentalisation (Bruch et al., 2011, Vasiliev et al., 2020) and expansion of grasslands from Anatolia to Europe (Syabryaj et al., 2007; Strömberg et al., 2007).

The wide open landscapes created during the late Miocene and the new land bridges favored the expansion of a new biome called Pikermian fauna (Bernor et al., 1996), with primates, rhinoceros, giraffes, gazelles, giant sloths, large felines, hyenas, etc. (Roussiakis et al., 2019). The same environment facilitated the expanding of primates and appearance of early hominines (in what is today's Greece, Bulgaria and Anatolia) between 9 to 7 Ma (Böhme et al., 2017), rebooting the existent Eurasian ecosystems, transforming Eurasia in what Bernor et al. (1996) calls a 'species factory'.

The combined analysis of terrestrial and aquatic biomarkers as well as their isotopic inventory, therefore not only allows to identify regional climatic events, but also permits to relate one of the major Neogene faunal crises in western Europe to paleoenvironmental changes in the Eastern Paratethys domain.

5.8 Conclusions

The integrated temperature, δ^2H and $\delta^{13}C$ isotope compositions of *n*-alkanes and alkenones combined with charcoal data reveal distinctive environmental conditions during the late Miocene in the Eastern Paratethys of Central Eurasia from the well-dated Panagia section (Taman Peninsula, Russia). Based on the multiproxy approach, we observe a series of important environmental events:

1) Between 9.68 and 9.66 Ma a short event generated much warmer and most probably more saline waters in the Eastern Paratethys. This event caused alkenone producers to thrive and marks the end of the Bessarabian stage. The warming can be explained either by i) an alleged marine water influx introducing the alkenone producers into the basin (i.e. a connection to an adjacent water body, possibly Mediterranean via proto-Aegean), although the exact location remains speculative, or ii) a warming of the basin associated with salinity increase as consequence of isolation and water level drop (i.e. a switch from open sea to lagoon conditions).
2) Three major drying events are observed in the Panagia record: at 9.65 Ma, 9.4 Ma and 7.9 Ma. The three events are well expressed in high $\delta^2H_{alkenones}$, indicating increased evaporation.
3) At 9.6 Ma a change towards increased contribution of C_4 plants occurs, indicating a gradual transition from forests towards open land vegetation. This interval is marked by an intensified fire activity in the area, as the charcoal concentration increases.
4) The onset of open type vegetation and the appearance of the Asteraceae plant family are likely to be the result of continentalisation and, possibly, increased seasonality.
5) Panagia section temperature trends do not follow those of the larger water bodies around Eurasia (Mediterranean, North Atlantic and Indian oceans), suggesting that the Eastern Paratethys evolved as a fragmented, closed and restricted basin(s), being subject to its own environmental conditions.

5.9 Acknowledgements

This work was financially supported by Netherlands Organization for Scientific Research (NWO) [grant 865.10.011] of W.K., by German Science Foundation (DFG) [grant VA 1221/2-1] of I.V. and Senckenberg Gesellschaft für Naturforschung. D.P. acknowledges the Fundação de Amparo à Pesquisa do Estado de São Paulo (FAPESP) for financial support [grant 2018/20733-6]. I.V. and W.K. thank the sampling team (A. Iosifidi, V. Popov, S. Popov and M. Stoica) during 2005–2006 campaigns. G.B. and I.V. thank Ulrich Treffert for support in the SBiK-F organic geochemistry laboratory. Special thanks from G.B. to the Department of Marine Microbiology and Biogeochemistry (NIOZ). We also thank the two anonymous reviewers for their constructive suggestions that improved the original manuscript.

References

Bendle, J.A.P., Rosell-Melé, A., Cox, N.J., Shennan, I., 2009. Alkenones, alkenoates, and organic matter in coastal environments of NW Scotland: Assessment of potential application for sea level reconstruction. Geochemistry Geophysics Geosystems, 10 (12).

Benthien, A., Zondervan, I., Engel, A., Hefter, J., Terbrüggen, A., Riebesell, U., 2007. Carbon isotopic fractionation during a mesocosm bloom experiment dominated by Emiliania huxleyi: Effects of CO2 concentration and primary production. Geochimica et Cosmochimica Acta, 71, 6, 1528−1541.

Bernor, R.L., Solounias, N., Swischer, C.C., Van Couvering, J.A. 1996. The corellation of three classical "pikermian" mammal faunas – Maragheh, Samos and Pikermi -with the European MN Unit System. In: Bernor, R.L., Fahlbusch, V., Mittman, H.-W (Eds.), The Evolution of Western Eurasian Neogene Mammal Faunas, Columbia University Press, New York. 137–154.

Bidigare, R.R., Fluegge, A., Freeman, K.H., Hanson, K.L., Hayes, J.M., Hollander, D., Jasper, J.P., King, L.L., Laws, E.A., Milder, J., Millero, F.J., Pancost, R., Popp, B.N., Steinberg, P.A., Wakeham, S.G., 1997. Consistent fractionation of 13C in nature and in the laboratory: growth-rate effects in some haptophyte algae. Global Biogeochem. Cycles, 13(1), 251–2.

Böhme, M., Ilg, A., Winklhofer, M., 2008. Late Miocene 'washhouse' climate in Europe. Earth and Planetary Science Letters 275, 393–401.

Böhme, M., Spassov, N., Ebner, M., Geraads, D., Hristova, L., Kirscher, U., Kötter, S., Linnemann, U., Prieto, J., Roussiakis, S., Theodorou, G., Uhlig, G., Winklhofer, M., 2017. Messinian age and savannah environment of the possible hominin *Graecopithecus* from Europe. PLOS ONE 12(5): e0177347. https://doi.org/10.1371/journal.pone.0177347

Böhme, M., Spassov, N., Majidifard, M.R., Gärtner, A., Kirscher, Marks, M., Dietzel, C.U., Uhlig, G., El Atfy, H., Begun, D.R., Winklhofer, M., 2021. Neogene hyperaridity in Arabia drove the directions of mammalian dispersal between Africa and Eurasia, Nature Communication Earth and Environment, 2, 85. https://doi.org/10.1038/s43247-021-00158-y.

Bollman, J., 1997. Morphology and biogeography of Gephyrocapsa coccoliths in Holocene sediments. Marine micropaleontology 29, 319−350.

Bruch, A.A., Utescher, T., Mosbrugger, V., 2011. Precipitation patterns in the Miocene of Central Europe and the development of continentality. Palaeogeography, Palaeoclimatology, Palaeoecology, 304, 202−211.

Casanovas-Vilar, I., van den Hoek Ostende, L.W., Furio, M., Madern, P.A., 2014. The range and extent of the Vallesian Crisis (Late Miocene): new prospects based on the micromammal record from the Vallès-Penedès basin (Catalonia, Spain). Journal of Iberian Geology, 40 (1), 29−48. https://doi.org/10.5209/rev_JIGE.2014.v40.n1.44086

Castañeda, I.S., Schouten, S., 2011. A review of molecular organic proxies for examining modern and ancient lacustrine environments. Quaternary Science Reviews, 30, 2851–2891.

Cerling, T.E., Harris, J.M., MacFadden, B.J., Leakey, M.G., Quade, J., Eisenmannn, V., Ehleringer, J.R., 1997. Global vegetation change through the Miocene/Pliocene Boundary. Nature, 389, 153–158.

De Jonge, C., Hopmans, E.C., Zell, C.I., Kim, J.-H., Schouten, S., and Sinninghe Damsté, J.S., 2014. Occurrence and abundance of 6-methyl branched glycerol dialkyl glycerol tetraethers in soils: Implications for palaeoclimate reconstruction. Geochimica et Cosmochimica Acta, 141, 97–112.

Domning, D.P., de Buffrénil, V., 1991. Hydrostasis in the Sirenia: Quantitative data and functional interpretations. Marine Mannal Science, 7 (4), 331–422.

Eglinton, G. and Hamilton, R.J., 1967. Leaf Epicuticular Waxes. Science, 156: 1322–1335.

El-Moslimany, A.P., 1990. Ecological significance of common nonarboreal pollen: examples from drylands of the Middle East. Review of Paleobotany and Palynology, 64, 343–350.

Englebrecht, A.C., Sachs, J.P, 2005. Determination of sediment provenance at drift sites using hydrogen isotopes and unsaturation ratios in alkenones. Geochimica et Cosmochimica Acta, 69, 17, 4253–4265.

Feakins, S.J., Sessions, A.L., 2010. Controls on the D/H ratios of plant leaf waxes in an arid ecosystem. Geochimica et Cosmochimica Acta, 74, 2128–2141.

Feakins, S.J., Liddy, H.M., Tauxe, L., Galy, V., Feng, X., Tierney, J.E., Miao, Y., Warny, S., 2020. Miocene C_4 grassland expansion as recorded by the Indus Fan. Paleoceanography and Paleoclimatology, 35, e2020PA003856, doi.org/10.1029/2020PA003856.

Feurdean, A. and Vasiliev, I., 2019. The contribution of fire to the late Miocene spread of grasslands in eastern Eurasia (Black Sea region). Scientific reports, 9:6950.

Fortelius, M., Eronen, J.T. Kaya, F., Tang, H., Raia, P., Puolamäki, K., 2014. Evolution of Neogene mammals in Eurasia: environmental forcing and biotic interactions. Annual Review of Earth and Planetary Science, 42, 579–604.

Freeman, K.H., Wakeham, S.G., 1992. Variations in the distributions and isotopic compositions of alkenones in Black Sea particles and sediments. Organic Geochemistry, 19, 1–3, 27–285.

Gol'din, P., Startsev, D., Krahmalnaya, T., 2014. The anatomy of the Late Miocene baleen whale Cetotherium Riabinini from Ukraine systematic paleontology. Acta Palaeontologica Polonica, no.59, pp: 795–814.

Gol'din, P., Startsev, D., 2017. A systematic review of cetothere baleen whales (Cetacea, Cetotheriidae) from the late Miocene of Crimea and Caucasus, with a new genus. Papers in Palaeontology, 3, 1, 49-68.

Gol'din, P., 2018. New Paratethyan dwarf baleen whales mark the origin of cetotheres. PeerJ.

Herbert, T.D., Lawrence, K.T., Tzanova, A., Cleaveland-Peterson, L., Gabalero-Gill, R., Kelly, K.S., 2016. Late Miocene global cooling and the rise of modern ecosystems, Nature Geoscience, 9, 843–847.

Hilgen, F.J., Lourens, L.J., Van Dam, J.A., Beu, A.G., Boyes, A.F., Cooper, R.A., Krijgsman, W., Ogg, J.G., Piller, W.E., Wilson, D.S., 2012. The Neogene period. The Geologic Time Scale, 2012(1–2), 923–978. https://doi.org/10.1016/B978-0-444-59425-9.00029-9.

Ivanov, D., Ashraf, A.R., Mosbrugger, V., Palamarev, E., 2002, Palynological evidence for Miocene climate change in the Forecarpathian Basin (Central Paratethys, NW Bulgaria). Palaeogeography, Palaeoclimatology Palaeoecology, 178, 19–37.

Ivanov, D., Utescher, T., Mosbrugger, V., Syabryaj, S., Djordjević-Milutinović, D., Molchanoff, S., 2011. Miocene vegetation and climate dynamics in Eastern and Central Paratethys (Southeastern Europe). Palaeogeography, Palaeoclimatology Palaeoecology, 304, 262–275.

Kim, J.H., Schouten, S., Hopmans, E.C., Donner, B., Sinninghe Damste, J.S., 2008. Global sediment core-top calibration of the TEX_{86} paleothermometer in the ocean. Geochimica et Cosmochimica Acta, 72, 1154–1173.

Kim, J.H., van der Meer, J., Schouten S., Helmke, P., Willmot, V., Sangiorgi, F., Koç, N., Hopmans, E.C., Sinninghe Damsté, J.S., 2010. New indices and calibrations derived from the distribution of crenarchaeol isoprenoid tetraether lipids: Implications for past sea surface temperature reconstructions. Geochimica et Cosmochimica Acta, 74, 4639–4654.

Kojumdgieva, E., Popov, N., 1988. Paléogéographie et evolution géodinamique de la Bulgarie Septentrionale au Neogène. Geologica Balcanica, 19 (1), 73−92.

Krijgsman, W., Stoica, M., Hoyle, T., Jorissen, E.L., Lazarev, S., Rausch, L., Bista, D., Alcicek, M.C., Ilgar, A., van den Hoek Ostende, L.W., Mayda, S., Raffi, I., Flecker, R., Mandic, O., Neubauer, T.A., Wesselingh, F.P., 2020. The myth of the Messinian Dardanelles: Late Miocene stratigraphy and palaeogeography of the ancient Aegean-Black Sea gateway. Palaeogeography, Palaeoclimatology, Palaeoecology, 560, 110033.

Mosbrugger, V., Utescher, T., Dilcher, D.L., 2005. Cenozoic continental climatic evolution of Central Europe, Proceedings of the National Academy of Sciences, 102, 42, www.pnas.orgcgidoi10.1073pnas.0505267102.

Niedermeyer, E.M., Forrest, M., Beckmann, B., Sessions, A.L., Mulch, A., Schefuß, E., 2016. Geochimica et Cosmochimica Acta, 184, 55–70.

Ogg, J., 2020. Geomagnetic Polarity Time Scale. In Geologic Time Scale 2020 (eds. Gradstein, F. M. et al.) 159–192 (Elsevier, 2020), doi: 10.1016/B978-0-12-824360-2.00005-X.

Pagani, M., Arthur, M.A., Freeman, K.H., 1999. Miocene evolution of atmospheric carbon dioxide. Paleoceanography, 14, 3, 273–292.

Palcu, D.V., Golovina, L.A., Vernyhorova, Y.V., Popov, S.V., Krijgsman, W., 2017. Middle Miocene paleoenvironmental crises in Central Eurasia caused by changes in marine gateway configuration. Global and Planetary Change, 158, 57–71.

Palcu, D.V., Vasiliev, I., Stoica, M., Krijgsman, W., 2019. The end of the Great Khersonian Drying of Eurasia: Magnetostratigraphic dating of the Maeotian transgression in the Eastern Paratethys. Basin Research, 31, 33–58.

Palcu, D.V., Patina, I.S., Şandric, I., Lazarev, S., Vasiliev, I., Stoica, M., Krijgsman, W., 2021. Late Miocene megalake regressions in Eurasia. Scientific reports, 11, 11471. doi.org/10.1038/s41598-021-91001-z.

Peterse, F., van der Meer, J., Schouten, S., Weijers, J.W.H., Fierer, N., Jacckson, R.B., Kim, J.-H., Sinninghe Damsté, J.S., 2012. Revised calibration of the MBT-CBT paleotemperature proxy based on branched tetraether membrane lipids in surface soils. Geochimica et Cosmochimica Acta, 96, 215–229.

Polissar, P.J., Freeman, K.H., 2010. Effects of aridity and vegetation on plant-wax dD in modern lake sedimets. Geochimica et Cosmichimica Acta, 74, 5785–5797.

Popov, S.V., Shcherba, I.G., Iluina, L.B., Nevesskaya, L.A., Paramonova, N.P., Khondkarian, S.O., Magyar, I., 2006. Late Miocene paleogeography of the Paratethys and its relation to the Mediterranean. Palaeogeography, Palaeoclimatology, Palaeoecology, 238, 91–106.

Popov, S.V., Rostovtseva, Y.V., Gillipova, N.Y., Golovina, L.A., Radionova, E.P., Goncharova, I.A, Vernyhorova, Y.V., Dykan, N.I., Pinchuk, T.N., Iljina, L.B., Koromyslova, A.V., Kocyrenko, T.M., Nikolaeva, I.A., Viskova, L.A., 2016. Paleontology and Stratigraphy of the Middle-Upper Miocene of the Taman Peninsula. Paleontological Journal, 50, 10, 1–168.

Popp, B.N., Laws, E.A., Dore, J., Hanson, K.L., Wakeham, S.G., 1998. Effect pf phytoplankton cell geometry on carbon isotopic fractionation. Geochimica et Cosmochimica Acta, 62, 1, 69–77.

Ramstein, G., Fluteau, F., Besse, J., Joussaume, S.,1997. Effect of orogeny, plate motion and land-sea distribution on Eurasian climate change over the past 30 million years. Nature, 386, 788–795.

Razumkova, E.S., 2012. Palynological Characterization of the Sarmatian Deposits of the Eastern Paratethys (Section Zelenskii Mountain–Panagiya, Taman Peninsula). Stratigraphy and Geological Correlation, 20, 1, 97–108.

Riabinin, A.I. 1934. New materials on the osteology of Cetotherium mayeri Brandt from the Upper Sarmatian of the Northern Caucasus. Trudy Vsesoyuznogo Geologorazvedochnogo Ob'edineniya 350, 1–15.

Rögl, F., 1999. Mediterranean and Paratethys. Facts and hypotheses of an Oligocene to Miocene Paleogeography (short overview). Geologica Carpathica, 50, 4, 339–349.

Roussiakis, S., Filis, P., Sklavounou, S., Giaourtsakis, I., Kargopoulos, N., Theodorou, G., 2019. Pikermi: a classical European fossil mammal geotope in the spotlight. European Geologist Journal, 48.

Sant, K., Palcu, D.V., Mandic, O., Krijgsman, W., 2017. Changing seas in the Early-Middle Miocene of Central Europe: a Mediterranean approach to Paratethyan stratigraphy. Terra Nova, 29: 273–281.

Sachse, D., Radke, J., Gleixner, G., 2004. Hydrogen isotope ratio of recent lacustrine sedimentary *n*-alkanes record modern climate variability. Geochimica et Cosmochimica Acta 68, 4877–4889.

Schouten, S., Hopmans, E.C., Schefuβ, E., Sinninghe Damsté, J.S., 2002. Distributional variations in marine crenarchaeotal membrane lipids: a new tool for reconstructing ancient sea water temperatures? Earth and Planetary Science Letters, 204, 265–274.

Schulz, H.-M., Schöner, A., Emeis, K.-C., 2000. Long-chain alkenone patterns in the Baltic Sea−an ocean-freshwater transition. Geochimica et Cosmochimica Acta, 64, 3, 469–477.

Strömberg, C.A.E., Werdelin, L., Friis, E.M., Saraç, G., 2007. The spread of grass-dominated habitats in Turkey and surrounding areas during the Cenozoic: Phytolith evidence. Palaeogeography, Palaeoclimatology, Palaeoecology, 250, 18–49.

Syabryaj, S., Utescher, T., Molchanoff, S., Bruch, A., 2007. Vegetation and palaeoclimate in the Miocene of Ukraine. Palaeogeography, Palaeoclimatology, Palaeoecology, 253, 153–168.

Ter Borgh, M., Vasiliev, I., Stoica, M., Knežević, S., Mațenco, L., Krijgsman, W., Rundić, L., Cloetingh, S., 2013. The isolation of the Pannonian basin (Central Paratethys): New constraints from magnetostratigraphy and biostratigraphy. Global and Planetary Change, 103, 99–118. https://doi.org/10.1016/j.gloplacha.2012.10.001

Tierney, J.E., 2012. GDGT thermometry: Lipid tools for reconstructing paleotemperatures. Reconstructing Earth's Deep-Time Climate. Paleontological Society Papers, 18, 115–131. https://doi.org/10.1017/s1089332600002588.

Tzanova, A., Herbert., T.D., Pererson, L., 2015. Cooling Mediterranean Sea surface temperatures during the Late Miocene provide a climate context for evolutionary transitions in Africa and Eurasia. Earth and Planetary Science Letters, 419, 71–80.

Van Dam, J.A., 1997. Geologica Ultraiectina 156.

van der Meer, M.T.J., Sangiorgi, F., Baas, M., Brinkhuis, H., Sinninghe Damsté, J.S., Schouten, S., 2008. Molecular isotopic and dinoflagellate evidence for Late Holocene freshening of the Black Sea. Earth and Planetary Science Letters, 267, 426–434.

Vasiliev, I., Reichart, G.J., Krijgsman, W., 2013. Impact of the Messinian Salinity Crisis on Black Sea hydrology-Insights from hydrogen isotopes analysis on biomarkers. Earth and Planetary Science Letters 362, 272–282.

Vasiliev, I., Reichart, G.J., Grothe, A., Sinninghe Damsté, J., Krijgsman, W., Sangiorgi, F., Weijers, J.W.H., van Roij, L., 2015. Recurrent phases of drought in the upper Miocene of the Black Sea region. Palaeogeography, Palaeoclimatology, Palaeoecology 423, 18–31.

Vasiliev, I., Mezger, E.M., Lugli, S., Reichart, G.J., Manzi, V., Roveri, M., 2017. How dry was the Mediterranean during the Messinian salinity crisis? Palaeogeography, Palaeoclimatology, Palaeoecology 471, 120–133.

Vasiliev, I., Reichart, G.J., Krijgsman, W., Mulch, A., 2019. Black Sea rivers capture drastic change in catchment-wide mean annual temperature and soil pH during the Miocene-to-Pliocene transition, Global and Planetary Change, 172, 428–439.

Vasiliev, I., Feurdean, A., Reichart, G.J., Mulch, A., 2020. Late Miocene intensification of continentality in the Black Sea Region. International Journal of Earth Sciences, 109, 831–846.

Wang, W.-M., 2004. On the origin and development of Artemisia (Asteraceae) in the geological past. Botanical Journal of the Linnean Society, 145, 331–336.

Weiss, G., Schouten, S., Sinninghe-Damsté, J.S., van der Meer, M.T.J., 2019. Constraining the application of hydrogen isotopic composition of alkenones as a salinity proxy using marine surface sediments. Geochimica et Cosmochimica Acta, 250, 34–48.

Weijers, J.W.H., Schouten, S., van der Donker, J., Hopmans E.C., Sinninghe Damsté, J., 2007 . Environmental controls on bacterial tetraether membrane lipid distribution in soils. Geochimica et Cosmochimica Acta 71, 703–713.

Wessels, W., 2009. Miocene rodent evolution and migration. Muroidea from Pakistan, Turkey and Northern Africa. Geologica Ultraiectina 307, 1−290.

Wiffen, J., De Buffrénil, V., De Ricqlès, A., Mazin, J.-M., 1995. Ontogenetic evolution of bone structurein Late Cretaceous Plesiosauria from New ZealandModifications ontogénétiques

de la structure osseuse chez les plésiosaures du Crétacé terminal de Nouvelle-Zélande. Geobios, 28:5, 625–640.

Chapter 6

Hypersalinity accompanies tectonic restriction in the Messinian Eastern Mediterranean

George Kontakiotis[1,*], **Geanina A. Butiseacă**[2,3*], Assimina Antonarakou[1], Konstantina Agiadi[4], Stergios D. Zarkogiannis[5], Emilija Krsnik[2,3], Evangelia Besiou[1], Willem Jan Zachariasse[6], Lucas Lourens[6], Danae Thivaiou[1], Efterpi Koskeridou[1], Pierre Moissette[1,7], Andreas Mulch[2,3], Vasileios Karakitsios[1], Iuliana Vasiliev[2]

[1]Faculty of Geology and Geoenvironment, School of Earth Sciences, Department of Historical Geology-Paleontology, National and Kapodistrian University of Athens, Panepistimiopolis, Zografou, 15784, Athens, Greece

[2]Senckenberg Biodiversity and Climate Research Centre (SBiK-F), Senckenberganlage 25, D-60325 Frankfurt am Main, Germany

[3]Institute of Geosciences, Goethe University Frankfurt, Altenhöferallee 1, 60438 Frankfurt am Main, Germany[4]Department of Palaeontology, Faculty of Earth Sciences, Geography and Astronomy, University of Vienna, Althanstrasse 14, Geozentrum (UZA II), 1090, Vienna, Austria

[5]Department of Earth Sciences, University of Oxford, Oxford OX1 3AN, UK

[6]Faculty of Geosciences, Department of Earth Sciences, Utrecht University, Budapestlaan 4, 3584 CD Utrecht, The Netherlands

[7]Muséum National d'Histoire Naturelle, Département Origines et Evolution, UMR7207 CR2P, 8 rue Buffon, 75005 Paris, France

This is a pre-copyedited, author-produced version, following peer review, of Kontakiotis, G., Butiseacă, G.A.*, Antonarakou, A., Agiadi, K., Zarkogiannis, S., Krsnik, E., Besiou, E., Zachariasse, J.-W., Lourens, L., Thivaiou, D., Koskeridou, E., Moissette, P., Mulch, A., Karakitsios, V., Vasiliev., I., 2022. Hypersalinity accompanies tectonic restriction in the Messinian Eastern Mediterranean. Palaeogeography, Palaeoclimatology, Palaeoecology, 592: 110903. https://doi.org/10.1016/j.palaeo.2022.110903*

**Equal contribution between the first two authors.*

Highlights

- Three restriction phases affected the eastern Mediterranean between 7.2 and 6.5 Ma.
- Colder water and normal salinity characterized the Mediterranean during 7.2–6.9 Ma.
- Periods of strong evaporation observed for the 6.9–6.7 Ma interval.
- Warm-hypersaline events (6.9–6.82 and 6.72 Ma) caused extreme environmental stress.
- Restriction at 6.7–6.5 Ma was induced by tectonics and modulated by climate.

Graphical abstract

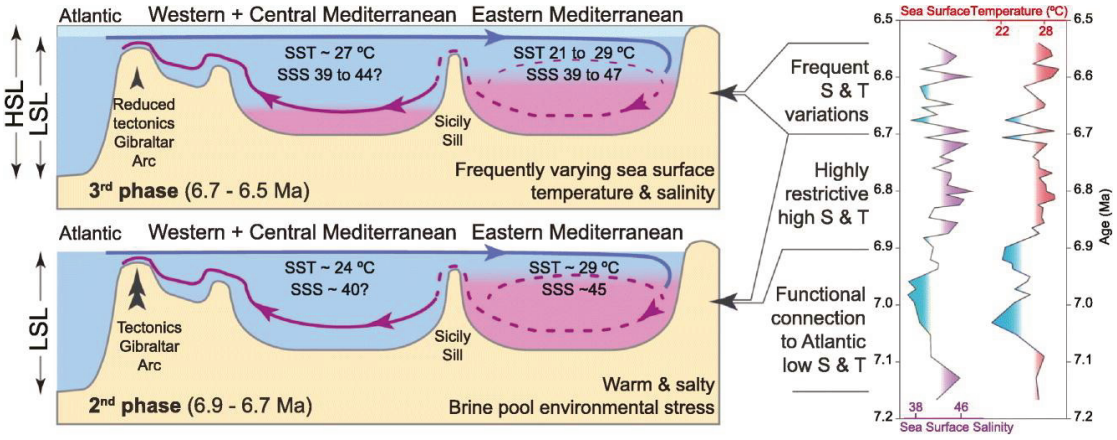

6.1 Abstract

This study describes the hydroclimate evolution of the eastern Mediterranean Basin during the early Messinian (7.2 to 6.5 Ma) time-interval based on analysis of a succession at Agios Myron (Crete, Greece), prior to the onset of the Messinian Salinity Crisis (5.96–5.33 Ma). Specifically, we report sea surface temperature and salinity reconstructions based on a combined analysis of biomarkers and oxygen isotopes of planktonic foraminifera. Data reveal that a negative water budget and strong hydrologic and climate variability characterized the eastern Mediterranean Basin at this time, and we identify three distinct phases. In phase 1 (7.2–6.9 Ma), a shift to more positive oxygen isotope values in planktonic foraminifera at ~7.2 Ma is attributed to progressive gateway restriction of Mediterranean–Atlantic corridors and subsequent cooling until 6.9 Ma. In phase 2 (6.9–6.7 Ma), distinct warm and hypersaline events (at 6.9–6.82 and 6.72 Ma) resulted in stressed marine microfauna during periods of strong evaporation. An important step-change in the Mediterranean restriction at 6.72 Ma may have resulted from shallowing of the Mediterranean gateways and reduced Mediterranean marine outflow. During phase 3 (6.7–6.5 Ma) this gateway shallowing reduced the oceanic input into the Mediterranean Basin causing significant hydrological changes, reflected in a wide range of temperature and salinity fluctuations accompanied by enhanced water column stratification. The data presented here counterbalance the general lack of quantitative temperature and especially salinity estimates available for the Mediterranean Messinian, time interval where we still highly rely on modelling for such evaluations. This study highlights the severity of preconditioning stages leading to the Messinian Salinity Crisis in the Mediterranean and sets values for extreme salinity conditions that could still host marine life.

6.2 Introduction

In the Mediterranean Basin, the latest Miocene stands out as a period of extreme environmental conditions, culminating with the Messinian Salinity Crisis (MSC) at 5.97–5.33 Ma (Krijgsman et al., 1999a; Manzi et al., 2013; Roveri et al., 2014). Severe restriction of connection to the open ocean characterized the MSC, ultimately leading to dramatic lowering of Mediterranean sea-level (e.g. Hsü et al., 1973; Capella et al., 2019; Flecker et al., 2015; Madof et al., 2019). During the Messinian (7.25–5.33 Ma), tectonic processes together with glacio-eustatic sea-level oscillations led to isolation of the Mediterranean Basin from the Atlantic ocean (e.g. Capella et

al., 2019; Flecker et al., 2015; Krijgsman et al., 2018). During the Messinian stage (7.25–5.33 Ma), tectonic processes in the Rifian and Betic gateways (Figure 6.1) together with glacio-eustatic sea-level oscillations led to isolation of the Mediterranean Basin from the Atlantic Ocean (e.g. Capella et al., 2019; Krijgsman et al., 2018), initially triggering the cyclic deposition of bio-siliceous deposits of the Tripoli Formation consisting of alternations of marls, limestones, diatomites and sapropels (Blanc-Valleron et al., 2002) and finally to the widespread deposition of massive evaporites (Hsü, 1972). These Messinian Mediterranean deposits have sparked intense interest in the sedimentology, cyclostratigraphy, paleontology and geochemistry of such prolonged restriction events (e.g. Hilgen and Krijgsman, 1999; Karakitsios et al., 2017a, 2017b; Moissette et al., 2018; Roveri et al., 2014; Sabino et al., 2020, 2021; Sierro et al., 2003; Vasiliev et al., 2017, 2019). Interestingly, the detailed sequence of Messinian events and their relationship to paleoceanography and global climate (i.e. sea level changes, hydrological budget, water-column characteristics and ecosystem response) remain poorly understood, mainly due to the scarcity of continuous, high-resolution climate and paleoceanographic archives (e.g. Tzanova et al., 2015; Zachariasse et al., 2021; Zachariasse and Lourens, 2021). Most available records cover long-term trends, but do not capture short term climate events and relationships required to assess high-frequency changes in sea surface temperature (SST) and sea surface salinity (SSS), parameters acting as main drivers of thermohaline circulation. Moreover, the particularity of such surface and/or bottom water changes from the eastern Mediterranean is that any pre-MSC paleoceanographic and paleoclimatic signal will be recorded in an amplified fashion due to the greater distance from the Gibraltar (Atlantic connection). Overall, this heightened sensitivity to the effects of climate variability, in terms of restrictions, underlines the prominent role of such marginal eastern Mediterranean sub-basins in the understanding of the MSC and global climate evolution during that period.

Here we present SST and SSS changes recorded in the Agios Myron section (central Crete, Greece), a sedimentary succession hosting early Messinian (~7.2–6.5 Ma) rhythmic sapropel-marl couplets. The cyclic sedimentary pattern is also recorded in oxygen stable isotope ratios ($\delta^{18}O$) of the climate-sensitive surface-dwelling planktonic foraminiferal species *Globigerinoides obliquus* and both Tetra Ether Index (TEX_{86}) and alkenone unsaturation ratio ($U^{K}_{37}{}'$) biomarker-based paleotemperature proxies. The combined TEX_{86}- and/or $U^{K}_{37}{}'$-SST reconstructions as well as the *G. obliquus* $\delta^{18}O$ record further allow to evaluate changes in the

early Messinian hydrology as recorded in the oxygen isotope composition of Mediterranean seawater ($\delta^{18}O_{SW}$). We discuss these combined SSS and SST records in the context of marine productivity, basin stratification and river runoff, as these are fundamental for the interpretation of the geochemical signals and the paleoceanographic evolution of the eastern Mediterranean before the MSC onset. Finally, we compare all the above paleoenvironmental data with previously published coeval Mediterranean records (Kontakiotis et al., 2019; Mayser et al., 2017; Tzanova et al., 2015; Vasiliev et al., 2019) to highlight the processes driving and regulating the hydrographic changes in the eastern Mediterranean Basin and the relation to its far end location relative to the Atlantic gateway.

6.3 Regional setting

6.3.1 Geological setting

The eastern Mediterranean basin (Figure 6.1) is a relic of the Neotethys Ocean in the Tethys domain, shaped by the collision and continued convergence of the African, Arabian, and Eurasian plates (e.g. Robertson et al., 2012). The island of Crete, situated in the central part of the basin (Figure 6.1), is part of the forearc accretionary zone and exhibits a horst structure that consists of a metamorphic nappe pile with sediments from various paleogeographical zones (e.g. van Hinsbergen and Meulenkamp, 2006). The uplift and exhumation of the nappe pile were accompanied by the structural fragmentation of the pre-Miocene basement to several blocks, which created new accommodation space by displacement during the Lower to Middle Miocene. The Heraklion Basin is one of the largest Neogene sedimentary basins of Crete, developed in the hanging wall of the Cretan detachment and filled with fluvial to deep marine Tortonian to Pliocene sedimentary rocks (e.g. van Hinsbergen and Meulenkamp, 2006; Zachariasse et al., 2011), but the present-day high topography of the surrounding mountains was largely shaped during the Pleistocene (e.g. Zachariasse et al., 2021). The northern block of the Heraklion Basin, hosting the Agios Myron section, emerged after 9.6 Ma and remained emerged until the latest Tortonian (~7.4 Ma) (Zachariasse et al., 2011, 2021). Subsequently, intermittent subsidence to upper bathyal depths in the early Messinian is manifested by the Agios Myron Formation (Zachariasse et al., 2021 and references therein).

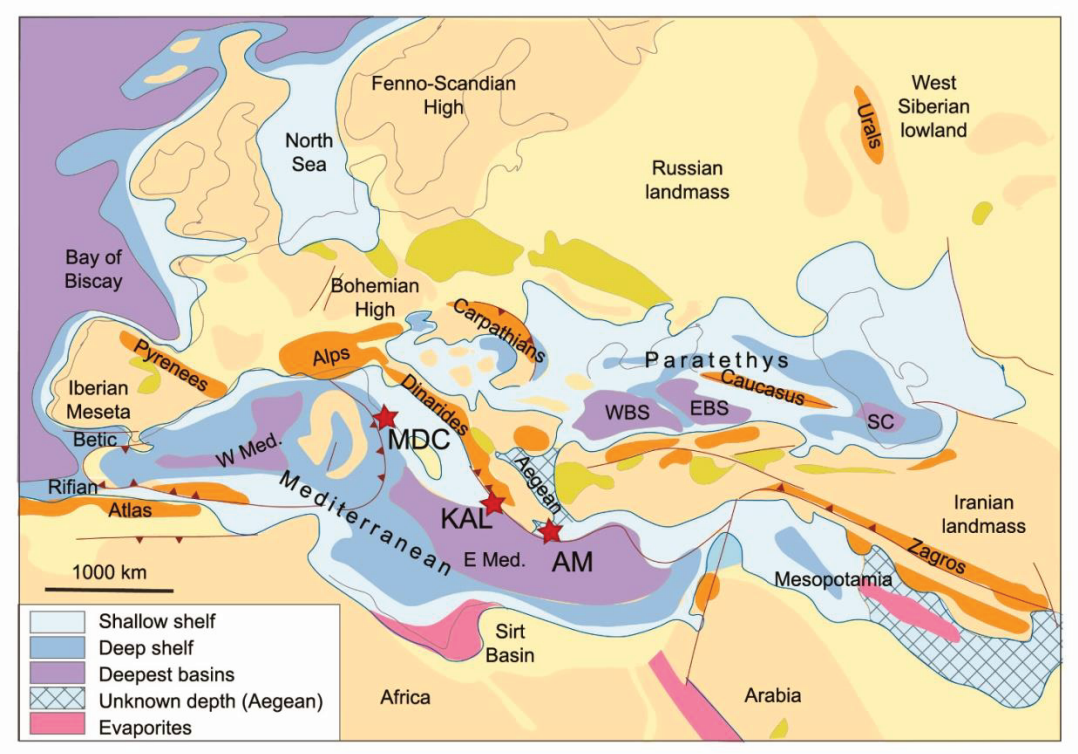

Figure 6.1 Paleogeography map for the Mediterranean-Paratethys domain during late Miocene (Ilyina et al., 2004). Note the paleolatitudinal location and their approximate position within the late Miocene Mediterranean basin for Agios Myron (AM), Kalamaki (KAL) and Monte dei Corvi (MDC) sections.

6.3.2 The Agios Myron section: lithology and chronometric scale

The Agios Myron section in central Crete (N 35°23'35.90", E 25°12'67.91") is the result of continuous hemi-pelagic sedimentation during the early Messinian. The section is ~25 m thick and consists of bluish-grey silty marls without clear sedimentary cyclicity in the basal seven meters, followed by a rhythmic alternation of blueish-grey homogeneous and brownish laminated marls (referred to here as sapropels) with three distinct ash layers (numbered 1 to 3) in the overlying 18 m (Figure 6.2). The Agios Myron region began to subside in the latest Tortonian and, based on the sudden appearance of sapropels, passed the upper depth limit for sapropel formation at 7.05 Ma (Zachariasse et al., 2021). The cyclically bedded sequence records 24 sedimentary cycles characterized by couplets of homogenous marls and sapropels, with an average sedimentation rate of 3.53 cm/kyr. The nature of the sedimentary cycles closely resembles other astronomically calibrated early Messinian Mediterranean sequences, with up to 32 documented precession cycles present between 7.2 and 6.5 Ma (Hilgen et al., 1995, 2000a, b).

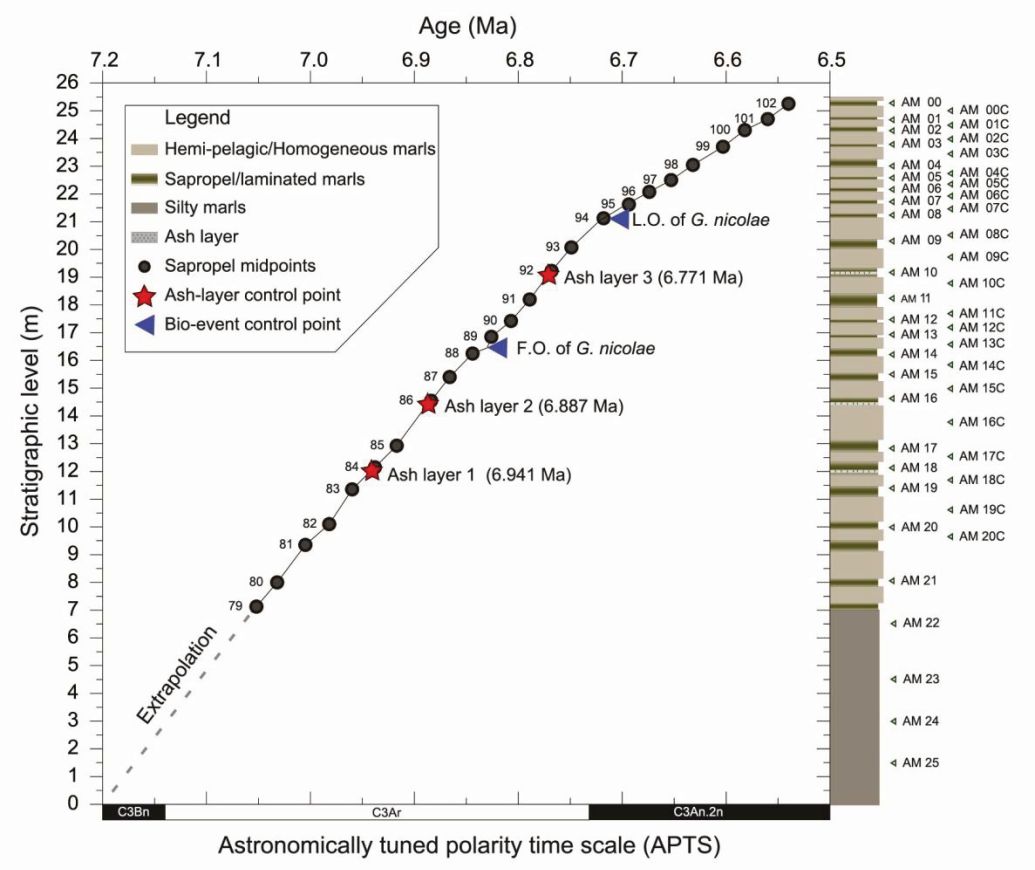

Figure 6.2 Age model of the study section created by linear interpolation between all control points (two planktonic foraminiferal bioevents symbolized with blue arrowheads, three tephra layers symbolized with red stars, and 24 astronomically dated sapropel midpoints for identified sedimentary cycles symbolized with black dots), as defined by the recent bio-cyclostratigraphic work of Zachariasse et al. (2021). The numbers next to black dots correspond to Metochia sedimentary cycles for the time-equivalent interval. At the lower part of the figure the polarity pattern of the astronomically dated polarity time scale (APTS; Lourens et al., 2004) is presented. In the right-hand side, the schematic lithological column of Agios Myron is shown with the location of the analyzed samples.

The robust time-stratigraphic frame of Agios Myron section is supported by the identification of planktonic foraminiferal bioevents, tephra layers and the overall correlation of bipartite sedimentary cycles with those of the nearby astronomically tuned Metochia section (Zachariasse et al., 2021). In particular, biostratigraphic events and tephra layers were used as reference points when correlating the identified cycles to the overall reference frame given in Hilgen et al. (1995) and Hilgen and Krijgsman (1999). The first and the last occurrence (FO and LO) of *Globorotalia nicolae*, astronomically tuned to 6.83 and 6.72 Ma in the Mediterranean Basin (Hilgen et al., 1995; Hilgen and Krijgsman, 1999; Lourens et al., 2004), were identified in samples AM 13C and AM 08, respectively. The Cretan ash layers 1 to 3 with the astronomical

ages of 6.941, 6.887 and 6.771 Ma (Hilgen et al., 1997; Kuiper et al., 2004) are stratigraphically located below samples AM 18, AM 16, and AM 10, respectively. The resulting age model (Figure 6.2) is based on the two astronomically calibrated planktonic foraminiferal bioevents, the three ash layers and supplemented by the additional dating of the mid points of the sapropel layers, assuming constant sedimentation rates between them, and established by linear interpolation between all control points (Figure 6.2). The age control for the lower most four samples is less well defined in the absence of biostratigraphic events and visible lithological cycles. However, these four oldest samples all belong to the earliest Messinian based on the continuous presence of *Globorotalia miotumida*. They are, therefore, younger than 7.25 Ma and older than the first well-dated sample at 7.05 Ma.

6.4 Material and methods

6.4.1 Lipid extraction, fraction separation and biomarker analyses

Forty-seven sedimentary rock samples were collected with an average spacing of 160 cm (34 kyr) for the basal silty marls and 40 cm (12 kyr) for the cyclically bedded marls and subjected to geochemical (biomarker and isotope) analyses. The samples (30–60 g weight) were dried and powdered using a pre-cleaned agate mortar and pestle. Lipids were extracted using a Soxhlet apparatus with a mixture of dichloromethane (DCM) and methanol (MeOH) (7.5:1; *v:v*) and pre-extracted cellulose filters. All extracts were evaporated to near dryness under N_2 flow with a TurboVap LV obtaining the total lipid extracts (TLE). Subsequently, elemental sulphur was removed using Cu shreds. The Cu was activated using 10% HCl, then rinsed with demineralized water until reaching neutral pH and further cleaned using MeOH and DCM. The TLE vials containing the activated Cu and magnetic rods were placed on a rotary table for ~16 h. The samples were filtered over a Na_2SO_4 column and dried subsequently. Desulphurization was repeated until no reaction with Cu was observed.

A fraction of the TLE was archived. The remaining TLE were then separated into fractions by Al_2O_3 column chromatography based on mixtures of solvents of increasing polarity. The apolar fraction was eluted using a mixture of n-hexane and DCM (9:1, *v:v*), the ketone fraction using DCM, and the polar fraction using a mixture of DCM/MeOH (1:1, *v:v*). The ketone fraction containing alkenones was purified using an $AgNO_3$ column and ethyl acetate. Alkenones were identified using Gas Chromatography-Mass Spectrometry (GC–MS) at the

Senckenberg Biodiversity and Climate Research Centre (SBiK-F) in Frankfurt am Main. The fractions (dissolved in *n*-hexane) were injected on-column at 70 °C (CP-Sil 5CB fused silica column (30 m × 0.32 mm i.d; film thickness 0.12 μm). The oven was set at constant pressure (100 kPa) and then programmed to increase to 130 °C at 20 °C min− 1, and to 320 °C at 5 °C min− 1 at which it was held isothermal for 10 min. The polar fraction containing glycerol dialkyl glycerol tetraethers (GDGTs) was dried under N_2 then dissolved in a 1 ml mixture of n-hexane (*n*-hex)/ isopropanol (IPA) (99:1, *v:v*) and dispersed using an ultrasonic bath (30 s), then filtered over a 0.45 mm PTFE filter using a 1 ml syringe. The filtered polar fraction containing GDGTs was analyzed at SBiK-F using an HPLC Shimadzu, UFLC performance (analytical column Alltech Prevail© Cyano 3 mm, 150–2.1 mm; eluents *n*-hex (A) and IPA (B) coupled with an ABSciex 3200 QTrap chemical ionization mass spectrometer (HPLC/APCIeMS). The injection volume was 5 ml. GDGTs were eluted isocratically from 0 to 5 min with 1% (B); then with a gradient to 1.8% (B) from 5 to 32.5 min, ramped to 30% (B) to min 33.5, held 10 min, back to 1% (B) in 1 min. Detection was achieved through single ion monitoring (scanned masses: 1018, 1020, 1022, 1032, 1034, 1036, 1046, 1048, 1050, 1292, 1296, 1298, 1300, 1302). Quantification of GDGTs was performed using the Analyst software.

6.4.2 Temperature proxies

Temperature estimates were obtained using both the TEX_{86} (Kim et al., 2010; Schouten et al., 2002, 2013) and U^{K}_{37}' (Brassell et al., 1986; Prahl and Wakeham, 1987) proxies. The former is based on the ratio of isoprenoidal (iso)GDGTs mainly produced by the *Archaea* group (Schouten et al., 2013), whereas the latter is based on the unsaturation of long-chain alkenones produced by haptophyte algae (Volkman et al., 1995). Both proxies exhibit a strong relationship with SST (e.g. Conte et al., 2006; Kim et al., 2008, 2010; Müller et al., 1998; Schouten et al., 2002). Using both TEX_{86} and U^{K}_{37}' was necessary due to the absence of alkenones in 23 out of the total of 47 analyzed samples. Parallel TEX_{86} and U^{K}_{37}' based SST are therefore, presented for only 24 levels.

6.4.2.1 Sea surface temperature estimates based on TEX^{H}_{86}

TEX_{86} values were calculated as follows (Schouten et al., 2002):

$$TEX86 = \frac{[GDGT-2]+[GDGT-3]+[GDGT-4']}{[GDGT-1]+[GDGT-2]+[GDGT-3]+[Cren']}$$

where GDGT-1, GDGT-2, GDGT-3 and Cren′ are isoprenoid GDGT's with the structures presented in Appendix 2, Supplementary Figure 6.1. TEX_{86} values were converted into SST using the calibration and recommendation of Kim et al. (2010) to apply the $TEX^{H}_{86} > 15$ °C for regions outside the polar and subpolar latitudes as follows:

$TEX^{H}_{86} = \log (TEX_{86})$ and the SST based on TEX_{86}^{H} ($TEX^{H}_{86} - SST$)

$TEX^{H}_{86} - SST = 68.4 \times (GDGT\ index - 2) + 38.6$, ($r^2 = 0.87$, $p<0.0001$).

Where:

$$GDGT\ index - 2 = \log \frac{[GDGT-2] + [GDGT-3] + [Cren']}{[GDGT-1] + [GDGT-2] + [GDGT-3] + [Cren']}$$

SST calculations based on TEX_{86}^{H} has a calibration residual standard (1σ) error of ±2.5 °C and is based upon 255 core-top sediments.

6.4.2.2 Sea surface temperature estimates based on $U^{K}_{37}{}'$

SST estimates were based on the degree of unsaturation of C_{37} alkenones ($U^{K}_{37}{}'$), which is primarily a function of temperature (Müller et al., 1998), by monitoring the ratio between the di- and tri-unsaturated alkenones:

$$UK37' = \frac{C37{:}2}{C37{:}2 + C37{:}3}$$

We used the transfer function $U^{K}_{37}{}' = 0.033T\ [°C] + 0.044$ (± 1°C), based on a global core-top calibration of Müller et al. (1998).

6.4.3 Stable oxygen isotopes of planktonic foraminifera

Forty-seven sediment samples were collected and processed following standard geochemical procedures. In short, the sedimentary rock samples were oven-dried at 50 °C overnight, weighed, and disaggregated in ultraclean water for six hours on a shaker table. To collect the coarse fraction, samples were wet-sieved using a 63 μm mesh. Then, the residues were sieved into sub-fractions for isotopic analyses. For $\delta^{18}O$ measurements, five *Globigerinoides obliquus* specimens were handpicked, at every level, from the 250–300 μm sieve fraction. This number of individuals was necessary to supply sufficient $CaCO_3$ (~100 μg) and to limit the effect of individual

variation on the $\delta^{18}O$ values, while the adopted size fraction was used to minimize intraspecific ontogenetic and growth rate effects on shell geochemistry (Elderfield et al., 2002). The choice of the shallow-dwelling species *G. obliquus* for $\delta^{18}O$ was made following earlier works of Seidenkrantz et al. (2000) and Kontakiotis et al. (2016, 2019) studying changes in the Mediterranean surface waters during the Neogene. Once picked, specimens were sonicated in MeOH for about 10 s to remove clay particles adhering to the *G. obliquus* tests and further rinsed five times in ultraclean water. The observation of shell microstructure of randomly selected specimens using a Jeol JSM 6360 Scanning Electron Microscopy (SEM) confirmed the relatively good preservation regime, based on their 'frosty' appearance (Antonarakou et al., 2019).

All picking, cleaning, and diagenesis screening were performed at the Department of Historical Geology-Paleontology in Athens. Isotopic analyses were performed using a Thermo 253, Thermo GasBench II coupled to a Thermo 253 isotope ratio mass spectrometer in continuous flow mode, thermostated sample tray and a GC PAL autosampler at the Goethe Universität – Senckenberg BiK-F Joint Stable Isotope Facility. During the project, analytical precision was 0.07‰ for $\delta^{18}O$. Replicates of 10% of the data reveal that reproducibility and natural sample variability are better than 0.1‰. Results are reported against Vienna Pee Dee Belemnite (VPDB) using the standard δ notation expressed in per mil (‰).

6.4.4 Estimates of sea surface salinity

Foraminiferal $\delta^{18}O$ records are a function of temperature and the ambient oxygen isotopic composition of seawater ($\delta^{18}O_{SW}$) in which the shell precipitated, which in turn depends on global ice volume and ocean salinity. If the temperature (T) component is accounted for, foraminiferal calcite $\delta^{18}O$ can be used to estimate past changes in salinity, because $\delta^{18}O_{SW}$ co-varies linearly with SSS (e.g. LeGrande and Schmidt, 2006), as both increase with evaporation and decrease through admixture of low-$\delta^{18}O$ freshwater. Based on this concept and in accordance with earlier studies (e.g. Antonarakou et al., 2015; Kontakiotis et al., 2019; Vasiliev et al., 2019), we used a multiproxy geochemical approach to estimate past SSS variability. To isolate the $\delta^{18}O_{SW}$ from the measured foraminiferal $\delta^{18}O_C$ values, the temperature component was removed using the *Orbulina universa* low-light paleotemperature equation of Bemis et al. (1998):

$$T = 16.5 - 4.80 * (\delta^{18}O_C - (\delta^{18}O_{SW} - 0.27‰)) (\pm 0.7°C)$$

Although the Bemis et al. (1998) equation has been calibrated within the range of 15–25 °C, its extrapolation to even higher temperatures (up to 30 °C) provides good agreement with field data in warmer environments (e.g. Sargasso Sea, Indian Ocean; Bouvier-Soumagnac and Duplessy, 1985; Williams et al., 1981), overall reflecting the entire temperature range observed into the Mediterranean during the Messinian. Moreover, the used equation has been considered as the most accurate equation for estimating paleo-SST (including the late Miocene) for symbiotic planktonic foraminifera in subtropical settings (Williams et al., 2005).

Removing temperature from the $\delta^{18}O$ record using the above equation yields the salinity proxy. To correct for the continental ice volume effect, we used the late Miocene record of eustatic sea level changes as modeled by Miller et al. (2011). Briefly, we linearly interpolated the Miller et al. (2011) record at the study time period, generated a record of global $\delta^{18}O_{SW}$ change (resulting from the melting of continental ice sheets) over the Messinian by converting the sea-level data into mean ocean $\delta^{18}O$ changes and applying a 0.008‰ increase per meter of sea level lowering (Siddall et al., 2003), and then subtracted this component from the $\delta^{18}O_{SW}$ profile to obtain the regional ice volume free $\delta^{18}O_{SW}$ ($\delta^{18}O_{IVF\text{-}SW}$) residual. The calculated $\delta^{18}O_{IVF\text{-}SW}$ values are due to changes in regional hydrography and therefore considered to approximate local variations in SSS. The $\delta^{18}O_{IVF\text{-}SW}$ record has merely an illustrative character and therefore is used to investigate the potential salinity effect on our results. To convert the $\delta^{18}O$ signal to absolute SSS values we used the modern $\delta^{18}O_{sw}$–Salinity relationship for the Mediterranean Sea $\delta^{18}O$ = 0.25*S – 8.2, exclusively considering the dataset which reflects surface waters with salinities higher than 36.2 (Pierre, 1999).

6.5 Results

6.5.1 Sea surface TEX^{H}_{86} and $U^{K}_{37}{}'$ based temperatures

The TEX^{H}_{86}-SST estimates range between 20.7 and 30.0 °C (average 26.6 °C), indicating almost 10 °C variation in Agios Myron section (Figure 6.3A; Supplementary table). Three intervals show TEX^{H}_{86}-SST values lower than 23 °C (at ~7.03, 6.91 and 6.68 Ma). The remainder of the record shows consistently higher SSTs. When analyzing the SST trends, the TEX^{H}_{86}-SSTs start with values averaging around 27 °C, from the base of the sampled section (7.17 Ma–7.09 Ma).

Afterwards, the first cooling step (20.7 °C) takes place until ~7.03 Ma, followed by a warming to 26 °C between 7.00 and 6.95 Ma. A marked cooling step (to 22 °C) occurs around 6.91 Ma, after which the SSTs increase again to steady values of ~27 °C, with a low variability (6.88–6.69 Ma). In this 190 kyr interval, only two higher SST values are observed: one at 6.82 Ma and another one at 6.75 Ma. Between 6.69 and 6.54 Ma, corresponding to the upper part of the section, SST shows pronounced variability. The TEX^{H}_{86}-SSTs values have an obvious increasing trend from 22.6 °C to more than 28 °C with a visible cyclic pattern and 3 to 4 °C amplitude between colder and warmer phases (Figure 6.3A).

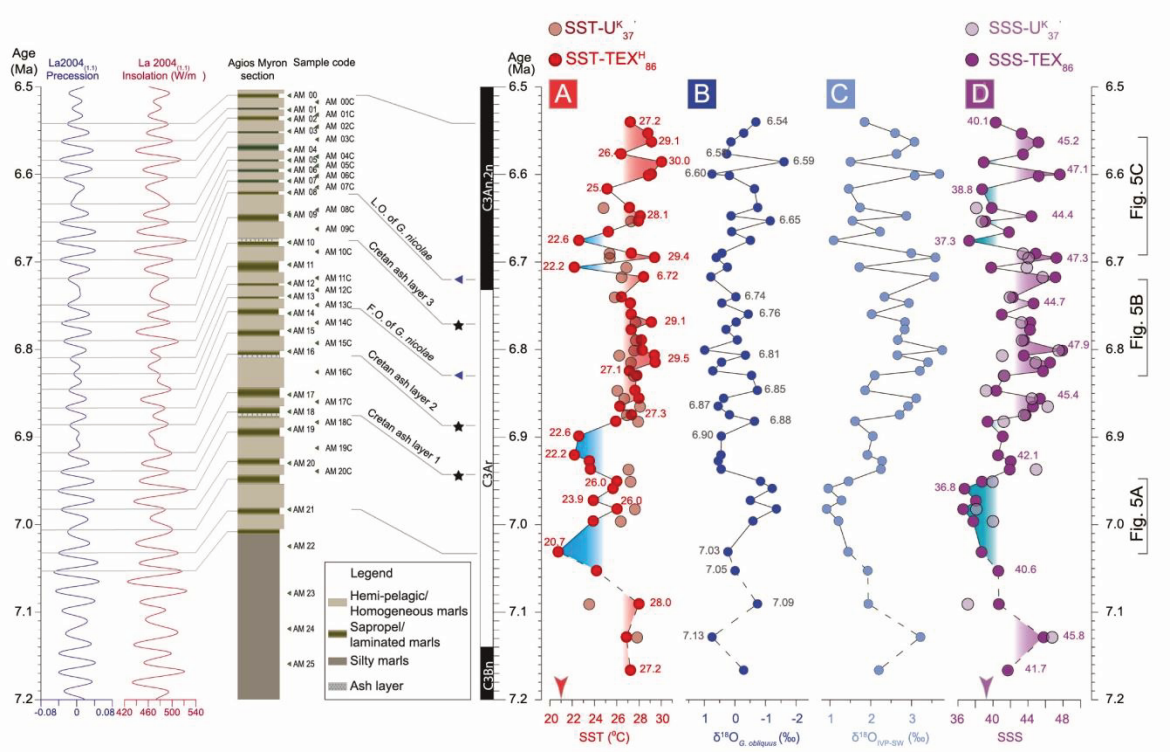

Figure 6.3 Agios Myron A) Sea surface temperature calculated based on TEX^{H}_{86} (SST-TEX^{H}_{86}) and U^{K}_{37}'; B) $\delta^{18}O$ measured on *Globigerinoides obliquus* ($\delta^{18}O_{G.\ obliquus}$); C) ice volume-free $\delta^{18}O$ surface sea water (IVF-$\delta^{18}O_{SW}$); D) sea surface salinities (SSS) based on both SST-TEX^{H}_{86} and SST-U^{K}_{37}'. On the left-hand side is the astronomical precession and insolation summer curve of Laskar et al. (2004), the lithological column, samples names and position, bioevents and ash layers used for calibration to the APTS (Lourens et al., 2004). For clarity, the red numbers next to SST data are obtained temperature estimates based on TEX^{H}_{86}, the grey numbers next to $\delta^{18}O_{G.\ obliquus}$ points indicate ages in Ma, while the purple numbers next to SSS indicate calculated salinity based on TEX^{H}_{86}. The arrows indicate the present-day values for SST and SSS.

U^{K}_{37}'-SSTs show the least variability (between 23.7 and 28.2 °C) averaging around 26.9 °C (Figures 6.3A, 6.4D; Appendix 2, Supplementary table). If we discount the sample at 7.1 Ma,

then the U^{K}_{37}'-SST average increases to 27 °C, with a variation of only 3.3 °C. Alkenones were present in 24 out of the total 47 samples analyzed and the low variation could be caused by the lower amount of U^{K}_{37}-SST values obtained (Figure 6.3a, 4d; Appendix 2, Supplementary table). It is noteworthy that, especially during cooler episodes as described by TEX^{H}_{86}-SSTs, fewer levels with alkenone occurrence were identified and therefore, less U^{K}_{37}'-SSTs are available in the Agios Myron section (Figures 6.3A, 6.4D).

6.5.2 Oxygen stable isotopes on *Globigerinoides obliquus*

Over the analyzed record, *G. obliquus* $\delta^{18}O$ values show an average of −0.08‰, with a minimum of –1.61‰ at 6.58 Ma and a maximum of 0.99‰ at 6.80 Ma (Figure 6.3B; Appendix 2, Supplementary table). The largest variability based on the standard deviation of the replicates is ~0.5‰. From the base of the section to ~6.95 Ma, $\delta^{18}O$ values display considerable scatter from 0.75 to –1.22‰, with the majority having negative values. In the cyclically-bedded interval, the planktonic $\delta^{18}O$ record correlates well with lithology, with lower $\delta^{18}O$ values occurring within sapropels, reflecting wet climatic conditions at times of minimum precession (Rohling et al., 2015). Less variable and rather higher $\delta^{18}O$ values are generally observed in the middle part of the section (~6.95–6.69 Ma). Within this interval, we observe significant increases in $\delta^{18}O$ values at ~6.93, 6.82, and 6.80 Ma, and corresponding decreases at ~6.97, 6.85 and 6.76 Ma. The shift towards higher values culminates about 6.7 Ma, where $\delta^{18}O$ values stabilize around 0.5‰. From this level towards the top of the section, a recovery to slightly lower values (around 0‰) is observed, except for the negative peak with the lowest value of the entire record (−1.61‰) at ~6.59 Ma (Figure 6.3B; Appendix 2, Supplementary table).

Following the results of previous studies on the Mediterranean Sea (Kontakiotis et al., 2016, 2019; Vasiliev et al., 2019), we also use $\delta^{18}O_{IVF\text{-}SW}$ as a direct method of isotopic tracing of eastern Mediterranean (hyper)saline events, since SST has been removed, leaving primarily a salinity signal in the $\delta^{18}O_{IVF\text{-}SW}$. There is a remarkable coincidence for both $\delta^{18}O_{IVF\text{-}SW}$ and SSS records (Figures. 6.3C, D) with distinct positive and negative excursions that reveal successive hypersaline and freshening events during the Messinian, described in detail in section 6.5.3.

6.5.3 Salinity reconstruction

Estimated SSS data at Agios Myron range from 38.1 to 48.2, and 38.5 to 47.8 calculated based on the contribution of TEX^{H}_{86}- and U^{K}_{37}'-SSTs, respectively (Figures 6.3D, 6.4B; Appendix 2, Supplementary table). The SSS based on both TEX^{H}_{86}-SSTs and U^{K}_{37}'-SSTs have strikingly similar amplitudes (~11 or 10, respectively). Remarkably, regardless of the choice of TEX^{H}_{86}-SSTs or U^{K}_{37}'-SSTs, maximum SSS values attain 47 to 48, typical of hypersaline conditions (Figures 6.3, 6.4; Appendix 2, Supplementary table).

Overall, the studied interval at the base of the section shows that hypersaline conditions that developed during the latest Tortonian (39.5 to 43.9, average 41.7; Kontakiotis et al., 2019), persisted immediately above the Tortonian/Messinian boundary (40.6–45.8, average 42.2 based on TEX^{H}_{86}-SSTs). Subsequently, the data document a freshening trend up to 6.95 Ma. The SSS values based on both TEX^{H}_{86}-SSTs and U^{K}_{37}'-SSTs displays a remarkable decline up to average of 38 and average of 36.6 respectively, indicating a brief, but gradual passage from hypersaline to saline and finally to normal marine conditions. The interval between 6.95 and 6.69 Ma indicates hypersaline surface water conditions in the eastern Mediterranean (39.4 to 47.9; average ~43.5 based on TEX^{H}_{86}-SSTs, and 39.2 to 47.5, average 43.5 based on U^{K}_{37}'-SSTs), regardless of the choice of SST proxy.

From 6.95 to 6.69 Ma, salinity increases systematically documented through a succession of five pronounced events of variable duration and magnitude (Figure 6.3D). We separate these events into three primary and two ancillary ones. The primary events are defined by a wider amplitude and duration, while the ancillary ones as those SSS increase appearing instantly. The first primary event occurred between 6.87 and 6.85 Ma. The second event, centered at 6.82 to 6.80 Ma, was equally brief but even more saline than the first, while the third one appears as equally large in amplitude but with a more persistent (6.72 to 6.69 Ma) salinity phase. All these primary events seem to be separated by short pauses (with relatively fresher conditions but still hypersaline) highlighting the high-frequency salinity variability through the Messinian. Following the high salinity interval between ~6.95−6.69 Ma, we observe a freshening towards the top of the record. However, for the 6.69−6.54 Ma interval a large variation in salinity (between 37.3 and 47.7; SSS based on TEX^{H}_{86}-SSTs) is observed (Figures 6.3D, 6.4B; Appendix 2, Supplementary table).

6.6 Discussion

6.6.1 Errors and uncertainties on applied temperature and salinity proxies

Overall, the most significant source of error is our normalization-to modern approach, which typically concerns all past sea surface temperature and salinity-related reconstructions. Regarding the temperature estimates, a significant limitation are possible seasonal offsets on the $\delta^{18}O$ and temperature signals due to growth and habitat differences between the planktonic foraminifera (*G. obliquus*) on one side, and Thaumarchaeota, producing isoGDGTs, and coccolithophoriids, the alkenone-producing haptophyte algae on the other side.

Both biomarker-based TEX_{86} and U^{K}_{37}' temperature proxies assume growth temperature (i.e. SST) as the main factor affecting the composition of the corresponding lipids. However, other factors like growth rate, nutrient levels, environmental stress and regional oceanographic conditions may play an unaccounted role in the lipid composition and, therefore, the resulting SST estimates (e.g. Leider et al., 2010; Elling et al., 2019). Recent studies from the modern Mediterranean basin warn about a possible bias in the TEX_{86} paleothermometer from deep dwelling marine archaea, showing a different GDGT membrane composition than epipelagic archaea (Kim et al., 2015; Besseling et al., 2019). However, the isoprenoidal GDGT2/GDGT3 ratios (Apendix 2, Supplementary table, Supplementary figure 6.2) in the Agios Myron section are typical for input from the upper water column in the present-day eastern Mediterranean (Kim et al., 2015). Alkenone paleothermometry (U^{K}_{37}'-based SST) appears more suitable/less biased in the Mediterranean Sea (Herbert et al., 2016); however, these alkenones were produced by extinct species of haptophytes (Herbert et al., 2016; Tzanova et al., 2015), a fact imposing a certain degree of uncertainty in all paleo-SST reconstructions. The exact alkenone producers are not known for the Agios Myron section. We infer that the most probable alkenone producers in the Agios Myron section would have been *Coccolithus pelagicus*, "normal sized" reticulofenestrids (including *Reticulofenestra haqii, R. pseudoumbilicus*) as documented from the closest, time-equivalent record from Pissouri (Cyprus; Kouwenhoven et al., 2006).

As we have no means to estimate the slope of the $\delta^{18}O_{sw}$–S relationship for the late Miocene, we used the modern relationship for the Mediterranean Basin (Pierre, 1999). Paleosalinity estimates assume that the $\delta^{18}O_{SW}$-S relationship is constant through space and time (i.e. spatiotemporal stationarity). Overall, future work requires more robust knowledge about these parameters through both upgraded records of SST proxies for the eastern Mediterranean

Sea and the development of a conservative $\delta^{18}O_{sw}$–S relationship underchanged past climatic conditions. We estimate the ±1σ uncertainty on calculated $\delta^{18}O_{SW}$ values to be ~0.38 ‰ based on the propagation of the 1σ analytical error on *G. obliquus* $\delta^{18}O$ values and the pooled standard deviation value of our SST replicates with the reported errors on the calibration equations of Müller et al. (1998) and Bemis et al. (1998). Absolute errors in $\delta^{18}O_{IVF\text{-}SW}$ are difficult to assess for the late Miocene, but are expected to be of minor importance as changes in global ice volume were small during this time interval and do not alter the relative changes between records (Williams et al., 2005). The propagated error suggests uncertainties of ~1.3 for Messinian salinity values, in accordance with previous reconstructions (Mehta et al., 2021).

Acknowledging the possible bias associated to the paleothermometry applications in increasingly old and undeciphered records, the parallel application of TEX_{86} and U^{K}_{37}' temperature proxies in conjunction with the standard assumption that the $\delta^{18}O_{SW}$-S relationship is constant through space and time, came as a viable solution in our attempt for obtaining the SSS estimates in the eastern Mediterranean during the early Messinian at an unprecedented time-resolution. Given that the obtained TEX^{H}_{86}-SSTs values are closely reproduced at 24 available levels by U^{K}_{37}'-SSTs (Figures 6.3A, 6.4D) we are safely encouraged to use the TEX^{H}_{86}-SST and U^{K}_{37}'-SST values for the further SSS calculations (Figures 6.3D, 6.4B) and subsequent discussion.

6.6.2 SST variability

The reconstructed Agios Myron temperature estimates generally exceed the modern mean annual SST of ~21 °C (at the site) by as much as 5.7 °C (Figures 6.3A, 6.4D), consistent with higher global temperatures for that time (e.g. Herbert et al., 2016). Additionally, for both TEX^{H}_{86}- and U^{K}_{37}'-SSTs, the ≤4–5 °C amplitude of SST change between warmer and colder periods within the 7.2–6.5 Ma time interval (Figures 6.3A, 6.4D) is smaller than the 8–9 °C glacial-interglacial variation recorded in the Mediterranean Sea during late Quaternary (Emeis et al., 2000). Surprisingly, the TEX^{H}_{86}-SSTs correlate well with the insolation curve (Figure 6.3A), although orbital tuning was not our initial target as we collected two samples per lithological cycle only. For the basal seven meters (~7.2–7.05 Ma), we refrain from firmly matching the TEX^{H}_{86}- SSTs to the insolation curve because the age constraints here are limited to the assumption of constant sedimentation rate for the five samples.

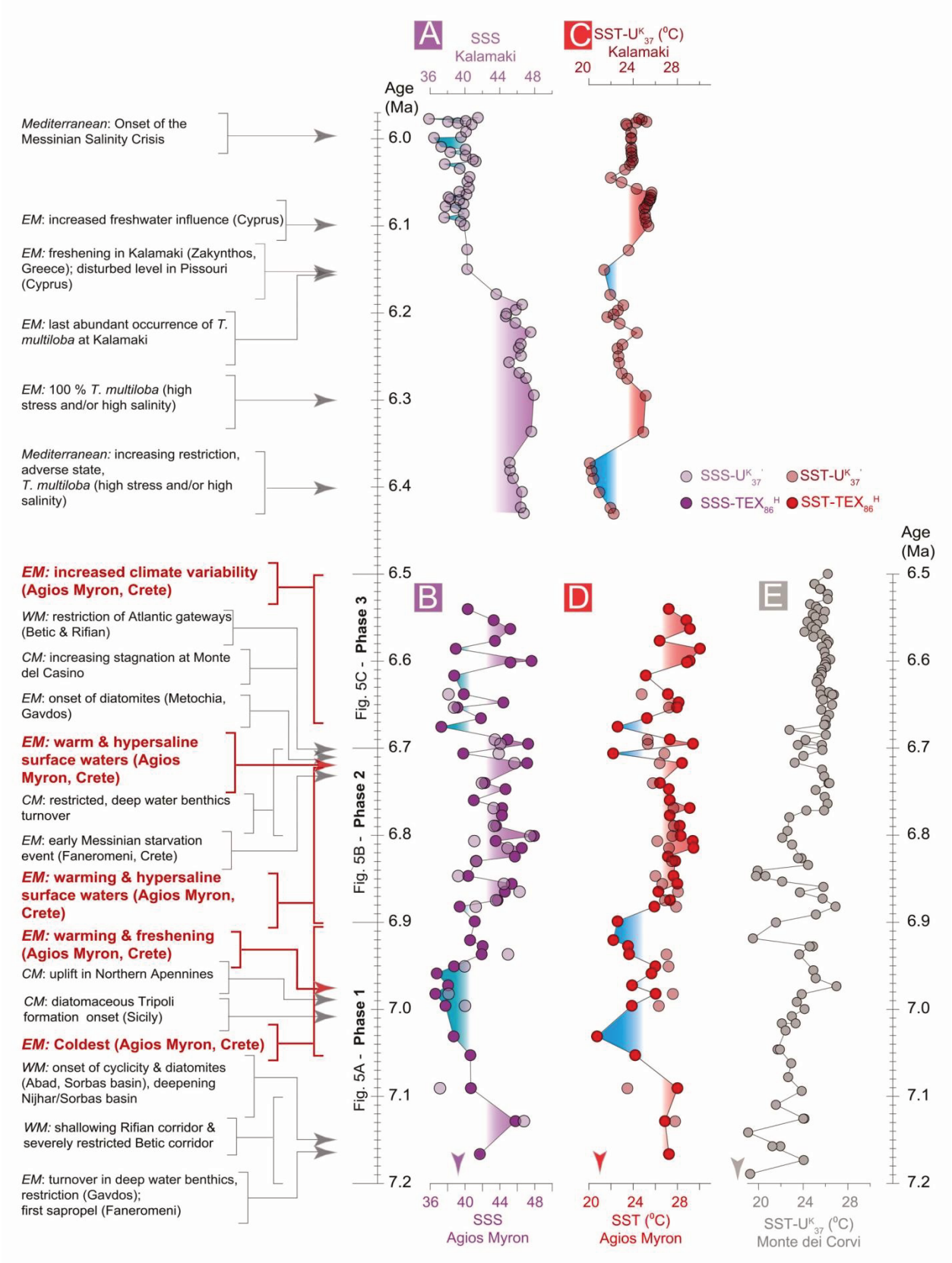

(*caption next page*)

Figure 6.4 Messinian SST and SSS data from Mediterranean between 7.17 and 5.96 Ma. The events affecting different parts and periods of the Mediterranean are compiled from: Hilgen and Krijgsman (1999), Kouwenhoven et al. (1999, 2003, and 2006), Blanc-Valleron et al. (2002), Sierro et al. (2001); Gennari et al. (2018), Krijgsman et al., (2018), and Vasiliev et al. (2019). In bold are events revealed by this study. EM, CM, and WM stand for eastern, central and western Mediterranean, respectively. Composite SSS of the eastern Mediterranean with data from A) Kalamaki Section (Zakynthos Island) for the interval between 6.46 and 5.96 Ma, and B) our data from Agios Myron (Crete) for the interval between 7.17 and 6.54 Ma. The arrow indicates the present-day SSS; Composite SST of the eastern Mediterranean from C) Kalamaki (SST- U^{K}_{37}') and D) Agios Myron (SST-TEX^{H}_{86} and U^{K}_{37}) sections. The arrow indicates the present-day SST at Agios Myron location; E) SST-UK 37 from Monte dei Corvi (Italy) from 7.2 to 6.4 Ma (Tzanova et al., 2015). The arrow indicates present-day SST at Monte dei Corvi location.

However, samples AM 25, AM 24 and AM 23 indicate warm Mediterranean surface waters (~27 °C) and all three samples fit to warm insolation peaks (Figure 6.3). For the first cyclic part (7.05–6.9 Ma) the TEX^{H}_{86}–SSTs record shows highest values at AM 19 (6.96 Ma), coinciding with one of the highest peaks in insolation (Figure 6.3). Afterwards, the cooling around 6.92 Ma (AM 17) and 6.90 Ma (AM 16C) coincide with minima in the insolation curve. The 6.9 to 6.7 Ma interval is characterized by low-amplitude precession influencing the insolation values. This feature is recorded in the TEX^{H}_{86}-SSTs as a long period of low variation albeit at high SST values (28 °C). In the youngest part of the record, the TEX^{H}_{86}-SSTs show large variability, likely induced by increased fluctuations in the insolation curve (Figure 6.3A). The high SST values at 6.65 Ma (AM 05) and 6.59 Ma (AM 02) correspond to the highest insolation values, whereas the 6.62 Ma (AM 03C) low value coincides with an insolation minimum.

6.6.3 SST comparison to other Mediterranean Messinian records

The calculated TEX^{H}_{86} and U^{K}_{37} SST range e covers realistic values throughout the 7.2 to 6.5 Ma interval (Figures 6.3A, 6.4D; Appendix 2, Supplementary table), comparable to previously reported late Miocene U^{K}_{37}-based SSTs from Monte dei Corvi (Figure 6.4e; northern Italy; Tzanova et al., 2015) and Kalamaki (Figure 6.4C; Zakynthos Island, Greece; Vasiliev et al., 2019). Although the different sampling resolution does not allow a detailed comparison among the reconstructed SST records, they show a comparable general trend with only some discrepancies between the SST ranges during the Messinian (Figures 6.4C-E). Tzanova et al. (2015) report SSTs between ~19.5 and 27.5 °C (Figure 6.4E), slightly lower than the equivalent U^{K}_{37}' estimates between ~23.7 and 28.2 °C for Agios Myron (Figure 6.4D). This apparent

discrepancy can be accounted for by the ~10° difference in paleolatitude between the Monte dei Corvi and Agios Myron sections (Figure 6.1). TEX^{H}_{86}-based SST estimates were not used until now for the pre-MSC interval and therefore direct comparison to equivalent Mediterranean records is impossible. However, the TEX^{H}_{86}-SSTs reproduce well the high values of the U^{K}_{37}'-SSTs obtained for Agios Myron. When analyzing the TEX^{H}_{86}–SSTs record, in the lower part of the Agios Myron section (~7.2–6.9 Ma), a shift towards 8 °C cooler conditions at 7.03 Ma is hardly recognizable within Monte dei Corvi U^{K}_{37}-SST estimates. There is only a ~ 2 °C decrease in Monte dei Corvi, but to values that are similar to Agios Myron TEXH86-SSTs (20–22 °C). At 6.88 Ma, the TEX^{H}_{86}-SST shows a prominent decrease by 4 °C to 22 °C, similar to the 5 °C decrease to 19.5 °C at Monte dei Corvi (Tzanova et al., 2015). Agios Myron TEX^{H}_{86}-SSTs do not capture the terminal cooling event observed in the high-resolution Monte Dei Corvi record at ~6.85 Ma, possibly due to the lower resolution of our sampling pattern. However, for certain time intervals the TEX^{H}_{86} paleothermometer records even higher temperatures as evidenced in the very warm (28.7–29.8 °C) interval documented at 6.81–6.80 Ma. In such cases, where the U^{K}_{37} index approaches the paleothermometers' limit of 1 (i.e. exclusive presence of $C_{37:2}$ alkenone), we succeed to avoid the underestimation of the magnitude of warmth by using TEX^{H}_{86}. In the upper part of the section (~6.8–6.5 Ma), we observe a rather large spread of values ranging from 22.6 °C to more than 28 °C (Figure 6.4D). In contrast to the rather stable, yet high SSTs around 24–25 °C at Monte dei Corvi (Figure 6.4E), the 6.8–6.5 Ma part of the Agios Myron record depicts a generally warm environment, but punctuated by colder peaks at 6.68, 6.62 and (less at) 6.57 Ma (Figure 6.4D). There is evidence from both Zakynthos (Kalamaki section; Figure 6.4C; Vasiliev et al., 2019) and Cyprus (Pissouri section; Mayser et al., 2017) that this variable temperature pattern continued until ~6.0 Ma.

6.6.4 Messinian sea surface salinity in the Mediterranean

The reconstructed long-term variability in SSS estimates of 36.6 to 47.9 exceeds the standard error of the measurements (Figures 6.3D, 6.4B; Appendix 2, Supplementary table). The SSS estimates are within the modelled range for the Mediterranean during the pre-evaporitic Messinian stage (Simon et al., 2017). The calculated values for the 7.2–6.5 Ma interval at Agios Myron indicate that the Mediterranean basin was characterized by hypersalinity for a significant amount of time, reaching almost 48 (Figure 6.4B). Yet, the values obtained here are similar to

the calculated U^{K}_{37}'-SSTs-derived SSS estimates of maximum of 47.9 (at 6.42 and 6.15 Ma) obtained in the eastern Mediterranean pre-evaporitic Kalamaki section (Figure 6.4A; Vasiliev et al., 2019). The SSS values from Agios Myron are higher than the Sr/Ca-derived SSS estimates for the 7.16–6.93 Ma time interval, but reach equal values of 38 at 6.98 Ma (Kontakiotis et al., 2019). Discrepancies on the SSS estimates may arise from the different proxies used for SST determination (i.e. biomarker- vs. foraminifera based) and the application of different linear $\delta^{18}O_{SW}$-S relationships (i.e. differential slopes and intercepts) in these studies depending on the latitudinal position of the analyzed sections (i.e. increase of evaporation from west to east, regional freshwater input).

Through this comparison, the analyzed settings exhibit a strong variability in slopes and appear to be specific for the region, ranging from 0.48 (westernmost Alboran Sea; Laube-Lenfant, 1996) to 0.41 (southwestern Mediterranean for S < 38; Kallel et al., 1997) to 0.25 (entire Mediterranean basin for S > 36.2; Pierre, 1999) and finally to 0.199 (northwestern and eastern Mediterranean for S >37.5; Kallel et al., 1997). The shallower slope observed in the eastern Mediterranean surface waters likely results from higher evaporation rates in eastern Mediterranean basins relative to the west, shifting the higher salinity water masses to higher oxygen isotopic values. Across the existing datasets, we selected that of Pierre (1999), as the most representative for the study area, covering a wide oceanic salinity range with salinities exceeding 36.2. Beyond the above SSS reconstructions, there are also sparse reports for hypersaline conditions in Mediterranean Messinian for specific (short) time intervals (e.g. 6.74 Ma – Zachariasse et al., 2021; Zachariasse and Lourens, 2021; 6.71 Ma – Blanc-Valleron et al., 2002; 6.68 Ma – Santarelli et al., 1998), further reinforcing our findings of high salinity values in Agios Myron.

Overall, considering all these references for enhanced salinity in the eastern Mediterranean Basin throughout the Messinian, we point out that the transition from normal marine to hypersaline conditions started at ~6.9 Ma, well before the initial observations of ~6.3 Ma (Bellanca et al., 2001; Blanc-Valleron et al., 2002), constraining in this way the stepwise evolution towards hypersaline conditions during the earliest Messinian, apparent in upper bathyal settings like the Heraklion Basin of Crete.

6.6.5 Hydro-climate changes marking the onset of the MSC

The prolonged Late Miocene cooling (~7.4–5.4 Ma) is associated with changes in atmospheric and oceanic circulation, which have been documented both within the subtropical Mediterranean basin (between 7.2 and 6.7 Ma; Kontakiotis et al., 2019; Tzanova et al., 2015) and globally in all oceans (e.g. between 7.1 and 5.4 Ma at tropical and mid- to high-latitude regions; Herbert et al., 2016).

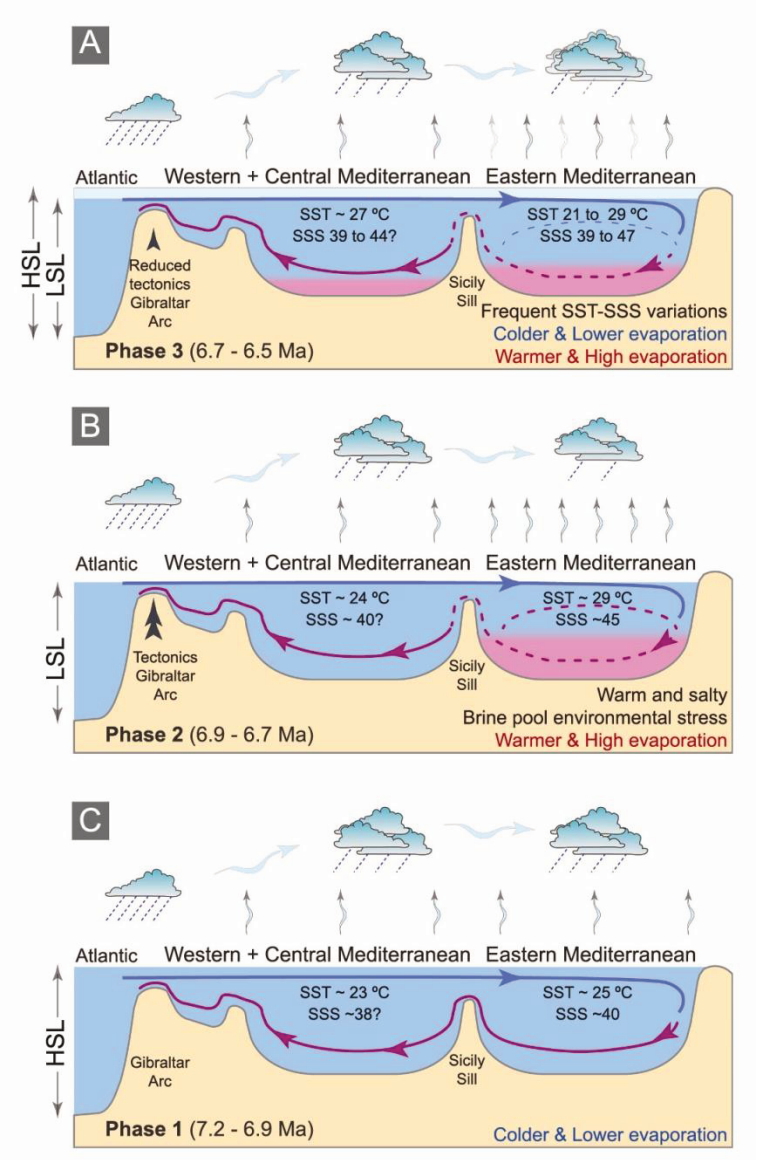

Figure 6.5 Schematic representation of the environmental conditions during important hydrologic changes in the early part of the Messinian Mediterranean Sea. A) During Phase1, Mediterranean experienced coldest times under close to normal saline conditions; B) during Phase 2, pronounced warming and hypersalinity appear, with possible salinity driven stratification of the water column in the eastern Mediterranean; and C) during Phase 3 intensification of climate and salinity variability, accompanied by enhanced stratification of the water column.

However, in the Mediterranean region the detailed sequence of climatic events and the range of related hydrologic variability through that period remain poorly understood. Importantly, the paleogeography of the Mediterranean region, the restriction and partial closure of the western Mediterranean corridors impose a different dynamic of the water circulation within the basin.

Such connectivity and hydrological changes revealed the recognition of evolutionary steps related to distinct paleoenvironmental phases, which developed gradually in a stepwise fashion in western (Sierro et al., 2003; Corbí et al., 2020; Bulian et al., 2021), central (Blanc-Valleron et al., 2002; Di Stefano et al., 2010) and eastern (Kouwenhoven et al., 1999, 2003, 2006; Gennari et al., 2018; Zachariasse et al., 2021; Zachariasse and Lourens, 2021) Mediterranean basins. The SST and SSS patterns revealed here provide context for a development in three consecutive phases (Figures 6.5A-C). Its stepwise character, evidenced by significant SST and SSS perturbations, highlights the presence of a transitional interval preceding the MSC. The concurrent progressive gateway restriction taking place in the western basin and the advent of hydrological changes from open marine to sluggish and hypersaline conditions in the eastern Mediterranean reflect a synergy between tectonics and climate during that period. However, the amplitude of these drivers for specific time intervals is still a matter of discussion.

6.6.5.1 Phase 1: ~7.2–6.9 Ma – Open marine conditions at the initial phase of the Messinian cooling

The oldest part of Agios Myron record exhibits a gradual transition from hypersaline to saline and finally to open marine conditions with TEX^{H}_{86}-SSTs fluctuating by 7 °C (between 20.7 and 28 °C) and SSSs varying between 36.6 and 45.8, with an average of 40.0 (Figure 6.5C). Phase 1 includes a two-step cold episode punctuated by a rebound to higher temperatures. The lower part of phase 1 (~7.21–7.05 Ma) corresponds to silty marls without sapropels followed by cyclic deposition of 7 marl/ sapropel couplets (~7.05–6.90 Ma). During this latter interval, the coldest excursions to 20.7 °C and 22.2 °C occurred at 7.03 and 6.91 Ma, respectively (Figure 6.3A). In between these minimum values, the average SST rebounds to ~26 °C (Figure 6.3A), which is close to the average SST recorded around the Tortonian/Messinian boundary (~25 °C, Kontakiotis et al., 2019; Tzanova et al., 2015). These minima at 7.03 and 6.91 Ma fall within the

relevant brief cooling period of ~7.1–6.9 Ma, when a strong SST decrease (~9 °C) was recorded in the nearby Cretan Faneromeni section (Kontakiotis et al., 2019).

Although there was no evidence of termination of this cooling trend in Faneromeni due to the diagenetic bias in Sr/Ca-SST after 6.9 Ma, the data from Agios Myron clearly place the end of the cooling in the eastern Mediterranean at 6.9 Ma, when a warm and hypersaline water column starts to develop ($\delta^{18}O_{IVF\text{-}SW}$ around 3 and SSS > 41; Figures 6.3C, d and 6.4B). Cooling and evaporation of the circum-Mediterranean basin at about 7.0 Ma are also supported by evidences like enhanced dust accumulation rates (e.g. Sahara dunes; Schuster et al., 2006), noticeable planktonic and benthic carbon isotopes shift towards lighter values (Late Miocene Carbon Isotope Shift; Kontakiotis et al., 2019; Bulian et al., 2022) related to increased aridity (e.g. Hodell et al., 1994) and vegetation changes towards more C_4 plant contribution (e.g. Uno et al., 2016) leading to the expansion of open habitats that could have invigorated eolian transport over the Mediterranean subsequently inducing increased silica contribution (Pellegrino et al., 2018) as visible from the diatomite rich layers accumulating from 7.17 Ma in the Sorbas Basin or in the Tripoli formation in Sicily (e.g. Hilgen and Krijgsman, 1999; Roveri et al., 2014; Sierro et al., 2003). We further note that the warmer period within phase 1 at 6.97 Ma is accompanied by fresher surface water ($1 < \delta^{18}O_{IVF\text{-}SW} < 2$ and SSS < 40; Figures 6.3C, D and 6.4B), typical for the upper Miocene and Pliocene Mediterranean paleoceanography.

6.6.5.2 Phase 2: 6.9–6.7 Ma – Enhanced restricted conditions and environmental stress due to increased temperature and salinity

From 6.9 to 6.7 Ma, the marine conditions changed significantly, with surface waters characterized by elevated temperatures and salinities, most likely associated with the progressive restriction of the Mediterranean basin (Figure 6.5B). At the beginning of phase 2 (6.87–6.81 Ma), excursions to positive $\delta^{18}O_{IVF\text{-}SW}$ (i.e. saltier) and subsequent high SSS values (40.4 to 46.5) suggest hypersaline sea surface conditions, which are consistent with observations in the Sicilian basin (e.g. Marianopoli section; Bellanca et al., 2001). Faunal development (reduction of benthic diversity and dominance of salinity-tolerant species) and geochemical (Mn/Al, V/Al) parameters from several eastern Mediterranean sections (Falconara/Gibliscemi, Monte del Casino, Metochia, Pissouri) further point towards intermittent periods of severely stressed benthic faunal communities around 6.8 Ma (Drinia et al., 2007; Kouwenhoven et al., 1999, 2006). This period

of increased environmental stress coincides with the highest salinity (47.9) in the Agios Myron record (Figures 6.3D, 6.4B; Appendix 2, Supplementary table).

Declining foraminiferal diversity and mass occurrences of phytoplankton adapted to high salinity throughout the Mediterranean are all evidence of increasing salinity stress (Kouwenhoven et al., 1999; Santarelli et al., 1998; Sierro et al., 2003). Although planktonic foraminiferal growth was progressively inhibited as a consequence of the subsequent high salinity (this study; Zachariasse et al., 2021; Zachariasse and Lourens, 2021), the reconstructed values remain within their tolerance ranges (Bijma et al., 1990) and below the relevant paleoecological thresholds (< 49; Fenton et al., 2000). Reconstructed SSTs from Agios Myron are ~28 °C (Figures 6.3A, 6.4D), thus confirming the dual character (thermal and salinity increase) of environmental stress over this interval. This pronounced warm and salty interval was interrupted by a rebound to relatively lower SSSs (40.4) under persistent warm conditions at 6.85 Ma (Figures 6.3D, 6.4B). The same hydrological regime was maintained until 6.72 Ma, where an abrupt and brief salty event (SSS = 47.2) is documented in Agios Myron (Figures 6.3D, 6.4B).

During this interval, temperature and salinity increase concomitantly. The extremely warm and saline surface waters, possibly due to their restricted outflow, indicate the reduction of the Atlantic influence over the Mediterranean Sea. This result is further supported by age-equivalent changes in Messinian gateway restriction (Krijgsman et al., 2018). Increasing isolation of the Mediterranean due to tectonics and/or eustacy may have led to increased residence times of water masses within the basin (e.g. Abad – Sierro et al., 2003; Agios Myron – Zachariasse et al., 2021; Gavdos – Zachariasse and Lourens, 2021) and in combination with warming (this study) the slow-down of thermohaline circulation and enhancement of water column stratification as supported by the increased difference between benthic and planktonic $\delta^{18}O$ values (Zachariasse and Lourens, 2021). Given that sensitivity of a basin to the variation of the surface heat decreases with increasing size of the gateway (Flecker et al., 2015; Karami et al., 2011) we conclude that during phase 2 the strongest response of salinity to hydro-climate variability reflects even smaller marine gateways. According to our data, this occurred at 6.72 Ma, 20 kyr later than the significant increase in $\delta^{18}O$ values in both benthic (0.7‰) and planktonic (0.5‰) foraminifera in Agios Myron (Zachariasse et al., 2021) as well as in other sections (e.g. average 1.72‰ and 0.97‰ $\delta^{18}O$ increases in Gavdos; Zachariasse and Lourens, 2021) along the Mediterranean Sea. The Mediterranean-wide character of this event could be

another evidence for gateway restriction, with its amplitude varying with location. Such gateway configuration changes (dimensions, bathymetry and geometry) as well as their control on Mediterranean water properties have been proposed by several studies (e.g. Blanc, 2006; Ivanovic et al., 2014; Meijer, 2012). For instance, Simon and Meijer (2015) indicated that Atlantic-Mediterranean exchange during the deposition of the Primary Lower Gypsum was as low as 10 to 25% when compared to the present-day value at the Strait of Gibraltar, while Krijgsman et al. (2018) estimated that longer and narrower straits existed at greater water depth. Therefore, we hypothesize that the gateway configuration and evolution through the Messinian acted as a key factor for the hydrological change reflected in phase 2 in the Agios Myron (this study, Zachariasse et al., 2021) and Gavdos sections (Zachariasse and Lourens, 2021), and such local effects (both restriction and hydrology related) prevail over the global cooling.

6.6.5.3 Phase 3: 6.7–6.5 Ma – Continuous warming, intense salinity fluctuations, enhanced stratification

The upper part of the Agios Myron section clearly demonstrates a distinct colder episode during the long-term warming trend with high-amplitude variability between ~6.8−6.5 Ma (Figures 6.3A, 6.5A). This ~0.2 Ma cold excursion starts at 6.7 Ma with a sharp drop in SST from 27 °C to 22 °C, followed by a recovery to 28 °C at 6.66 Ma and a second drop to 24 °C around 6.61 Ma (Figures 6.3A; 6.4D). This variable pattern continues up to 6.54 Ma with additional SST maxima and minima. Similarly, both $\delta^{18}O$ and reconstructed SSS present a strikingly variable pattern, reflecting the evolution towards an environment mostly characterized by hypersaline conditions (positive $\delta^{18}O_{IVF\text{-}SW}$ shifts and/or maximum SSS values) with some freshening episodes (negative $\delta^{18}O_{IVF\text{-}SW}$ shifts and/or minimum SSS values) (Figure 6.5C, D). In this interval the cyclic pattern is visible and obvious in the Agios Myron section.

Similar variations of the depositional environment were reported throughout the eastern Mediterranean because of its more restricted configuration compared to the western basin. Organic dinocyst data from the Faneromeni section indicate hypersaline surface waters at 6.68 Ma (Santarelli et al., 1998) , and combined benthic foraminifera faunal and geochemical data from the study section as well as the nearby Metochia section further show permanent hypersaline deep-water conditions after 6.74 ± 0.04 Ma (Zachariasse et al., 2021; Zachariasse and Lourens, 2021). It is worthy to note that such salinity change lag between deepand surface-

waters is not well understood yet and requires further investigation. Moreover, the first diatomites at Gavdos appear at 6.72 Ma (Drinia et al., 2007; Zachariasse et al., 2021), time when the western Mediterranean sedimentation changes to alternation of sapropels and homogeneous marls with irregularly intercalated diatomites (Roger et al., 2000; Cornée et al., 2002). The fact that SSS values strongly fluctuate in phase 3 while deep water remains hypersaline could be explained by occasional freshwater inputs, because the hypersaline subsurface water mixes less well and therefore runoff should have a clear effect on sea surface salinities. Regarding the potential source of these freshwater inputs, recent observations from Cyprus (Mayser et al., 2017) suggest a stronger dilution by continental waters from runoff (both from North Africa and Anatolia Plateau catchments) rather than an increase of oceanic inputs. This inflow of less saline surface waters, together with the persistence of strongly saline intermediate and hypersaline deep waters of the marginal eastern Mediterranean basin could have caused a strong stratification in the water column, preventing bottom ventilation and favoring sapropel formation.

6.6.6 Tectonic versus climatic drivers on the Messinian evolution of the MSC

During the Tortonian/Messinian boundary, the open AtlanticMediterranean exchanges maintained relatively stable marine conditions, expressed through a relatively cool and fresh upper water column for the eastern Mediterranean (Kontakiotis et al., 2019). The reduction in efficiency of gateways between the Atlantic Ocean and the Mediterranean Sea started at about 7.2 Ma (initial stage of the Late Miocene cooling) because of the tectonic uplift of the Rifian and Betic corridors (Kouwenhoven et al., 1999; Krijgsman et al., 1999b). Tectonic control was likely to be dominant during the earliest Messinian (Phase 1; 7.2–6.9 Ma; Fig. 6.5C) since all known gateways (through Morocco and Spain) were closed around this time except for a long, narrow channel at Gibraltar (Krijgsman et al., 2018). Although the possibility of the existence of a proto-Gibraltar strait as the main source of Atlantic inflow in the earliest Messinian has been multidisciplinary surveyed based on foraminiferal and sedimentological records (El Achalhi et al., 2016; Bulian et al., 2021) and computational reconstructions (Krijgsman et al., 2018), further investigations are needed to be completely validated. Shallower gateways caused higher temperatures and salinities in the upper water column, whereas the reduction of the vertical circulation led to bottom water stagnation or at least to significant circulation slowdown. In Agios Myron, SST increases at ~6.95 Ma, while SSS follows at ~6.9 Ma. During the salinity

increase identified in the eastern Mediterranean from 6.9 to 6.7 Ma, faunal diversity decreased (less diversified planktonic faunas dominated by two or three species; Zachariasse et al., 2021) as conditions deteriorated once the oceanic link was weakened (Zachariasse and Lourens, 2021). As a result, the eastern Mediterranean basin turned into a warm and hypersaline pool with increased environmental stress (Phase 2; Figure 6.5B). Additionally, the Sicily channel may have limited the connections between the western and the eastern Mediterranean (Bialik et al., 2021) amplifying the differences in basin conditions (Gladstone et al., 2007). The termination of elevated SST and SSS recorded at 6.72 Ma was further accompanied by a change in the processes governing surface water productivity controlling the onset of the diatomite deposition on Gavdos Island (Zachariasse et al., 2021). Phase 3 (6.7–6.5 Ma; Figure 6.5A), characterized by large fluctuations of SST and SSS under dominant climate control, can be considered as the transition from the initiation of hypersalinity (at ~6.9 Ma) to the onset of the MSC marked by deposition of subaqueous evaporites. The cooling at 6.68 Ma was accompanied by enhanced water column stratification that lasted over the entire phase 3, as supported by increased difference in the oxygen isotopic values between benthic and planktonic foraminifera from both Agios Myron (Zachariasse et al., 2021) and Gavdos (Zachariasse and Lourens, 2021). SSS fluctuations and increasingly stagnating bottom waters at 6.7 Ma in the eastern and central Mediterranean along with the reduction in terrigenous supply in the eastern Mediterranean (Blanc-Valleron et al., 2002; Kouwenhoven et al., 2006; Santarelli et al., 1998) were consequences of restrictions along the Betic and Rifian corridors (e.g. Sierro et al., 2001; van Assen et al., 2006; Hüsing et al., 2009). These short-term climatic fluctuations induced strong changes in the SSS (from high saline to diluted conditions), evident especially at times of increased continental input during summer insolation maxima resulting in a dilution of the surface waters responsible for the subsequent density driven stratification of the water column.

6.7 Conclusions

The Agios Myron section (Crete) contains a key sedimentary succession with marl-sapropel cyclicity to assess the hydroclimatic conditions prior to the onset of the MSC. The presented geochemical (biomarker and oxygen isotope) data indicate that the stratigraphic interval from 7.2 to 6.5 Ma, approximately 0.5 Myr before the onset of the MSC, is characterized by high-

frequency SST and SSS oscillations whose amplitude strongly exceeds those of the global oceans.

Overall, these oscillations are in phase with precession, indicating a solar insolation as the primary driver, with subordinate controls through tectonic and glacio-eustatic processes. During the pre-evaporitic Phase 1 (7.2–6.9 Ma), however, it is likely that tectonic activity caused restriction and reduced Mediterranean circulation with climate forcing superimposed on the stepwise evolution of the basin. In particular, the observed temperature and salinity variability recorded in the Agios Myron section provides evidence of fluctuating and increasing environmental stress, in accordance with the stepwise restriction of the eastern Mediterranean Basin preceding the deposition of evaporites. After the beginning of the Messinian, the open Atlantic-Mediterranean exchanges maintained relatively stable marine conditions, expressed through a relatively cool and fresh upper water column for the eastern Mediterranean.

At ~6.9 Ma, the onset of Phase 2, the combined effect of a larger water deficit and/or the abrupt isolation of the Mediterranean Basin at a greater and probably faster pace (also related to the mode of gateway flow as a result of the passage configurations) led to the development of a hypersaline warm pool. An important increase in heat flux highlights a warm doublepeak centered at 6.9–6.8 and 6.72 Ma, which is attributed to thermal and salinity stress, respectively. In between, the freshening event recognized at 6.8–6.7 Ma indicates that the Mediterranean Sea episodically experienced fully marine connections to the Atlantic Ocean, possibly related to the variation in volume periodic overflow (e.g. the Sicilian sill).

Phase 3, between 6.72 and 6.54 Ma, was characterized by a wide range, precession-scale sea surface temperature and salinity fluctuations. Increased continental inputs in the North African and Anatolian Plateau riverine runoff resulted in the freshening of surface waters – now quantified in this study – and led to the reduction of the vertical circulation and enhanced water column stratification during warm intervals.

6.8 Acknowledgments

We thank Ulrich Treffert for help in the organic geochemistry laboratory and Jens Fiebig for support in the Goethe University-Senckenberg BiK-F Stable Isotope Facility. This research was financed by the GreekGerman collaboration project (IKYDA-DAAD): “Quantification of the environmental changes in the Eastern Mediterranean at the onset of the Messinian Salinity Crisis (Crete-Greece)” (QUANTMES) of IV and WK. Collaboration was made possible through the COST Action CA15103 “Uncovering the Mediterranean salt giant” (MEDSALT) supported by COST (European Cooperation in Science and Technology). Analyses were supported by the DFG grant number 398614017 of IV. We thank William Ryan and the two anonymous reviewers for their comments and suggestions that significantly improved this manuscript.

References

Antonarakou, A., Kontakiotis, G., Mortyn, P.G., Drinia, H., Sprovieri, M., Besiou, E., Tripsanas, E., 2015. Biotic and geochemical ($\delta^{18}O$, $\delta^{13}C$, Mg/Ca, Ba/Ca) responses of *Globigerinoides ruber* morphotypes to upper water column variations during the last deglaciation, Gulf of Mexico, Geochimica et Cosmochimica Acta, 170, 69–93. https://doi.org/10.1016/j.gca.2015.08.003

Antonarakou, A., Kontakiotis, G., Vasilatos, C., Besiou, E., Zarkogiannis, S., Drinia, H., Mortyn, P. G., Tsaparas, N., Makri, P., Karakitsios, V., 2019. Evaluating the effect of marine diagenesis on Late Miocene pre-evaporitic sedimentary successions of eastern Mediterranean Sea. IOP Conference Series: Earth and Environmental Sciences, 221, 012051. https://doi.org/10.1088/1755-1315/221/1/012051

Bellanca, A., Caruso, A., Ferruzza, G., Neri, R., Rouchy, J. M., Sprovieri, M., Blanc-Valleron, M.M., 2001. Transition from marine to hypersaline conditions in the Messinian Tripoli Formation from the marginal areas of the central Sicilian Basin. Sedimentary Geology, 140, 87–105. https://doi.org/10.1016/S0037-0738(00)00173-1

Bemis, B.E., Spero H.J., Bijma J., Lea, D.W., 1998. Reevaluation of the oxygen isotopic composition of planktonic foraminifera: experimental results and revised paleotemperature equations. Paleoceanography, 13(2), 150–160. http://dx.doi.org/10.1029/98PA00070

Besseling, M., Hopmans, E.C., Koenen, M., van der Meer, M.T.J., Vreugdenhil, S., Schouten, S., Sinninghe Damsté, J.S., Villanueva, L., 2019. Depth-related differences in archaeal populations impact the isoprenoid tetraether lipid composition of the Mediterranean Sea water column. Org. Geochem. 135, 16–31. https://doi.org/ 10.1016/j.orggeochem.2019.06.008.

Bialik, O.M., Zammit, R., Micallef, A., 2021. Architecture and sequence stratigraphy of the Upper Coralline Limestone formation, Malta – implications for Eastern Mediterranean restriction prior to the Messinian Salinity Crisis. The Depositional Record, 00, 1–15. https://doi.org/10.1002/dep2.138

Bijma, J., Faber Jr., W.W., Hemleben, C., 1990. Temperature and salinity limits for growth and survival of some planktonic foraminifers in laboratory cultures. Journal of Foraminiferal Research, 20, 95–116. https://doi.org/10.2113/gsjfr.20.2.95

Blanc, P.L., 2006. Improved modelling of the Messinian Salinity Crisis and conceptual implications. Palaeogeography, Palaeoclimatology, Palaeoecology, 238, 349–372. https://doi.org/10.1016/j.palaeo.2006.03.033

Blanc-Valleron, M.-M., Pierre, C., Caulet, J.P., Caruso, A., Rouchy, J.-M., Cespuglio, G., Sprovieri, R., Pestrea, S., Di Stefano, E., 2002. Sedimentary, stable isotope and micropaleontological records of paleoceanographic change in the Messinian Tripoli Formation (Sicily, Italy). Palaeogeography, Palaeoclimatology, Palaeoecology, 185, 255–286. https://doi.org/10.1016/S0031-0182(02)00302-4

Bouvier-Soumagnac, Y., Duplessy, J.-C., 1985. Carbon and oxygen isotopic composition of planktonic foraminifera from laboratory culture, plankton tows and recent sediment: implications for the reconstruction of paleoclimatic conditions and of the global carbon cycle. J. Foraminiferal Res. 15, 302–320.

Brassell, S.C., Eglinton, G., Marlowe, I.T., Pflaumann, U., Sarnthein, M., 1986. Molecular stratigraphy as a new tool for climatic assessment. Nature, 320, 129–133. https://doi.org/10.1038/320129a0

Bulian, F., Sierro, F.J., Ledesma, S., Jiménez-Espejo, F.J., Bassetti, M.-A., 2021. Messinian West Alboran Sea record in the proximity of Gibraltar: early signs of Atlantic-Mediterranean gateway restriction. Marine Geology 434, 106430. https://doi. org/10.1016/j.margeo.2021.106430.

Bulian, F., Kouwenhoven, T.J., Jim´enez-Espejo, F.J., Krijgsman, W., Andersen, N., Sierro, F.J., 2022. Impact of the Mediterranean-Atlantic connectivity and the late Miocene carbon shift on deep-sea communities in the Western Alboran Basin. Palaeogeogr. Palaeoclimatol. Palaeoecol. 589, 110841 https://doi.org/10.1016/j. palaeo.2022.110841.

Capella, W., Flecker, R., Hernández-Molina, F.J., Simon, D., Meijer, P.T., Rogerson, M., Sierro, F.J., Krijgsman, W., 2019. Mediterranean isolation preconditioning the earth system for late Miocene climate cooling. Scientific Reports, 9, 3795. https://doi.org/10.1038/s41598-019-40208-2

Conte, M.H., Sicre, M.A., Ruhlemann, C., Weber, J.C., Schulte, S., Schulz-Bull, D., Blanz, T., 2006. Global temperature calibration of the alkenone unsaturation index ($U^{K'}_{37}$) in surface waters and comparison with surface sediments. Geochemistry Geophysics Geosystems, 7. https://doi.org/10.1029/2005gc001054

Corbí, H., Soria, J.M., Giannetti, A., Yébenes, A., 2020. The step-by-step restriction of the Mediterranean (start, amplification, and consolidation phases) preceding the Messinian Salinity Crisis (climax phase) in the Bajo Segura basin. Geo-Mar. Lett. 40, 341–361. https://doi.org/10.1007/s00367-020-00647-7.

Cornée, J.J., Roger, S., Münch, P., Saint-Martin, J.P., Féraud, G., Conesa, G., Pestrea, S., 2002. Messinian events: new constraints from sedimentological investigations and new 40Ar/39Ar ages in the Melilla –Nador basin (Morocco). Sediment. Geol. 151, 127–147.

Di Stefano, A., Verducci, M., Lirer, F., Ferraro, L., Iaccarino, S.M., Hüsing, S.K., Hilgen, F.J., 2010. Paleoenvironmental conditions preceding the Messinian Salinity Crisis in the Central Mediterranean: Integrated data from the Upper Miocene Trave section (Italy). Palaeogeogr. Palaeoclimatol. Palaeoecol. 297 (1), 37–53. https://doi.org/ 10.1016/j.palaeo.2010.07.012.

Drinia, H., Antonarakou, A., Tsaparas, N., Kontakiotis, G., 2007. Palaeoenvironmental conditions preceding the Messinian salinity crisis: a case study from Gavdos Island. Geobios, 40, 251–265. https://doi.org/10.1016/j.geobios.2007.02.003

Drury, A.J., Lee, G.P., Gray, W.R., Lyle, M., Westerhold, T., Shevenell, A.E., John, C.M., 2018. Deciphering the state of the late Miocene to early Pliocene equatorial Pacific. Paleoceanography, 33(3), 246–263. https://doi.org/10.1002/2017PA003245

El Achalhi, M., Münch, P., Cornée, J.J., Azdimousa, A., Melinte-Dobrinescu, M., Quillévéré, F., Drinia, H., Fauquette, S., Jiménez-Moreno, G., Merzeraud, G., Ben, Moussa A., El Kharim, Y., Feddi, N., 2016. The late Miocene MediterraneanAtlantic connections through the North Rifian Corridor: New insights from the Boudinar and Arbaa Taourirt basins (northeastern Rif, Morocco). Palaeogeogr. Palaeoclimatol. Palaeoecol. 459, 131–152.

Elderfield, H., Vautravers, M., Cooper, M., 2002. The relationship between shell size and Mg/Ca, Sr/Ca, $\delta^{18}O$, and $\delta^{13}C$ of species of planktonic foraminifera. Geochemistry Geophysics Geosystems 3(8), 4052. https://doi.org/10.1029/2001GC000194

Elling, F.J., Gottschalk, J., Doeana, K.D., Kusch, S., Hurley, S.J., Pearson, A., 2019. Archaeal lipid biomarker constraints on the Paleocene-Eocene carbon isotope excursion. Nat. Commun. 10 (1) https://doi.org/10.1038/s41467-019-12553-3.

Emeis, K.C., Struck. U., Schulz, H.M, Rosenberg, R., Bernasconi, S., Erlenkeuser, H., Sakamoto, T., Martinez-Ruiz, F., 2000. Temperature and salinity variations of Mediterranean Sea surface waters over the last 16,000 years from records of planktonic stable oxygen isotopes and alkenone unsaturation ratios. Palaeogeography, Palaeoclimatology, Palaeoecology, 158, 259–280. https://doi.org/10.1016/S0031-0182(00)00053-5

Fenton, M., Geiselhart, S., Rohling, E.J., Hemleben, C., 2000. Aplanktonic zones in the Red Sea. Marine Micropaleontology, 40, 277–294. https://doi.org/10.1016/S0377-8398(00)00042-6

Flecker, R., Krijgsman, W., Capella, W., de Castro Martíns, C., Dmitrieva, E., Mayser, J.P., Marzocchi, A., Modestu, S., Ochoa, D., Simon, D., Tulbure, M., van den Berg, B., van der Schee, M., de Lange, G., Ellam, R., Govers, R., Gutjahr, M., Hilgen, F., Kouwenhoven, T., Lofi, J., Meijer, P., Sierro, F.J., Bachiri, N., Barhoun, N., Alami, A. C., Chacon, B., Flores, J.A., Gregory, J., Howard, J., Lunt, D., Ochoa, M., Pancost, R., Vincent, S., Yousafi, M.Z., 2015. Evolution of the Late Miocene Mediterranean–Atlantic gateways and their impact on regional and global environmental change. Earth-Science Reviews, 150, 365–392. https://doi.org/10.1016/j.earscirev.2015.08.007

Gennari, R., Lozar F., Turco E., Dela Pierre F., Manzi V., Natalicchio M., Lugli S., Roveri M., Schreiber, C., Taviani, M., 2018. Integrated stratigraphy and paleoceanographic evolution of the pre-evaporitic phase of the Messinian salinity crisis in the Eastern Mediterranean as recorded in the Tokhni section (Cyprus Island). Newsletter on Stratigraphy, 51, 1–23. DOI: 10.1127/nos/2017/0350

Gladstone, R., Flecker R., Valdes P., Lunt D., Markwick P., 2007. The Mediterranean hydrologic budget from a Late Miocene global climate simulation. Palaeogeography, Palaeoclimatology, Palaeoecology, 251, 254–267. https://doi.org/10.1016/j.palaeo.2007.03.050

Herbert, T.D., Lawrence, K.T., Tzanova, A., Peterson, L.C., Caballero-Gill, R., Kelly, C.S., 2016. Late Miocene global cooling and the rise of modern ecosystems. Nature Geoscience, 9, 843–847. http://dx.doi.org/10.1038/NGEO2813.

Hilgen, F.J., Krijgsman, W., 1999. Cyclostratigraphy and astrochronology of the Tripoli diatomite Formation (pre-evaporite Messinian, Sicily, Italy). Terra Nova 11, 16–22. https://doi.org/10.1046/j.1365-3121.1999.00221.x.

Hilgen, F.J., Krijgsman, W., Langereis, C.G., Lourens, L.J., Santarelli, A., Zachariasse, W.J., 1995. Extending the astronomical (polarity) time scale into the Miocene. Earth Planet. Sci. Lett. 136, 495–510. https://doi.org/10.1016/0012-821X(95)00207-S. Hilgen, F., Krijgsman, W., Wijbrans, J.R., 1997. Direct comparison of astronomical and 40Ar/39Ar ages of ash beds: potential implications for the age of mineral dating standards. Geophys. Res. Lett. 24 (16), 2043–2046. https://doi.org/10.1029/ 97GL02029.

Hilgen, F.J., Bissoli, L., Iaccarino, S., Krijgsman, W., Meijer, R., Negri, A., Villa, G., 2000. Integrated stratigraphy and astrochronology of the Messinian GSSP at Oued Akrech (Atlantic Morocco). Earth Planet. Sci. Lett. 182, 237–251. https://doi.org/10.1016/ S0012-821X(00)00247-8.

Hodell, D.A., Benson, R.H., Kent, D.V., Boersma, A., Rakic-El Bied, K., 1994. Magnetostratigraphic, biostratigraphic, and stable isotope stratigraphy of an Upper Miocene drill core from the Sal´e Briqueterie (Northwest Morocco): A high-resolution chronology for the Messinian stage. Paleoceanography 9 (6), 835–855. https://doi. org/10.1029/94PA01838.

Hsü, K.J., 1972. Origin of saline giants: a critical review after the discovery of the Mediterranean evaporites. Earth-Science Reviews, 8, 371–396. https://doi.org/10.1016/0012-8252(72)90062-1

Hüsing, S.K., Kuiper, K.F., Link, W., Hilgen, F.J., Krijgsman, W., 2009. The upper Tortonian–lower Messinian at Monte dei Corvi (Northern Apennines, Italy): Completing a Mediterranean reference section for the Tortonian Stage. Earth and Planetary Science Letters, 282 (1–4), 140–157. https://doi.org/10.1016/j.epsl.2009.03.010

Ilyina, L.B., Shcherba, I.G., Khondkarian, S.O., 2004. Map 8: Middle Late Miocene (Late Tortonian – Early Messinian – Early Maeotian – Late Pannonian) in Lithological-Paleogeographic maps of Paratethys. Editors: Popov, S.V., Rögl, F., Rozanov, A.Y., Steininger, F.F., Shcherba, I.G., Kovac, M., Courier Forschungsinstitut Senckenberg, Vol. 250, maps 1-10 (annex), Late Eocene to Pliocene.

Ivanovic, R.F, Valdes, P.J., Flecker, R., Gutjahr, M., 2014. Modelling global-scale climate impacts of the late Miocene Messinian Salinity Crisis. Climate of the Past, 10, 607–622. https://doi.org/10.5194/cp-10-607-2014

Kallel, N., Paterne, M., Duplessy, J.C., Vergnaud-Grazzini, C., Pujol, C., Labeyrie, L.D., Arnold, M., Fontugne, M., Pierre, C., 1997. Enhanced rainfall on Mediterranean region during the last sapropel event. Oceanol. Acta 20 (5), 697–712.

Karakitsios, V., Roveri, M., Lugli, S., Manzi, V., Gennari, R., Antonarakou, A., Triantaphyllou, M., Agiadi, K., Kontakiotis, G., Kafousia, N., de Rafelis, M., 2017. A record of the Messinian salinity crisis in the eastern Ionian tectonically active domain (Greece, eastern Mediterranean). Basin Research, 29(2), 203–233. https://doi.org/10.1111/bre.12173

Karakitsios, V., Cornée, J.-J., Tsourou, T., Moissette, P., Kontakiotis, G., Agiadi, K., Manoutsoglou, E., Triantaphyllou, M., Koskeridou, E., Drinia, H., Roussos, D., 2017. Messinian salinity crisis record under strong freshwater input in marginal, intermediate, and deep environments: The case of the North Aegean. Palaeogeography, Palaeoclimatology, Palaeoecology, 485, 316–335. https://doi.org/10.1016/j.palaeo.2017.06.023

Karami, M.P., de Leeuw, A., Krijgsman, W., Meijer, P.T., Wortel, M.J.R., 2011. The role of gateways in the evolution of temperature and salinity of semi-enclosed basins: An oceanic box model for the Miocene Mediterranean Sea and Paratethys. Global and Planetary Change, 79, 73–88. https://doi.org/10.1016/j.gloplacha.2011.07.011

Kim, J.-H., Schouten, S., Hopmans, E.C., Donner, B., Sinninghe Damsté, J.S., 2008. Global sediment core-top calibration of the TEX_{86} paleothermometer in the ocean. Geochimica et Cosmochimica Acta, 72(4), 1154-1173. https://doi.org/10.1016/i.gca.2007.12.010

Kim, J.H., van der Meer, J., Schouten, S., Helmke, P., Willmott, V., Sangiorgi, F., Koç, N., Hopmans, E., Sinninghe Damsté, J.S., 2010. New indices and calibrations derived from the distribution of crenarchaeal isoprenoid tetraether lipids: Implications for past sea surface temperature reconstructions. Geochimica et Cosmochimica Acta, 74(16). https://doi.org/10.1016/j.gca.2010.05.027

Kontakiotis, G., Karakitsios, V., Mortyn, P. G., Antonarakou, A., Drinia, H., Anastasakis, G., Agiadi, K., Kafousia, N., De Rafelis, M., 2016. New insights into the early Pliocene hydrographic dynamics and their relationship to the climatic evolution of the

Mediterranean Sea. Palaeogeography, Palaeoclimatology, Palaeoecology, 459, 348–364. https://doi.org/10.1016/j.palaeo.2016.07.025

Kontakiotis, G., Besiou, E., Antonarakou, A., Zarkogiannis, S.D., Kostis, A., Mortyn, P.G., Moissette, P., Cornée, J.- J., Schulbert, C., Drinia, H., Anastasakis, G., Karakitsios, V., 2019. Decoding sea surface and paleoclimate conditions in the eastern Mediterranean over the Tortonian-Messinian Transition. Palaeogeography, Palaeoclimatology, Palaeoecology, 534, 109312. https://doi.org/10.1016/j.palaeo.2019.109312

Kouwenhoven, T.J., Seidenkrantz, M.S., van Der Zwaan, G.J., 1999. Deep-water changes: The near-synchronous disappearance of a group of benthic foraminifera from the late Miocene Mediterranean. Palaeogeography, Palaeoclimatology, Palaeoecology, 152, 259–281. https://doi.org/10.1016/S0031-0182(99)00065-6

Kouwenhoven, T.J., Hilgen, F.J., van der Zwaan, G.J., 2003. Late Tortonian–early Messinian stepwise disruption of the Mediterranean–Atlantic connections: constraints from benthic foraminiferal and geochemical data. Palaeogeography, Palaeoclimatology, Palaeoecology, 198, 303–319. https://doi.org/10.1016/S0031-0182(03)00472-3

Kouwenhoven, T.J., van der Zwaan, G.J., 2006. A reconstruction of late Miocene Mediterranean circulation patterns using benthic foraminifera. Palaeogeography, Palaeoclimatology, Palaeoecology, 238, 373–385. https://doi.org/10.1016/j.palaeo.2006.03.035

Kouwenhoven, T.J., Morigi, C., Negri, A., Giunta, S., Krijgsman, W., Rouchy, J.M., 2006. Paleoenvironmental evolution of the eastern Mediterranean during the Messinian: Constraints from integrated microfossil data of the Pissouri Basin (Cyprus). Marine Micropaleontology 60, 17–44. https://doi.org/10.1016/j.marmicro.2006.02.005

Krijgsman, W., Hilgen, F.J., Raffi, I., Sierro, F.J., Wilson, D. S., 1999. Chronology, causes and progression of the Messinian salinity crisis. Nature, 400, 652–655. https://doi.org/10.1038/23231

Krijgsman, W., Langereis, C.G., 2000. Magnetostratigraphy of the Zobzit and Koudiat Zarga sections (Taza–Guercif basin, Morocco): implications for the evolution of the Rifian Corridor. Marine and Petroleum Geology, 17, 359–371. https://doi.org/10.1016/S0264-8172(99)00029-X

Krijgsman, W., Capella, W., Simon, D., Hilgen, F.J., Kouwenhoven, T.J., Meijer, P. Th., Sierro, F.J., Tulbure, M.A., van den Berg, B.C.J., van der Schee, M., Flecker, R., 2018. The

Gibraltar Corridor: Watergate of the Messinian Salinity Crisis. Marine Geology, 403, 238–246. https://doi.org/10.1016/j.margeo.2018.06.008

Kuiper, K.F., Hilgen, F., Steenbrink, J., Wijbrans, J.R., 2004. $^{40}Ar/^{39}Ar$ ages of tephras intercalated in astronomically tuned Neogene sedimentary sequences in the Eastern Mediterranean. Earth and Planetary Science Letters, 222(2), 583–597. https://doi.org/10.1016/j.epsl.2004.03.005

Laskar, J., Robutel, P., Joutel, F., Gastineau, M., Correia, A.C.M., Levrard, B., 2004. A long-term numerical solution for the insolation quantities of the Earth. Astronomy & Astrophysics, 428, 261–285. https://doi.org/10.1051/0004-6361:20041335

Laube-Lenfant, E., 1996. Utilisation des isotopes naturels ^{18}O de l'eau et ^{13}C du carbone inorganique dissous comme traceurs oc´eaniques dans les zones frontales et d'upwelling. Cas du Pacifique ´equatorial et de la mer d'Alboran. Doctoral Thesis. University Pierre et Marie Curie, 319.

LeGrande, A.N., Schmidt, G.A., 2006. Global gridded data set of the oxygen isotopic composition in seawater. Geophysical Research Letters, 33(12), L12604. https://doi.org/10.1029/2006GL026011

Leider, A., Hinrichs, K., Mollenhauer, G., Versteegh, G., 2010. Core-top calibration of the lipid-based U37K′ and TEX86 temperature proxies on the southern Italian shelf (SW Adriatic Sea, Gulf of Taranto). Earth Planet. Sci. Lett. 300, 112–124.

Lourens, L.J., Hilgen, F.J., Laskar, J., Shackleton, N.J., Wilson, D.S., 2004. The Neogene Period. In: F. M. Gradstein, J. G. Ogg, A. G. Smith (Eds.), A Geologic Time Scale 2004, Cambridge University Press, Cambridge, 409–440. https://doi.org/10.1017/CBO9780511536045

Madof, A.S., Bertoni, C., Lofi, J., 2019. Discovery of vast fluvial deposits provides evidence for drawdown during the late Miocene Messinian salinity crisis. Geology, 47, 171–174. https://doi.org/10.1130/G45873.1

Manzi, V., Gennari, R., Hilgen, F., Krijgsman, W., Lugli, S., Roveri, M., Sierro, F.J., 2013. Age refinement of the Messinian salinity crisis onset in the Mediterranean. Terra Nova 25, 315–322. https://doi.org/10.1111/ter.12038.

Mayser, J.P., Flecker, R., Marzzochi, A., Kouwvernhoven, T.J., Lunt, D.J., Pancost, R.D. 2017. Precession driven changes in terrestrial organic matter input to the Eastern Mediterranean

leading up to the Messinian Salinity Crisis. Earth Planetary Science Letters, 462, 199–211. https://doi.org/10.1016/j.epsl.2017.01.029

Mehta, S., Singh, A., Thirumalai, K., 2021. Uncertainty in paleosalinity estimates from foraminiferal geochemical records in the northern Indian Ocean. Palaeogeography, Palaeoclimatology, Palaeoecology, 569, 110326. https://doi.org/10.1016/j.palaeo.2021.110326

Meijer, P.T., 2012. Hydraulic theory of sea straits applied to the onset of the Messinian Salinity Crisis. Marine Geology, 326, 131–139. https://doi.org/10.1016/j.margeo.2012.09.001

Meulenkamp, J.E., Dermitzakis, M., Georgiadou-Dikeoulia, E., Jonkers, H.A., Böger, H., 1979. Field guide to the Neogene of Crete, University of Athens, Athens.

Miller, K.G., Mountain, G.S., Wright, J.D., Browning, J.V., 2011. A 180-million-year record of sea level and ice volume variations from continental margin and deep-sea isotopic records. Oceanography, 24(2), 40–53. https://doi.org/10.5670/oceanog.2011.26

Moissette, P., Cornée, J.-J., Antonarakou, A., Kontakiotis, G., Drinia, H., Koskeridou, E., Tsourou, T., Agiadi, K., Karakitsios, V., 2018. Palaeoenvironmental changes at the Tortonian/Messinian boundary: A deep-sea sedimentary record of the eastern Mediterranean Sea. Palaeogeography, Palaeoclimatology, Palaeoecology, 505, 217–233. https://doi.org/10.1016/j.palaeo.2018.05.046

Müller, P.J., Kirst, G., Ruhland, G., von Storch, I., Rosell-Melé, A., 1998. Calibration of the alkenone paleotemperature index $U_{37}^{K'}$ based on core-tops from the eastern South Atlantic and the global ocean (60°N–60°S). Geochimica et Cosmochimica Acta, 62, 1757–1772. https://doi.org/10.1016/S0016-7037(98)00097-0

Pellegrino, L., Dela Pierre, F., Natalicchio, M., Carnevale, G., 2018. The Messinian diatomite deposition in the Mediterranean region and its relationships to the global silica cycle. Earth Sci. Rev. 178, 154–176. https://doi.org/10.1016/j. earscirev.2018.01.018.

Pierre, C., 1999. The oxygen and carbon isotope distribution in the Mediterranean water masses. Marine Geology, 153, 41–55. https://doi.org/10.1016/S0025-3227(98)00090-5

Prahl, F.G., Wakeham, S.G., 1987. Calibration of unsaturation patterns in long-chain ketone compositions for paleotemperature assessment. Nature, 330(6146), 367–369. https://doi.org/10.1038/330367a0

Robertson, A.H.F., Parlak O., Ustaömer, T., 2012. Overview of the Palaeozoic–Neogene evolution of Neotethys in the Eastern Mediterranean region (Southern Turkey, Cyprus, Syria). Petroleum Geoscience, 18, 381–404. https://doi.org/10.1144/petgeo2011-091

Roger, S., Münch, P., Cornée, J.J., Saint-Martin, J.P., Fraud, G., Conesa, G., Pestrea, S., Ben Moussa, A., 2000. 40Ar/39Ar dating of the preevaporitic Messinian marine sequences of the Melilla basin (Morocco): a proposal for some bio-sedimentary events as isochrons around the Alboran Sea. Earth Planet. Sci. Lett. 179, 101–113.

Rohling, E.J., Marino, G., Grant, K.M., 2015. Mediterranean climate and oceanography, and the periodic development of anoxic events (sapropels). Earth-Science Reviews, 143, 62–97. https://doi.org/10.1016/j.earscirev.2015.01.008

Roveri, M., Flecker, R., Krijgsman, W., Lofi, J., Lugli, S., Manzi, V., Sierro, F.J., Bertini, A., Camerlenghi, A., De Lange, G., Govers, R., Hilgen, F.J., Hübscher, C., Meijer, P.T., Stoica, M., 2014. The Messinian Salinity Crisis: Past and future of a great challenge for marine sciences. Marine Geology, 352, 25–58. https://doi.org/10.1016/j.margeo.2014.02.002

Sabino, M., Schefuß, E., Natalicchio M., Dela Pierre, F., Birgel, D., Bortels, D., Schnetger, B., Peckmann, J., 2020. Climatic and hydrologic variability in the northern Mediterranean across the onset of the Messinian salinity crisis. Palaeogeography, Palaeoclimatology, Palaeoecology, 545, 109632. https://doi.org/10.1016/j.palaeo.2020.109632

Sabino, M., Birgel, D., Natalicchio, M., Dela Pierre, F., Peckmann, J., 2021. Carbon isotope excursions during the late Miocene recorded by lipids of marine Thaumarchaeota, Piedmont Basin, Mediterranean Sea. Geology 50 (1), 32–36. https://doi.org/10.1130/G49360.1.

Santarelli, A., Brinkhuis, H., Hilgen, F.J., Lourens, L.J., Versteegh, G.J.M., Visscher, H., 1998. Orbital signatures in a Late Miocene dinoflagellate record from Crete (Greece). Marine Micropaleontology, 33, 273–297. https://doi.org/10.1016/S0377-8398(97)00042-X

Schouten, S., Hopmans, E.C., Schefuss, E., Sinninghe Damsté, J.S., 2002. Distributional variations in marine crenarchaeotal membrane lipids: a new tool for reconstructing ancient sea water temperatures?. Earth and Planetary Science Letters, 204(1–2), 265–274. https://doi.org/10.1016/s0012-821x(02)00979-2

Schouten, S., Hopmans, E.C., Sinninghe Damsté, J.S., 2013. The organic geochemistry of glycerol dialkyl glycerol tetraether lipids: A review. Organic Geochemistry, 54, 19–61. https://doi.org/10.1016/j.orggeochem.2012.09.006

Schuster, M., Duringer, P., Ghienne, J.F., Vignaud, P., Mackaye, H.T., Likius, A., Brunet, M., 2006. The age of the Sahara Desert. Science, 311, 821–821. DOI: 10.1126/science.1120161

Seidenkrantz, M.-S., Kouwenhoven, T.J., Jorissen, F.J., Shackleton, N.J., van der Zwaan, G.J., 2000. Benthic foraminifera as indicators of changing Mediterranean–Atlantic water exchange in the late Miocene. Marine Geology, 163, 387–407. https://doi.org/10.1016/S0025-3227(99)00116-4

Siddall, M., Rohling, E.J., Almogi-Labin, A., Hemleben, Ch., Meischner, D., Schmelzer, I., Smeed, D.A., 2003. Sea-level fluctuations during the last glacial cycle. Nature 423(6942), 853–858. https://doi.org/10.1038/nature01690

Sierro, F.J., Hilgen, F.J., Krijgsman, W., Flores, J.A., 2001. The Abad composite (SE Spain): a Messinian reference section for the Mediterranean and the APTS. Palaeogeography, Palaeoclimatology, Palaeoecology, 168, 141–169. https://doi.org/10.1016/S0031-0182(00)00253-4

Sierro, F.J., Flores, J.A., Frances, G., Vazquez, A., Utrilla, R., Zamarreno, I., Erlenkeuser, H., Barcena, M. A., 2003. Orbitally-controlled oscillations in planktic communities and cyclic changes in western Mediterranean hydrography during the Messinian. Palaeogeography, Palaeoclimatology, Palaeoecology, 190, 289–316. https://doi.org/10.1016/S0031-0182(02)00611-9

Simon, D., Meijer, P., 2015. Dimensions of the Atlantic–Mediterranean connection that caused the Messinian Salinity Crisis. Marine Geology, 364, 53–64. https://doi.org/10.1016/j.margeo.2015.02.004

Simon, D., Marzocchi, A., Flecker, R., Lunt, D., Hilgen, F., Meijer, P., 2017. Quantifying the Mediterranean freshwater budget throughout the late salinity crisis. Earth and Planetary Science Letters, 472, 25–37. https://doi.org/10.1016/j.epsl.2017.05.013

Tzanova, A., Herbert, T.D., Peterson, L., 2015. Cooling Mediterranean Sea surface temperatures during the Late Miocene provide a climate context for evolutionary transitions in Africa

and Eurasia. Earth Planetary Science Letters, 419, 71–80. https://doi.org/10.1016/j.epsl.2015.03.016

Uno, K.T., Polissar, P.J., Jackson, K.E., deMenocal, P.B., 2016. Neogene biomarker record of vegetation change in eastern Africa. Proceedings of the National Academy of Sciences, 113(23), 6355–6363. https://doi.org/10.1073/pnas.1521267113

van Assen, E., Kuiper, K.F., Barhoun, N., Krijgsman, W., Sierro, F.J., 2006. Messinian astrochronology of the Melilla Basin: stepwise restriction of the Mediterranean–Atlantic connection through Morocco. Palaeogeography, Palaeoclimatology, Palaeoecology, 238, 15–31. https://doi.org/10.1016/j.palaeo.2006.03.014

van Hinsbergen, D.J.J., Meulenkamp, J.E., 2006. Neogene supradetachment basin development on Crete (Greece) during exhumation of the South Aegean core complex. Basin Research, 18, 103–124. https://doi.org/10.1111/j.1365-2117.2005.00282.x

Vasiliev, I., Mezger, E.M., Lugli, S., Reichart, G.J, Manzi, V., Roveri, M., 2017. How dry was the Mediterranean during the Messinian Salinity Crisis?. Palaeogeography, Palaeoclimatology, Palaeoecology, 471, 120–133. https://doi.org/10.1016/j.palaeo.2017.01.032

Vasiliev, I., Karakitsios, V., Bouloubassi, I., Agiadi, K., Kontakiotis, G., Antonarakou, A., Triantaphyllou, M., Gogou, A., Kafousia, N., de Rafélis, M., Zarkogiannis, S., Kaczmar, F., Parinos, C., Pasadakis, N., 2019. Large sea surface temperature, salinity, and productivity-preservation changes preceding the onset of the Messinian Salinity Crisis in the eastern Mediterranean Sea. Paleoceanography and Paleoclimatology, 34(2), 182–202. https://doi.org/10.1029/2018PA003438

Volkman, J.K., Barrett, S.M., Blackburn, S.I., Sikes, E.L., 1995. Alkenones in Gephyrocapsa oceanica: Implications for studies of paleoclimate. Geochimica et Cosmochimica Acta, 59(3), 513–520. https://doi.org/10.1016/0016-7037(95)00325-t

Williams, D.F., Bé, A.W.H., Fairbanks, R.G., 1981. Seasonal stable isotopic variations in living planktonic foraminifera from Bermuda plankton tows. Palaeogeogr. Palaeoclimatol. Palaeoecol. 33, 71–102.

Williams, M., Haywood, A.M., Taylor, S.P., Valdes, P.J., Sellwood, B.W., Hillenbrand, C.D., 2005. Evaluating the efficacy of planktonic foraminifer calcite delta O-18 data for sea

surface temperature reconstruction for the Late Miocene. Geobios, 38, 843–863. https://doi.org/10.1016/j.geobios.2004.12.001

Zachariasse, W.J., van Hinsbergen, D.J.J., Fortuin, A.R., 2011. Formation and fragmentation of a late Miocene supradetachment basin in central Crete: implications for exhumation mechanisms of high-pressure rocks in the Aegean forearc. Basin Research, 23, 678–701. https://doi.org/10.1111/j.1365-2117.2011.00507.x

Zachariasse, W.J., Lourens, L.J., 2021. The Messinian on Gavdos (Greece) and the status of currently used ages for the onset of the MSC and gypsum precipitation. Newsl. Stratigr. https://doi.org/10.1127/nos/2021/0677.

Zachariasse, W.J., Kontakiotis, G., Lourens, L.J., Antonarakou, A., 2021. The Messinian of Agios Myron (Crete, Greece): A key to better understanding diatomite formation on Gavdos (south of Crete). Palaeogeography, Palaeoclimatology, Palaeoecology, 581. https://doi.org/10.1016/j.palaeo.2021.110633

Zachos, J., Pagani, M., Sloan, L., Thomas, E., Billups, K., 2001. Trends, rhythms, and aberrations in global climate 65 Ma to present. Science, 292(5517), 686–693. doi: 10.1126/science.1059412

Chapter 7

Multiple crises preceded the Mediterranean Salinity Crisis: Aridification and vegetation changes revealed by biomarkers and stable isotopes

Geanina A. Butiseacă[1,2,3]*, Marcel T.J. van der Meer[4], George Kontakiotis[5], Konstantina Agiadi[6], Danae Thivaiou[5], Evangelia Besiou[5], Assimina Antonarakou[5], Andreas Mulch[1,2], Iuliana Vasiliev[1]

[1]*Senckenberg Biodiversity and Climate Research Centre (SBiK-F), Senckenberganlage 25, D-60325 Frankfurt am Main, Germany*

[2]*Institute of Geosciences, Goethe University Frankfurt, Altenhöferalle 1, 60438, Frankfurt am Main, Germany*

[3]*Eberhard Karls Universität Tübingen, Institute of Archaeological Sciences, Palaeoanthropology Department, Tübingen, Germany*

[4]*Royal Netherlands Institute for Sea Research, Department of Marine Microbiology and Biogeochemistry, P.O. Box 59, 1790 AB, Den Burg, Texel, The Netherlands*

[5]*Faculty of Geology and Geoenvironment, School of Earth Sciences, Department of Historical Geology-Paleontology, National and Kapodistrian University of Athens, Panepistimiopolis, Zografou, 15784, Athens, Greece*

[6]*Department of Palaeontology, University of Vienna, Josef-Holaubek-Platz 2, UZA II, 1090, Vienna, Austria*

*e-mail: butiseacageanina@gmail.com; https://orcid.org/0000-0002-1579-1998

This is a pre-copyedited, author-produced version, submitted for peer-review, of Butiseacă, G.A., van der Meer, M.T.J., Kontakiotis, G., Besiou, E., Agiadi, K., Antonarakou, A., Mulch, A., Vasiliev, I.. Aridification and vegetation changes revealed by biomarkers and stable isotopes. Global and Planetary Change, 217: 103951. https://doi.org/10.1016/j.gloplacha.2022.103951

7.1 Abstract

During the Messinian (7.24–5.33 Ma), the highly dynamic Mediterranean environment was concomitantly governed by global climate changes and regional tectonic activity affecting the connectivity to the global ocean. The combined effects generated extreme and rapid paleoenvironmental changes culminating in the Messinian Salinity Crisis (MSC; 5.96–5.33 Ma). Here, we reconstruct paleoenvironmental conditions recorded in the Agios Myron section (Crete Island, Greece) between ~7.2 and 6.5 Ma that indicate marked changes affecting the eastern Mediterranean region prior to the onset of the MSC. Hydrogen isotope ratios measured on alkenones produced by haptophyte algae within the Mediterranean water column, coupled to carbon isotopes measured on long chain n-alkanes produced by higher terrestrial plants show three important dry periods peaking at 6.98, 6.82 and 6.62 Ma accompanied by shifts in vegetation, transitioning from dominantly C_3 to markedly increased C_4 plants contribution and intermittent recurrence of C_3 vegetation at ~6.99 Ma and 6.78 Ma. Mean annual air temperatures reconstructed using branched glycerol dialkyl glycerol tetraethers (brGDGTs) average 13 °C with an overall pattern that permits orbitally-controlled pacing of the regional climate. Additionally, the branched and isoprenoid tetraether index and bulk carbon and oxygen isotope ratios indicate changes in the source(s) of organic matter and evolution of the basin towards a closed and arid system. These results support a model of ongoing restriction affecting the eastern Mediterranean Sea from ~7 Ma onwards and reveal a protracted aridisation of the Mediterranean domain prior to the onset of the MSC.

7.2 Introduction

The Mediterranean basin hosts some of the best-dated geological sections for the upper Miocene, many of them acting as reference sections for the geological time scale (e.g. Hilgen et al., 1999; 2000; Hüsing et al., 2009). The region has been investigated extensively using micropalaeontology, magnetostratigraphy and radiometric dating, resulting in precise astronomically-tuned sections (e.g. Hilgen et al., 1999; Krijgsman et al., 1999; 2002; Kouwenhoven et al., 2006; Drinia et al., 2007; Zachariasse et al., 2021). However, paleoclimate proxy data embedded within this tight temporal framework are still scarce (e.g. Tsanova et al., 2015; Mayser et al., 2017; Vasiliev et al., 2017; Kontakiotis et al., 2019) and usually focused on the late Messinian with a predominant emphasis on the Messinian Salinity Crisis (MSC; e.g.

Vasiliev et al., 2017; Natalicchio et al., 2017; Sabino et al., 2020). Recently, the Agios Myron section (Crete Island, Greece; Figure 7.1) was biostratigraphically dated and astronomically tuned (Zachariasse et al. 2021). Based on the resulting age model for the early Messinian (~7.2–6.5 Ma), a combined analysis of biomarkers and oxygen isotopes ($\delta^{18}O$) on planktonic foraminifera permitted the reconstruction of sea surface temperatures (SSTs) and associated salinities (SSSs) (Kontakiotis, Butiseacă et al., 2022). Consequently, in Agios Myron section, a series of events was identified defining the paleoenvironmental evolution of the eastern Mediterranean between ~7.2–6.5 Ma (Kontakiotis, Butiseacă et al., 2022): during an overall cooling phase 1 (7.2–6.9 Ma), freshening of Mediterranean surface waters (SSS = 38) coincided with the warmest temperatures (SST = 26 °C). Two distinct warm (SST = 29 °C) and hypersaline events (at 6.9–6.82 and 6.72 Ma with SSS = 47 to 48) characterized phase 2 (6.9–6.7 Ma). During phase 3 (6.7–6.5 Ma), increased climatic variability is reflected in a wide range of recorded temperature and salinity values (SST between 23–30 °C and SSS between 37−48).

Here, we build upon the available age model (Zachariasse et al., 2021) and the SST and SSS reconstructions (Kontakiotis, Butiseacă et al., 2022) and provide a comprehensive integration of marine and continental proxy records for the eastern Mediterranean. We achieve this by coupling the existing biomarker record to compound-specific hydrogen ($\delta^{2}H$) and carbon ($\delta^{13}C$) isotope data that collectively track a complex array of events and reflect the interplay between gateway restriction, basin isolation and orbital oscillations. We analyze changes in the hydrological budget of the Mediterranean basin through 1) $\delta^{2}H$ values from alkenones (produced by haptophyte algae within the Mediterranean Sea surface water), and 2) we track changes in the vegetation surrounding the basin using $\delta^{13}C$ values of *n*-alkanes (originating from higher terrestrial plants). We further reconstruct 3) mean annual air temperatures (MAT) and 4) paleo-soil pH based on branched glycerol dialkyl glycerol tetraethers (brGDGTs), biomarkers produced primarily by soil bacteria in the basin catchment. Additionally, we use the branched and isoprenoid tetraether (BIT) index 5) to detect changes in the source(s) of organic matter. The biomarker data are supplemented by 6) carbon ($\delta^{13}C$) and oxygen ($\delta^{18}O$) isotope ratios measured on bulk sedimentary rocks to monitor the long-term trends in paleoenvironmental conditions affecting the eastern Mediterranean basin. Our results indicate that, in the eastern Mediterranean, the crisis leading to the deposition of the km-thick evaporites in the Mediterranean during the MSC was initiated already during the early Messinian and reflects rather the cumulative effect of

successive highly evaporative events progressing in intensity throughout the Messinian, ultimately culminating with the MSC. These events are associated with large-scale aridification and fundamental changes in vegetation composition, a pattern earlier identified throughout the entire North Africa and the Middle East (e.g. Uno et al., 2016; Targhi et al., 2021; Böhme et al., 2021) and now recognized also in the sedimentary record of the eastern Mediterranean.

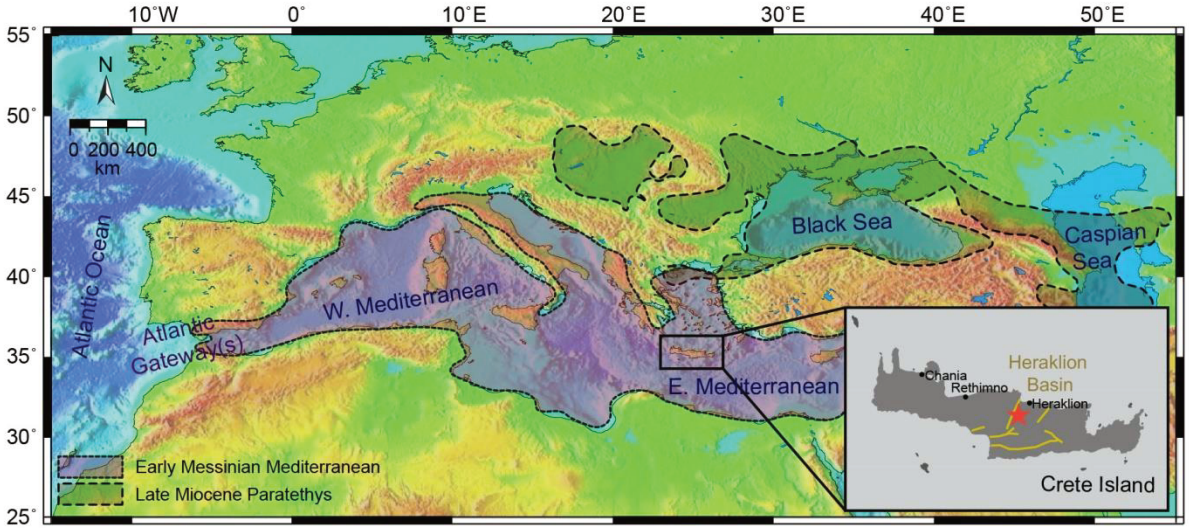

Figure 7.1 Map showing the location of Agios Myron section and Heraklion basin within the Mediterranean domain.

7.3 Chronostratigraphy

The ~25-m thick Agios Myron section (N 35°23′ 35.90", E 25°12′67.91") is located in the Heraklion basin (Crete Island, Greece; Fig. 7.1). The lowest seven meters of the section consist of silty marls without any visually identifiable evidence for cyclic deposition, while the overlying deposits (up to 25 m) show a clear cyclic alternation of blueish-grey homogeneous and brownish laminated marl couplets (the latter referred to here as sapropels) of various thicknesses (Figure 7.2). The sedimentary succession is rich in macrofauna, with bivalves being the most abundant (e.g. pycnodonts, cardiids, lucinids, veneriids, pectinids), followed by gastropods (e.g. buccinids), bryozoans, fish and occasionally plant remains mostly preserved in the upper part, where cyclic alternations of homogeneous and laminated marls are visible (Figure 7.2).

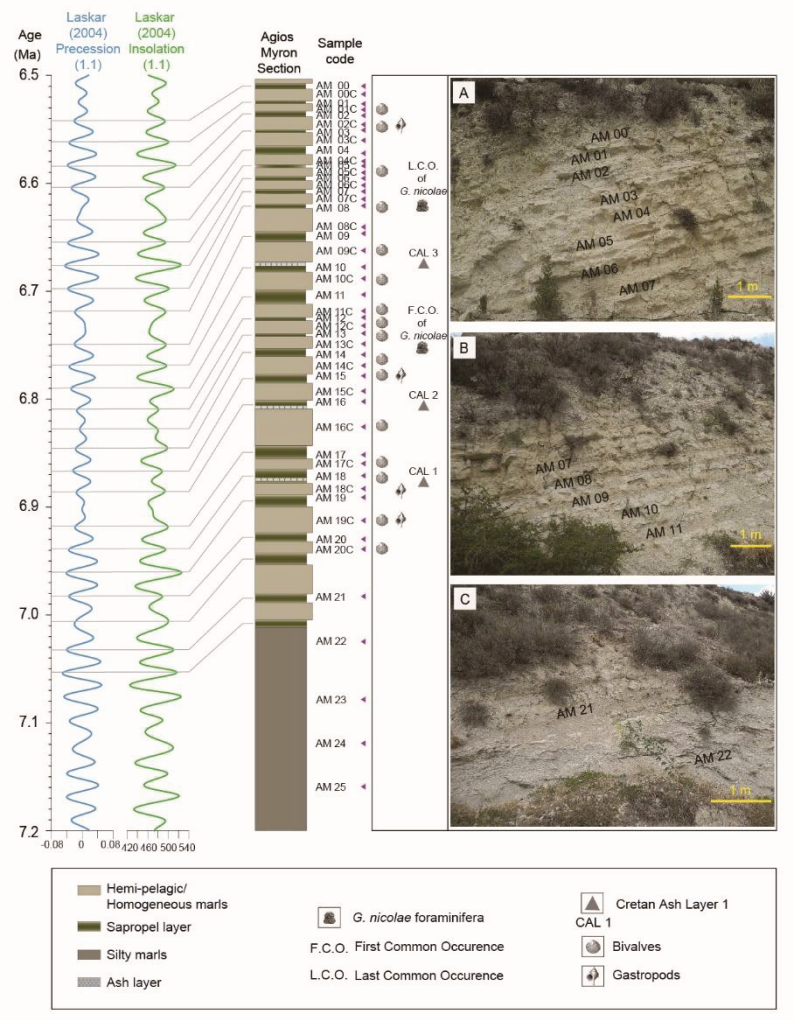

Figure 7.2 Correlation of Agios Myron section with the precession and isolation curves (Laskar, 2004). The stratigraphic log is bordered by sample names, identified planktonic foraminiferal bioevents, ash layers, as well as field pictures depicting the main lithology and cyclicity (A−C).

The present age model is based on the combination of astronomically calibrated planktonic foraminiferal bioevents, tephra layers (Cretan Ash Layers; CAL1–3; Figure 7.2) and the midpoints of the sapropels (Zachariasse et al., 2021). The astronomically tuned part of the Agios Myron section covers the 7.05−6.54 Ma time interval. The age control for the four lowermost samples is less well defined in the absence of biostratigraphic events and visible lithological cycles (Zachariasse et al., 2021). However, these four oldest samples were assigned to the earliest Messinian based on the continuous presence of *Globorotalia miotumida*, hence they are considered younger than 7.25 Ma and older than the first astronomically dated sample at 7.05 Ma (Kontakiotis, Butiseacă et al., 2022).

7.4. Material and methods

7.4.1. Lipid extraction, fraction separation and analysis

Forty-seven sedimentary rock samples were dried, weighed and ground using agate mortar and pestle. Lipids were extracted using Soxhlets with a mixture of dichloromethane (DCM) and methanol (MeOH) 7.5:1 (*v:v*) and pre-extracted cellulose thimbles. Extracts were evaporated to near dryness under N_2 flow using a TurboVap LV. Subsequently elemental sulphur was removed from the total lipid extracts (TLE) using Cu shreds. Cu was activated using 10% HCl, the acid was then removed and Cu was rinsed with demineralized water until neutral pH was achieved. The Cu was further cleaned using MeOH and DCM. The vials containing TLE, activated Cu and magnetic rods were placed on a rotary table for >16 hours. Afterwards, the TLEs were filtered over a Na_2SO_4 column to remove Cu fragments and water. The remaining solvents were evaporated using N_2. The desulphurization step was repeated until no reaction with the Cu was observed. 10% of the TLE was archived while the rest was further separated into fractions containing different lipids using Al_2O_3 column chromatography. The apolar fraction was eluted using a mixture of *n*-hexane and DCM (9:1, *v:v*), followed by a ketone fraction using DCM, while a mixture of DCM/MeOH (1:1, *v:v*) was used to obtain the polar fraction. The apolar fraction containing n-alkanes was purified using $AgNO_3$ column, eluting with n-hexane. The ketone fraction containing alkenones was also purified using $AgNO_3$ column by eluting with ethyl acetate. Both *n*-alkanes and alkenones were analyzed and identified based on mass spectra and retention time by Gas Chromatography-Mass Spectrometry (GC-MS) using a Thermo Scientific Trace GC Ultra machine at the Senckenberg Biodiversity and Climate Research Centre (SBiK-F) in Frankfurt am Main, Germany.

7.4.2 Compound specific stable isotopes analysis

7.4.2.1 δ^2H analysis on long chain alkenones (C_{37} and C_{38})

δ2H values of 21 samples were determined by GC/Thermal Conversion (TC)/ isotope ratio monitoring MS (irMS) using an Agilent GC coupled to a Thermo Electron DELTAPlus XL mass spectrometer at the Royal Netherlands Institute for Sea Research (NIOZ). The alkenone fraction was injected manually on-column on a RTX column of 60 m length, 0.32 mm diameter and 0.25 film thickness. The injection volume was 1.0−1.5 µl, with the TC reactor set at 1425 °C. The H3+ -factor was determined daily and was 6.0 ± 0.3 ppm mV-1. Samples were replicated

between one to four times depending on the available material, aiming for peaks of >1500 mV for compounds of interest. Hydrogen gas with a predetermined isotopic composition was used as monitoring gas and the isotope values were calibrated against in-house lab standard "Mix B" (A. Schimmelmann; Indiana University). A squalane standard was co-injected with every sample with an average value of −166 ± 0.3‰ over all injections. C_{37} alkenones were integrated as one single peak for obtaining the most accurate value possible.

7.4.2.2 $\delta^{13}C$ analysis on long chain (C_{29} and C_{31}) n-alkanes

$\delta^{13}C$ values of individual long chain n-alkanes (for 17 samples) were measured on the cleaned apolar fraction using a GC-irMS under similar conditions than the $\delta^{2}H$ measurements, but with a combustion interface rather than thermal conversion. The $\delta^{13}C$ values (expressed relative to V-PDB) were calculated by comparison to a CO_2 reference gas (calibrated against NBS-19). Standard deviations were determined using a co-injected standard and are ± 0.3‰.

7.4.3 HPLC analysis

7.4.3.1 Preparation and analysis.

The polar fraction containing GDGTs was dried under a gentle stream of N_2 then dissolved in a 1-ml mixture of *n*-hexane (*n*-hex)/isopropanol (IPA)-(99:1, *v:v*), slightly dispersed using an ultrasonic bath (up to 30 s per sample) and filtered over a 0.45 mm PTFE filter using a 1 ml syringe. Polar compounds were measured at the Senckenberg-BiK-F laboratory using an HPLC Shimadzu, UFLC performance, Alltech Prevail© Cyano 3 mm, 150−2.1 mm analytical column; eluents *n*-hex (A) and IPA (B) coupled with an ABSciex 3200 QTrap chemical ionization mass spectrometer (HPLC/APCIeMS). We used an injection volume of 5 ml for each sample and GDGTs detection was achieved through single ion monitoring (scanned masses: 1018, 1020, 1022, 1032, 1034, 1036, 1046, 1048, 1050, 1292, 1296, 1298, 1300, 1302). Both isoprenoid and branched GDGTs were analyzed within a single acquisition run for each sample. Quantification was performed using the Analyst software and the peaks were integrated manually for each sample multiple times.

7.4.3.2 Mean annual temperature calculation (MAT) and paleo soil pH

Estimates of continental MAT are based on the relative distribution of brGDGT membrane lipids. The distribution of brGDGTs, expressed as the Methylation index of Branched Tetraethers (MBT) and the Cyclisation ratio of Branched Tetraethers (CBT), displays a significant linear correlation with modern MAT in the range of −6 to 27 °C (Weijers et al., 2007). For MAT and soil pH calculation, we used the Peterse et al. (2012) calibration, where:

$$MAT' = 0.81 - 5.67 \times CBT + 31 \times MBT'$$

$$pH = 7.90 - 1.97 \times CBT$$

MBT' and CBT are expressed as:

MBT'= [(GDGT Ia + GDGT Ib + GDGT Ic)] / [(GDGT Ia + GDGT Ib + GDGT Ic) + (GDGT IIa + GDGT IIb + GDGT IIIb) + (GDGT IIIa)]

and

CBT= −log (GDGT Ib + GDGT IIb) / (GDGT Ia + GDGT IIa)

where GDGT I − GDGT III are branched GDGTs.

7.4.3.3 BIT Index

The BIT (Branched and Isoprenoid Tetraethers) index defines the terrigenous versus aquatic components of organic input into the basin (marine or lacustrine). The BIT index is the ratio of the three major brGDGTs (mostly terrigenous) to isoGDGT Crenarchaeol (aquatic) (Hopmans et al., 2004):

BIT= [(GDGT-I) + (GDGT-II) + (GDGT-III)] / [(crenarchaeol) + (GDGT-I) + (GDGT-II) + (GDGT-III)]

Crenarchaeol is a compound derived from Thaumarchaeota (Sinninghe Damste et al., 2002), accounting for ~20% of the picoplankton in the ocean, although in subordinate abundance it can also occur in soils (Weijers et al., 2007). BrGDGTs occur in high abundances in terrestrial settings, including soils and peats (Hopmans et al., 2004; Peterse et al., 2012). BIT values close to 1 indicate a predominantly terrigenous source, while low values (close to 0) indicate a strong aquatic source of the organic matter (Schouten et al., 2013).

7.4.4. $\delta^{13}C$ and $\delta^{18}O$ analysis on bulk sedimentary rocks

Samples were dried and drilled with a manual precision drill at the SBiK-F laboratory after being tested with HCl 10% for carbonate presence. The obtained sample powder was weighed and placed into exetainer vials. Isotopic ratios were analyzed at the Goethe University−Senckenberg BiK-F Stable Isotope Facility using a Thermo Scientific MAT 253 mass spectrometer and a Thermo Scientific GasBench II in continuous flow mode, following the protocol of Spötl & Vennemann (2003). All samples were calibrated and measured against standard reference materials (Carrara marble, NBS 18 and Merck). Isotopic values were calculated against a CO_2 reference gas with a precision of 0.06‰ for $\delta^{13}C$ and 0.08‰ for $\delta^{18}O$, respectively. All values are presented with respect to Vienna Pee Dee Belemnite (VPDB).

7.5. Results

7.5.1. Compound specific stable isotopes on biomarkers

7.5.1.1. δ^2H on long chain alkenones

Alkenones are intermittently present in the section between 7.12 and 6.59 Ma (Figure 7.3E). The δ^2H values of C_{37} alkenones (δ^2H_{C37}) vary between −199 and −155‰ (Figure 7.3E; Appendix 3, Table 1), with an average value of −179‰. Between 7.12 and 7.03 Ma, measured δ^2H_{C37} values vary between –183‰ and –178‰ with an average of –181‰ followed by a first maximum of –155‰ at 6.99−6.98 Ma. Subsequently, δ^2H_{C37} values decrease markedly to –187‰ (at 6.97 Ma). Between 6.97 and 6.83 Ma δ^2H_{C37} remains relatively low except for a short positive excursion at 6.86 Ma (–176‰). At 6.82 Ma, δ^2H_{C37} values increase sharply to –159‰, then decrease progressively until 6.78 Ma to attain an overall minimum of –199‰. At 6.77 Ma, there is another short positive (ca. 30‰) excursion in the δ^2H_{C37} values. Between 6.76−6.65 Ma, δ^2H_{C37} decreases with a mean value of –189‰, after which values increase again up to –157‰ at 6.60 Ma. The interval between 6.87−6.76 Ma registers the largest variability in the section (ca. 40‰). The δ^2H values of C_{38} alkenones (δ^2H_{C38}) follow a similar trend with slightly lower absolute values (Appendix 3, Table 7.1). Samples AM 22 (7.05 Ma) and AM 01C (6.58 Ma) have much higher relative contributions of C_{38} alkenones, therefore we could only measure δ^2H_{C38}.

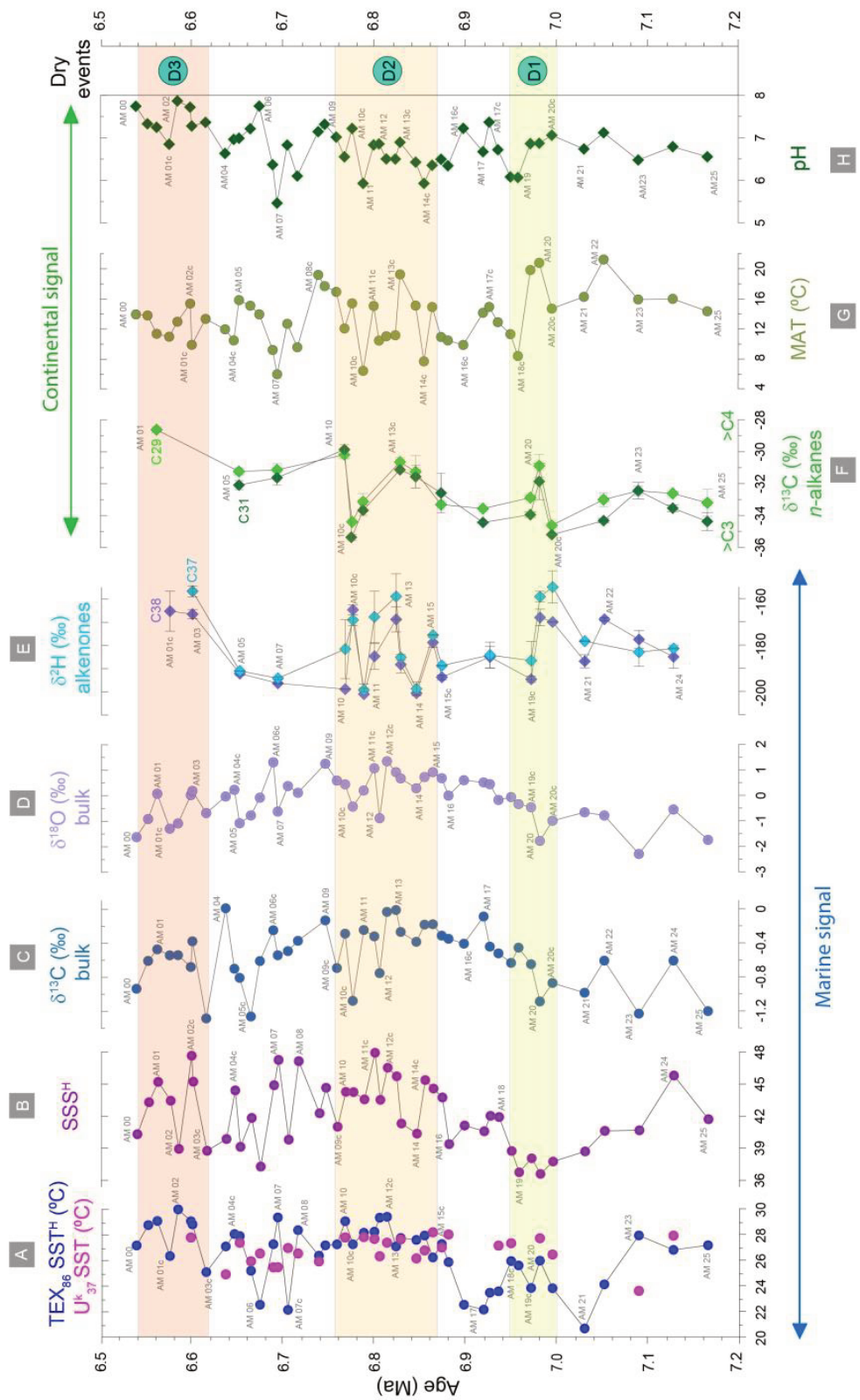

(capture next page)

Figure 7.3 Summarized results indicating marine and continental signal inferred by a series of proxies: A) TEX_{86} and U^{K}_{37} SST sea surface temperature (SST^{H} and U^{K}_{37}; Kontakiotis, Butiseacă et al., 2022) B) Sea surface salinity (SSS^{H}, Kontakiotis, Butiseacă et al., 2022); C) $\delta^{13}C$ on bulk sediments; D) $\delta^{18}O$ on bulk sediments; E) $\delta^{2}H$ on alkenones; F) $\delta^{13}C$ on *n*-alkanes; G) Mean annual temperature (MAT); H) Paleo soil pH derived from GDGTs analysis. Error bars are based on the standard deviation of a series of replicate analyses and indicate standard errors of the means. S1−S3 indicates the main restriction events observed in the section. With blue arrow are indicated the marine proxies, while with green the continental ones. $>C_3$, $>C_4$ in G panel indicates the vegetation type.

7.5.1.2 $\delta^{13}C$ on long chain n-alkanes

The $\delta^{13}C$ values of C_{29} *n*-alkanes ($\delta^{13}C_{C29}$) vary between –34.6‰ and –28.6‰ (Figure 7.3F; Appendix 3, Table 7.2), with an average of –32.2‰. Up section, from 7.16 Ma, $\delta^{13}C_{C29}$ values decrease until 6.99 Ma, attaining the minimum value of –34.6‰. We observe a positive excursion at 6.98 Ma to –30.9‰. $\delta^{13}C_{C29}$ values remain relatively low at (avg.) –34.6‰ and reach another maximum of −30.6‰ at 6.83Ma. At 6.78 Ma a brief sharp drop of 2‰ is recorded. Between 6.76 and 6.56 Ma the $\delta^{13}C_{C29}$ remain high and reach a third maximum of –28.6 ‰ at 6.56 Ma. Values of $\delta^{13}C_{C29}$ and $\delta^{13}C_{C31}$ generally co-vary throughout the section (Appendix 3, Table 7.2).

7.5.2. MAT estimates based on brGDGTs

Measured MAT values range from 6 °C to 21 °C (Figure 7.3G; Appendix 3, Table 7.3) with a mean value of 13.4 °C. From ~7.2 Ma to 7.05 Ma MAT values increases gradually (from 14 °C to 21 °C) to reach the overall maximum in the section. From 7.05 to 6.7 Ma, MAT follows an overall cooling trend (from 21 °C to 6 °C), then gently increases to ca. 14 °C until the end of the section.

7.5.3. Soil pH estimates based on brGDGTs

Paleo-soil pH values in the Agios Myron section increase in a stepwise manner, with values ranging between 5.5 and 7.9 (Figure 7.3H; Appendix 3, Table 7.3) and presenting an average value of 6.8. Between 7.16–6.97 Ma the pH is rather constant (~6.8). From 6.95–6.74 Ma its amplitude is increasing, with a variability of 1.4 around an average value of 7.0 with the largest internal variability in the section between 6.72−6.54 Ma.

7.5.4 BIT Index

The Agios Myron BIT indices are highly variable (Figure 7.4A; Appendix 3, Table 7.3) ranging between ~0.26 to ~0.88, indicating input of organic matter from variable sources. From 7.16 to 6.88 Ma, BIT values are higher, ranging between ~0.52 and ~0.86, with a mean value of 0.72. Between 6.87 and 6.80 Ma, BIT values decrease, reaching the lowest of 0.26−0.38. Overall, in this time interval, values are ranging between 0.26 and 0.62, with a mean value of 0.46. From 6.80 Ma until the end of the section at 6.54 Ma, BIT values increase again from ca. 0.59 to 0.88.

The BIT index values vary with lithology, with homogeneous marls generally exhibiting lower values than laminated marls, except couplets AM 18−AM 18C (6.95−6.93 Ma), AM 17−AM 17C (6.93−6.92 Ma), AM 14−AM 14C (6.85−6.84 Ma), AM 11−AM 11C (6.80−6.79 Ma), AM 10−AM 10C (6.77−6.76 Ma) and AM 07−AM 07C (6.70−6.69 Ma) (Figure 7.4).

7.5.5. Carbon and oxygen isotopes of bulk sediments

The $\delta^{13}C$ record of bulk sedimentary rock material ($\delta^{13}C_{bulk}$) ranges from –1.29‰ to −0.01‰ with an overall average of –0.56‰ (Figure 7.3C; Appendix 3). Between 7.16 and 6.98 Ma, $\delta^{13}C_{bulk}$ values display a rather large variability (–1.23‰ to –0.61‰, average –0.94‰). From 6.97 to 6.82 Ma, $\delta^{13}C_{bulk}$ values display a positive trend from ca –0.65‰ to –0.01‰ (average value of –0.33‰). Between 6.81–6.54 Ma, the $\delta^{13}C_{bulk}$ values show increased variability. The mean value for this interval is –0.59‰, with a minimum of –1.29‰ and a maximum value of 0.01‰, the highest in the entire section. Overall, the $\delta^{13}C_{bulk}$ data show an increasing trend in the lower part of the section up to ~6.8 Ma, followed by a decreasing trend until the end of the record, at 6.54 Ma.

The $\delta^{18}O_{bulk}$ record has a mean value of –0.15‰ and co-varies with $\delta^{13}C_{bulk}$ (Figure 3D; Appendix 3, Table 7.4). From the base of the section to 6.98 Ma, $\delta^{18}O$ values show an increasing trend and a large variability with values between –2.30‰ and –0.55‰. Between 6.97 and 6.82 Ma, values are increasing up to 0.91‰, most of them being positive. Values have a smaller variability (1.80‰), with an average value of 0.40‰. In the upper part of the section (6.81–6.54 Ma), the isotopic values follow an overall decreasing trend, but with a larger amplitude. Values for this interval vary between –1.64 and 1.30‰, with an average value of –0.16‰.

7.6. Discussion

During the late Miocene, hydrological conditions in the Mediterranean basin were strongly influenced by the interplay between tectonics promoting gateway restriction and global climate change (e.g. Manzi et al., 2013; Hilgen et al., 2007). Tectonically controlled changes in the basin configuration, and ultimately in marine connections (Flecker et al., 2015), led to changes in water circulation patterns, atmospheric circulation and ultimately vegetation and fauna. The initiation of the northern hemisphere glaciation enhanced the climatic changes during the latest Miocene, contributing to a stepwise aridification (Herbert et al., 2016).

7.6.1 Early Messinian climate: installation of drier conditions at 7.0 Ma

The Mediterranean climate conditions during the Messinian share similarities with the present day (e.g. Kontakiotis et al., 2019), with dry and hot summers and wet winters (Rohling et al., 2015) and a strong influence of westerlies (Quan et al., 2014). A change in atmospheric circulation patterns from trade winds to westerlies (Quan et al., 2014) during the Tortonian (11.61−7.25 Ma), may have induced weakening of the Asian and African monsoons, and thus a reduction in precipitation amount and an increase in aridity. The expansion of aridity in the Mediterranean area during the late Miocene was also enhanced by changes in circulation patterns in the North Atlantic (Eronen et al., 2012) and Atlantic moisture distribution (Bosmans et al., 2020) as a consequence of restriction of the Betic and Rifian corridors and closure of paratethyan gateways (Pérez-Asensio et al., 2012; Ng et al., 2021 a, b).

Our δ^2H_{C37} data show a +23‰ shift (from 7.03 to 7.00 Ma) in the Agios Myron section, suggesting the onset of an evaporative period at ca. 7 Ma associated with a cooling of 7 °C in the marine domain, peaking at 7.03 Ma, when the SST^H data attain a minimum of 20.7 °C (Kontakiotis, Butiseacă et. al., 2022). This dry and cold interval recorded at Agios Myron coincides with the first aridification episodes of the Sahara, when eolian dunes appear in the Chad Basin indicating recurrent desert conditions also starting at ca. 7 Ma (Schuster et al., 2006).

7.6.2 Hydrological changes in the eastern Mediterranean: Protracted basin isolation between 7.0 and 6.6 Ma

The δ^2H_{C37} data from Agios Myron reach a value of −155‰, 30‰ higher than the highest value of −185‰ recorded in the eastern Mediterranean basin (during the glacial-interglacial

transition at ~120 ka; van der Meer et al., 2007). We interpret these high δ^2H_{C37} values as an expression of enhanced evaporation affecting the Mediterranean basin. Considering that present-day marine δ^2H_{C37} values are typically below −180‰ (e.g. in the Sargasso Sea at 31° N; Englebrecht and Sachs, 2005), we propose a strongly negative water balance for the Mediterranean Basin, where water loss by evaporation must have outpaced precipitation and river runoff from the basin catchment. Similarly high δ^2H_{C37} values have been reported in regions affected by basin-wide massive evaporation e.g. during the latest phase of the MSC (Vasiliev et al., 2017) or during recurrent droughts affecting the Paratethys-Black Sea region during the late Miocene (Vasiliev et al., 2013, 2015, 2020; Butiseacă et al., 2021). The large (44‰) variation in δ^2H_{C37} values from Agios Myron (Figure 7.3E) indicates severe hydrological changes within the Mediterranean Basin between 7.0 and 6.6 Ma, as δ^2H_{C37} values depend mainly on the δ^2H of the water and salinity (Schouten et al., 2005).

Three marked periods characterized by high δ^2H_{C37} values (up to−155‰; Figure 7.3E), occur within the Agios Myron section that we interpret to reflect dryer conditions (D1-D3 intervals in Figure 7.3). In between these three intervals, δ^2H_{C37} drops to values as low as −199‰, similar to those recorded in present-day open marine environments (Englebrecht and Sachs, 2005; Weiss et al., 2019). The first interval with high δ^2H_{C37} (D1; δ^2H_{37} = −155‰, centred at ~6.98 Ma; Figure 7.3) coincides with relatively high SST (26 °C), reduced SSS (~38; Kontakiotis, Butiseacă et al., 2022) and a minor decrease (ca. 0.22‰ and 0.79‰, respectively) in isotopic values to $\delta^{13}C_{bulk}$ = −1.09‰ and $\delta^{18}O_{bulk}$ = −1.79‰ (Figure 7.3C, D). At the same time, the $\delta^{13}C_{n\text{-alkane}}$ values (Figure 7.3F) record a positive shift of ~5‰, consistent with a higher C_4 plant contribution ($\delta^{13}C_{29}$ of −30.9‰), reflecting generally drier conditions concomitant with an increase in MAT values (Figure 7.3G). Collectively, these proxy data point to a dry phase (i.e. high δ^2H_{37} and high $\delta^{13}C_{n\text{-alkanes}}$) associated with warm conditions (high SST and MAT) at 6.98 Ma. Reduced salinity in the Mediterranean basin during this interval is consistent with a rather efficient water exchange via the Atlantic gateway(s) and inflow from the Atlantic Ocean outpacing the net evaporative loss, in agreement with the initiation and strengthening of Mediterranean outflow during that time (Ng et al., 2021b).

The second time interval characterized by high δ^2H_{C37} values is centered at 6.82 Ma (D2 with δ^2H_{37} reaching −157‰; Figure 7.3E). It is associated with high SST^H (29 °C) and high SSS values (~48). The essential difference between the first (D1) and this second (D2) period is that

salinity values are very high during D2. During D2, $\delta^{13}C_{n\text{-alkanes}}$ values are high up to 6.83 Ma and towards the termination of D2 (ca. −31 to −32‰) but drop to as low as −34.4‰ at ca. 6.77 Ma D2 pointing to continental carbon input with a higher C_4 contribution at the beginning and end of D2. All continental proxy data (MAT, $\delta^{13}C_{n\text{-alkanes}}$, pH; Figure 7.3) show large variability during D2 similar to the $\delta^{2}H_{37alkenones}$ and $\delta^{13}C_{bulk}$ and $\delta^{18}O_{bulk}$ values, suggesting that this time interval may be characterized by a series of consecutive smaller events (peaking at ~6.78, 6.83 and 6.86 Ma). We propose that this variability within the basin reflects the efficiency of the Atlantic gateway(s), where the basin restriction alternated with increased Atlantic input during sea-level high-stands associated with warm phases. This finding is further supported by parallel evidence of Messinian gateways restriction, with no evidence of Atlantic connection after 6.9 Ma (Krijgsman et al., 2018). Increasing isolation of the Mediterranean due to tectonics and/or eustacy may have led to increased water residence times, which in combination with basin-wide warming resulted in the slow-down of the thermohaline circulation and the enhancement of water column stratification (Kontakiotis, Butiseacă et al., 2022). The recorded changes from the continental proxies show however a shift towards more C_4 vegetation during a generally continental cooling trend (Figures 7.3, 7.4), suggesting a decoupling between the marine and continental domains.

The beginning of a third dry period (D3) is recorded at 6.62 Ma ($\delta^{2}H_{37}$ = −157‰ in Figure 7.3E), this time with high variability in both SST and SSS values. The termination of D3 is, however, not properly constrained by our data, because the section ends at 6.54 Ma. Importantly, the high $\delta^{2}H_{C37alkenones}$ values are accompanied by high $\delta^{13}C_{n\text{-alkanes}}$ values (−28.6‰; Figure 7.3F), suggesting that a highly evaporative Mediterranean basin coincided with increased C_4 plant contribution in the catchment during D3.

Contrary to the first major evaporitic phase (D1), which took place when salinity was lowest (~38), D2 and D3 are associated with high(er) salinity (~48) and very warm surface waters. Just before the first dry phase (D1), SST values reach a minimum in the section (~20 °C), while the MAT starts to decrease (from 21 to 16 °C), representing probably an expression of the global Messinian cooling event (Figure 7.3).

During D2 and D3, our collective data indicate that evaporative conditions in the eastern Mediterranean were associated with warmer surface waters and shifts in vegetation towards more C_4 contribution in the basin catchment (Figure 7.3A, F). This relative increase in evaporation

could have been the result of 1) a general warming in the circum-Mediterranean area, 2) a reduced connectivity to the Atlantic Ocean or 3) a more local change in bathymetry (i.e. in Heraklion basin). Interestingly, the MAT (Figure 7.3G) data indicate an overall cooling trend, suggesting a decoupling from the generally warm marine domain during D2–D3. A global increase in temperature would be expected to generate uniform warming both in the terrestrial and marine domains. This decoupling could be the result of enhanced water column stratification, which is supported by evidence of Messinian gateway restrictions (Krijgsman et al., 2018; Bulian et. al, 2021). Additionally, it is enhanced by tectonically-controlled changes in the Heraklion basin, where intermittent shallowing/isolation of the basin generates a warmer water column when the water surface is reduced. Alongside the general Mediterranean restriction, Zachariasse et al. (2021) identified a change in the bathymetry at Agios Myron location between ~6.78 and 6.6 Ma, from a deeper (~ −500 m) to a shallower (~ −100 m) setting during D2–D3 (Zachariasse et al., 2021). Comparing our results with this bathymetric curve (Figure 7.4), we observe that almost all evaporative episodes correlate with positive changes in the basin topography, indicating a local tectonic overprint.

A restricted basin system during the deposition of Agios Myron is also supported by the positive covariance between $\delta^{13}C_{bulk}$ and $\delta^{18}O_{bulk}$ data as well as their absolute values (e.g. Leng and Marshall, 2004; Meijers et al., 2020) (Appendix 3, Table 7.4, Supplementary figure). Agios Myron $\delta^{13}C_{bulk}$ and $\delta^{18}O_{bulk}$ data suggest a more restricted, increasingly evaporative system for the upper part of the section, most probably due to its position within the small Heraklion basin. As $\delta^{13}C$ bulk values additionally reflect changes in productivity (Li and Ku, 1997), the increase in $\delta^{13}C_{bulk}$ could be indicative of an increase in basin productivity, while the increase in $\delta^{18}O_{bulk}$ points to increased evaporation and consequently increasing salinity. The increased $\delta^{13}C_{bulk}$ and $\delta^{18}O_{bulk}$ values associated with increased SSS values could also be associated with increasingly stagnating bottom waters in the entire eastern Mediterranean after 6.7 Ma (Blanc-Valleron et al., 2002; Kouwenhoven et al., 2006).

7.6.3 Alkenone production and organic matter sources

The exact alkenone producers for the Agios Myron section are not known, thus we refer to the closest documentation of abundances of coccolithophorids (i.e. alkenone producers) from the time-equivalent record (Pissouri, Cyprus; Kouwenhoven et al., 2006). Similarly to Pissouri, we

infer that the best candidates as alkenone producers could have been *Coccolithus pelagicus*, "normal sized" reticulofenestrids, *Helicosphaera carteri* and *Umbilicosphaera* spp.. In the Pissouri section, *Coccolithus pelagicus* appears in small percentages until 6.6 Ma, and only rarely reported afterward. Large sized reticulofenestrids are more abundant until 6.8 Ma, when the highest SSS values are recorded in Agios Myron, while the small sized ones become dominant after 6.8 Ma (Kouwenhoven et al., 2006), when the SSS record in Agios Myron indicates a decrease in salinity, albeit with a large variability (Figure 7.3B). Importantly, the largest amplitude in δ^2H_{C37} (of 44‰), centered at 6.82 Ma in Agios Myron, occurs while there is no apparent major change in the assemblage of potential alkenone producers at Pissouri. This observation supports the idea that the changes in our δ^2H_{C37} record are determined by changes in the δ^2H of the Mediterranean water (i.e. evaporation/precipitation) and not by changes in the alkenone producer assemblage.

Major algal blooms (including alkenone producers) are correlated with eutrophication, elemental and nutrients enrichment taking place when increased sediment supply occurs in the basin. The occurrence of alkenones in Agios Myron is limited to the ~7.0−6.6 Ma interval, with no alkenones detected from 6.66 Ma up the top of the section (Figure 7.3A, E). The presence of alkenones is discontinuous, pointing to changes in nutrient supplies, productive species or alkenone preservation. Based on the changes in foraminiferal populations more eutrophic conditions are inferred after 6.72 Ma in both the Metochia and Agios Myron sections (Zachariase et al., 2021). For instance, a nutrient enrichment of subsurface waters through a better developed deep chlorophyll maximum was observed, which led to an explosion of *Globigerina bulloides* group and neogloboquadriniids. Seasonal nutrient inputs could have originated also in the newly formed Saharan dunes, with winter storms bringing dust over the eastern Mediterranean (Lourens et al., 2001) as terrestrial input from North Africa is confirmed at ~7.1 Ma further to the north, in central Greece (Böhme et al., 2017).

The BIT index shows an important change in the source of organic matter at 6.87 Ma (Figure 7.4A; Appendix 3, Table 7.3). Between 7.16 to 6.88 Ma and 6.80 to 6.54 Ma, mean BIT values of 0.73 indicate a more terrigenous/soil source of organic matter that contrast BIT indices of 0.46, indicating an dominantly aquatic production for the interval between 6.87 and 6.80 Ma. This observation is consistent with results from Crete (Ploutis section) and Zakynthos (Kalamaki

section) indicating a mixed origin of the organic matter during the Late Miocene (Kontakiotis et al., 2020, 2021).

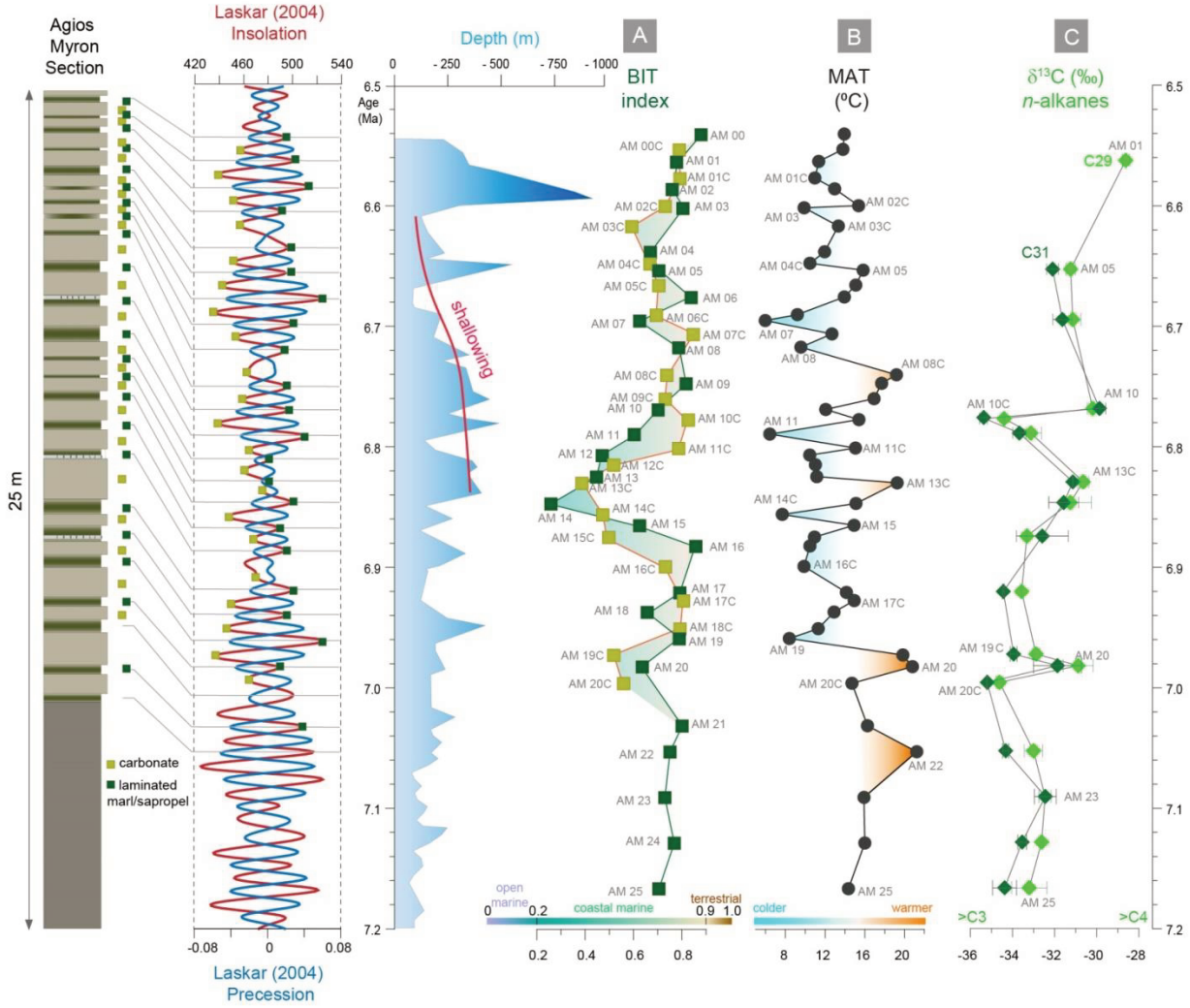

Figure 7.4 Stratigraphic log correlated with orbital parameters: precession, isolation, obliquity and excentricity and summarized proxies indicating an orbital control over the Agios Myron sediments: A) BIT Index; B) Mean annual temperature; C) $\delta^{13}C$ on *n*-alkanes. The yellow squares indicate the carbonate layers, while the green ones the laminated marls/sapropels.

The Nile and the Saharan rivers may have served as the main east Mediterranean suppliers of clastic sediments during Tortonian-Messinian (Gladstone et al., 2007), with additional contributions from mainland Greece (Karakitsios et al., 2017), western Anatolia, and the proto-Crete islands due to their proximity and position within the Aegean-Mediterranean domain.

The 6.87−6.80 Ma interval is also associated with increased SSTs, SSSs and higher δ^2H_{C37} values, with low BIT values centered at ~ 6.85 Ma. The low BIT values could indicate that the increasingly dry climate had starved the basin in terrestrial sediment and organic matter input and the BIT registers only the local (marine) organic matter production. Low BIT values correspond to increases in $\delta^{13}C_{n\text{-alkanes}}$ and δ^2H_{C37} because low precipitation leads to low riverine discharge of sediment and organic compounds from land. Another explanation would be a change in elevation or distance from terrestrial source as the Heraklion basin was forming at the time (Fassoulas, 2001). This could have resulted in more riverine/terrigenous input when the basin was in a higher tectonic position/closer to land and more marine/aquatic organic matter production when the basin was deeper (i.e. more available accommodation space). When compared to the reconstructed bathymetry (Zachariasse et al., 2021), we observe that low BIT values (~0.2) from 6.84 correlate with a deepening of ~260 m. It is therefore possible that the terrigenous organic matter input and in-situ production in the basin were affected by the development of the Heraklion basin.

7.6.4 Vegetation changes in the Eastern Mediterranean between 7.2–6.5 Ma: the emergence of C_4 ecosystems

The $\delta^{13}C_{n\text{-alkane}}$ values of plant waxes reflect the contribution of the main vegetation types, with values of ca. –33‰ for C_3 plants (e.g. trees and shrubs) and –21.7‰ for C_4 plants (e.g. grasses, succulents, halophytes) (O'Leary, 1988; Kohn, 2010). The average –30.3‰ value of $\delta^{13}C_{29\ n\text{-alkanes}}$ in the Agios Myron record indicates input from a C_3-dominated ecosystem, with an overall increasing C_4 contribution towards the top of the section (Figure 7.4F; Appendix 3, Table 2). We observe two major positive shifts in $\delta^{13}C$ of similar amplitude (~5‰): at 6.99–6.98 Ma (from –33.2 to –28.5‰) and at 6.77–6.76 Ma (from –32.9 to –28.4‰). These two shifts appear at times of marked warming (MAT increase; Figure 7.3G) and increased evaporation (higher $\delta^2H_{alkenones}$; Figure 7.3E). A third shift seems to occur at 6.56 Ma, as suggested by the AM 01 sample (−28.6‰). However, with only one available data point we cannot asses the complete event.

The first positive shift in $\delta^{13}C_{n\text{-alkanes}}$ at 6.99–6.98 Ma is accompanied by increasing SST, MAT, $\delta^2H_{alkenones}$ (i.e. dryer conditions), higher $\delta^{13}C_{bulk}$ and $\delta^{18}O_{bulk}$, lower pH and low SSS, while the second shift in $\delta^{13}C_{n\text{-alkanes}}$ at 6.77–6.76 Ma is accompanied by an overall decrease in SST and SSS, a pronounced negative excursion in $\delta^2H_{alkenones}$, and increased values of MAT,

$\delta^{13}C_{bulk}$ and $\delta^{18}O_{bulk}$. While the MAT, $\delta^{13}C_{bulk}$ and $\delta^{18}O_{bulk}$ values have the same trend in both events, $\delta^{2}H_{alkenones}$, SST and SSS have opposite trends. The 6.99–6.98 Ma shift in $\delta^{13}C_{n\text{-alkanes}}$ occurs during warm and dryer conditions, while the 6.77–6.76 Ma shift takes place in a wetter period, with lower temperatures on land suggesting different climatic mechanisms. Our data here indicate that overall the continental domain underwent changes in vegetation towards more C_4 contribution over decreasing temperatures.

The large-scale fossil vegetation records support the presence of a mixed flora around the Mediterranean during the early Messinian, dominated by trees (e.g. Velitzelos et al., 2014; Zidianakis et al., 2007; Ioakim and Koufos, 2009), but with an increasing presence of open land vegetation (grasses and sedges) (e.g. Ioakim et al., 2005). Increasing presence of xerophytic elements in the area during the Messinian is documented through pollen (Ioakim et al., 2005; Böhme et al., 2017), attesting the presence of Compositae, Graminae and Amaranthaceae families (including Chenopodiaceae), vegetation characteristic to open and dry environments.

The $\delta^{13}C_{n\text{-alkanes}}$ data presented here offers a first isotope-based reporting of changes towards plants adapted to drier habitats appearing already at ~7 Ma in the Mediterranean region. Similar $\delta^{13}C_{n\text{-alkanes}}$ data from the younger (~6.5 to 5.9 Ma) Cyprus (Mayser et al., 2017) and north Italy (~6.1-5.9 Ma; Sabino et al., 2020) successions follow the expected decrease in C_3 contribution in the benefit of the better adapted C_4 plants for the rest of the Messinian (Figure 7.5) as more C_4 vegetation adapted to more arid conditions covered the entire Sahara-Mediterranean-Middle East area for that time (Uno et al., 2016; Böhme et al., 2021).

The 5‰ positive shifts of $\delta^{13}C_{n\text{-alkanes}}$ from Agios Myron section point towards a pronounced physiological response of plants in terms of water intake and environmental stress in general, as a consequence of the new climatic conditions (i.e. a colder and drier northern hemisphere), over imposed by tectonic control (i.e. Atlantic-Mediterranean gateway restriction).

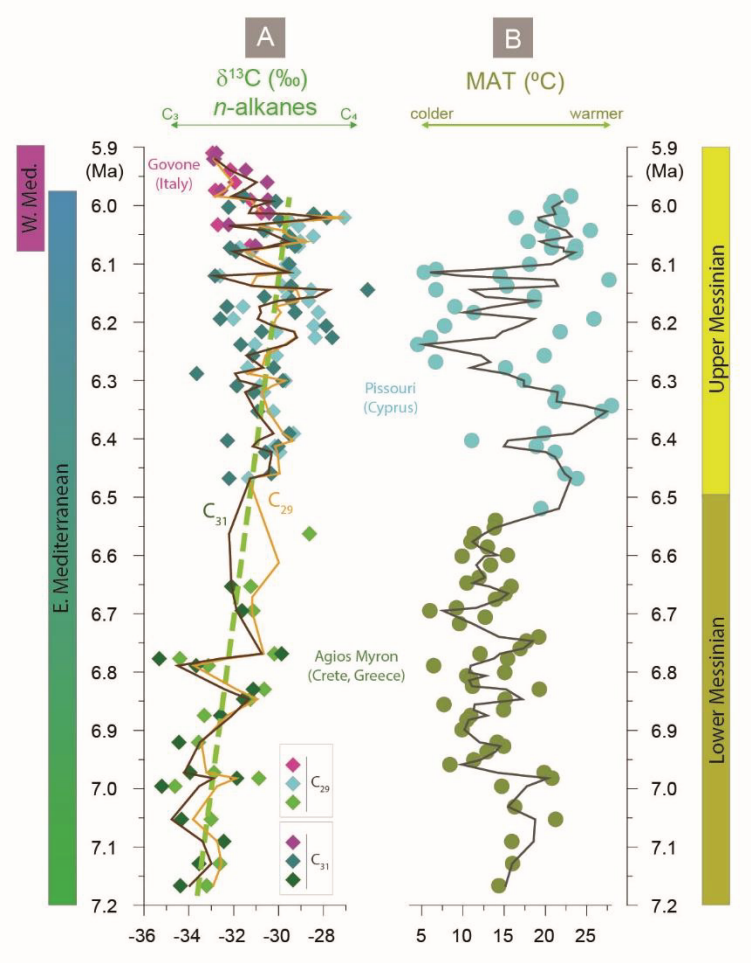

Figure 7.5 $\delta^{13}C_{n\text{-alkanes}}$ and MAT Messinian Mediterranean records (Govone, Sabino et al., 2020; Pissouri, Mayser et al., 2017; Agios Myron, this study).

7.6.5. The eastern Mediterranean in the Messinian climatic context

The Agios Myron section (~7.2−6.5 Ma) covers the early Messinian stage and documents a series of precursor events of the MSC. Our data point to a protracted restriction and aridity history of the eastern Mediterranean that was marked by transient periods of episodic dry conditions and accompanying shifts in vegetation in the basin catchment. Although the entire Mediterranean Basin was subjected to restriction as a consequence of the altered Atlantic gateways (e.g. Flecker et al., 2015), Agios Myron is also influenced by the development of the Heraklion basin, which shallows considerably between ~6.85−6.6 Ma Zachariase et al., 2021). A similar complex overlap between a global/regional (i.e. northern hemisphere glaciation; Atlantic-Mediterranean gateway restrictions) and local signals in marginal basins was also identified in the western Mediterranean Basin (e.g. Bulian et al., 2022).

Agios Myron currently provides the only early Messinian MAT record in the Mediterranean (Figure 7.6; Appendix 3, Table 7.5). Air temperatures vary widely between 6 and 21°C similar to the late Messinian (~6.5−5.9 Ma) Pissouri record (Mayser et al., 2017), where MAT cover a range of 5 °C to 28 °C. Pre- and early Messinian sites of the Paratethys in Russia, Serbia and Bulgaria provide an average MAT value of 14−17°C based on branched GDGTs, pollen and leaf physiology, respectively (Vasiliev et al., 2019; Butiseacă et al., 2021; Ivanov et al., 2002; Utesher et al., 2007), while pollen analysis from the Southern Rifian Corridor (Morocco) (Targhi et al., 2021) indicates MATs of 20−24 °C. Late Messinian MATs from Bulgaria and the Black Sea range between 6 °C and 25 °C with an average of ~16 °C (Ivanov et al., 2021; Vasiliev et al., 2020). Collectively, these data document a remarkable similarity of MAT values between the Mediterranean and Paratethys regions for the Messinian stage.

Overall, biomarker data from Agios Myron (Crete) suggest a decoupling between the marine and continental domains after ~7 Ma, with increased temperatures and salinities offshore and an overall cooling on land (in the catchment of the Mediterranean Basin), probably as a consequence of both tectonics and an orbitally paced climate, as suggested for other sections around the Mediterranean (e.g. Bulian et al., 2022). This development paralleled an increase in C_4 vegetation similar to the observations from the Pissouri section (Cyprus) for the ~6.5−5.9 Ma time interval (Mayser et al. 2017). When compared to the Agios Myron $\delta^{13}C_{C29n\text{-alkanes}}$ data, the $\delta^{13}C_{C29n\text{-alkanes}}$ values from Pissouri indicate an even higher C_4 contribution (–32.6‰ to –27.1‰) indicating that the expansion of C_4 vegetation continued throughout the Messinian stage in the eastern Mediterranean (Figure 7.5). This change in vegetation observed in Agios Myron is associated with a larger-scale aridity induced by global cooling and changes in precipitation patterns (i.e. weakening of the African monsoon, Zhang et al., 2014) and may also be the direct response to intense aridification of the north African continent including the development of the Sahara desert (Schuster et al., 2006), Arabia (Böhme et al., 2021) and Paratethys domain (Vasiliev et al., 2020; Butiseacă et al., 2021), that started ~2 Myr earlier.

The drastic late Miocene changes in vegetation and landscapes led to the reshaping of the European continent and the creation of land bridges. These not only favoured the migration of plants but also of new faunal elements now occupying free ecological niches (Koufos et al., 2005). The same environment facilitated the evolution of primates and appearance of early hominines at ~7.2 Ma (Böhme et al., 2017), indicating that the terrestrial ecosystems adapted

easier to the new climatic conditions (i.e. colder and dryer) and their biodiversity was less negatively impacted in comparison to their marine counterparts.

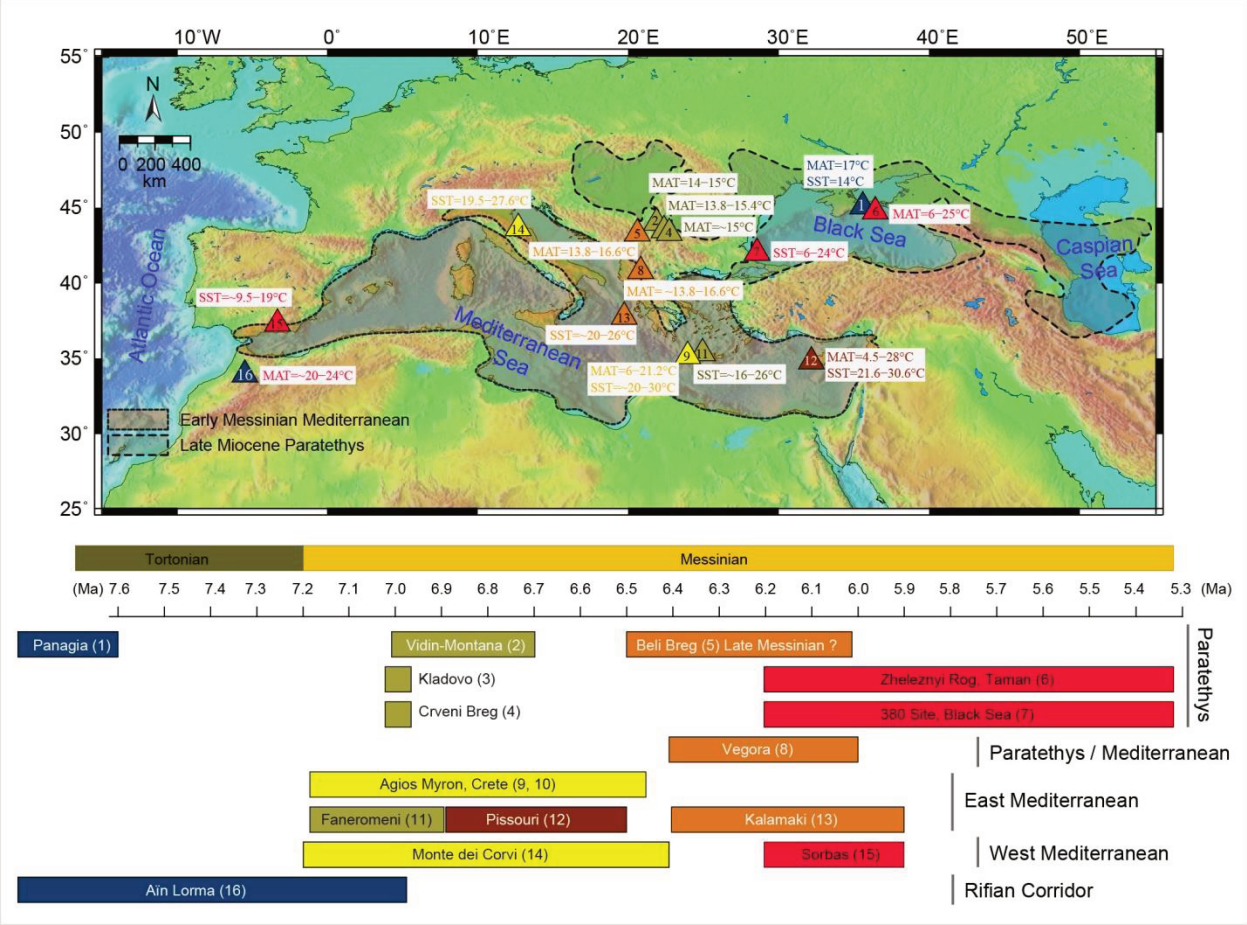

Figure 7.6 Map showing the distribution of temperature during Messinian: 1. Taman, Panagia (Russia); 2. Vidin-Montana (Bulgaria); 3. Kladovo (Serbia); 4. Crveni Breg (Serbia); 5. Beli Breg (Bulgaria); 6. Taman, Zheleznyi Rog (Russia); 7. 380 Site (Black Sea); 8. Vegora (N. Greece); 9−10 Agios Myron (Crete, Greece); 11. Faneromeni (E. Crete, Greece); 12. Pissouri (Cyprus); 13. Kalamaki (Zakinthos, Greece); 14. Monte dei Corvi (Italy); 15. Sorbas (Spain); 16. Aïn Lorma (Morocco). Basemap modified after Vasiliev et al. (2017). Details are presented in Appendix 3, Table 7.5. The lower bars are indicating the time lengths of each section. With colors are indicated sections of similar age.

7.7 Conclusions

Our integrated biomarker and isotope data from Crete (Greece) support a series of significant environmental changes in the eastern Mediterranean Basin between ~7.2 and 6.5 Ma, confirming increased restriction of the eastern Mediterranean during the early Messinian.

$\delta^2H_{C37\ alkenones}$ values indicate two periods with highly evaporative conditions peaking at 6.98 and 6.82 Ma (up to −155‰) and the beginning of a third one at 6.62 Ma (−157‰), associated with increasing SSTs and SSSs that remain high after 6.88 Ma. The highly evaporative intervals are associated with shifts in vegetation. $\delta^{13}C_{C29 n\text{-alkanes}}$ indicate important increases in C_4 contribution, between 6.99–6.98 Ma, 6.77–6.76 Ma and from 6.56 Ma, coupled with an overall increasing C_4 vegetation trend during the entire early Messinian, supporting a change in vegetation in the eastern Mediterranean catchment. If during the first $\delta^{13}C_{n\text{-alkanes}}$ shift the marine and continental signals are indicating similar environmental conditions (drier, more C_4 vegetation), proxies behave differently by the time of the second shift (different $\delta^2H_{alkenones,}$ SSTs and SSSs), supporting a decoupling of the marine environment from the continental influence. BIT index values also indicate important changes in the organic matter source between ~6.8−6.6 Ma, suggesting a more terrigenous source which could be translated into a shallowing of the basin under tectonic control. A shallowing of the basin in this time interval and its evolution towards a more enclosed system is also supported by $\delta^{13}C$ and $\delta^{18}O$ data on bulk.

Collectively, the Agios Myron data confirm the presence of restricted conditions in the eastern Mediterranean since the early Messinian and reveal an ongoing isolation and aridification of the Mediterranean domain, both under tectonic (acting mostly over the local accommodation space and regional basin connection) and global climate influence (with great impact over moisture and vegetation).

7.8 Acknowledgements

We thank Ulrich Treffert for help in the organic geochemistry laboratory and Jens Fiebig for support in the Goethe University-Senckenberg BiK-F Stable Isotope Facility. This research was financed by the Greek-German collaboration project (IKYDA-DAAD): "Quantification of the environmental changes in the Eastern Mediterranean at the onset of the Messinian Salinity Crisis (Crete-Greece)" (QUANTMES) of IV and VK. Collaboration was made possible through the COST Action CA15103 “Uncovering the Mediterranean salt giant” (MEDSALT) supported by COST (European Cooperation in Science and Technology). Analyses were supported by the DFG grant number 398614017 of IV. GAB transmits special thanks to Ronald van Bommel, Monique Verweij and Jort Ossebaar from NIOZ for help in the stable isotope laboratory.

References

Blanc-Valleron, M.-M., Pierre, C., Caulet, J.P., Caruso, A., Rouchy, J.-M., Cespuglio, G., Sprovieri, R., Pestrea, S., Di Stefano, E., 2002. Sedimentary, stable isotope and micropaleontological records of paleoceanographic change in the Messinian Tripoli Formation (Sicily, Italy). Palaeogeogr. Palaeoclimatol. Palaeoecol., 185, 255–286. https://doi.org/10.1016/S0031-0182(02)00302-4

Bouchal, J.M., Güner, T.H., Velitzelos, D., Velitzelos, E., Denk, T., 2020. Messinian vegetation and climate of the intermontane Florina–Ptolemais–Servia Basin, NW Greece inferred from palaeobotanical data: how well do plant fossils reflect past environments? Royal Society Open Science 7: 192067. http://dx.doi.org/10.1098/rsos.192067

Butiseacă, G.A., Vasiliev, I., van der Meer, M.T.J., Krijgsman, W., Palcu, D.V., Feurdean, A., Niedermeyer, E.M., Mulch., A., 2021. Severe late Miocene droughts affected Eurasia. Global and Planetary Change, 206, 103644 https://doi.org/10.1016/j.gloplacha.2021.103644.

Böhme, M., Spassov, N., Ebner, M., Geraads, D., Hristova, L., Kirscher, U., Kötter, S., Linnemann, U., Prieto, J., Roussiakis, S., Theodorou, G., Uhlig, G., Winklhofer, M., 2017. Messinian age and savannah environment of the possible hominin *Graecopithecus* from Europe. PLOS ONE 12(5): e0177347. https://doi.org/10.1371/journal.pone.0177347

Böhme, M., Spasov, N., Majidifard, M.R., Gärtner, A., Kirscher, U., Marks, M., Dietzel, C., Uhlig, G., El Atfy, H., Begun, D.R., Winklhofer, M., 2021. Neogene hyperaridity in Arabia drove the direction of mammalian dispersal between Africa and Eurasia. Nature Communications Earth & Environment, 2 (85). https://doi.org/10.1038/s43247-021-00158-y

Bosmans, J.H.C., van der Ent, R.J., Haarsma, R.J., Drijfhout, S.S., Hilgen, F.J., 2020. Precession and obliquity induced changes in moisture sources for enhanced precipitation over the Mediterranean Sea. Paleoceanography and Paleoclimatology, 35 (1). https://doi.org/10.1029/2019PA003655

Drinia, H., Antonarakou, A., Tsaparas, N., Kontakiotis, G., 2007. Palaeoenvironmental conditions preceding the Messinian Salinity Crisis: A case study from Gavdos Island. Geobios, 40, 251–265.

Englebrecht, A.C., Sachs J.P., 2005. Determination of sediment provenance at drift sites using hydrogen isotopes and unsaturation ratios in alkenones. Geochim. Cosmochim. Acta, 69, 4253−4265. https:/doi.org/10.1016/j.gca.2005.04.011

Eronen, J.T., Fortelius, M., Micheels, A., Portmann, F.T., Puolamäki, K., Janis, C.M., 2012. Neogene aridification of the Northern Hemisphere. Geology 40:823-826https://doi.org/10.1130/G33147.1

Fassoulas, C., 2001. The tectonic development of a Neogene basin at the leading edge of the active European margin: the Heraklion basin, Crete, Greece. Journal of Geodynamics, 31, 49-70. https://doi.org/10.1016/S0264-3707(00)00017-X

Flecker, R., Krijgsman, W., Capella, W., de Castro, M.C., Dmitrieva, E., Mayser, J.P., Marzocchi, A., Modestu, S., Ochoa, D., Simon, D., Tulbure, M., van den Berg, B., van der Schee, M., de Lange, G., Ellam, R., Govers, R., Gutjahr, M.,,Hilgen F., Kouwenhoven, T., Lofi, J., Meijer, P., Sierro, J.F., Bachiri, N., Barhoun, N., Alami A.C., Chacon, B., Flores, J.A., Gregory, J., Howard, J., Lunt, D., Ochoa, M., Pancost, R., Vincent, S., Yousfi, M.Z., 2015. Evolution of the late Miocene Mediterranean-Atlantic gateways and their impact on regional and global environmental change. Earth-Science Reviews, 150, 365−392. https://doi.org/10.1016/j.earscirev.2015.08.007

Gladstone, R., Flecker, R., Valdes, P.J., Lunt, D., Markwick, P., 2007. The Mediterranean hydrologic budget from a Late Miocene global climate simulation. Palaeogeography, Palaeoclimatology and Palaeoecology, 251, 254–267. https://doi.org/10.1016/j.palaeo.2007.03.050

Hilgen, F.J., Krijgsman, W., 1999. Cyclostratigraphy and astrochronology of the Tripoli diatomite Formation (pre-evaporite Messinian, Sicily, Italy). Terra Nova, 11, 16–22. https://doi.org/10.1046/j.1365-3121.1999.00221.x

Hilgen, F.J., Iaccarino, S., Krijgsman, W., Villa, G., Langereis, C.G.,Zachariasse, W.J. 2000. The global boundary stratotype section and point (GSSP) of the Messinian stage 841 (uppermost Miocene). Episodes, 23, 172–178. 842 https://doi.org/10.18814/epiiugs/2000/v23i3/004

Hilgen, F., Kuiper, K., Krijgsman, W., Snel, E., van der Laan, E., 2007. Astronomical tuning as the basis for high resolution chronostratigraphy: the intricate history of the Messinian Salinity Crisis Stratigraphy, 4 (2–3) 231−238.

Hopmans, E.C., Weijers, J.W.H., Schefuss, E., Herfort, L., Sinninghe Damsté, J.S., Schouten, S., 2004. A novel proxy for terrestrial organic matter in sediments based on branched and isoprenoid tetraether lipids. Earth and Planetary Science Letters, 224, 107–116. https://doi.org/ 10.1016/j.epsl.2004.05.012

Hüsing, S. K., Kuiper, K. F., Link, W., Hilgen, F. J., Krijgsman, W., 2009. The upper Tortonian–lower Messinian at Monte dei Corvi (Northern Apennines, Italy): Completing a Mediterranean reference section for the Tortonian Stage. Earth and Planetary Science Letters, 282 (1–4), 140–157. https://doi.org/10.1016/j.epsl.2009.03.010

Ioakim, C., Rondoyanni, T., Mettos, A., 2005. The Miocene Basins of Greece (Eastern Mediterranean) from a palaeoclimatic perspective. Revue de Paléobiologie, 24, 2.

Ioakim, C., Koufos, G.D., 2009. The late Miocene mammal faunas of the Mytilinii Basin, Samos Island, Greece: new collection. 3. Palynology. In: Koufos, G.D., Nagel, D. (Eds.), The Late Miocene Mammal Faunas of Samos. Beiträge zur Paläontologie, 31, 27–35.

Ivanov., D.A., Ashraf, A.R., Mosbrugger, V., Palmarev, E., 2002. Miocene microflora and paleoclimate reconstructions from three sites in Bulgaria. Pangaea. https://doi.org/10.1594/PANGAEA.596352

Ivanov, D., Utescher, T., Djorgova, N., Bozukov, V., Ashraf, A.R., 2020. The late Miocene Beli Breg Basin (Bulgaria): paleoecology and climate reconstructions based on pollen data. Paleobiodiversity and Palaeoenvironments 101, 79−102. https://doi.org/10.1007/s12549-020-00475-8

Karakitsios, V., Cornée, J.-J., Tsourou, T., Moissette, P., Kontakiotis, G., Agiadi, K., Manoutsoglou, E., Triantaphyllou, M., Koskeridou, E., Drinia, H., Roussos, D., 2017. Messinian salinity crisis record under strong freshwater input in marginal, intermediate, and deep environments: The case of the North Aegean. Palaeogeogr., Palaeoclimatol., Palaeoecol., 485, 316–335, https://doi.org/10.1016/j.palaeo.2017.06.023.

Kim, J.H., van der Meer, J., Schouten, S., Helmke, P., Willmott, V., Sangiorgi, F., Koç, N., Hopmans E.C., Sinnighe Damsté, J.S., 2010. New indices and calibrations derived from the distribution of crenarchaeal isoprenoid tetraether lipids: Implications for past sea surface temperature reconstructions. Geochimica Et Cosmochimica Acta, 74(16). https://doi.org/10.1016/j.gca.2010.05.027

Krijgsman, W., Hilgen, F.J., Raffi, I., Sierro, F.J., Wilson, D.S., 1999. Chronology, causes and progression of the Messinian salinity crisis. Nature, 400, 652−655. https://doi.org/10.1038/23231

Krijgsman, W., 2002. The Mediterranean: Mare Nostrum of earth sciences. Earth and Planetary Science Letters 205, 1–12.

Krijgsman, W., Capella, W., Simon., D., Hilgen, F.J., Kouwenhoven, T.J., Meijer, P.T., Sierro, F.J., Tulbure., M.A., van der Berg, B.C.J., van der Schee, M., Flecker, R., 2018. The Gibraltar Corridor: Watergate of the Messinian Salinity Crisis. Marine Geology 403, 238–246. https://doi.org/10.1016/j.margeo.2018.06.008

Kohn, M.J., 2010. Carbon isotope compositions of terrestrial C_3 plants as indicators of (paleo)ecology and (paleo)climate. Proceedings of the National Academy of Sciences of the United States of America 107, 19691–19695. https://doi.org/10.1073/pnas.1004933107

Kontakiotis, G., Besiou, E., Antonarakou, A., Zarkogiannis, S.D., Kostis, A., Mortyn, P.G., Moisette, P., Cornée, J.-J., Schulbert, C., Drinia, H., Anastasakis, G., Karakitsios, V., 2019. Decoding sea surface and paleoclimate conditions in the eastern Mediterranean over the Tortonian-Messinian Transition. Palaeogeography, Palaeoclimatology, Palaeoecology, 534. https://doi.org/10.1016/j.palaeo.2019.109312

Kontakiotis, G., Karakitsios, V., Cornée, J.-J., Moissette, P., Zarkogiannis, S.D., Pasadakis, N., Koskeridou, E., Manoutsoglou, E., Drinia, H., Antonarakou, A., 2020. Preliminary results based on geochemical sedimentary constraints on the hydrocarbon potential and depositional environment of a Messinian sub-salt mixed siliciclastic-carbonate succession onshore Crete (Plouti section, eastern Mediterranean). Med. Geosc. Rev. 2, 247–265. https://doi.org/10.1007/s42990-020-00033-6

Kontakiotis, G., Karakitsios, V., Maravelis, A.G., Zarkogiannis, S.D., Agiadi, K., Antonarakou, A., Pasadakis, N., Zelilidis, A., 2021. Integrated isotopic and organic geochemical constraints on the depositional controls and source rock quality of the Neogene Kalamaki sedimentary successions (Zakynthos Island, Ionian Sea). Med. Geosc. Rev. 3, 193–217. https://doi.org/10.1007/s42990-020-00045-2.

Kontakiotis, G., Butiseacă, G.-A., Karakitsios, V., Antonarakou, A., Zarkogiannis, S., Agiadi, K., Krsnik, E., Besiou, E., Zachariasse, J.-W., Lourens, L., Thivaiou, D., Koskeridou, E.,

Moissette, P., Mulch, A., Vasiliev., I., 2022. Hypersalinity accompanies tectonic restriction in the eastern Mediterranean prior to the Messinian Salinity Crisis. Palaeogeography, Palaeoclimatology, Palaeoecology 592(2):110903. https://doi.org/10.1016/j.palaeo.2022.110903

Koufos, G.D., Kostopoulos, D., Vlachou, T.D., 2005. Neogene/Quaternary mammalian migrations in Eastern Mediterranean. Belgian Journal of Zoology, 135 (2), 181−190.

Kouwenhoven, T.J., Morigi, C., Negri, A., Giunta, S., Krijgsman, W., Rouchy, J.M., 2006. Paleoenvironmental evolution of the eastern Mediterranean during the Messinian: Constraints from integrated microfossil data of the Pissouri Basin (Cyprus). Marine Micropaleontology 60, 17−44. https://doi.org/10.1016/j.marmicro.2006.02.005

Laskar, J., Robutel, P., Joutel, F., Gastineau, M., Correia, A.C.M., & Levrard, B. 2004. A long-term numerical solution for the insolation quantities of the Earth. Astronomy & Astrophysics, 428, 261–285. https://doi.org/10.1051/0004-6361:20041335.

Leng, M.J., and Marshall, J.D., 2004, Palaeoclimate interpretation of stable isotope data from lake sediment archives. Quaternary Science Reviews, 23, 811–831. https://doi .org/10.1016/j.quascirev.2003.06.012

Li, H.-C., and Ku, T.-L., 1997, $\delta^{13}C$–$\delta^{18}C$ covariance as a paleo hydrological indicator for closed-basin lakes. Palaeogeography, Palaeoclimatology, Palaeoecology, 133, 69–80. https:// doi.org/10.1016/S0031-0182(96)00153-8

Lourens, L.J., Wehausen, R., Brumsack, H.J., 2001. Geological constraints on tidal dissipation and dynamical ellipticity of the Earth over the past three million years. Nature 409, 1029 – 1033. https://doi.org/10.1038/35059062

Mancini, A.M., Gennari, R., Ziveri, P., Mortyn, P.G., Stolwijk, D.J., Lozar, F., 2020. Calcareous nannofossil and foraminiferal trace element records in the Sorbas Basin: A new piece of the Messinian Salinity Crisis onset puzzle. Palaeogeography, Palaeoclimatology, Palaeoecology 554. https://doi.org/10.1016/j.palaeo.2020.109796

Manzi, V., Gennari, R., Hilgen, F., Krijgsman, W., Lugli, S., Roveri, M., Sierro, F.J., 2013. Age refinement of the Messinian salinity crisis onset in the Mediterranean.Terra Nova, 25 (4) 315 – 322. https://doi.org/10.1111/ter.12038

Mayser, J.P., Flecker, R., Marzocchi, A., Kouwenhoven, T., Lunt, D., Pancost, R., 2017. Precession driven changes in terrestrial organic matter input to the Eastern Mediterranean

leading up to the Messinian Salinity Crisis. Earth and Planetary Science Letters, 462, 199-211. https://doi.org/10.1016/j.epsl.2017.01.029

Meijers, M.J.M., Brocard, G.Y., Whitney, D.L., Mulch, A., 2020. Paleoenvironmental conditions and drainage evolution of the Central Anatolian lake system (Turkey) during late Miocene to Pliocene surface uplift. GEOSPHERE, 16 (2), 490-509. https://doi.org/10.1130/GES02135.1

Müller, P.J., Kirst, G., Ruhland, G., von Storch, I., Rosell-Mele, A., 1998. Calibration of the alkenone paleotemperature index U-37(K') based on core-tops from the eastern South Atlantic and the global ocean (60˚N–60˚S). Geochim. Cosmochim. Acta, 62, 1757–1772.

Natalicchio, M., Birgel, D., Peckman, J., Carnevale, G., Liu, X., Hinrichs, K.-U., Dela Pierre, F., 2017. An archaeal biomarker record of paleoenvironmental change across the onset of the Messinian salinity crisis in the absence of evaporites (Piedmont Basin, Italy). Organic Geochemistry 113, 242−253.

https://doi.org/10.1016/j.orggeochem.2017.08.014

Ng, Z.L., Hernández-Molina, F.J., Duarte, D., Sierro, F.J., Ledesma, S., Rogerson, M., Llave, E., Roque, C., Manar, M.A., 2021a. Latest Miocene restriction of the Mediterranean Outflow Water: a perspective from the Gulf of Cádiz. Geo-Marine Letters 41 (23). https://doi.org/10.1007/s00367-021-00693-9

Ng, Z.L., Hernández-Molina, F.J., Duarte, D., Sierro, F.J., Roque, C., Manar, M.A., 2021b. Late Miocene contourite depositional system of the Gulf of Cádiz: The sedimentary signature of the paleo-Mediterranean Outflow Water. Marine Geology 442. https://doi.org/10.1016/j.margeo.2021.106605

O'Leary, M.H., 1988. Carbon Isotopes in Photosynthesis. BioScience 38, 328–336. http://doi.org/10.2307/1310735

Pérez-Asensio, J.N., Aguirre, J., Schmiedl, G., Civis, J., 2012. Impact of restriction of the Atlantic-Mediterranean gateway on the Mediterranean Outflow Water and eastern Atlantic circulation during the Messinian. Paleoceanograpgy 27 (3). https://doi.org/10.1029/2012PA002309

Peterse, F., van der Meer, J., Schouten, S., Weijers, J.W.H., Fierer, N., Jacckson, R.B., Kim, J.-H., Sinninghe Damsté, J.S., 2012. Revised calibration of the MBT-CBT paleotemperature

proxy based on branched tetraether membrane lipids in surface soils. Geochimica et Cosmochimica Acta, 96:215–229. https://doi.org/10.1016/j.gca.2012.08.011

Quan, C., Liu, Y.-S., Tang, H., Utescher, T., 2014. Miocene schift of European atmospheric circulation from trade wind to westerlies. Scientific Reports 4, 5660. https://doi.org/10.1038/srep05660

Rohling, E.J., Marino, G., Grant, K.M., 2015. Mediterranean climate and oceanography, and the periodic developments of anoxic events (sapropels). Earth-Science Reviews, 143, 62−97. https://doi.org/10.1016/j.earscirev.2015.01.008

Roussiakis, S., Filis, P., Sklavounou, S., Giaourtsakis, I., Kargopoulos, N., Theodorou, G., 2019. Pikermi: a classical European fossil mammal geotope in the spotlight. European Geologist Journal, 48.

Sabino, M., Schefuß, E., Natalicchio M., Dela Pierre, F., Birgel, D., Bortels, D., Schnetger, B., & Peckmann, J., 2020. Climatic and hydrologic variability in the northern Mediterranean across the onset of the Messinian salinity crisis. Palaeogeography, Palaeoclimatology, Palaeoecology, 545, 109632. https://doi.org/10.1016/j.palaeo.2020.109632

Schouten, S., Hopmans, E.C., Sinninghe Damsté, J.S., 2013. The organic geochemistry of glycerol dialkyl glycerol tetraether lipids: A review. Organic Geochemistry 54, 19–61. doi:10.1016/j.orggeochem.2012.09.006.

Schouten, S., Ossebar, J., Schreiber, K., Kienhuis, M.V.M., Langer, G., Bijma, J., 2005. The effect of temperature and salinity on the stable hydrogen isotopic composition of long chain alkenones produced by *Emiliania huxleyi* and *Gephyrocapsa oceanica*. Biogeosciences Discussions, 2 (6), 1681–1695. https://bg.copernicus.org/articles/3/113/2006/

Schuster, M., Duringer, P., Ois Ghienne, J.-F., Vignaud, P., Mackaye, H.T., Likius, A., Brunet, M., 2006. The age of Sahara Desert. Science, 311. http://doi.org/10.1126/science.1120161

Sierro, F.J., Flores, J.A., Zamarreño, I., Vásquez, a., Utrilla, R., Francés, G., Hilgem, F.J., Krijgsman, W., 1999. Messinian pre-evaporite sapropels and precession-induced oscillations in western Mediterranean climate. (1999) Marine Geology, 153 (1-4), pp. 137-146. 10.1016/S0025-3227(98)00085-1

Sinninghe Damsté, J.S., Schouten, S., Hopmans, E.C., van Duin, A.C.T., Geenevasen, J.A.J., 2002. Crenarchaeol: the characteristic core glycerol dibiphytanyl glycerol tetraether membrane lipid of cosmopolitan pelagic crenarchaeota. Journal of lipid research 43 (10), 1641-1651. 10.1194/jlr.m200148-jlr200

Spötl, C., Vennemann, T.W., 2003. Continous-flow isotope ratio mass spectrometric analysis of carbonate minerals. Rapid Communications in Mass Spectrometry17, 1004-1006. http://doi.org/ 10.1002/rcm.1010

Targhi, S., Barhoun, N., Taoufiq, B.N., Achab, M., Ait Salem, A., Yousfi, M.Z., 2021. Vegetation climate and marine environmental reconstruction in the western Mediterranean (southern Rifian corridor, Morocco) over the Tortonian-Messinian transition. Helyon 7, 208569. https://doi.org/10.1016/j.heliyon.2021.e08569

Tzanova, A., Herbert, T., Peterson, L., 2015. Cooling Mediterranean Sea surface temperatures during the Late Miocene provide a climate context for evolutionary transitions in Africa and Eurasia. Earth and Planetary Science Letters. 419. http://doi.org/10.1016/j.epsl.2015.03.016

Uno, K.T., Polissar, P.J., Jackson, K.E., deMenocal, P.B., 2016. Neogene biomarker record of vegetation change in eastern Africa. Proceedings of the National Academy of Sciences, 113(23), 6355–6363. https://doi.org/10.1073/pnas.1521267113

Utescher, T., Djordjevic- Milutinovic, D., Bruch, A., Mosbrugger, V., 2007. Paleoclimate and vegetation change in Serbia during the last 30 Ma. Palaeogeography, Palaeoclimatology, Palaeoecology 253, 157–168. https://doi.org/10.1016/j.palaeo.2007.03.037

Van der Meer, M.T.J., Sangiorgi, F., Baas, M., Brinkhuis, H., Sinninghe Damsté, J.S., Schouten, S., 2007. Molecular isotopic and dinoflagellate evidence for Late Holocene freshening of the Black Sea. Earth and Planetary Science Letters 267 (3−4), 426−434. http://doi.org/ 10.1016/j.epsl.2007.12.001

Vasiliev, I., Mezger, E.M., Lugli, S., Reichart, G.J, Manzi, V., Roveri, M., 2017. How dry was the Mediterranean during the Messinian Salinity Crisis? Palaeogeography, Palaeoclimatology, Palaeoecology, 471, 120–133. https://doi.org/10.1016/j.palaeo.2017.01.032

Vasiliev, I., Reichart, G.J., Krijgsman, W., Mulch, A., 2019. Black Sea rivers capture drastic change in catchment-wide mean annual temperature and soil pH during the Miocene-to-

Pliocene transition, Global and Planetary Change, 172, 428–439. https://doi.org/10.1016/j.gloplacha.2018.10.016

Vasiliev, I., Feurdean, A., Reichart, G.J., Mulch, A., 2020. Late Miocene intensification of continentality in the Black Sea Region. International Journal of Earth Sciences, 109, 831–846. https://doi.org/10.1007/s00531-020-01832-w

Velitzelos, D., Bouchal, J.M., Denk, T., 2014. Review of the Cenozoic floras and vegetation of Greece. Review of Palaeobotany and Palynology 204, 56-117. https://doi.org/10.1016/j.revpalbo.2014.02.006

Weiss, G.M, Schouten, S., Sinninghe-Damsté, J.S., van der Meer, M.T.J., 2019. Constraining the application of hydrogen isotopic composition of alkenones as a salinity proxy using marine surface sediments. Geochimica et Cosmochimica Acta, 250, 34–48. https://doi.org/10.1016/j.gca.2019.01.038

Weijers, J.W.H., Schouten, S., van der Donker, J., Hopmans E.C., Sinninghe Damsté, J., 2007. Environmental controls on bacterial tetraether membrane lipid distribution in soils. Geochimica et Cosmochimica Acta 71, 703–713. https://doi.org/10.1016/j.gca.2006.10.003

Zachariasse, W.J., Kontakiotis, G., Lourens, L.J., Antonarakou, A., 2021. The Messinian of Agios Myron (Crete, Greece): a key to better understanding diatomite formation south of Crete, on Gavdos Island. Palaeogeography, Palaeoclimatology, Palaeoecology, 581, 110633. https://doi.org/10.1016/j.palaeo.2021.110633

Zhang, Z., Ramstein, G., Schustre, M., Li, C., Contoux, C., Yan, Q., 2014. Aridification of the Sahara desert caused by Tethys Sea shrinkage during the Late Miocene, Nature, 513, 401. https://doi.org/10.1038/nature13705

Zidianakis, G., Mohr, B.A.R., Fassoulas, C., 2007. A late Miocene leaf assemblage from Vrysses, western Crete, Greece, and its paleoenvironmental and paleoclimatic interpretation. Geodiversitas 29, 351–377.

Chapter 8

Preliminary results other sites

8.1 Turkey − Belenyenice section

Field team: **Geanina A. Butiseacă**[1,2], Peter Joniak[3], Maya Kováčová[3], Pablo Peláez-Campomanes[4], Samuel Rybár[3], Wout Krijgsman[5], Sergei Lazarev[5], Lars W. van den Hoek Ostende[6], Serdar Maida[7], Melike Bilgin[3,6], Panagiotis Skandalos[6], Çilga Sanem Koç[8,9], Yanell Braumuller[6] (2018−2019)

Laboratory team: **Geanina A. Butiseacă**[1,2], Clemens Schmitt[1], Iuliana Vasiliev[1]

[1]*Senckenberg Biodiversity and Climate Research Centre (BiK-F), Senckenberganlage 25, D-60325 Frankfurt am Main, Germany*

[2]*Institute of Geosciences, Goethe University Frankfurt, Altenhöferalle 1, 60438, Frankfurt am Main, Germany*

[3]*Department of Geology & Palaeontology, Comenius University, 84215 Bratislava, Slovakia*

[4]*Museo Nacional de Cienscias Naturales, Jose Gutierrez Abascal st. 2, 28006, Madrid, Spain.*

[5]*Fort Hoofddijk, Paleomagnetic Laboratory, Utrecht University, Budapestlaan17, 3584 CD, Utrecht, The Netherlands*

[6]*Naturalis Biodiversity Center, P.O. Box 9517, 2300RA Leiden, The Netherlands*

[7]*Department of Biology, EGE University, 35100 Izmir, Turkey*

[8]*Botanical Garden and Herbarium Application and Research Center, EGE University, 35040, Bornova, Izmir, Turkey*

[9]*Department of Physical Geography, Utrecht University, Vening Meinesz Building A Princetonlaan 8a, 3584 CB Utrecht, The Netherlands*

8.1.1 Sampling and stratigraphy

Belenyenice section is located in the western side of Anatolia, on the north margin of Manisa graben (Figure 8.1). By comparison with similar sedimentary sequences in proximity (e.g. Bozkurt and Sözbilir, 2006; Özkaymak and Sözbilir, 2008), the section was preliminary dated as Miocene − early Pliocene and belonging to the regional Karadağ formation. The scarce macro-mammal fossil material (possible *Gomphotherium sp.)* discovered in the median part of the section, gives though a preliminary age as middle-late Miocene (MN 5−6, Langhian-Serravallian local stages; Kaysery Özer et al., 2014). Due to the poor preservation of the material, possibly reworked from older deposits, I will take in consideration the time interval provided by the sedimentological record (i.e. late Miocene − Early Pliocene).

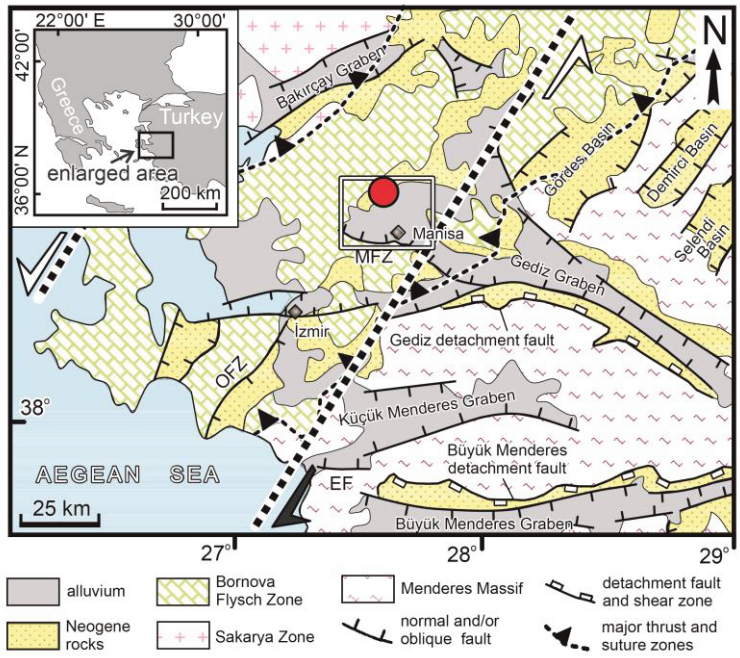

Figure 8.1 Geological map of western Turkey showing the major tectonostratigraphic units and the study area location. Abbreviations EF, MF, OFZ, refer to the Efes Fault, Manisa Fault and Orhanelı Fault Zone, respectively. The red circle indicates Belenyenice section. The bold dotted lines indicate the İzmir-Balıkesir Transfer Zone. Map after Özkaymak and Sözbilir (2008).

The section was sampled during 2018 and 2019 as an anthropic opening resulted from the emplacement of a new artificial lake in the area. The section consists of two parallel profiles (Figure 8.2E) and has a total thickness of 44.5 m. The sampled profiles are currently inaccessible due to the lake construction, further sampling being impossible. The lower part of the section

comprises clays, volcanic debris, sandstones and conglomerates (0−12 m), typically assigned to Karadağ formation (late Miocene − Pliocene deposits formed along Manisa Fault (Bozkurt and Sözbilir, 2006). The middle part (12−34 m) is dominated by diatomites and occasionally occurrence of coal layers, sandstone and tufa. This part probably belongs to the volcano-sedimentary formation before Karadağ. The upper part of the section (35−44.5 m) consists of sandstones and conglomerates in the base, and mudstone and coal intercalations in the rest. The coal layers have cm to mm layers and sulphur laminations. The sediments are abundant in paleontological material, covering microfauna (e.g. ostracods, diatoms, micro mammals), macrofauna (e.g. gastropods, bivalves, mammals) and flora (e.g. *Phragmites*, *Typha*), indicating a rich ecosystem that maintained through time, but also excellent preserving conditions. Determination and quantification are in process, analysis being performed at the University of Bratislava (Slovakia), Museo Nacional de Cienscias Naturales (Madrid, Spain) and University of Aegean (EGE, Izmir, Turkey).

8.1.2 Laboratory measurements − stable $\delta^{13}C$ and $\delta^{18}O$ isotopes on bulk sedimentary rocks

Eighty seven samples were drilled, weighted and examined for $\delta^{13}C$ and $\delta^{18}O$ in the joined Goethe University − Senckenberg BiK-F Stable Isotope Facility from Frankfurt am Main, Germany. Only 73 samples contained sufficient carbonate (in the maximum 2000 μg allowed on the specific protocol) to be measured. The samples correspond to bulk material, both on sedimentary rocks (Table 8.1) and paleosoil carbonate nodules (Table 8.2). Samples were dried and drilled with a manual electric drill at SBiK-F laboratory after being tested with HCl 10% to estimate the carbonate presence. The obtained powder was weighed and placed in vials. The $\delta^{13}C$ and $\delta^{18}O$ ratios were analyzed using a Thermo Scientific MAT 253 mass spectrometry and a Thermo Scientific GasBench II in continuous flow mode, following the protocol of Spötl & Vennemann, 2003. All samples were calibrated and measured against standard reference materials (Carrara marble, NBS 18 and Merck). Isotopic values were calculated against a CO_2 reference gas with a precision of 0.06‰ for $\delta^{13}C$ and 0.08‰ for $\delta^{18}O$, respectively. $\delta^{13}C$ values are presented with respect to VPDB, while $\delta^{18}O$ were converted to SMOW using the equation of Coplen et al. (1993) (Tables 8.1, 8.2).

Nodules sample name	Str.level (m)	$\delta^{13}C$	$\delta^{13}C$ STDEV	$\delta^{18}O$	$\delta^{18}O$ STDEV	$\delta^{18}O$ SMOW
BL 112N	40.53	-8.13	0.02	-4.83	0.03	25.93
BL 111N	40.44	-7.87	-4.92	-4.92	0.03	25.84
BL 108N	39.49	-8.81	0.01	-4.93	0.03	25.83
BL 106N	38.88	-9.81	0.02	-4.35	0.03	26.42
BL 103N	37.83	-8.43	0.01	-4.84	0.03	25.92
BL 052N	32.49	-7.56	0.02	-5.18	0.02	25.57
BL 047N	30.41	-7.91	0.02	-5.13	0.04	25.62
BL 046N	30.09	-7.20	0.02	-5.52	0.04	25.22
BL 043N	29.62	-7.08	0.02	-5.80	0.03	24.94

Table 8.1 $\delta^{13}C$ and $\delta^{18}O$ stable isotopes on nodules. BL stands for Belenyenice while N stands for nodule.

Sample name	Str.level (m)	$\delta^{13}C$	$\delta^{13}C$ STDEV	$\delta^{18}O$ VPDB	$\delta^{18}O$ STDEV	$\delta^{18}O$ SMOW
BL 122	42.50	-3.52	0.02	-8.78	0.06	21.86
BL 118	41.85	-6.81	0.04	-9.90	0.05	20.71
BL 116	41.48	-3.16	0.04	-10.74	0.06	19.84
BL 115	41.38	-6.22	0.02	-10.17	0.04	20.43
BL 114	41.12	-5.11	0.02	-7.72	0.03	22.95
BL 113	40.94	-5.10	0.01	-8.25	0.04	22.41
BL 111	40.44	-3.76	0.04	-9.33	0.04	21.29
BL 110	40.21	-3.77	0.03	-9.10	0.06	21.52
BL 108	39.49	-6.72	0.01	-9.90	0.03	20.71
BL 107	39.26	-3.31	0.01	-7.89	0.03	22.77
BL 106	38.88	-2.98	0.03	-9.85	0.04	20.75
BL 105	38.40	-2.03	0.01	-8.88	0.03	21.76
BL 104	38.24	-3.54	0.02	-9.46	0.03	21.16
BL 103	37.83	-2.95	0.02	-7.98	0.03	22.68
BL 101	37.30	-6.72	0.02	-7.30	0.01	23.39
BL 100	37.13	-4.25	0.02	-7.71	0.03	22.96
BL 066	34.21	1.20	0.02	0.54	0.03	31.46
BL 061	33.80	-12.36	0.03	-12.46	0.02	18.06
BL 060	33.77	-6.66	0.02	-6.48	0.03	24.23
BL 059	33.74	-4.39	0.02	-8.73	0.03	21.91
BL 057	33.66	-4.94	0.02	-8.65	0.03	22.00
BL 056	33.48	-4.24	0.01	-8.72	0.03	21.92
BL 055	33.13	-4.12	0.05	-8.33	0.08	22.33
BL 053	32.57	-4.24	0.02	-9.52	0.03	21.10
BL 052	32.49	-2.92	0.01	-9.36	0.03	21.26
BL 051	31.96	-6.11	0.01	-7.52	0.03	23.15
BL 049	30.86	-3.15	0.03	-8.12	0.03	22.54
BL 048	30.70	-3.33	0.02	-8.48	0.03	22.17
BL 046	30.09	-4.58	0.02	-9.55	0.02	21.06
BL 045	30.05	-3.94	0.03	-9.82	0.03	20.79
BL 044	29.86	-3.93	0.01	-9.79	0.04	20.82
BL 042	29.54	-2.81	0.04	-5.95	0.03	24.77
BL 041	29.00	-4.45	0.02	-7.82	0.04	22.84
BL 040	28.20	-4.02	0.01	-8.62	0.02	22.02
BL 039	28.02	-5.56	0.01	-8.24	0.03	22.42
BL 038	27.62	-4.55	0.01	-8.60	0.04	22.04
BL 037	27.30	-4.03	0.02	-8.60	0.03	22.04
BL 036	27.00	-4.36	0.02	-7.60	0.03	23.08
BL 035	26.77	-4.18	0.03	-6.99	0.03	23.70
BL 034	26.49	-3.96	0.02	-5.84	0.03	24.89
BL 033	26.20	-2.82	0.01	-10.04	0.02	20.56
BL 032	25.94	-2.71	0.03	-9.92	0.02	20.69
BL 031	25.40	-1.80	0.01	-6.13	0.04	24.59
BL 030	25.03	-1.99	0.01	-5.30	0.03	25.44
BL 028	24.80	-3.80	0.03	-6.00	0.05	24.73
BL 026	24.44	-2.69	0.03	-9.27	0.07	21.35
BL 025	24.40	-1.81	0.02	-7.99	0.04	22.67
BL 023	24.15	0.03	0.01	-6.51	0.03	24.20
BL 020	23.60	1.31	0.02	-0.58	0.02	30.32
BL 019	23.42	0.55	0.02	-3.14	0.04	27.67
BL 018	23.00	0.42	0.02	-5.51	0.02	25.23
BL 016	22.05	0.30	0.01	-4.91	0.04	25.85
BL 013	21.00	0.55	0.02	-3.85	0.04	26.94
BL 012	20.87	1.18	0.02	-2.79	0.04	28.04
BL 011	20.80	0.92	0.03	-5.71	0.05	25.02
BL 010	20.50	-0.67	0.01	-3.76	0.04	27.03
BL 009	20.40	1.23	0.03	-5.47	0.03	25.27
BL 008	20.23	-1.80	0.01	-3.73	0.03	27.07
BL 007	20.09	-0.18	0.02	-3.14	0.03	27.67
BL 006	20.01	-0.87	0.01	-4.26	0.02	26.52
BL 005	19.90	0.29	0.02	-3.73	0.03	27.06
BL 004	19.05	0.54	0.03	-4.75	0.03	26.01
BL 001	18.03	-0.17	0.02	-4.33	0.02	26.44
W 21	8.40	-5.11	0.07	-9.53	0.13	21.09

Table 8.2 $\delta^{13}C$ and $\delta^{18}O$ stable isotopes on bulk sedimentary rocks.

8.1.3 Preliminary remarks

The lower part of the section covers multiple alluvial plain deposits and some lake-clay deposits (0−12 m)**.** After 12 m (12−30) the sedimentation becomes dominated by diatomites. Diatoms are single-celled silica organisms, which had been associated with silica consumption. Accumulation of volcanic ash in a lake over time would lead to intense diatom productivity, therefore thick successions of diatomites, the case in our section. The upper part of the section is formed by normal lake deposits (multiple lake phases), occasionally intersected by alluvial deposits. Probably paleo-rivers were debouching in the lake, carrying various sediments from the vicinity. The depocenters seem to migrate over time because they intersect the section at different places (e.g. lobe margin, alluvial plain, margin of alluvial plain). This fact can be attributed to the extremely active tectonics in the area, Belenyenice-Manisa being part of one of the most active extensional structures in west Anatolia, Manisa Graben (Özkaymak and Sözbilir, 2008), related to the Anatolian strike-slip system.

The area and section are affected by multiple fault systems of different ages. Some of the observed faults are sin-depositional; while others are recent, altering considerably the stratigraphic sequence (Figure 8.2A-D). Manisa fault zone is a reactivated structure with at least three different motions since the Miocene. The earliest motion was sinistral and consistent with an E/W trending contraction during the Miocene–Early Pliocene. The second active period corresponds to Plio–Quaternary, when the faulting plane changes to dextral, associated with NE/SW trending extension. The youngest configuration is Quaternary and characterized by an almost dip-slip normal faulting, with NE/SW trending extensional tectonic regime (Özkaymak and Sözbilir, 2008). Due to the numerous faults that have both vertical and horizontal displacement, the dating of the section through paleomagnetism was not possible. Hopefully, further ash dating is going to provide a reasonable age.

$\delta^{13}C$ and $\delta^{18}O$ values have an overall slightly decreasing trend, suggesting a slowly cooling towards the top of the section. For the first half part of the section isotopic values are more stable (6.87‰ for $\delta^{13}C$ and 9.76‰ for $\delta^{18}O$), while the upper part has a higher variability (13.56‰ for $\delta^{13}C$ and 13.40‰ for $\delta^{18}O$). The $\delta^{13}C$ and $\delta^{18}O$ isotopic values positive covariance (Figure 8.3) suggest a dry, more closed system for the first half of the section, covering the diatoms formation interval.

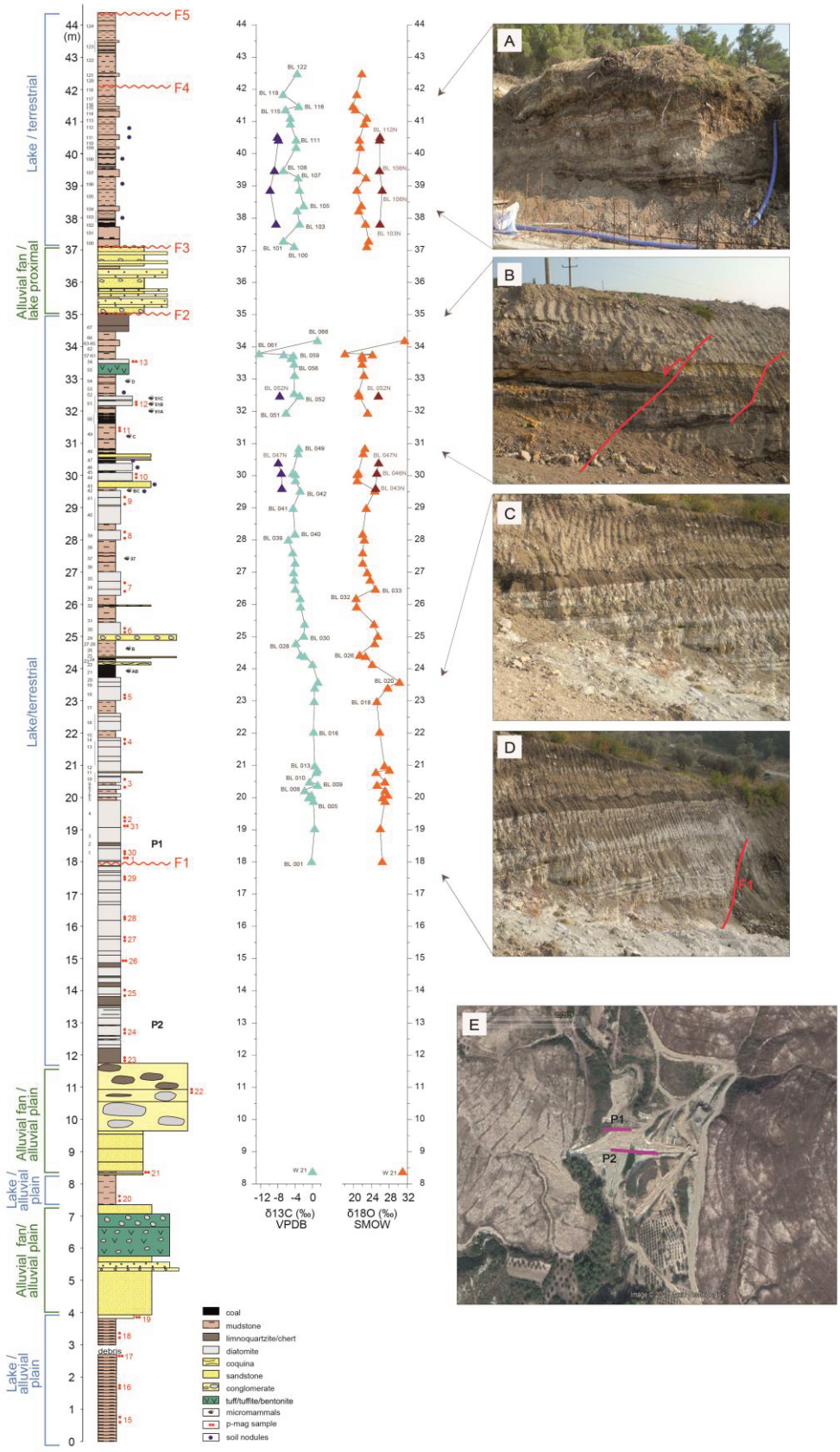

Figure 8.2 Synthetic log for Belenyenice section (Turkey). On the left side is presented the lithology together with depositional environments. On the log are marked the samples and the faults crossing the section. In the central part are plot the $\delta^{13}C$ and $\delta^{18}O$ isotopic values on bulk sediments and nodules. A-D: pictures from the field illustrating the main geological features. E: Google Earth map with the 2 profiles of the section (P1 and P2).

The lake evolution might have been influenced also by the volcanic activity in the area. Sedimentological data suggest multiple eruptions that have deposited almost 20 m of ash in Belenyenice Lake. For the second part of the section the conditions are changing, transitioning to an overall wetter climate. This time the $\delta^{13}C$ and $\delta^{18}O$ isotopic values covary negatively, indicating a more open system (Figure 8.3).

At only 2 times the $\delta^{13}C$ and $\delta^{18}O$ values indicate a completely closed system, at sample BL 20 (23.60 m) and BL 66 (34.21 m). A first event is registered exactly before the first coal deposits in the section (at 23.60 m; Figures 8.2, 8.3). Both $\delta^{13}C$ and $\delta^{18}O$ show a positive excursion at this level, followed by a drop in values with ~ −5‰ for $\delta^{13}C$ and −10‰ for $\delta^{18}O$. This level also yields the maximum registered value of $\delta^{13}C$ 1.31‰. The second event is registered at 34.21 m, when $\delta^{18}O$ value reaches the maximum value of 31.46 ‰.

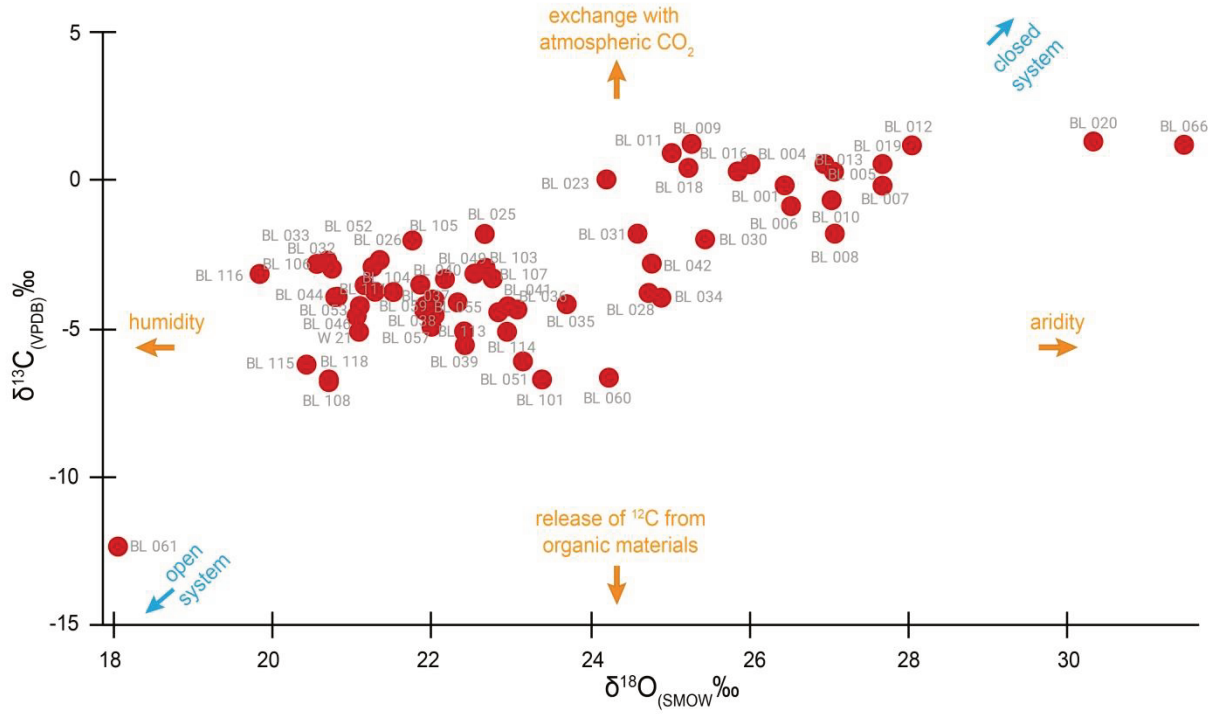

Figure 8.3 Diagram showing the distribution of $\delta^{13}C$ against $\delta^{18}C$ on bulk carbonates.

The high isotopic values are associated with the deposition of a ~70 cm layer of chert followed by a fault. Before BL 66, at 33.80 m (BL 61) is recorded the only completely opened system in the section, when both $\delta^{13}C$ and $\delta^{18}O$ attain the minimum values (−12.36‰ $\delta^{13}C$ and 18.06‰ $\delta^{18}O$). It is possible that this shift in values from BL 61 to BL 66 to be caused by

tectonics, the fault opening the lake and creating a connection with another basin (possibly marine) for a short time interval, then closing it back and sealing the lake again.The $\delta^{13}C$ and $\delta^{18}O$ isotopic values of soil nodules are not following the trend of the layers they were collected from, suggesting different forming conditions, as soil nodules form later. Overall, the $\delta^{13}C_{nodules}$ are more negative than the $\delta^{13}C_{bulk}$ values, while $\delta^{18}O_{nodules}$ are more positive than the $\delta^{18}O_{bulk}$ values (Figure 8.2), as expected.

8.2 Bulgaria – Bolata, Kamen Briag, Kavarna sections

Field team: **Geanina A. Butiseacă**[1,2,3], Traian Răbăgia[3], Lorena Apachiței[3,4], Eugen Visnevschi[3] (2014−2016)

Laboratory team: **Geanina A. Butiseacă**[1,2,3], Iuliana Vasiliev[1], Eva M. Niedermeyer[1]

[1]*Senckenberg Biodiversity and Climate Research Centre (BiK-F), Senckenberganlage 25, D-60325 Frankfurt am Main, Germany*

[2]*Institute of Geosciences, Goethe University Frankfurt, Altenhöferalle 1, 60438, Frankfurt am Main, Germany*

[3]*Danubian Energy Consulting, Academiei 35-37, Entrance A, Floor 6, Suite 11, 01001, Bucharest, Romania*

[4]*OMV Petrom, Romania, Coralilor 22, Bucharest, Romania.*

8.2.1 Sampling and stratigraphy

Three composite sections were investigated in NE Bulgaria (Figure 8.4), that outcrop on the Black Sea shore and cover the Late Miocene, Sarmatian (*s.l.*) local stage, Bessarabian and Khersonian substages. The sedimentary accumulations in Bulgaria are the proximal equivalent of the late Miocene in Taman Peninsula. Dominant are bioacumulated, oolitic and detrital limestones, but also lagoonal deposits with marls and diatomites. In general, Sarmatian deposits are prograding and gently dipping towards south, with sin-sedimentary structures or re-activated local deformations (mainly normal faults).

Bessarabian is generally present through clays in the base (Kavarna area), and detrital, oolitic and lumashelic limestones in rest. The Middle-Upper Bessarabian deposits are shallow intertidal deposits dominated by high energy, as indicated by oolites and shell parts in the lumashels. The Khersonian deposits and a part of the Bessarabian are karstified, karst topography being filled with laterites and bauxites. The upper part of Khersonian is marked by numerous unconformities and intervals with red aragonite crystals. The red deposits accompanying the aragonite (laterites/ bauxites) are similar to the other karstified deposits,

suggesting they were formed during Khersonian also, at moments when the shelf was exposed. The aragonite layers were interpreted as high evaporative bays (Koleva-Rekalova, 2001), but they were probably lagoonal based on the deposits geometry. The aragonitic layers are part of the uppermost Khersonian in NW and NE Bulgaria, locally known as Florentin Formation.

The sampling and stratigraphic observations took place in several campaigns during 2015−2016, but previous mapping in the area was done since 2013. The exact age of these deposits was not possible to be determined due to lithology and tectonics.

Figure 8.4 Kamen Briag, Bolata and Kavarna composite sections locations. With yellow numbers are located the outcrops included in the composite profiles, while with yellow line is marked the Bulgarian border.

8.2.1.1 Bolata Section

Bolata is a 39 m composite section, with outcrops surrounding the Bolata bay on the bulgarian shore (43°22'N, 28°28'E), a small graben structure. The deposits from here are Khersonian, possibly with a bit of Bessarabian in the base. Based on the sedimentology and the paleontological elements of Bolata and Kamen Briag sections we have defined several lithological units, named from A (older, base Khersonian) to J (younger, top Khersonian) (Figure 8.5). Units are delimited by unconformities, angular or regular.

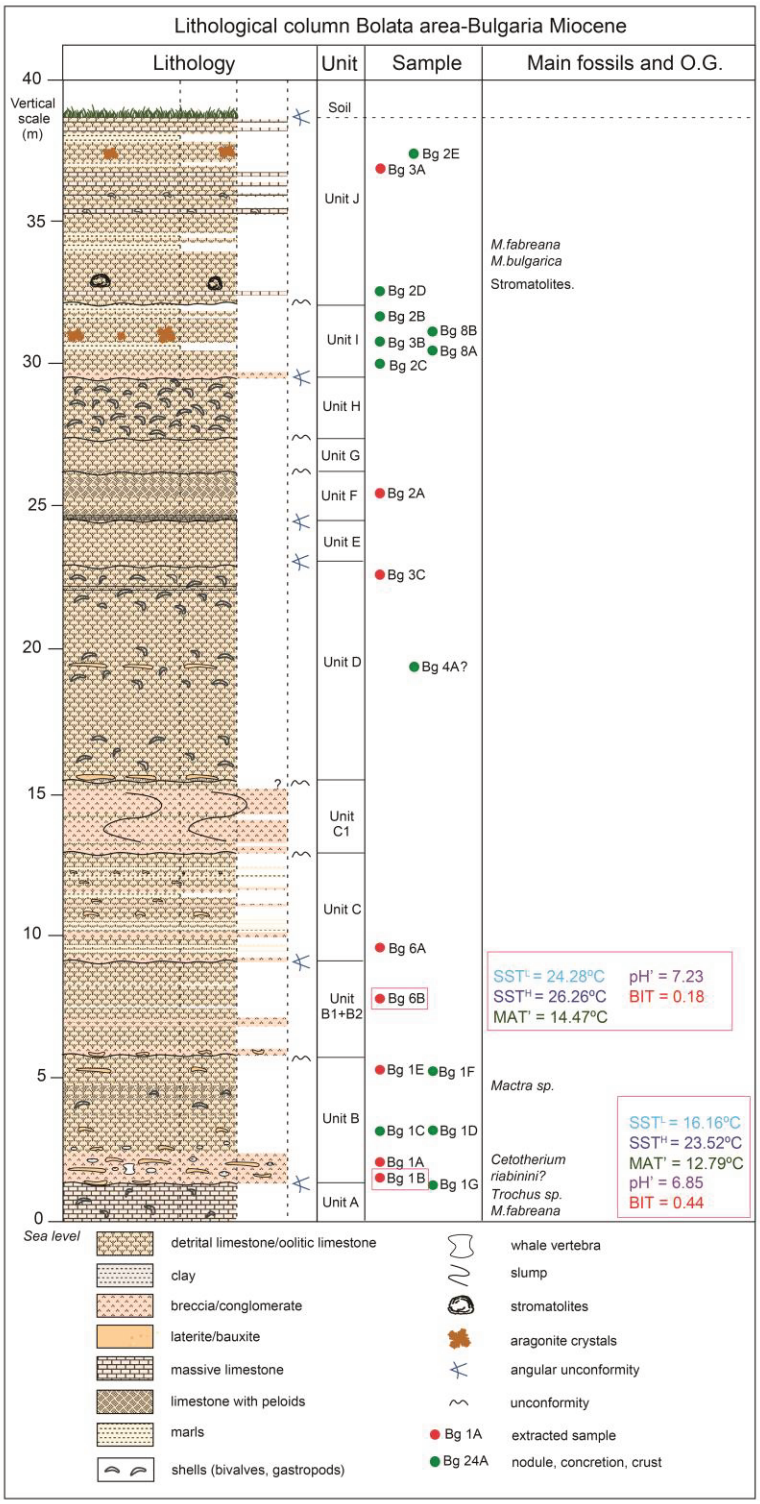

Figure 8.5 Stratigraphic log Bolata section. O.G. stands for organic geochemistry samples.

Unit A comprises mainly of massive limestones with fossils and detrital limestones. Unit B is mainly detrital with a conglomeratic level in base with clasts of limestones and clay. The

contact with unit A is an erosional surface, sitting angular, karstified and with whale bones just after the contact. B unit has two other divisions (B1 and B2), delimited by normal erosional unconformities. Unit C comprises of intercalations of different types of limestones, with clays and conglomeratic layers, sitting also angularly on unit B. Unit C1 is a breccia of ~2.5 m with sin-sedimentation deformations (slumps). Unit D is the thickest in Bolata section (~13 m) and is a mixture off detrital, lumashelic and oolitic limestone, delimited by two normal unconformities. E unit is mainly formed by oolitic and detrital limestones and is delimited by angular unconformities. F unit is mainly peloidal and detrital limestone, while G is very similar in lithology with E unit. H unit comprises mostly from detrital and organogenic limestones, very rich in mollusks. I unit is formed by intercalations of organogenic and detrital limestones with clays, and is extremely interesting as it contains aragonite crystals in the middle. The bottom of this unit is an angular surface with conglomerates. Unit J is the last one and it comprises of ~7 m intercalations of limestones and clays. Aragonite appears again, close to the top, with bright red crystals, rich in Fe^{3+}. Close to the base of this unit, there is also a level with stromatolites, with constructions usually of few centimeters height. The limit between the khersonian and quaternary sediments is an angular unconformity.

The section is extremely rich in fauna and affected by numerous unconformities. Most of them appear to be tectonic, caused by vertical or tilting movements, but also erosional, possibly a combination between tectonics and eustatic changes. The section also presents numerous crusts from dissolution and reprecipitation, dissolution planes, karst holes, concretions and nodules. From this section there were taken eight samples for biomarkers and thirteen for stable isotopes.

8.2.1.2 Kamen Briag Section

Kamen Briag profile is the northernmost sampled (~10 km north of Bolata) and is located on the Black Sea cliff, across the village with the same name (43°27'N, 28°33'E). The profile is ~37m thick and covers mostly Khersonian, as Bolata section, but the units have visible differences in thickness, as well as some of the internal structures. The most visible differences are in units C1, I and J. C1 unit is much thicker in Kamen Briag section, almost 6 m, double than in Bolata (Figure 8.6). The internal deformations are the same, but at a larger scale. I unit is very interesting as it presents a layer with herringbone cross stratification, but also swalley cross stratification.

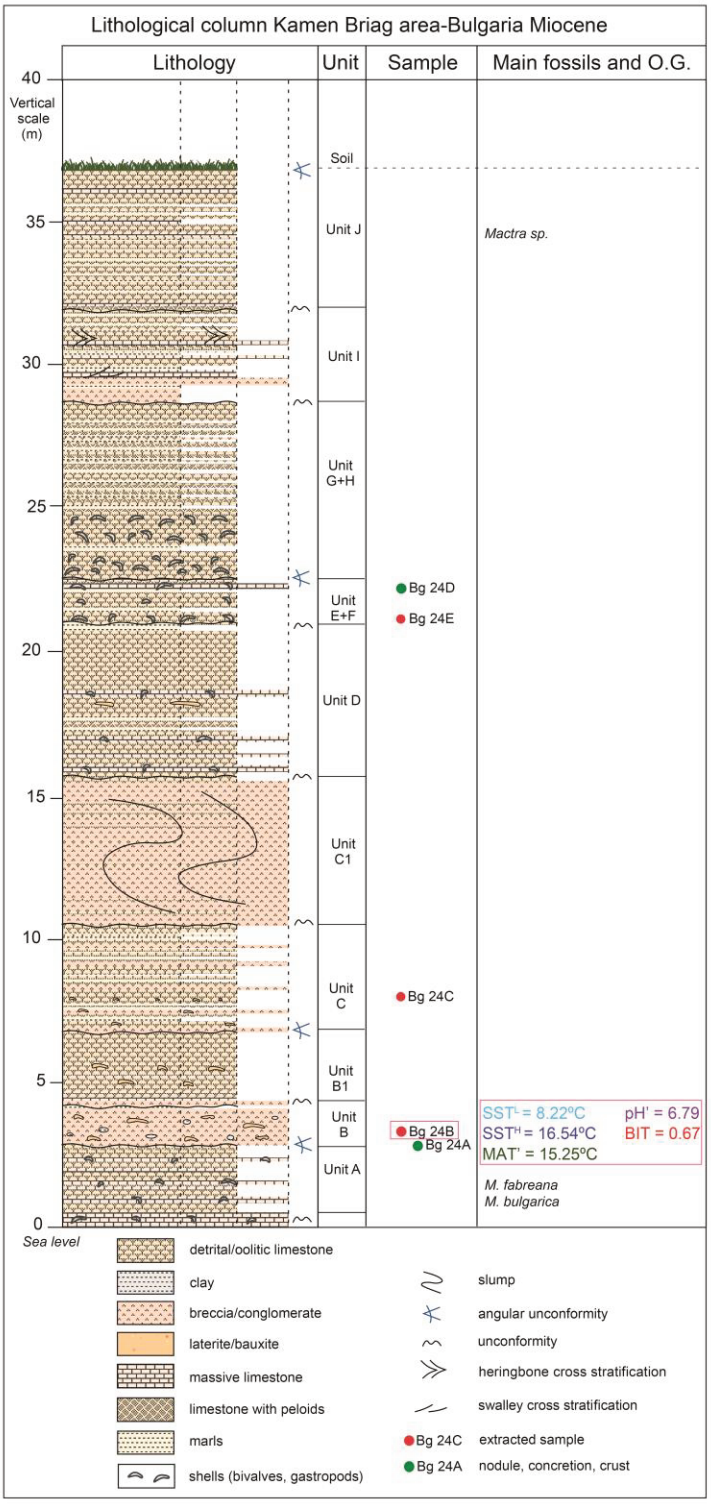

Figure 8.6 Stratigraphic log Kamen Briag section. O.G. stands for organic geochemistry.

The herringbone direction indicates S-N tidal current direction. The swalley cross stratification indicates the same direction. Another particularity of Kamen Briag section is that J unit does not have aragonite or stromatolite build-ups. This might be due to the different position in the basin (a more exposed area in this case, with higher energy), or they were not preserved due to hiatuses in the sedimentary record.

8.2.1.3 Kavarna Section

Kavarna section is also a composite, including outcrops between Kavarna city and Kaliakra Cape and is the southernmost analyzed. The mapped section has ~55 m, but due to the landslides in the area it was not possible to map the entire cliff. The area overlaps with a massive landslide area (Ikantalaka; Evsatiev and Evlogiev, 2013), situated along a master fault parallel with the shore.

The lowermost part of the section comprises mostly of laminated marls and clays, with marine mammal (whales and dolphins) bones in the base. At ~2.5 m a coal layer is registered, suggesting a swamp environment. The fossil assemblages are changing until about 11.5 m, indicating a passing to a brackish lagoon possibly freshened, with marine episodes. At 11.5 the lagoon dries, as the fine sediments are crossed by drying cracks of ~3 m depths (Figure 8.7). The cracks are filled with fine sand and fragments of bones. The upper part of this surface is indurated.

Until about 34 m, the basin deepens again, dominant being clays, diatomites and lithographic limestones, with occasional mollusks. After this point the sediments are again exposed, as bauxites and laterite form and numerous unconformities are registered the next ~11 m. At 45 m we have recognized the J unit described in the previous sections, with aragonite in the top part. Paleomagnetism analysis was previously conducted for the median part, but dating was not possible.

For this section twenty three samples were collected for organic geochemistry and twelve for supplementary analyses from crusts and nodules. Eight were successfully analyzed for biomarkers with results presented in Figure 8.8 and Table 8.3.

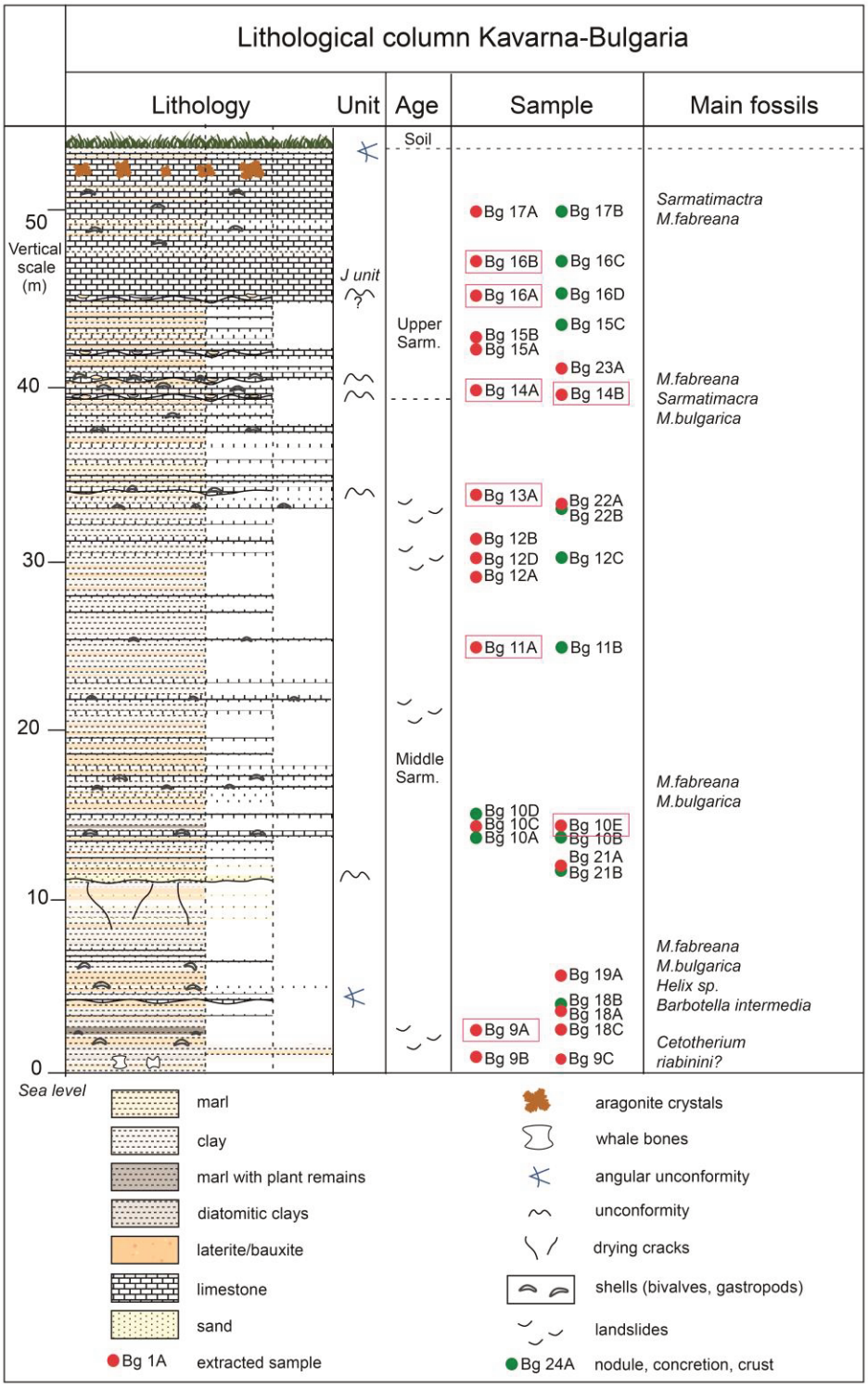

Figure 8.7 Stratigraphic log of Kavarna section.

8.2.2 Laboratory preparation and biomarker measurements

A total of 34 samples were extracted at Senckenberg BiK-F using a Buchi speed extractor. Samples were previously frozen, and then dried using an ALPHA 1-2 LDplus Freeze dryer for about 6h. After drying, samples were ground using mortar and pestle and prepared for extraction. For these samples were used 20 ml cells, DCM:MeOH, *v:v* 9:1. Fractionation of samples was done using deactivated silica gel column, using 20 gr of SiO2 and 1 ml miliQ water. For fraction A (*n*-alkanes) the column was eluted with hexane. Fraction B (ketons) was eluted with DCM:Hex, *v:v* 2:1. For fraction C (polars) were used DCM:MeOH, *v:v* 1:1, while for D (rest) only MeOH. Unfortunately, this method was not appropriate for the samples and fractions separation was not properly done. For this reason results were obtained only for 11 samples (Table 8.3). For the other samples analyzed in the previous chapters the laboratory procedures were changed, to attain proper fraction separations (see Chapters 5−7).

Sample Name	SST^{L} (<15°C)	SST^{H} (>30°C)	MAT'	pH'	BIT	Location
BG 6B	24.28	26.26	14.47	7.23	0.18	Bolata
BG 1B	16.16	23.52	12.79	6.85	0.44	Bolata
BG 24B	8.22	16.54	15.25	6.79	0.67	Kamen Briag
BG 16B	21.41	28.77	10.22	6.90	0.96	Kavarna
BG 16A	24.47	30.21	12.20	7.38	0.98	Kavarna
BG 14A	20.41	32.92	10.41	7.31	0.95	Kavarna
BG 14B	19.74	33.56	10.18	7.33	0.85	Kavarna
BG 13A	17.04	27.92	10.54	8.06	0.89	Kavarna
BG 11A	19.42	29.28	8.91	6.50	0.81	Kavarna
BG 10E	22.65	27.28	20.31	8.02	0.86	Kavarna
BG 9A	19.64	27.63	7.50	6.84	0.49	Kavarna

Table 8.3 Biomarker data results: SST = sea surface temperature; MAT = mean air annual temperature; pH = soil pH and BIT index = Branched isoprenoidal tetraethers index.

8.2.3 Preliminary remarks

From the three analyzed profiles, Kamen Briag and Bolata are very similar in lithology, but with different layer thickness. The sedimentation in the two sections suggests a high energy environment, under direct influence of waves and currents, close to the shore. The sedimentation is carbonated, with both autochthonous (e.g. oolites) and alochtonous elements (e.g. limestone or marl clasts eroded from mainland or local older exposed sediments). At Kavarna profile location

(SW), the sedimentation is very different, except the upper part, which is the same as in the other section case (J unit) (Figure 8.8).

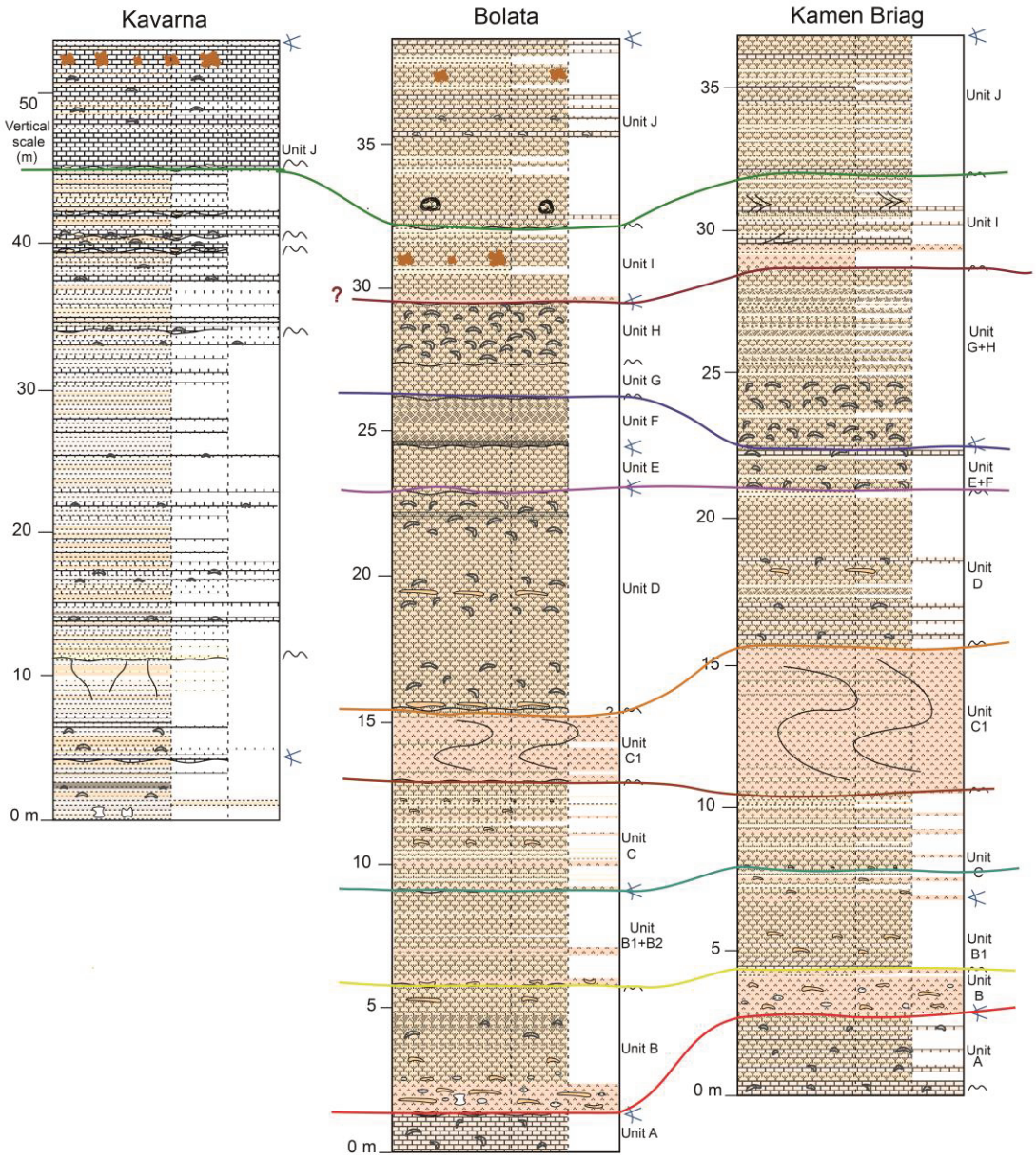

Figure 8.8 Log correlation between the three profiles, from SW (Kavarna) to NE (Kamen Briag). With colored lines are delimited the stratigraphic units.

As inferred by fossils present in the section, marine then brackish and terrestrial (i.e. mammals, mollusks and plants) and sediments geometry and composition, Kavarna section seems to have been part of a golf that was later isolated and transformed into a lagoon. Parts of

the former shore are eroded nowadays, but at Kaliakra and inland close to Varna were observed numerous stromatolite buildups, which were probably part of a barrier behind which a lagoon evolved. The area is very active tectonically (Shanov, 2005) with faults of different age, from late Miocene to Quaternary. Probably the isolation of the lagoon is connected with the tectonic activity, as well as the numerous unconformities observed in the outcrops.

From the 34 samples collected for biomarkers, only 11 were successfully analyzed, with the highest number of samples in Kavarna section. The SSTs were obtained by using TEX_{86} (TetraEther indeX of tetraethers consisting of 86 carbon atoms), calculated according to the definition of Schouten et al. (2002) and converted into SST using the calibration of Kim et al. (2010). MAT' and pH were calculated according to Peterse et al., (2012) taking in consideration the expanded period of time (~2 Myr). Branched isoprenoidal tetraethers index (BIT index) was calculated according to Hopmans et al., 2004.

Preliminary data from Kavarna (Figure 8.9, Table 8.3) show SST^H between ~27 and 33 °C, with the highest values (> 30 °C) corresponding to laterites, as expected, in karstified limestones (39−44 m). SST^L varies between ~19 and 24 °C and follows a similar pattern with SST^H. MAT' shows temperatures on land between ~8 to 20 °C, with highest temperatures in sample 10E (14.50 m), a fine limestone with reprecipitated calcite crystals on the surface. pH fluctuates between ~6.5 and 8, with highest values in sample 10E again (8.02) and 13A (8.06; ~34 m), both samples having the same lithology. BIT values range between 0.49 and 0.98 with a mean value of 0.85. BIT values indicate a dominant more terrigenous organic matter source, except sample 9A which was taken from above the level with whale bones. An interesting change can be observed between samples 14B-14A, first being taken from the unconformity level, while the second just above it. In this very short interval is a difference of 1 °C both on SST and MAT, while the BIT values change from 0.85 to 0.95.

The two samples analyzed from Bolata are 1B (1.6 m) and 6B (7.70 m) from unit B-B2 (Figure 8.5). Both samples are bauxites. 1B was sampled just above the limit with unit A and registers a SST^H of ~24 °C, MAT' of ~13 °C, pH of 6.85 and BIT of 0.44. The second sample registers slightly higher temperatures, with SST^H of ~26 °C, MAT' of ~15 °C, pH of 7.23 and BIT of 0.18. The SSTs are overall a bit lower than at Kavarna, but still high. The only sample from Kamen Briag comes also from unit B (24B, 3.2 m) and registers a much lower SST^H, of ~17 °C (Figure 8.6). MAT' at 24B location is ~15 °C, pH 6.79, while BIT is 0.67.

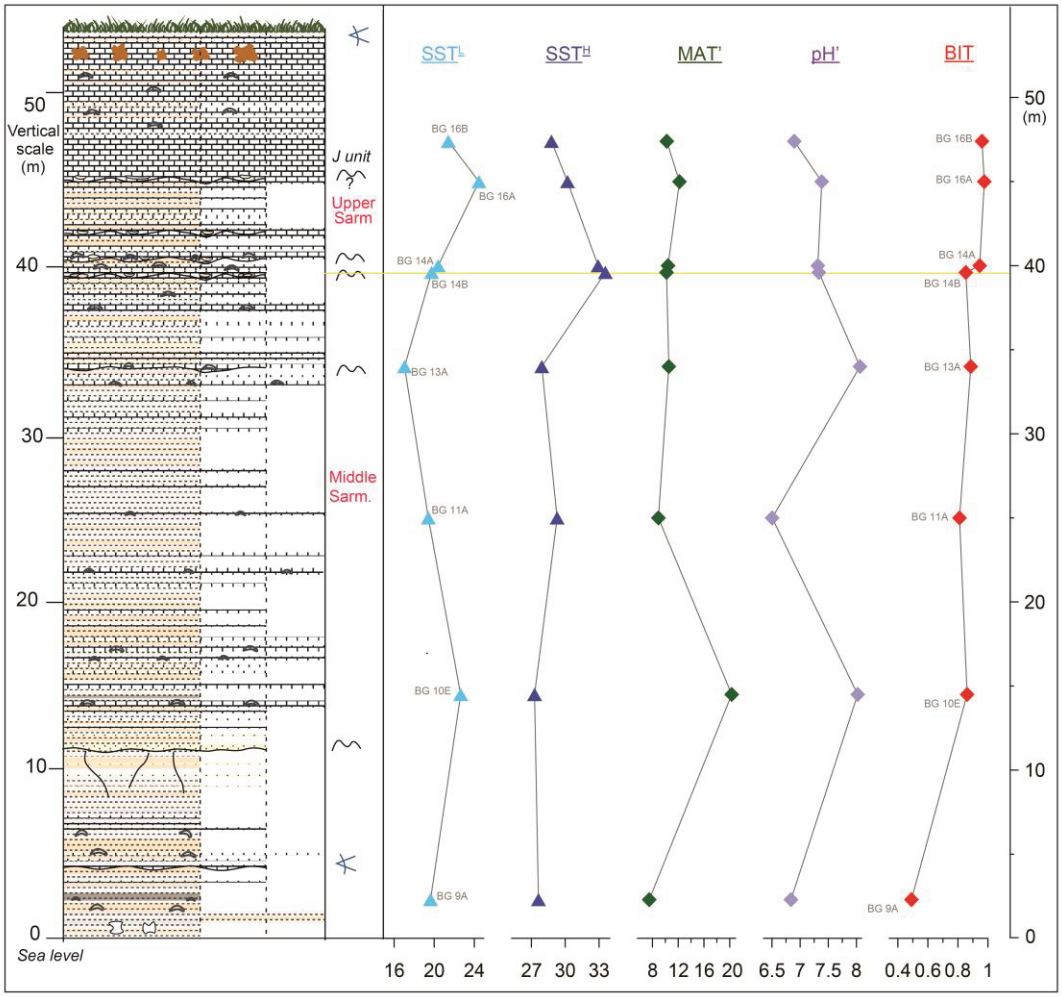

Figure 8.9 Preliminary biomarkers results from Kavarna profile. SST = sea surface temperature; MAT = mean air annual temperature; pH = soil pH and BIT index = Branched isoprenoidal tetraethers index. In the left side is depicted the lithostratigraphic log. All temperatures are in Celsius degrees (°C).

Overall, the SSTs registered in Bulgaria in the three analyzed sections indicate a very warm water column, with normal MATs onland. pH values are indicating the presence of increasing alkaline soils in the catchment area, while BIT values point towards a main continental source of organic matter. The presented data are extremely useful in understanding the late Miocene Balkans−W. Black Sea area, offering information not only about climate, but also about the sedimentology and tectonics and the dynamics of paleoshores.

8.3 Romania – Putna and Slănic sections

Field team: **Geanina A. Butiseacă**[1,2], Iuliana Vasiliev[1], Sorin Butiseacă[3] (2016−2017)

Laboratory team: **Geanina A. Butiseacă**[1,2], Iuliana Vasiliev[1], Eva M., Niedermeyer[1]

[1]*Senckenberg Biodiversity and Climate Research Centre (BiK-F), Senckenberganlage 25, D-60325 Frankfurt am Main, Germany*

[2]*Institute of Geosciences, Goethe University Frankfurt, Altenhöferalle 1, 60438, Frankfurt am Main, Germany*

[3]*Incalor SA, Bălcescu 33B, Buzău, Romania.*

8.3.1 Sampling and stratigraphy

Two sections from Romania were sampled in 2016, Putna and Slănic, both in the eastern side of Carpathians (Figure 8.10). Stratigraphically, the two sections are part of the Dacian Basin, central Paratethys; while tectonically are part of the Carpathian foredeep.

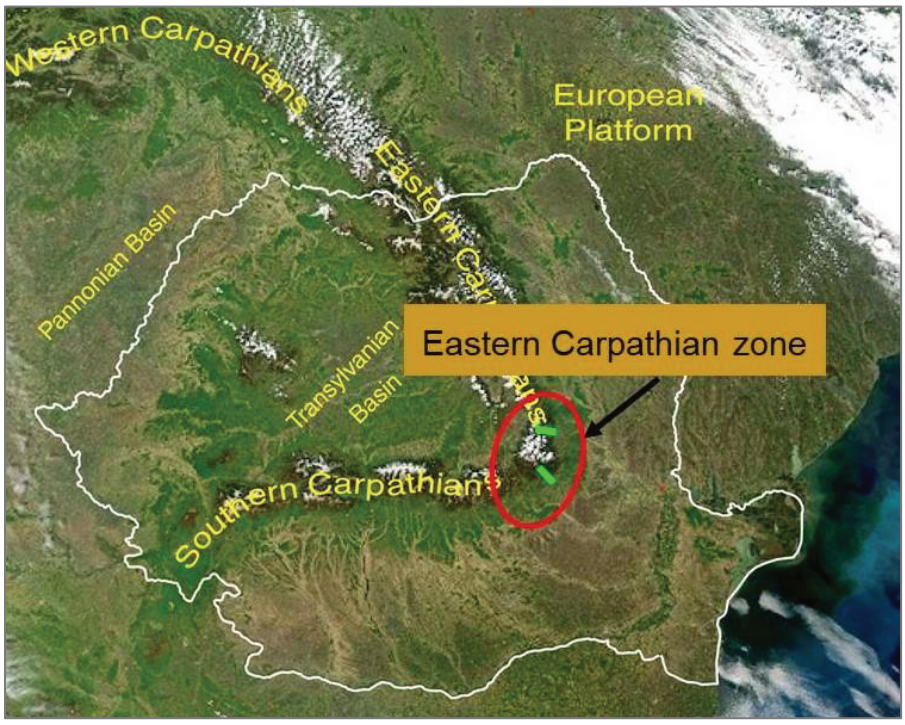

Figure 8.10 Location map of the two sampled sections in Romania (green lines), Putna in the north and Slănic in the south.

8.3.1.1 Putna Section

Putna is situated on Putna river valley (45°53'N, 26°49'E) which crosses the eastern Carpathians from W to E (Figure 8.10). The valley was sampled in 2016, covering a part of Badenian, all Sarmatian and Meotian local stages (Figure 8.11), roughly the interval between 13 to ~6 Ma. The fieldwork took place in a period with heavy rains, thus the access to outcrops was limited as the water level was above 1.5m high in some places.

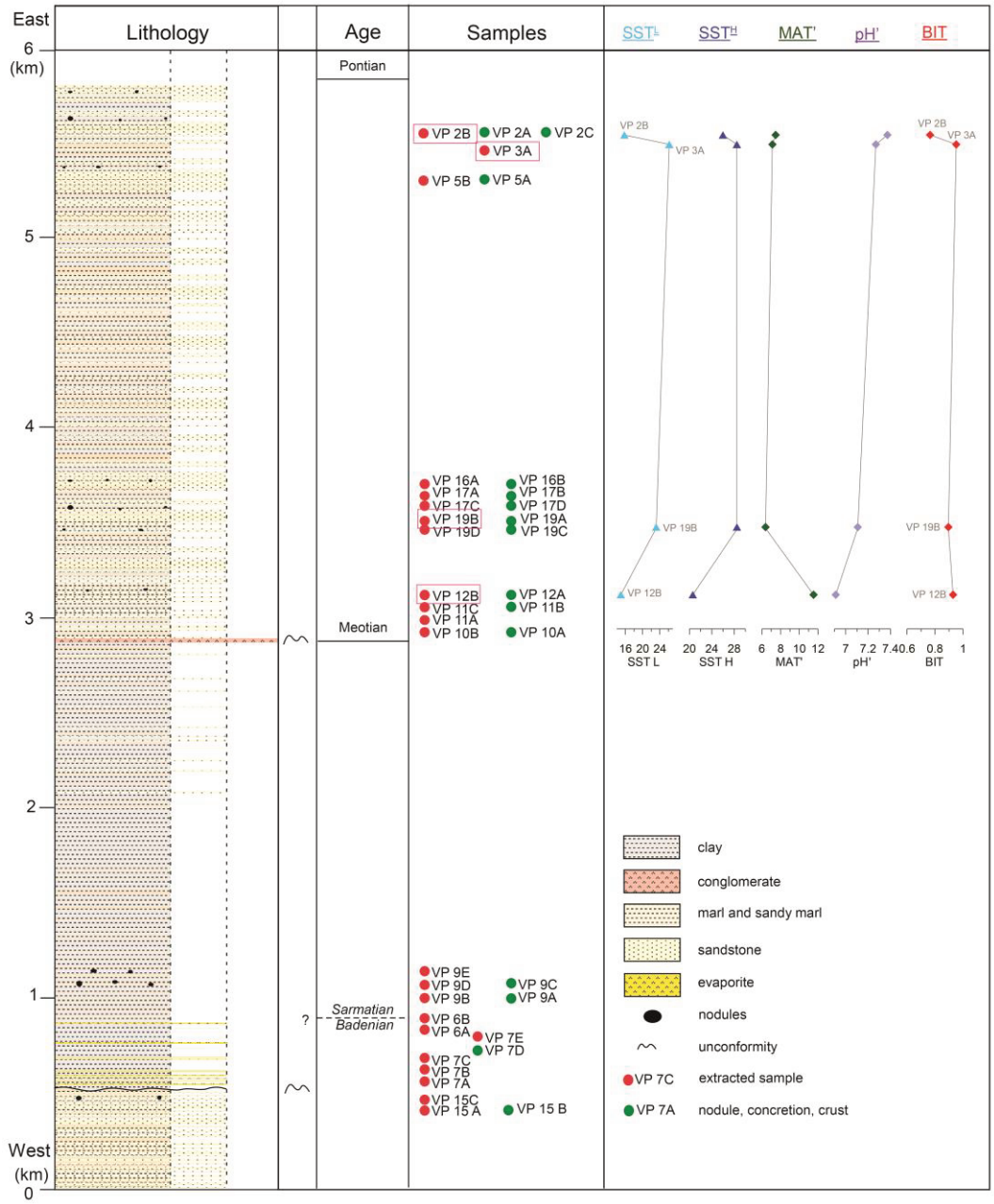

Figure 8.11 Putna lithostratigraphic log and preliminary organic geochemistry data. SST = sea surface temperature; MAT = mean air annual temperature; pH = soil pH and BIT index = Branched isoprenoidal tetraethers index.

The upper Badenian is present through intercalations of clays, marls and sandstones, but also clays with evaporites (i.e. gypsum). Sarmatian is mainly pelitic with dominant clays and marls, with fine sandstones intercalations in both top and base. The Sarmatian−Meotian limit is marked by a conglomeratic level, with centimetric subrounded clasts. Meotian is more clastic, with intercalations of sandstones and clays, dominant being sandstones. Strata are in general vertical or overturned, main compressional direction being SW-NE.

8.3.1.2 Slănicul de Buzău

Slănic Section is situated on the valley with the same name, at the curvature of the Carpathians (45°29'N, 26°39'E) in Romania (Figure 8.10). The section covers the upper part of Sarmatian, until the Sarmatian−Meotian limit. The lithology comprises of intercalations of clays, sandstones and red clays with nodules. Access to outcrops was possible only on half of the section. The median part contains only clays that are sliding into the river. Strata are in the same tectonic position as on Putna Valley.

8.3.2 Laboratory preparation and biomarker measurements

A total of twenty three samples were extracted for Putna section and four from Slănic. From these, only a total of six were successfully finished (four from Putna and two from Slănic). The protocol followed is the same as for the samples in Bulgaria. Putna meassured samples are all Meotian, two from the base of Meotian and two from the top. The preliminary results (SST, MAT, pH and BIT are presented in Table 8.4.

Sample Name	SST^{L} (<15°C)	SST^{H} (>30°C)	MAT'	pH'	BIT	Location
VP 2B	15.75	25.98	7.46	7.37	0.76	Putna
VP 3A	26.20	28.47	7.12	7.27	0.95	Putna
VP 19B	23.15	28.49	6.38	7.11	0.90	Putna
VP 12B	14.93	20.60	11.53	6.91	0.93	Putna
S 2A	26.55	21.93	11.94	5.95	0.27	Slanic
S 1C	28.85	27.48	14.86	7.59	0.19	Slanic

Table 8.4 Preliminary biomarkers data from Putna (VP samples) and Slănic (S samples) sections. SST = sea surface temperature; MAT = mean air annual temperature; pH = soil pH and BIT index = Branched isoprenoidal tetraethers index.

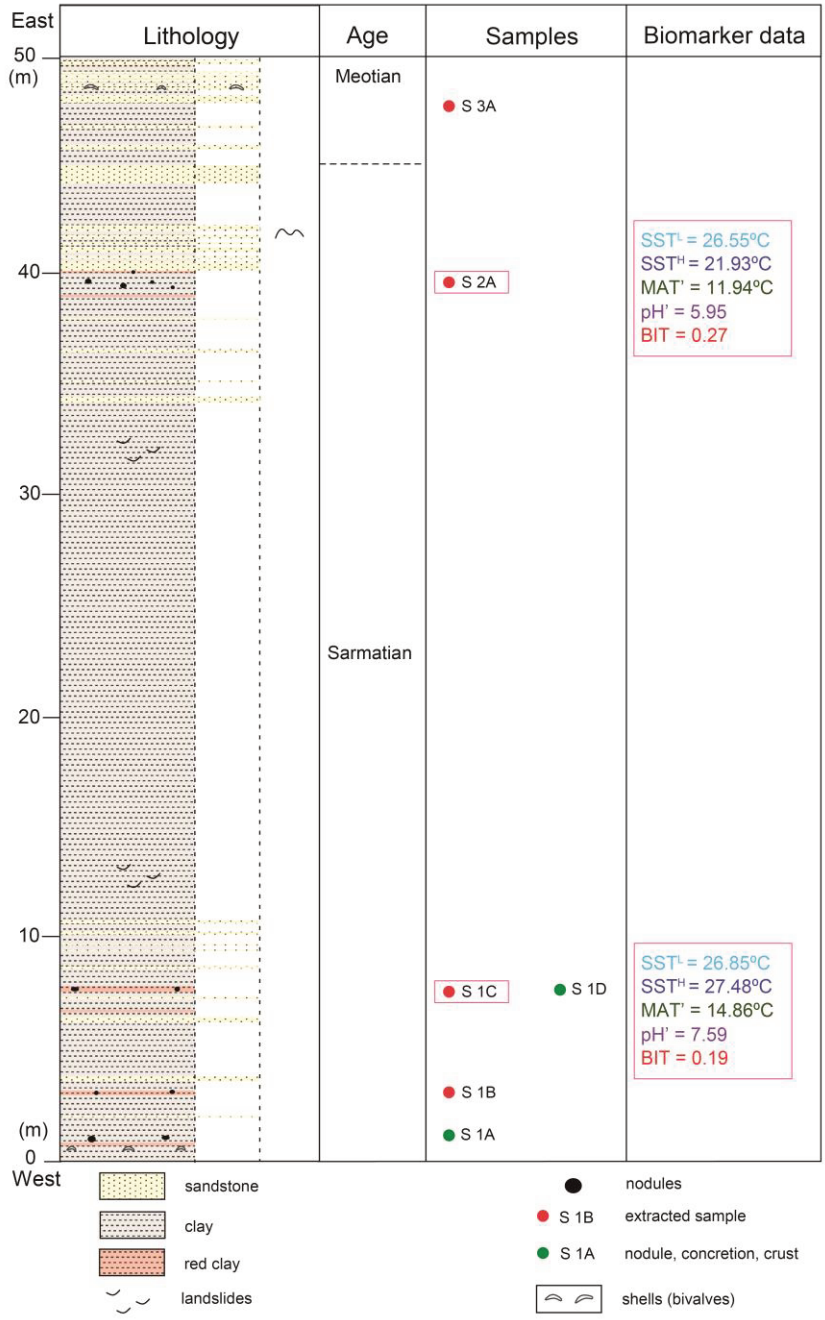

Figure 8.12 Slănic lithostratigraphic log together with preliminary organic geochemistry data. With red rectangles are marked the samples measured for biomarkers and the results. SST = sea surface temperature; MAT = mean air annual temperature; pH = soil pH and BIT index = Branched isoprenoidal tetraethers index.

8.3.3 Preliminary remarks

Measured SST^H data from Putna section (Table 8.4; Figure 8.11) vary between ~20 to 28 °C, showing a large variation. SST^L are overall smaller (~15 to 26 °C), but following the same trend

as SST^H. MAT' ranges between ~6 and 12 °C, indicating an overall lower temperature onland, probably due to the higher topography of the catchment area as the Carpathians were forming (Tărăpoancă, 2004). As the Dacian Basin functioned as a semi-inclosed area during Meotian (Jipa and Olariu, 2009), most probably we observe a decoupling of the marine and continental systems, with waters much warmer than the rest of the area. pH values range between ~6.9 and 7.4, with a mean value of 7.17. BIT values vary between 0.76 and 0.95, indicating an overall increased terrigenous organic matter input. This can be the result of the proximity of the orogeny area, paleo-valleys dejecting sediments directly in the basin.

For Slănic section, the SST^H data (Figure Table 8.4; Figure 8.12) show SST^H of ~27 °C in the base (sample S 1C) and MAT' of ~15 °C. The pH for the analyzed sample is 7.59, while BIT index value is 0.19. The sample in the top (S 2A) registers lower temperatures, with SST^H of ~22 °C and MAT' of ~12 °C. The pH in this case is more acidic (5.95), while BIT index is scoring 0.27. S 1C sample registers the lowest pH and BIT values in the Carpathian foredeep. The sedimentation also changes after this sample, more sandstones forming, indicating an increased coarse sediment supply in the basin at the section location.

References

Bozkurt, E., Sözbilir, H., 2006. Evolution of the Large scale active Manisa Fault, Soutwest Turkey: Implications on Fault Development and Regional Tectonics. Geodinamica Acta 19 (6), 427–453.

Coplen T.B., Kendall C., Hopple J., 1983. Comparison of stable isotope reference samples. Nature, 302(5905), 236.

Evstatiev, D., Evlogiev, Y., 2013. Landslides along the Northern Black Sea coast between Vara city and Kavarna town (Bulgaria). Geo-Eco-Marina 19, 39−57.

Hopmans, E.C., Weijers, J.W.H., Schefuss, E., Herfort, L., Sinninghe Damsté, J.S., Schouten, S., 2004. A novel proxy for terrestrial organic matter in sediments based on branched and isoprenoid tetraether lipids. Earth and Planetary Science Letters, 224, 107–116.

Jipa, D.C., Olariu, C., 2009. Dacian Basin. Depositional Architectre and Sedimentary History of a Paratethys Sea. Geo-Eco-Marina. Special Publication no.3.

Kaysery, Özer, M.S., Akgün, F., Mayda, S., Kaya, T., 2014. Palynofloras and vertebrates from Muğla-Ören region (S-W Turkey) and paleoclimate of the Middle Burdigalian-Langhian period in Turkey. Bulletin of Geosciences 89 (1). DOI 10.3140/bull.geosci.1407.

Kim, J.H., van der Meer, J., Schouten S., Helmke, P., Willmot, V., Sangiorgi, F., Koç, N., Hopmans, E.C., Sinninghe Damsté, J.S., 2010. New indices and calibrations derived from the distribution of crenarchaeal isoprenoid tetraether lipids: Implications for past sea surface temperature reconstructions. Geochimica et Cosmochimica Acta, 74, 4639–4654.

Koleva-Rekalova, E., 2001. Attemt for correlation of the Miocene (Sarmatian)aragonite sediments from North Bulgaria. Comptes rendus de l'Académie bulgare des Sciences, Tome 54 (12), 67−72.

Özkaymak, Ç., Sözbilir, H., 2008. Stratigraphic and Structural Evidence for Fault Reactivation: The Active Manisa Fault Zone, Western Anatolia. Turkish Journal of Earth Sciences 17, 615–635.

Peterse, F., van der Meer, J., Schouten, S., Weijers, J.W.H., Fierer, N., Jacckson, R.B., Kim, J.-H., Sinninghe Damsté, J.S., 2012. Revised calibration of the MBT-CBT paleotemperature proxy based on branched tetraether membrane lipids in surface soils. Geochimica et Cosmochimica Acta, 96, 215–229.

Schouten, S., Hopmans, E.C., Schefuβ, E., Sinninghe Damsté, J.S., 2002. Distributional variations in marine crenarchaeotal membrane lipids: a new tool for reconstructing ancient sea water temperatures? Earth and Planetary Science Letters, 204, 265–274.

Shanov, S., 2005. Post-Cretaceous to recent stress fields in the SE Moesian Platform (Bulgaria). Tectonophysics 410, 217−233.

Spötl, C., Vennemann, T.W., 2003. Continous-flow isotope ratio mass spectrometric analysis of carbonate minerals. Rapid Communications in Mass Spectrometry17, 1004-1006.

Tărăpoancă, M., 2004, Architecture, 3D geometry and tectonic evolution of the Carpathians foreland basin: Netherlands Research School of Sedimentary Geology (NSG), publication no. 2004.01.03 (PhD thesis).

Chapter 9

Summary and outlook

9.1 Summary

This thesis is focusing on the impact of Paratethys and Mediterranean water bodies over the Eurasian climate and the interplay between climate, tectonics and biosphere during the late Miocene. This target was the interval between 12.7 and 7.65 Ma for Paratethys, following the Eastern Paratethys restriction and isolation, and 7.2−6.5 Ma (the early Messinian) in Mediterranean, zooming on the effects of gateway restrictions over the eastern Mediterranean and the new born Aegean domain. In both cases restriction is overlapping with large scale climatic changes and tectonic reconfiguration, leading a sort of symbiotic relationship.

Paratethys was a giant epicontinental sea that covered a large part of Eurasia since Paleogene. Due to the Eurasia-Afro-Arabia collision and formation of the Alpine-Himalayan belt (Rögl, 1999; Popov et al., 2006), the Paratethys was divided during the late Miocene in smaller basins that in time were isolated of each other. The protracted isolation and intense continentalisation of paratethyan realm led to changes in humidity distribution, basin connectivity, sediment sources and salinity. These changes had in turn major consequences over water circulation, water availability, vegetation cover and biota. These changes are more intense after 11.6 Ma, when the Eastern Paratethys lost any sustained marine connection, evolving into an enclosed system with endemic fauna (Harzhauser and Piller, 2007).

Mediterranean Sea is a Mezozoic oceanic relic squeezed between Africa, Europe, Anatolia and Arabia, as Africa continued to subduct beneath the European plate. As opposed to Paratethys, it maintained the open connection with the ocean until Messinian, when the two Atlantic gateways (Betic and Rifian corridors) closed for a short time, isolating the basin. The cut off resulted in a dramatic drop down and onset of evaporitic precipitation in marginal basins, the event receiving the name of Messinian Salinity Crisis (5.97−5.55). The restriction affected all marine ecosystems, due to changes in salinity and stratification of water column.

The main objectives of this thesis were:

(1) build valid paleo-temperatures records for both basins based on biomarkers;

(2) reconstruct the hydrology for the late Miocene time interval;

(3) identify vegetation composition and changes;

(4) identify paleo-fires in the late Miocene sediment records;

(5) identify the biotic response to the overall climate and tectonic changes.

All the above objectives were attained with results published in specific journals (Chapters 5−7).

Based on **Panagia section** (Taman Peninsula, Russia) the longest Paratethys temperature record was completed (~5 Myr), covering the interval between 12.7 and 7.65 Ma. A comprehensive SST and MAT records was obtained, as well as soil pH and carbon ($\delta^{13}C$) and hydrogen ($\delta^{2}H$) stable isotopic compositions on *n*-alkanes and alkenones. The main findings are concentrated around three prolonged periods with severe droughts affecting the late Miocene circum-Paratethys region peaking at 9.65, 9.4 and 7.9 Ma, associated with a transition towards open land vegetation, intensification of fire activity and enhanced evaporation and aridity.

The time intervals with dryer conditions recorded in Panagia coincide with periods of mammal turnover and dispersal in Eurasia indicating that major environmental changes occurred in the circum-Paratethys region and Paratethys fragmentation had a great impact on the terrestrial ecosystems, when periods of prolonged droughts generated biotic crises and animal displacements across the Eurasian continent. The $\delta^{13}C_{C29n\text{-alkane}}$ values and charcoal morphologies from Panagia indicate an increased contribution of C_4 plants adapted to drier conditions at 9.66 Ma. Similarly high $\delta^{13}C_{C29n\text{-alkane}}$ values continue until 9.4 Ma, when in Western Europe increased seasonality accelerated the demise of the evergreen subtropical woodlands and expansion of grasslands from Anatolia and Middle East to Europe.

As a result of basin fragmentation and climatic stress, the Eastern Paratethys sub-basins progressively lost their marine properties and turned into brackish-fresh water bodies fed primarily by riverine input. The shallower areas became in time emerged, obstructing connections and isolating the biota, inducing rapid adjusting or extinctions. Thus, the Paratethys harbored a highly endemic fauna (Rögl, 1999), such as dwarf whales, dolphins, seals (among mammals), as well as fish and other taxa (mollusks, ostracods, diatoms, foraminifera, algae, etc.).

Collectively the data structured and analyzed in chapter five support a model in which the Eastern Paratethys evolved as a largely (en)closed system, registering paleoenvironmental signals that are governed by interbasinal connectivity (or lack of it) and regional climate changes in the basin catchment. Acting as an important source of humidity for Western and Central Asia, the size and areal extent of the Paratethys water body is likely to have had a major impact on hydroclimate patterns in the Eurasian interior, with the cumulative fluctuations in both hydrology and surface temperature enhancing the aridity and seasonality, with different partition of moisture over the year. Our combined data suggests a decoupling of Paratethys from the global system as isolation advanced, dominated by regional tectonics and ultimately the Paratethys volume and areal extent reduction.

The Mediterranean datasets based on **Agios Myron** section (Crete, Greece; 7.2−6.5 Ma) cover a plenora of biomarker based proxies (SSTs both on GDGTs and alkenones, SSSs, MATs, pH, BIT), as well as stable isotope data ($\delta^{13}C$ on *n*-alkanes, $\delta^{2}H$ on alkenones, $\delta^{18}O$ on planktonic foraminifera, $\delta^{13}C$ and $\delta^{18}O$ on bulk sedimentary rocks). The large number of used proxies is bringing new insights into the pre-MSC time interval, revealing that the Mediterranean was already passing through major environmental issues, being marked by at least two smaller crises peaking at ~7.0 and 6.82 Ma (and a possible third one starting at 6.6 Ma), progressing in intensity throughout the early Messinian. These smaller scale events are characterized by high water temperatures, hypersalinity and increased evaporation in the marine domain, decoupled from the continental influence. This work highlights the severity of preconditioning stages leading to the Messinian Salinity Crisis in the Mediterranean and sets values for extreme salinity conditions that could still host marine life, mostly small size taxa. During the salinity increase identified in the eastern Mediterranean from 6.9 to 6.7 Ma, faunal diversity decreased as the eastern Mediterranean basin turned into a warm and hypersaline pool with increased environmental stress. Increased runoff and continental inputs from North Africa, Anatolia and continental Greece resulted in the freshening of surface waters, now quantified in chapter six, and led to the reduction of the vertical circulation and enhanced water column stratification during warm intervals, as well as major algae bloomings due to enhanced eutrophication.

Additionally, an orbitally paced climate is superimposed over the gateway restriction and local tectonic movements in the Aegean domain. The climate oscillations are in phase with

precession indicating a solar insolation as the primary driver, with subordinate controls through tectonic and glacio-eustatic processes.

Onland, a progressive change towards dominant C_4 vegetation is registered, associated with overall cooling temperatures. The $\delta^{13}C_{n\text{-alkanes}}$ data presented here offers a first isotope-based reporting of changes towards plants adapted to drier habitats appearing already at ~7 Ma in the Mediterranean. The presence of xerophytic elements in the area during the Messinian (Ioakim et al., 2005; Böhme et al., 2017), vegetation characteristic to open and dry landscapes, coincides with the first dunes in North Africa (Schuster et al., 2006), linking the extensive Saharan and Mediterranean domain aridisation with the global cooling.

Collectively, the Agios Myron data confirm and quantify the presence of restricted conditions in the eastern Mediterranean since the early Messinian and reveal an ongoing isolation and aridification of the Mediterranean domain, both under tectonic (acting mostly over the local accommodation space and regional basin connection) and global climate influence (with great impact over moisture and vegetation). Although the entire Mediterranean Basin was subjected to restriction as a consequence of altered Atlantic gateways (Flecker et al., 2015), Agios Myron registers also a local signal, induced by the development of the Heraklion basin, which shallows considerably between ~6.85−6.6 Ma (Zachariase et al., 2021), an overlap between a global/regional (i.e. northern hemisphere glaciation; Atlantic-Mediterranean gateway restrictions) and local signals being identified in other in other marginal basins the western Mediterranean Basin too (Bulian et al., 2022). Agios Myron currently provides the only early Messinian MAT record in the Mediterranean and the only $\delta^{13}C_{n\text{-alkanes}}$ and $\delta^{2}H_{alkenones}$ for this time period.

With the new datasets, both Panagia and Agios Myron sections became reference sections for the eastern Paratethys and eastern Mediterranean domains.

Additionally, preliminary biomarker data from other sections in Bulgaria and Romania are presented (central and eastern Paratethys), as well as $\delta^{13}C$ and $\delta^{18}O$ on bulk sedimentary rocks from Turkey (the continental bridge between Paratethys and Mediterranean). The paratethyan data sets present similarities with Panagia, but dating was not yet possible.

9.2 Outlook

As both Paratethys and Mediterranean were fragmented during the late Miocene, the newly basins evolved separately having a different climatic and organic signal. With this in mind, the future steps should be concentrated in getting a valid dataset for each basin in order to properly discriminate between the global and local signal, tectonic and climatic, as organic geochemistry is still an 'infant' science. For Paratethys, data from Romania, Bulgaria and Turkey in chapter 8 are paving this road, but proper sampling and dating should be done for the entire Dacian basin, Pannonian and Vienna basins in order to assess the general climatic picture. The Mediterranean is a bit better pictured, but the focus was mostly on the western side due to the Atlantic connectivity and the Messinian Salinity Crisis. The natural approach would be to look also outside of this perimeter and analyze the entire late Miocene.

Another important step would be the investigation of biological events, both extinction and speciation, with organic geochemistry, chemistry and stable isopes tools, in order to understand the exact changes in the water column when these events happened. Understanding how marine organisms behave in time of crises is extremely important also in modern context as the temperature and acidity of the planetary ocean is rapidly increasing. The rapid changes in the Paratethys-Mediterranean domain and the impact over biota populating it can be used as a possible analogue for the future Earth marine system as is the closest major crisis in the Earth's history. The enhanced aridisation and evaporation associated with interupted connectivity are also important as more rivers are damed, starving in water and sediments the drainage basins, leading to basinal crises (e.g. Aral Sea).

References

Böhme, M., Spassov, N., Ebner, M., Geraads, D., Hristova, L., Kirscher, U., Kötter, S., Linnemann, U., Prieto, J., Roussiakis, S., Theodorou, G., Uhlig, G., Winklhofer, M., 2017. Messinian age and savannah environment of the possible hominin Graecopithecus from Europe. Plos one.

Bulian, F., Kouwenhoven, T.J., Jim´enez-Espejo, F.J., Krijgsman, W., Andersen, N., Sierro, F.J., 2022. Impact of the Mediterranean-Atlantic connectivity and the late Miocene carbon shift on deep-sea communities in the Western Alboran Basin. Palaeogeogr. Palaeoclimatol. Palaeoecol. 589, 110841 https://doi.org/10.1016/j. palaeo.2022.110841.

Flecker, R., Krijgsman, W., Capella, W., de Castro Martíns, C., Dmitrieva, E., Mayser, J.P., Marzocchi, A., Modestu, S., Ochoa, D., Simon, D., Tulbure, M., van den Berg, B., van der Schee, M., de Lange, G., Ellam, R., Govers, R., Gutjahr, M., Hilgen, F., Kouwenhoven, T., Lofi, J., Meijer, P., Sierro, F.J., Bachiri, N., Barhoun, N., Alami, A. C., Chacon, B., Flores, J.A., Gregory, J., Howard, J., Lunt, D., Ochoa, M., Pancost, R., Vincent, S., Yousafi, M.Z., 2015. Evolution of the Late Miocene Mediterranean–Atlantic gateways and their impact on regional and global environmental change. Earth-Science Reviews, 150, 365–392. https://doi.org/10.1016/j.earscirev.2015.08.007

Harzhauser, M., and Piller, W.E., 2007. Benchmark data of a changing sea − Palaeogeography, Palaeobiogeography and events in the Central Paratethys during the Miocene: Palaeogeography, Palaeoclimatology, Palaeoecology, 253 (1–2), 8–3. doi:10.1016/j.palaeo.2007.03.031.

Ioakim, C., Rondoyanni, T., Mettos, A., 2005. The Miocene Basins of Greece (Eastern Mediterranean) from a palaeoclimatic perspective. Revue de Paléobiologie, Genève 24, 2.

Popov, S.V., Shcherba, I.G., Iluina, L.B., Nevesskaya, L.A., Paramonova, N.P., Khondkarian, S.O., Magyar, I., 2006. Late Miocene paleogeography of the Paratethys and its relation to the Mediterranean. Palaeogeography, Palaeoclimatology, Palaeoecology, 238, 91–106.

Rögl, F., 1999. Mediterranean and paratethys. Facts and hypotheses of an Oligocene to Miocene Paleogeography (short overview): Geologica Carpathica, 50 (4), 339–349.

Schuster, M., Duringer, P., Ghienne, J.F., Vignaud, P., Mackaye, H.T., Likius, A., Brunet, M., 2006. The age of the Sahara Desert. Science, 311, 821–821. DOI: 10.1126/science.1120161

Zachariasse, W.J., Kontakiotis, G., Lourens, L.J., Antonarakou, A., 2021. The Messinian of Agios Myron (Crete, Greece): A key to better understanding diatomite formation on Gavdos (south of Crete). Palaeogeography, Palaeoclimatology, Palaeoecology, 581. https://doi.org/10.1016/j.palaeo.2021.110633

Chapter 10

Zusammenfassung und Ausblick

10.1 Zusammenfassung

Diese Arbeit befasst sich mit dem Einfluss der Paratethys und der mediterranen Wasserkörper auf das eurasische Klima und dem Zusammenspiel von Klima, Tektonik und Biosphäre im späten Miozän. Die Zielintervalle dieser Arbeit liegen zwischen 12.7 und 7.65 Mio. Jahre für die Paratethys, im Anschluss an die östliche Paratethys-Beschränkung und Isolierung, und zwischen 7.2 und 6.5 Mio. Jahre (frühe Messinian) im Mittelmeerraum, wodurch die Auswirkungen der Gateway-Beschränkungen auf das östliche Mittelmeer und die neu entstandene Ägäis-Domäne untersucht wurden. In beiden Fällen überschneiden sich die Beschränkungen mit großräumigen klimatischen Veränderungen und tektonischen Umgestaltungen, was zu einer Art symbiotischer Beziehung führt.

Die Paratethys war ein riesiges epikontinentales Meer, das seit dem Paläogen einen großen Teil Eurasiens bedeckte. Infolge der Kollision zwischen Eurasien, Afrika und der Arabischen Halbinsel und der Bildung des Alpen-Himalaya-Gürtels (Rögl, 1999; Popov et al., 2006) wurde die Paratethys im späten Miozän in kleinere Becken aufgespalten, die im Laufe der Zeit voneinander isoliert wurden. Die langfristige Isolierung und die intensive Kontinentalisierung des paratethysischen Raums führten zu Veränderungen in der Feuchtigkeitsverteilung, der Verbindung der Becken, den Sedimentquellen und dem Salzgehalt. Diese Veränderungen hatten wiederum erhebliche Auswirkungen auf die Wasserzirkulation, die Wasserverfügbarkeit, die Vegetationsdecke und die Biota. Diese Veränderungen sind nach 11.6 Mio. Jahren am stärksten, als die östliche Paratethys jede dauerhafte Meeresverbindung verlor und sich zu einem geschlossenen System mit endemischer Fauna entwickelte (Harzhauser und Piller, 2007).

Das Mittelmeer ist ein ozeanisches Relikt aus dem Mesozoikum, das zwischen Afrika, Europa, Anatolien und der Arabischen Halbinsel eingeklemmt ist, während sich Afrika weiterhin unter die europäische Platte absenkt. Im Gegensatz zur Paratethys blieb das Mittelmeer bis zum

Messinium mit dem Ozean verbunden, bevor sich die beiden atlantischen Einfallstore (betischer und rifischer Korridor) für kurze Zeit schlossen und das Becken somit isolierten. Die Unterbrechung führte zu einem dramatischen Rückgang und mächtigen Evaporitablagerungen in den Randbecken, was dem Ereignis den Namen Messinische Salinitätskrise (5.97−5.55 Mio. Jahre) einbrachte. Die Einschränkung wirkte sich auf alle marinen Ökosysteme aus, da sich der Salzgehalt und die Schichtung der Wassersäule veränderten.

Die Hauptziele dieser Arbeit waren:

(1) Erstellung gültiger Paläo-Temperaturdaten für beide Becken auf der Grundlage von Biomarker-Analysen;

(2) die Rekonstruktion der Hydrologie für das späte Miozän;

(3) Identifizierung der Vegetationszusammensetzung und ihrer Veränderungen;

(4) Identifizierung von Paläo-Bränden in den Sedimentaufzeichnungen des späten Miozäns;

(5) Ermittlung der biotischen Reaktion auf die allgemeinen Klimabedingungen und tektonische Veränderungen.

Alle oben genannten Ziele wurden mit Ergebnissen belegt, die in speziellen Fachzeitschriften veröffentlicht wurden (Kapitel 5−7).

Auf der Grundlage des Panagia-Abschnitts (Taman-Halbinsel, Russland) wurde die längste Temperaturaufzeichnung der Paratethys (~5 Myr) vervollständigt, die den Zeitraum zwischen 12.7 und 7.65 Mio. Jahre abdeckt. Es wurden umfassende SST- und MAT-Daten sowie der pH-Wert des Bodens und die stabile Isotopenzusammensetzung von Kohlenstoff ($\delta^{13}C$) und Wasserstoff ($\delta^{2}H$) in *n*-Alkanen und Alkenonen ermittelt. Die wichtigsten Ergebnisse konzentrieren sich auf drei längere Perioden mit schweren Dürren in der spätmiozänen Zirkum-Paratethys-Region, die bei 9.65, 9.4 und 7.9 Mio. Jahre ihren Höhepunkt erreichten und mit einem Übergang zu einer offenen Landvegetation, einer Intensivierung der Feueraktivität und einer erhöhten Verdunstung und Trockenheit einhergingen.

Die in Panagia aufgezeichneten Zeitintervalle mit trockeneren Bedingungen fallen mit Perioden der Säugetierfluktuation und -ausbreitung in Eurasien zusammen, was darauf hindeutet,

dass in der Zirkum-Paratethys-Region große Umweltveränderungen stattfanden und die Fragmentierung der Paratethys große Auswirkungen auf die terrestrischen Ökosysteme hatte. Demzufolge verursachten Perioden lang anhaltender Dürren biotische Krisen und Tierverschiebungen auf dem eurasischen Kontinent.. Die $\delta^{13}C_{C29n\text{-Alkan}}$-Werte und die Morphologie der Holzkohle aus Panagia deuten auf einen erhöhten Beitrag von C_4-Pflanzen hin, die an trockenere Bedingungen um 9.66 Mio. Jahre angepasst waren. Ähnlich hohe $\delta^{13}C_{C29n\text{-Alkan}}$ Werte setzen sich bis 9.4 Mio. Jahre fort, als in Westeuropa die zunehmende Saisonalität den Niedergang der immergrünen subtropischen Wälder und die Ausbreitung von Grasland aus Anatolien und dem Nahen Osten nach Europa beschleunigte.

Infolge der Beckenfragmentierung und des Klimastresses verloren die östlichen Paratethys-Teilbecken nach und nach ihre marinen Eigenschaften und wurden zu brackig-frischen Gewässern, die hauptsächlich durch Flusseinleitungen gespeist wurden. Die flacheren Gebiete wurden im Laufe der Zeit immer tiefer, wodurch die Verbindungen unterbrochen und die Biota isoliert wurden, was zu einer schnellen Anpassung oder zum Aussterben führte. So beherbergte die Paratethys eine hochgradig endemische Fauna (Rögl, 1999), wie z.B. Zwergwale, Delphine, Robben (unter den Säugetieren), sowie Fische und andere Taxa (Mollusken, Ostrakoden, Kieselalgen, Foraminiferen, Algen, etc.).

Insgesamt stützen die in Kapitel 5 strukturierten und analysierten Daten ein Modell, in dem sich die östliche Paratethys als ein weitgehend (ab-)geschlossenes System entwickelte, das paläoökologische Signale registrierte, die von der interbasinalen Konnektivität (oder deren Fehlen) und regionalen Klimaveränderungen im Einzugsgebiet des Beckens bestimmt wurden. Als wichtige Feuchtigkeitsquelle für West- und Zentralasien hatten Größe und Ausdehnung des Paratethys-Wasserkörpers wahrscheinlich einen großen Einfluss auf die hydroklimatischen Muster im eurasischen Landesinneren, wobei die kumulativen Schwankungen der Hydrologie und der Oberflächentemperatur die Trockenheit und die Saisonabhängigkeit verstärkten und die Feuchtigkeit im Jahresverlauf unterschiedlich verteilten. Unsere kombinierten Daten deuten darauf hin, dass sich die Paratethys im Zuge der fortschreitenden Isolation vom globalen System abkoppelte, wobei die regionale Tektonik und letztlich die Verringerung des Volumens und der Flächenausdehnung der Paratethys im Vordergrund stehen.

Die mediterranen Datensätze, die auf dem Abschnitt Agios Myron (Kreta, Griechenland; 7.2−6.5 Mio. Jahre) basieren, umfassen eine Vielzahl von Biomarker-basierten Proxies (SSTs

sowohl von GDGTs als auch von Alkenonen, SSSs, MATs, pH, BIT) sowie stabile Isotopendaten ($\delta^{13}C$ von *n*-Alkanen, $\delta^{2}H$ von Alkenonen, $\delta^{18}O$ von planktonischen Foraminiferen, $\delta^{13}C$ und $\delta^{18}O$ von Sedimentgestein). Die große Zahl der verwendeten Proxies ermöglicht neue Einblicke in das Zeitintervall vor der MSC und zeigt, dass der Mittelmeerraum bereits große Umweltveränderungen durchlief, die durch mindestens zwei kleinere Krisen gekennzeichnet waren, die ihren Höhepunkt bei ~7.0 und 6.82 Mio. Jahren erreichten (und eine mögliche dritte, die bei 6.6 Mio. Jahren begann) und während des frühen Messiniums an Intensität zunahmen. Diese kleineren Ereignisse sind durch hohe Wassertemperaturen, Hypersalinität und erhöhte Verdunstung im marinen Bereich gekennzeichnet, der vom kontinentalen Einfluss abgekoppelt war. Diese Arbeit unterstreicht die Schwere der Vorstufen, die zur Messinischen Salinitätskrise im Mittelmeer geführt haben, und legt Werte für extreme Salzgehalte fest, bei denen nur noch wenige Meerslebewesen, vor allem kleine Taxa, überleben konnten. Während des im östlichen Mittelmeer festgestellten Anstiegs des Salzgehalts zwischen 6.9 und 6.7 Mio. Jahren nahm die Vielfalt der Fauna ab, da sich das östliche Mittelmeer zu einem warmen und hypersalinen Becken mit erhöhtem Umweltstress entwickelte. Erhöhte Abflüsse und kontinentale Einträge aus Nordafrika, Anatolien und dem griechischen Festland führten zu einer Auffrischung des Oberflächenwassers, die in Kapitel 6 quantifiziert wurden, und des Weitern zu einer Verringerung der vertikalen Zirkulation und einer verstärkten Schichtung der Wassersäule während der warmen Perioden sowie zu großen Algenblüten aufgrund einer verstärkten Eutrophierung.

Zusätzlich überlagerte ein orbital getaktetes Klima die Gateway-Beschränkung und die lokalen tektonischen Bewegungen in der Ägäis. Die Klimaschwankungen sind phasengleich mit dem Präzession-Zyklus, was auf die Sonneneinstrahlung als primäre Antriebskraft hinweist, mit untergeordneter Steuerung durch tektonische und eustatische Prozesse.

Im Landesinneren ist eine fortschreitende Veränderung hin zu einer dominanten C_4-Vegetation zu beobachten, die mit einer allgemeinen Abkühlung der Temperaturen einhergeht. Die hier vorgestellten $\delta^{13}C_{n\text{-}Alkan}$-Daten bieten einen ersten isotopenbasierten Einblick über Vegetationsveränderungen hin zu Pflanzen, die an trockenere Lebensräume angepasst waren und bereits bei ~7 Mio. Jahren im Mittelmeerraum auftraten. Das Vorhandensein xerophytischer Elemente in dem Gebiet während des Messiniums (Ioakim et al., 2005; Böhme et al., 2017), einer Vegetation, die für offene und trockene Landschaften charakteristisch ist, fällt mit den

ersten Dünen in Nordafrika zusammen (Schuster et al., 2006), was die weitgehende Aridisierung der Sahara und des Mittelmeerraums mit der globalen Abkühlung in Verbindung bringt.

Insgesamt bestätigen und quantifizieren die Daten von Agios Myron das Vorhandensein eingeschränkter Bedingungen im östlichen Mittelmeerraum seit dem frühen Messinium und zeigen eine anhaltende Isolierung und Aridifizierung des Mittelmeerraums, die sowohl unter tektonischem (vor allem über den lokalen Akkommodationsraum und die regionale Beckenverbindung) als auch unter globalem Klimaeinfluss (mit großen Auswirkungen auf Feuchtigkeit und Vegetation) stattfand. Obwohl das gesamte Mittelmeerbecken als Folge der veränderten atlantischen Gateways einer Restriktion unterworfen war (Flecker et al., 2015), registrierte Agios Myron auch ein lokales Signal, das durch die Entwicklung des Heraklion-Beckens ausgelöst wurde, das sich zwischen ~6.85-6.6 Mio. Jahren deutlich abflacht (Zachariase et al., 2021), wobei eine Überschneidung zwischen globalen/regionalen (z.B. Vergletscherung der Nordhemisphäre; Beschränkungen des atlantisch-mediterranen Gateways) und lokalen Signalen auch in anderen Randbecken des westlichen Mittelmeerraums festgestellt wurde (Bulian et al., 2022). Agios Myron liefert derzeit die einzige frühmessinische MAT-Aufzeichnung im Mittelmeerraum und die einzigen $\delta^{13}C_{n\text{-}Alkane}$ und $\delta^{2}H_{alkenone}$ -Daten für diesen Zeitraum.

Mit den neuen Datensätzen wurden die beiden Abschnitte Panagia und Agios Myron zu Referenzabschnitten für die östliche Paratethys und den östlichen Mittelmeerraum.

Darüber hinaus werden vorläufige Biomarkerdaten aus anderen Abschnitten in Bulgarien und Rumänien (zentrale und östliche Paratethys) sowie $\delta^{13}C$ und $\delta^{18}O$ aus Massensedimentgestein aus der Türkei (der kontinentalen Brücke zwischen Paratethys und Mittelmeer) vorgestellt. Die Paratethys-Datensätze weisen Ähnlichkeiten mit Panagia auf, eine Datierung war jedoch noch nicht möglich.

10.2 Ausblick

Da sowohl die Paratethys als auch das Mittelmeer im späten Miozän zersplittert wurden, haben sich die neu entstandenen Becken getrennt voneinander entwickelt und ein unterschiedliches klimatisches und organisches Signal erhalten. Vor diesem Hintergrund sollten sich die zukünftigen wissenschaftlichen Bemühungen darauf konzentrieren, für jedes Becken einen gültigen Datensatz zu ermitteln, um zwischen dem globalen und dem lokalen tektonischen und klimatischen Signal unterscheiden zu können. Für die Paratethys ebnen die Daten aus Rumänien, Bulgarien und der Türkei in Kapitel 8 diesen Weg, doch sollten für das gesamte Daker-Becken, das Pannonische und das Wiener Becken geeignete Probenahmen und Datierungen vorgenommen werden, um das allgemeine Klimabild zu bewerten. Der Mittelmeerraum ist etwas besser abgebildet, aber der Schwerpunkt lag aufgrund der atlantischen Verbindung und der messinischen Salinitätskrise hauptsächlich auf dem westlichen Mittelmeerraum. Der natürliche Ansatz wäre, auch außerhalb dieses Gebiets zu schauen und das gesamte späte Miozän zu analysieren.

Ein weiterer wichtiger Schritt wäre die Untersuchung der biologischen Ereignisse, sowohl des Aussterbens als auch der Speziation, mit Hilfe der organischen Geochemie, der Chemie und der stabilen Isotope, um die genauen Veränderungen in der Wassersäule zu verstehen als diese Ereignisse stattfanden. Zu verstehen, wie sich Meeresorganismen in Krisenzeiten verhalten ist auch in der heutigen Zeit äußerst wichtig, da sowohl die Temperatur als auch der Säuregehalt des Ozeans rapide ansteigen. Die raschen Veränderungen in der Paratethys-Mittelmeer-Domäne und die Auswirkungen auf die sie bevölkernden Biota können als mögliche Analogie für das künftige marine System der Erde herangezogen werden, da es sich um die nächste große Krise in der Erdgeschichte handelt. Die verstärkte Aridisierung und Verdunstung, die mit der unterbrochenen Verbindung einhergehen, sind ebenfalls von Bedeutung, da immer mehr Flüsse gestaut werden, wodurch die Einzugsgebiete an Wasser und Sedimenten verarmen, was zu Umweltkrisen führt (z. B. Aralsee).

Appendices

(A1) Appendix to chapter 5: Severe late Miocene droughts affected Western Eurasia

Geanina A. Butiseacă, Iuliana Vasiliev, Marcel T.J. van der Meer, Wout Krijgsman, Dan V. Palcu, Angelica Feurdean, Eva M. Niedermeyer, Andreas Mulch

Organic geochemistry methods

1. Lipid extraction, fractions separation and analyses

Fifty-seven sedimentary rock samples weighing between 14 and 32 g were dried and thoroughly ground using agate mortar and pestle. Lipids of the powdered samples were extracted using a Soxhlet apparatus with a mixture of dichloromethane (DCM) and methanol (MeOH) 9:1 (*v:v*) and pre-extracted cellulose filters. All extracts were evaporated to near dryness under nitrogen flow using a TurboVap LV. Subsequently, the elemental sulphur was removed using Cu shreds. The Cu was first activated using 10% HCl, the acid was removed with demineralized water and the Cu was further cleaned using MeOH and DCM. The vials containing total lipids extracts (TLE), activated Cu and magnetic stirrer bars were placed on a rotary table for >16 hours. Afterwards, the TLEs were filtered over a Na_2SO_4 column to remove Cu and water. The remaining solvents were evaporated using N_2. The desulphurization step was repeated up to 13 times until no reaction with the Cu was observed.

A fraction of the TLE was archived. The rest was then separated into fractions containing different lipids using Al_2O_3 column chromatography. The apolar fraction was eluted using a mixture of *n*-hexane and DCM (9:1, *v:v*), followed by a ketone fraction using DCM, while a mixture of DCM/MeOH (1:1, *v:v*) was used to obtain the polar fraction. The apolar fraction containing *n*-alkanes was purified using $AgNO_3$ column. The *n*-alkanes were identified based on mass spectra and retention time using Gas Chromatography-Mass Spectrometry (GC-MS) instrument from the Senckenberg Biodiversity and Climate Research Centre (SBiK-F) in

Frankfurt. The $AgNO_3$ column was successful in purifying ~20% of the samples. The remaining 80% were additionally purified using urea adduction to isolate the strait chain *n*-alkanes. To this end, the apolar fractions containing the saturated *n*-alkanes were dissolved in 200 µl MeOH/urea (~10%, H_2NCONH_2, Merck) solution. Subsequently, 200 µl acetone and 200 µl *n*-hexane were added to the solution, frozen (–20ºC) and dried under N_2 flow. Urea crystals were washed with *n*-hexane to remove the non-adductable branched and cyclic compounds and subsequently dissolved in a 500 µl MeOH and 500 µl MilliQ ultra-pure water mixture. The *n*-alkanes were extracted from the solution using *n*-hexane. After urea adduction the *n*-alkanes were once again measured using the GC–MS. The ketone fraction containing alkenones was occasionally purified using $AgNO_3$ column and ethyl acetate and subsequently measured on the GC-MS. The polar fraction containing GDGTs was dried under a gentile stream of N_2 then dissolved in a 1 ml mixture of *n*-hexane (*n*-hex)/isopropanol (IPA)-(99:1, *v:v*) and slightly dispersed using an ultrasonic bath (up to 30s per sample) and filtered over a 0.45 mm PTFE filter using a 1 ml syringe.

2. HPLC /MS analysis

2.1. HPLC preparation and analysis.

The filtered polar fractions containing GDGTs were analyzed at the Senckenberg-BiK-F laboratory using an HPLC Shimadzu, UFLC performance, Alltech Prevail© Cyano 3 mm, 150 − 2.1 mm analytical column; eluents *n*-hex (A) and IPA (B) coupled with an ABSciex 3200 QTrap chemical ionization mass spectrometer (HPLC/APCIeMS). The injection volume was 5 ml for each sample and GDGTs were eluted isocratically from 0 to 5 min with 1% (B); a gradient to 1.8% (B) from 5 to 32.5 min, ramped to 30% (B) at 33.5 min, held 10 min, and reduced to 1% (B) in 1 min. Detection was achieved through single ion monitoring (scanned masses: 1018, 1020, 1022, 1032, 1034, 1036, 1046, 1048, 1050, 1292, 1296, 1298, 1300, 1302). The polar fraction was re-concentrated in volumes between 0.5 ml to 0.05 ml in the cases where after measurement the GDGTs concentration was found to be too low. We analyzed both isoprenoid and branched GDGTs within a single acquisition run for each sample (Supplementary Figure 5.1). Quantification of GDGTs was performed using Analyst software and the peaks were integrated manually for each sample.

2.2. Temperature calculation

The SST were obtained by using TEX_{86} (TetraEther indeX of tetraethers consisting of 86 carbon atoms) proxy based on the relative abundance of isoGDGT lipids (Schouten et al., 2002). TEX_{86} values were calculated according to the definition of Schouten et al. (2002) as:

TEX_{86}= [(GDGT-1) + (GDGT-2) + (*Cren'*)] /

[(GDGT-0) + (GDGT-1) + (GDGT-2) + (*Cren'*)]

where *GDGT-0*, *GDGT-1, GDGT-2* and *Cren'* are isoprenoid GDGTs with the structures presented in Supplementary Figure 5.2. TEX_{86} values were converted into SST using the calibration and recommendation of Kim et al. (2010) to apply the TEX_{86}^{H} above 15ºC (i.e. outside the polar and subpolar domains):

$SST^{H} = 68.4 \times TEX_{86}^{H} + 38.6$

Here TEX_{86}^{L} is = log ((GDGT-2) / GDGT-1 + GDGT-2 + GDGT-3))

$TEX_{86}^{H} = \log (TEX_{86})$

$SST^{L} = 67.5 \times TEX_{86}^{L} + 46.9$

The distribution of brGDGTs, expressed as the Methylation index of Branched Tetraethers (MBT) and the Cyclisation ratio of Branched Tetraethers (CBT) displays a significant linear correlation with modern MAT in the range of 6 to 27ºC (Weijers et al., 2007a). The initial definition of MAT and pH proxies was subject to subsequent recalibration and refinement (e.g. Peterse et al., 2012; De Jonge et al., 2014). From the multiple existent calibrations, we chose to use Peterse et al., (2012) as a more conservative choice given that the expected environmental changes for the ~ 5 Ma duration of the studied interval are large where:

$MAAT = 0.81 - 5.67 \times CBT + 31 \times MBT'$

$pH = 7.90 - 1.97 \times CBT$

Where MBT' and CBT are expressed as:

MBT'= [(GDGT Ia + GDGT Ib + GDGT Ic)] / [(GDGT Ia + GDGT Ib + GDGT Ic) +

(GDGT IIa + GDGT IIb + GDGT IIIb) + (GDGT IIIa)]

and

CBT= −log (GDGT Ib + GDGT IIb) / (GDGT Ia + GDGT IIa)

where GDGT I − GDGT III are branched GDGTs with the structures presented in Supplementary Figure 5.2.

3. GC-MS purification and analysis of n-alkanes and alkenones.

The apolar fraction containing the *n*-alkanes was purified for GC–MS (at SBiK-F) by using $AgNO_3$ and urea adduction. After the purification the saturated *n*-alkanes were eluted using *n*-hexane. The ketone fraction (alkenones) was also eluted with *n*-hexane, measured and further purified with ethyl acetate (EtAc) when necessary. The fractions (dissolved in *n*-hexane) were injected on-column at 70ºC (CP-Sil 5CB fused silica column (30 m × 0.32 mm i.d.; film thickness 0.1 μm). The oven was set at constant pressure (100 kPa) and then programmed to increase to 130°C at 20°C min^{-1}, and then at 5°C min^{-1} to 320°C at which it was held isothermal for 10 min. *n*-Alkanes were identified using a known external standard mixture (Alk C7-C40 - Supelco 49452-U, 1000 ng/μl).

4. δ^2H analysis on alkenones and n-alkanes

The δ^2H was determined by GC/Thermal Conversion (TC)/ isotope monitoring MS (irMS) using an Agilent GC coupled to a Thermo Electron DELTA Plus XL mass spectrometer, via a Conflo IV. Alkane and alkenone fractions were injected on column-on a RTX column of 60 m length, 0.32 mm, 0.5 um df, using manual injection at the Royal Netherlands Institute for Sea Research (NIOZ) (Weiss et al, 2019). The injection volume was approximately 1-1.5 μl, with the TC reactor set to a temperature of 1425˚C. The daily determined H_3^+ -factor was 6.0 ± 0.3 ppm mV^{-1}. Samples were replicated up to three times depending on the available material and reproducibility, aiming for peaks of approximately 1500 to 2000 mV for compounds of interest. Hydrogen gas with a predetermined isotopic composition was used as monitoring gas for both ketone and apolar fractions and the isotope values were calibrated against in-house lab standards, Mixture B (A. Schimmelmann; Indiana University). For alkenones, a squalane standard was co-injected with every sample and its average value over all analyses was −166 ± 0.3‰. For the alkenones, all C_{37} alkenones were integrated as one single peak for comparison with previous studies as well as obtaining the most robust hydrogen isotope value possible.

5. $\delta^{13}C$ analysis on alkenones and n-alkanes

The carbon isotope ratios ($\delta^{13}C$) of individual *n*-alkanes and alkenones were measured on the purified and adducted apolar and alkenone fractions on the GC-irMS using similar conditions as for $\delta^{2}H$ measurements. The $\delta^{13}C$ values, expressed relative to the V-PDB standard, were calculated by comparison to a CO_2 reference gas (calibrated against NBS-19). Standards deviations were determined using a co-injected standard and are ± 0.3‰.

6. Charcoal preparation and quantification

To evaluate past burning biomass in the region, charcoal particles were extracted from 58 samples, in compliance with the organic geochemistry sampling. From each sample, 2 cm^3 were dissolved in water and then bleached with NaOCl (24 h) to remove organic matter. Samples were further wet-sieved and split into 90 µm, 120 µm and 180 µm fractions. The material was transferred to a Petri dish and examined with an Olympus SZX7 stereomicroscope at 30 x to 60 x magnification. Sedimentary charcoal particles were counted and categorized into 1) poaceae (grass), 2) forbs (other herbaceous plants) and 3) wood (ligneous material) morphotypes following the methodology highlighted in Feurdean and Vasiliev (2019). The charcoal counts of each morphotype were transformed into percentages of the total charcoal counts (Figs 5.4E, 5.5F).

Supplementary figures:

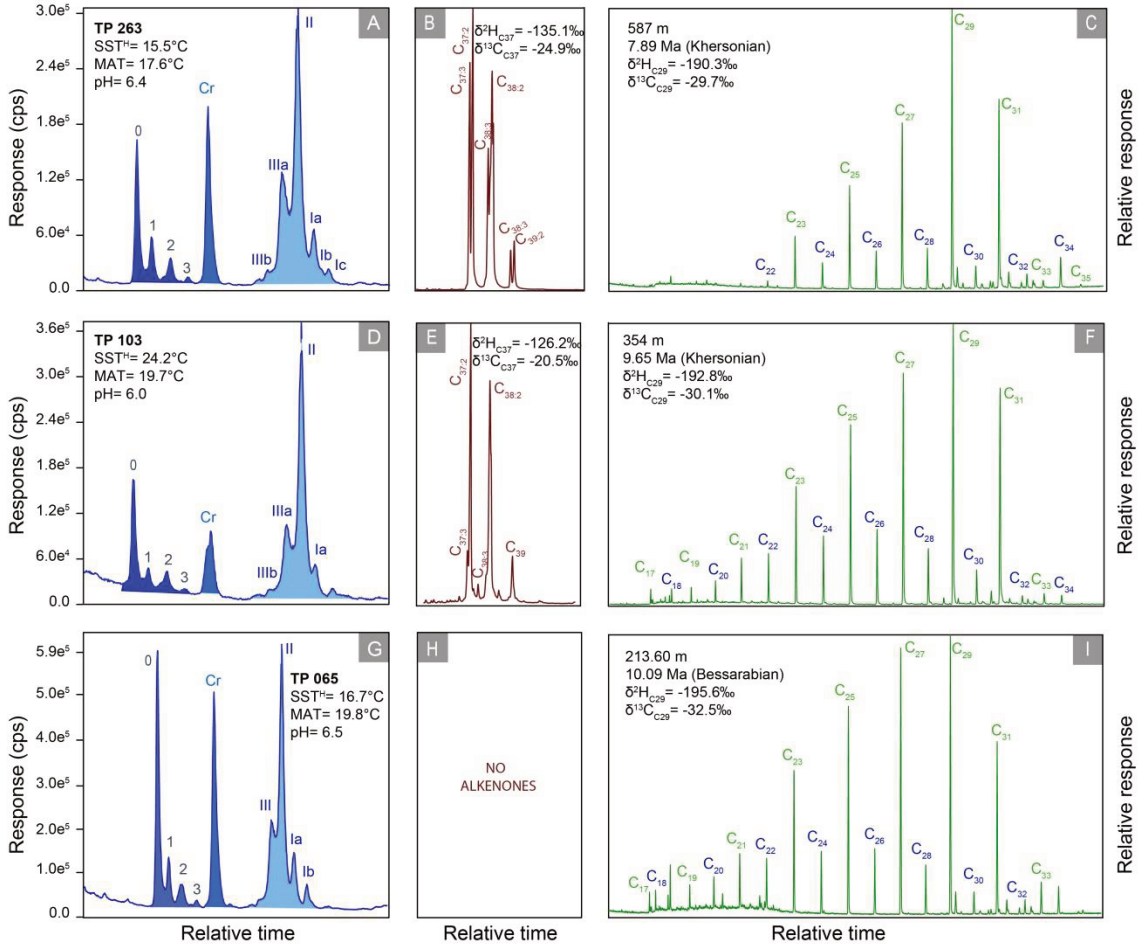

Supplementary figure 5.1 Representative chromatograms of biomarker fractions from Panagia sedimentary succession. The selected samples are TP 065 (A-C), TP 103 (D-F) and TP 263 (G-I). From left to right: chromatograms of GDGT's showing the distribution of isoprenoidal (0, 1, 2, 3) vs. branched (III, II, I) - A, D, G chromatograms. Cr indicates the crenarchaeol. The alkenone fraction: TP 103 and TP 263 have alkenones (B, E), while TP 065 does not (H). The adducts of the apolar fraction: note the dominance of odds (green) over even (in blue) (C, F, I chromatograms). TP65 and TP103 register a mixed signal, aquatic and terrestrial, while TP 263 registers a stronger terrestrial signal.

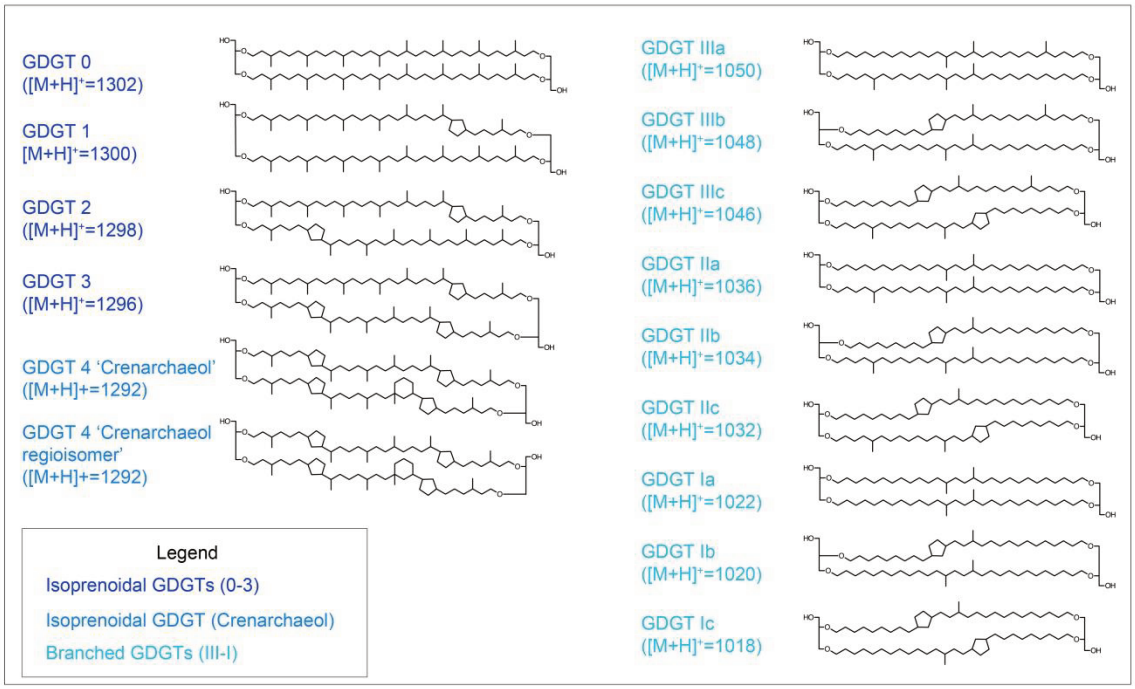

Supplementary figure 5.2 GDGT's structures after Tierney (2012)

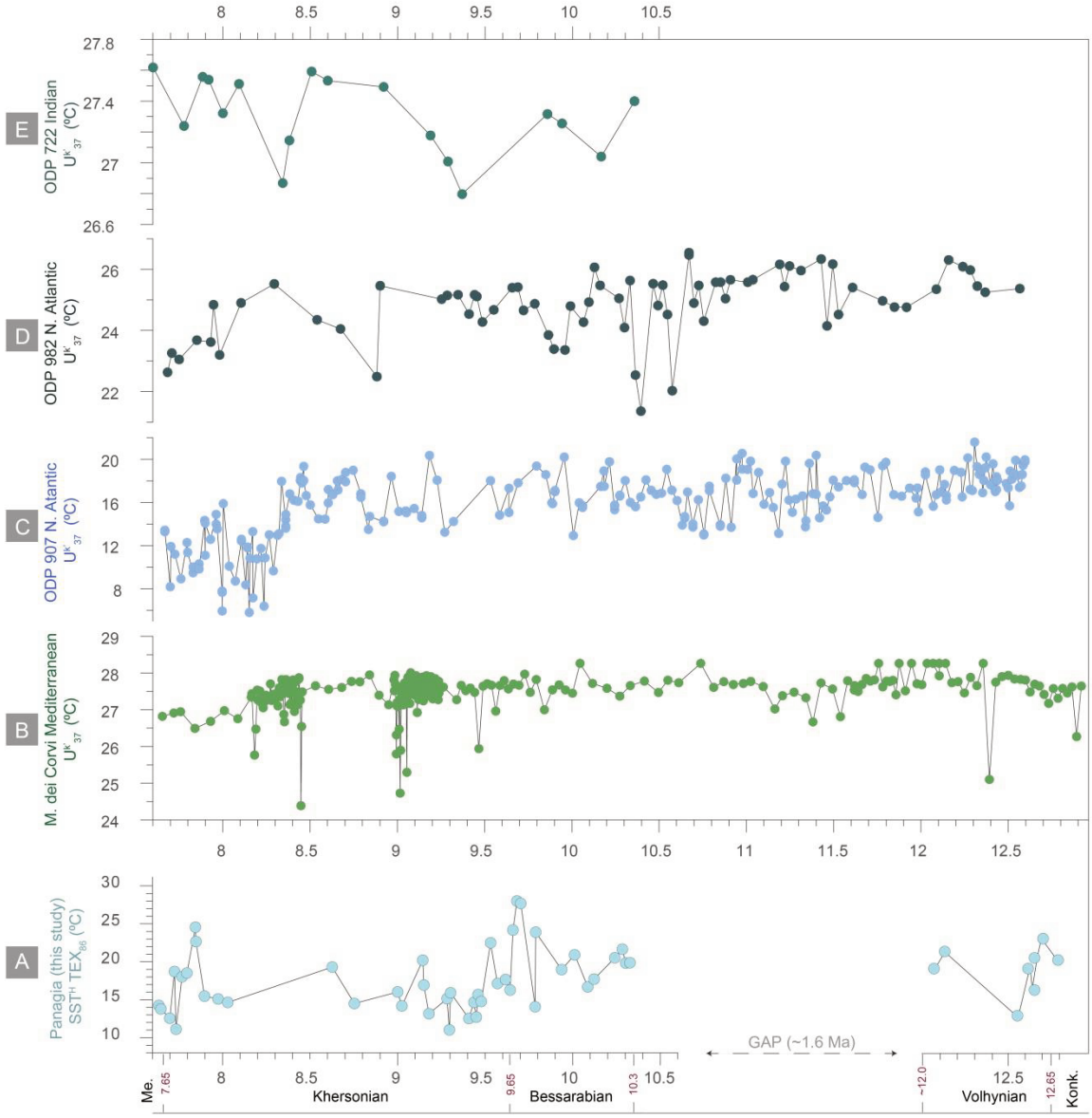

Supplementary figure 5.3 Panagia SST record (based on TEX_{86}) (A) compared with global temperature records inferred from alkenones: B) Monte dei Corvi (Mediterranean Sea, Tsanova et al., 2015); C) ODP 907 (Northern Atlantic Ocean); D) ODP 982 (Northern Atlantic Ocean), and E) ODP 722 (Indian Ocean) (Herbert et al., 2016). In the left side are depicted the Paratethys local stages names and ages in Myr.

Supplementary tables:

Sample code	Stratigraphic level (m)	Age (Ma)	SST (5-30ºC)	SST^{L} (<15ºC)	SST^{H} (>30ºC)	MAT	pH
TP 342	630.43	7.64	14.0	16.0	14.3	17.5	7.3
TP 335	626.71	7.65	13.6	13.2	13.8	16.4	6.7
TP 327	622.66	7.70	12.6	13.5	12.6	15.9	7.1
TP 318	617.67	7.73	18.0	19.9	18.7	18.4	6.8
TP 315	615.99	7.73	11.5	11.1	11.1	18.8	7.1
TP 305	610.40	7.77	17.3	19.6	18.0	17.1	6.6
TP 296	605.39	7.80	17.8	19.4	18.5	18.5	7.2
TP 280	596.47	7.85	24.2	26.4	24.6	18.8	6.5
TP 279	595.91	7.85	22.1	25.4	22.7	16.8	6.5
TP 263	587.00	7.90	15.0	15.8	15.5	17.6	6.4
TP 256	572.82	7.97	14.7	15.6	15.1	16.6	6.5
TP 251	562.69	8.03	14.3	16.5	14.7	17.4	6.5
TP 226	512.05	8.63	18.6	19.2	19.3	17.3	6.2
TP 221	505.00	8.75	14.2	12.5	14.5	13.9	6.7
TP 205	483.20	9.00	15.5	15.3	16.0	17.0	6.5
TP 202	481.03	9.02	13.9	11.5	14.2	16.1	6.5
TP 186	463.87	9.14	19.5	19.2	20.2	17.1	6.4
TP 183	454.95	9.15	16.3	15.8	16.9	18.9	6.5
TP 180	454.90	9.18	13.1	13.5	13.2	16.0	6.9
TP 161	428.70	9.28	14.7	14.4	15.1	18.4	6.1
TP 159	425.18	9.30	11.4	10.9	11.0	18.2	6.6
TP 156	412.28	9.30	15.4	13.8	15.9	18.6	6.4
TP 149	415.85	9.41	12.6	13.4	12.5	18.7	6.4
TP 145	412.31	9.44	14.3	10.6	14.7	16.7	6.0
TP 142	408.89	9.45	12.7	12.2	12.7	18.0	6.2
TP 124	406.44	9.46	15.2	13.2	15.7	18.8	6.3
TP 122	401.92	9.48	14.4	13.9	14.8	15.6	6.1
TP 116	388.63	9.53	19.5	18.3	19.4	15.0	6.3
TP 114	379.34	9.57	26.4	11.8	23.6	17.7	6.1
TP 113	377.56	9.57	16.5	15.5	17.1	17.3	6.0
TP 108	367.35	9.62	17.0	17.5	17.7	19.4	6.1
TP 106	362.52	9.64	15.7	17.4	16.3	15.9	6.4
TP 103	354.00	9.66	23.8	26.0	24.2	19.7	6.0
TP 098	344.30	9.68	28.6	31.7	28.0	18.1	5.9
TP 093	335.20	9.70	28.1	28.1	27.7	18.0	6.3
TP 088	290.00	9.79	13.8	10.2	14.1	18.3	6.3
TP 087	289.20	9.79	23.5	26.1	23.9	n.d.	n.d.
TP 082	252.00	9.94	18.2	18.1	19.0	18.6	6.4
TP 073	235.90	10.01	20.2	22.8	20.9	19.5	6.3
TP 065	213.60	10.09	16.1	17.6	16.7	19.8	6.5
TP 059	202.90	10.12	17.0	16.7	17.7	18.6	6.4
TP 050	176.80	10.24	19.8	15.6	20.5	17.6	5.5
TP 042	162.20	10.28	21.0	18.1	21.7	18.1	5.6
TP 039	155.70	10.30	19.1	13.3	19.8	17.7	5.5
TP 032	134.00	10.33	19.1	14.3	19.9	17.3	5.6
TP 027	58.00	12.08	18.7	18.3	19.4	16.4	6.2
TP 025	54.50	12.13	20.7	22.2	21.4	17.5	6.5
TP 014	13.60	12.55	12.7	10.7	12.8	16.1	5.9
TP 012	10.60	12.62	18.7	14.4	19.4	16.7	5.9
TP 011	10.10	12.63	15.9	11.3	16.5	13.9	5.7
TP 009	8.80	12.66	20.0	16.5	20.8	15.9	6.0
TP 007	7.80	12.68	22.6	22.6	23.1	16.5	5.8
TP 004	4.90	12.76	19.9	15.4	20.6	14.9	5.7

Supplementary table 5.1 Temperature (SST, MAT) and paleo-pH data obtained from GDGTs.

Sample code	Stratigraphic level (m)	Age (Ma)	*N*-alkanes						Alkenones					
			$\delta^2H_{n\,C29}$	St. dev. $\delta^2H_{n\,C29}$	$N\delta^2H_{n\,C29}$	$\delta^2H_{n\,C31}$	St. dev. $\delta^2H_{n\,C31}$	$N\delta^2H_{n\,C31}$	δ^2H_{C37}	St. dev. δ^2H_{C37}	$N\delta^2H_{C37}$	δ^2H_{C38}	St. dev. δ^2H_{C38}	$N\delta^2H_{C38}$
TP 342	630.43	7.64	n.d.	n.d.	n.d.	n.d.	n.d.	n.d.	-168.0	6.1	2	-163.2	0.5	2
TP 335	626.71	7.65	n.d.	n.d.	n.d.	n.d.	n.d.	n.d.	-162.9	0.0	1	-180.4	0.0	1
TP 327	622.66	7.70	-191.9	2.4	2	-191.9	0.3	2	n.d.	n.d.	n.d.	n.d.	n.d.	n.d.
TP 318	617.67	7.73	n.d.	n.d.	n.d.	n.d.	n.d.	n.d.	-161.9	0.0	1	-172.4	0.0	1
TP 315	615.99	7.73	n.d.	n.d.	n.d.	n.d.	n.d.	n.d.	-182.0	3.1	2	-178.4	3.2	2
TP 305	610.40	7.77	-192.7	0.1	2	-192.3	1.0	2	-178.0	1.2	3	-173.1	3.2	3
TP 296	605.39	7.80	n.d.	n.d.	n.d.	n.d.	n.d.	n.d.	-188.4	4.9	3	-188.7	1.1	2
TP 280	596.47	7.85	-164.4	1.4	2	-159.5	1.5	2	-148.6	0.0	1	-146.0	0.0	1
TP 263	587.00	7.90	-190.3	1.0	2	-187.2	1.2	2	-135.1	0.3	2	-133.7	3.0	2
TP 256	572.82	7.97	n.d.	n.d.	n.d.	n.d.	n.d.	n.d.	-129.4	1.6	2	-125.3	1.6	2
TP 251	562.69	8.03	n.d.	n.d.	n.d.	n.d.	n.d.	n.d.	-163.2	0.0	2	-151.5	0.3	2
TP 226	512.05	8.63	n.d.	n.d.	n.d.	n.d.	n.d.	n.d.	n.d.	n.d.	n.d.	-192.9	1.3	2
TP 221	505.00	8.75	-180.1	0.3	2	-181.4	1.2	2	n.d.	n.d.	n.d.	n.d.	n.d.	n.d.
TP 205	483.20	9.00	n.d.	n.d.	n.d.	n.d.	n.d.	n.d.	-201.8	1.0	2	-190.6	0.0	1
TP 183	454.95	9.15	n.d.	n.d.	n.d.	n.d.	n.d.	n.d.	-175.5	3.3	2	-174.6	0.2	2
TP 180	454.90	9.18	-175.7	2.3	3	-180.0	2.8	3	-180.7	1.2	2	-187.6	5.4	2
TP 149	415.85	9.41	n.d.	n.d.	n.d.	n.d.	n.d.	n.d.	-148.8	6.9	2	-127.8	2.1	2
TP 145	412.31	9.44	-189.5	1.4	3	-187.5	2.6	3	n.d.	n.d.	n.d.	n.d.	n.d.	n.d.
TP 142	408.89	9.45	n.d.	n.d.	n.d.	n.d.	n.d.	n.d.	-145.4	3.1	2	-138.1	0.6	2
TP 114	379.34	9.56	-182.4	0.4	2	-184.3	0.6	2	n.d.	n.d.	n.d.	n.d.	n.d.	n.d.
TP 113	377.56	9.57	n.d.	n.d.	n.d.	n.d.	n.d.	n.d.	-169.1	0.0	1	-166.7	0.0	1
TP 103	354.00	9.66	-192.8	3.2	2	-187.5	0.8	2	-126.2	2.4	3	-133.8	3.7	3
TP 088	290.00	9.79	-182.8	1.3	2	-185.0	4.6	2	n.d.	n.d.	n.d.	n.d.	n.d.	n.d.
TP 073	235.90	10.01	-190.5	0.7	2	-189.5	1.4	2	n.d.	n.d.	n.d.	n.d.	n.d.	n.d.
TP 065	213.60	10.09	-195.6	0.5	2	-193.8	0.6	2	n.d.	n.d.	n.d.	n.d.	n.d.	n.d.
TP 059	202.90	10.12	-190.1	0.0	1	-186.5	0.0	1	n.d.	n.d.	n.d.	n.d.	n.d.	n.d.
TP 042	162.20	10.28	-187.2	0.0	1	-184.1	0.0	1	n.d.	n.d.	n.d.	n.d.	n.d.	n.d.
TP 032	134.00	10.33	-188.3	1.3	2	-186.2	1.1	2	n.d.	n.d.	n.d.	n.d.	n.d.	n.d.
TP 025	54.50	12.13	-164.6	3.3	2	-175.1	1.2	2	n.d.	n.d.	n.d.	n.d.	n.d.	n.d.
TP 015	14.50	12.49	-175.9	0.2	2	-174.9	1.5	2	n.d.	n.d.	n.d.	n.d.	n.d.	n.d.
TP 011	10.10	12.63	-191.3	0.4	2	-187.0	1.9	2	n.d.	n.d.	n.d.	n.d.	n.d.	n.d.

Supplementary table 5.2 δ^2H on *n*-alkanes and long chain alkenones on samples from Panagia section.

Sample code	Stratigraphic level (m)	Age (Ma)	*N*-alkanes						Alkenones					
			$\delta^{13}C_{n\ C29}$	St. dev. $\delta^{13}C_{n\ C29}$	$N\delta^{13}C_{n\ C29}$	$\delta^{13}C_{n\ C31}$	St. dev. $\delta^{13}C_{n\ C31}$	$N\delta^{13}C_{n\ C29}$	$\delta^{13}C_{C37}$	St. dev. $\delta^{13}C_{C37}$	$N\delta^{13}C_{37}$	$\delta^{13}C_{C37}$	St. dev. $\delta^{13}C_{C37}$	$N\delta^{13}C_{38}$
TP 342	630.43	7.64	n.d.	n.d.	n.d.	n.d.	n.d.	n.d.	-24.4	0.1	2	-24.6	0.1	2
TP 335	626.71	7.65	-32.2	0.2	2	-33.7	0.1	2	-25.6	0.4	2	-24.8	0.1	2
TP 327	622.66	7.70	-30.2	0.1	2	-30.8	1.4	2	n.d.	n.d.	n.d.	n.d.	n.d.	n.d.
TP 318	617.67	7.73	n.d.	n.d.	n.d.	n.d.	n.d.	n.d.	-24.2	0.0	2	-24.5	0.2	2
TP 315	615.99	7.73	n.d.	n.d.	n.d.	n.d.	n.d.	n.d.	-26.1	0.6	2	-26.5	0.5	2
TP 305	610.40	7.77	-33.6	0.1	2	-34.7	0.1	2	-25.6	0.3	2	-25.3	0.3	2
TP 296	605.39	7.80	-28.9	0.2	2	-29.1	0.0	2	-25.7	0.2	2	-25.3	0.1	2
TP 280	596.47	7.85	-32.5	0.2	2	-32.7	0.3	2	n.d.	n.d.	n.d.	-25.9	0.0	2
TP 263	587.00	7.90	-29.7	0.9	2	-29.8	1.0	2	-24.9	0.1	2	-25.2	0.2	2
TP 251	562.69	8.03	-30.6	0.0	2	-31.7	0.1	2	-24.6	0.3	2	-25.5	0.4	2
TP 226	512.05	8.63	-32.5	0.4	2	-34.7	0.2	2	n.d.	n.d.	n.d.	-24.3	0.2	2
TP 221	505.00	8.75	-33.6	0.0	2	-34.9	0.2	2	n.d.	n.d.	n.d.	n.d.	n.d.	n.d.
TP 205	483.20	9.00	n.d.	n.d.	n.d.	n.d.	n.d.	n.d.	-25.5	0.0	2	-24.3	0.0	2
TP 202	481.03	9.02	-32.0	0.3	2	-33.2	0.7	2	n.d.	n.d.	n.d.	n.d.	n.d.	n.d.
TP 183	454.95	9.15	n.d.	n.d.	n.d.	n.d.	n.d.	n.d.	-22.1	0.0	2	-22.7	0.1	2
TP 180	454.90	9.18	-31.3	1.1	3	-32.7	3.0	3	-25.5	0.0	2	-25.2	0.1	2
TP 161	428.70	9.28	-32.7	0.1	2	-34.6	0.1	2	n.d.	n.d.	n.d.	n.d.	n.d.	n.d.
TP 159	425.18	9.30	-29.2	0.5	2	-31.4	0.2	2	n.d.	n.d.	n.d.	n.d.	n.d.	n.d.
TP 149	415.85	9.41	n.d.	n.d.	n.d.	n.d.	n.d.	n.d.	-23.5	0.2	3	-22.2	0.3	3
TP 145	412.31	9.44	-30.0	0.2	3	-30.4	0.3	3	n.d.	n.d.	n.d.	n.d.	n.d.	n.d.
TP 142	408.89	9.45	n.d.	n.d.	n.d.	n.d.	n.d.	n.d.	-21.3	0.3	2	-21.3	0.1	2
TP 124	406.44	9.46	-30.3	1.1	2	-32.0	0.9	2	n.d.	n.d.	n.d.	n.d.	n.d.	n.d.
TP 122	401.92	9.48	-30.3	0.0	2	-30.6	0.1	2	n.d.	n.d.	n.d.	n.d.	n.d.	n.d.
TP 114	379.34	9.57	-29.7	0.5	3	-29.6	0.6	3	n.d.	n.d.	n.d.	n.d.	n.d.	n.d.
TP 113	377.56	9.57	n.d.	n.d.	n.d.	n.d.	n.d.	n.d.	-23.3	0.2	2	-23.0	0.0	2
TP 106	362.52	9.64	-30.8	1.0	2	-32.7	0.6	2	n.d.	n.d.	n.d.	n.d.	n.d.	n.d.
TP 103	354.00	9.66	-30.1	0.1	2	-30.5	0.2	2	-20.5	0.0	2	-20.2	0.2	2
TP 093	335.20	9.70	-31.2	0.8	3	-32.7	0.8	3	n.d.	n.d.	n.d.	n.d.	n.d.	n.d.
TP 088	290.00	9.79	-33.2	0.0	2	-34.2	0.1	2	n.d.	n.d.	n.d.	n.d.	n.d.	n.d.
TP 073	235.90	10.01	-31.1	0.1	2	-31.1	0.1	2	n.d.	n.d.	n.d.	n.d.	n.d.	n.d.
TP 065	213.60	10.09	-32.5	1.1	3	-33.6	1.1	3	n.d.	n.d.	n.d.	n.d.	n.d.	n.d.
TP 059	202.90	10.12	-30.7	0.1	2	-31.7	0.2	2	n.d.	n.d.	n.d.	n.d.	n.d.	n.d.
TP 042	162.20	10.28	-30.7	0.1	2	-32.5	0.0	2	n.d.	n.d.	n.d.	n.d.	n.d.	n.d.
TP 039	155.70	10.30	-32.3	0.2	2	-34.3	0.1	2	n.d.	n.d.	n.d.	n.d.	n.d.	n.d.
TP 032	134.00	10.33	-33.1	0.4	2	-33.6	0.1	2	n.d.	n.d.	n.d.	n.d.	n.d.	n.d.
TP 029	128.90	10.33	-30.4	0.3	3	-32.0	0.6	3	n.d.	n.d.	n.d.	n.d.	n.d.	n.d.
TP 025	54.50	12.13	-33.2	0.5	2	-36.0	0.4	2	n.d.	n.d.	n.d.	n.d.	n.d.	n.d.
TP 015	14.50	12.49	-30.1	0.2	2	-30.6	0.1	2	n.d.	n.d.	n.d.	n.d.	n.d.	n.d.
TP 011	10.10	12.63	-30.4	0.1	3	-30.9	0.1	3	n.d.	n.d.	n.d.	n.d.	n.d.	n.d.
TP 007	7.80	12.68	-30.5	0.1	2	-31.9	0.2	2	n.d.	n.d.	n.d.	n.d.	n.d.	n.d.

Supplementary table 5.3 $\delta^{13}C$ on *n*-alkanes and long chain alkenones.

Sample code	Stratigraphic level (m)	Age (Ma)	Total counts charcoal	Total Poaceae Counts	Total Forbs counts	Total Wood	Total 180 (µm)	Total 125 (µm)	Total 90 (µm)	Total charcoal counts/ cm^3	Total Poaceae counts/ cm^3	Total Forbs counts/ cm^3	Total Wood counts/ cm^3	Total 180µm/ cm^3	Total 125µm/ cm^3	Total 90µm/ cm^3	Poaceae/ all counts (%)	Forbs/ all counts (%)	Wood/ all counts (%)
TP 343	630.43	7.64	10	5	5	0	0	2	8	5.0	2.5	2.5	0.0	0.0	1.0	4.0	50.0	50.0	0.0
TP 327	622.66	7.70	6	4	2	0	0	0	6	3.0	2.0	1.0	0.0	0.0	0.0	3.0	66.7	33.3	0.0
TP 318	617.67	7.73	0	0	0	0	0	0	0	0.0	0.0	0.0	0.0	0.0	0.0	0.0	0.0	0.0	0.0
TP 307	611.51	7.76	6	1	5	0	0	3	3	3.0	0.5	2.5	0.0	0.0	1.5	1.5	16.7	83.3	0.0
TP 296	605.39	7.80	16	8	4	4	2	6	8	8.0	4.0	2.0	2.0	1.0	3.0	4.0	50.0	25.0	25.0
TP 280	596.47	7.85	14	14	0	0	5	9	0	7.0	7.0	0.0	0.0	2.5	4.5	0.0	100.0	0.0	0.0
TP 277	594.80	7.85	15	8	4	3	5	1	9	6.0	3.2	1.6	1.2	2.0	0.4	3.6	53.3	26.7	20.0
TP 263	587.00	7.90	3	2	1	0	0	1	2	1.5	1.0	0.5	0.0	0.0	0.5	1.0	66.7	33.3	0.0
TP 259	578.90	7.94	3	1	2	0	0	0	3	1.5	0.5	1.0	0.0	0.0	0.0	1.5	33.3	66.7	0.0
TP 256	572.82	7.97	3	3	0	0	0	0	3	1.5	1.5	0.0	0.0	0.0	0.0	1.5	100.0	0.0	0.0
TP 251	562.69	8.03	4	3	0	1	1	0	3	2.0	1.5	0.0	0.5	0.5	0.0	1.5	75.0	0.0	25.0
TP 242	544.46	8.15	15	13	0	2	4	7	4	7.5	6.5	0.0	1.0	2.0	3.5	2.0	86.7	0.0	13.3
TP 221	505.00	8.75	18	9	8	1	0	13	5	9.0	4.5	4.0	0.5	0.0	6.5	2.5	50.0	44.4	5.6
TP 205	483.20	9.00	14	9	3	2	2	2	10	7.0	4.5	1.5	1.0	1.0	1.0	5.0	64.3	21.4	14.3
TP 202	481.03	9.02	77	66	10	1	4	7	66	38.5	33.0	5.0	0.5	2.0	3.5	33.0	85.7	13.0	1.3
TP 195	476.59	9.07	7	4	2	1	1	1	5	3.5	2.0	1.0	0.5	0.5	0.5	2.5	57.1	28.6	14.3
TP 186	463.87	9.14	3	0	2	1	0	1	2	1.5	0.0	1.0	0.5	0.0	0.5	1.0	0.0	66.7	33.3
TP 180	454.90	9.18	40	16	17	7	0	17	23	20.0	8.0	8.5	3.5	0.0	8.5	11.5	40.0	42.5	17.5
TP 174	446.78	9.21	5	3	2	0	0	2	3	2.5	1.5	1.0	0.0	0.0	1.0	1.5	60.0	40.0	0.0
TP 163	431.53	9.27	20	11	9	0	5	5	10	10.0	5.5	4.5	0.0	2.5	2.5	5.0	55.0	45.0	0.0
TP 159	425.18	9.30	22	11	7	4	4	3	15	11.0	5.5	3.5	2.0	2.0	1.5	7.5	50.0	31.8	18.2
TP 153	418.67	9.36	3	0	3	0	0	0	3	1.2	0.0	1.2	0.0	0.0	0.0	1.2	0.0	100.0	0.0
TP 149	415.85	9.41	15	14	1	0	0	0	15	7.5	7.0	0.5	0.0	0.0	0.0	7.5	93.3	6.7	0.0
TP 145	412.31	9.44	8	8	0	0	2	0	6	4.0	4.0	0.0	0.0	1.0	0.0	3.0	100.0	0.0	0.0
TP 142	408.89	9.45	6	5	1	0	0	2	4	3.0	2.5	0.5	0.0	0.0	1.0	2.0	83.3	16.7	0.0
TP 124	406.44	9.46	7	7	0	0	0	2	5	3.5	3.5	0.0	0.0	0.0	1.0	2.5	100.0	0.0	0.0
TP 122	401.92	9.48	12	6	3	3	2	0	10	6.0	3.0	1.5	1.5	1.0	0.0	5.0	50.0	25.0	25.0
TP 120	398.99	9.49	7	4	2	1	0	3	4	3.5	2.0	1.0	0.5	0.0	1.5	2.0	57.1	28.6	14.3
TP 118	394.15	9.51	42	29	12	1	8	12	22	21.0	14.5	6.0	0.5	4.0	6.0	11.0	69.0	28.6	2.4
TP 116	388.63	9.53	8	3	3	2	0	3	5	4.0	1.5	1.5	1.0	0.0	1.5	2.5	37.5	37.5	25.0
TP 114	379.34	9.57	6	2	4	0	0	3	3	3.0	1.0	2.0	0.0	0.0	1.5	1.5	33.3	66.7	0.0
TP 113	377.56	9.57	8	5	3	0	0	3	5	4.0	2.5	1.5	0.0	0.0	1.5	2.5	62.5	37.5	0.0
TP 111	372.91	9.59	8	4	2	2	2	0	6	3.2	1.6	0.8	0.8	0.8	0.0	2.4	50.0	25.0	25.0
TP 108	367.35	9.62	7	2	4	1	0	2	5	3.5	1.0	2.0	0.5	0.0	1.0	2.5	28.6	57.1	14.3
TP 106	362.52	9.64	19	8	5	6	1	5	13	9.5	4.0	2.5	3.0	0.5	2.5	6.5	42.1	26.3	31.6
TP 103	354.00	9.66	13	11	2	0	2	1	10	6.5	5.5	1.0	0.0	1.0	0.5	5.0	84.6	15.4	0.0
TP 098	344.30	9.68	1	1	0	0	0	0	1	0.5	0.5	0.0	0.0	0.0	0.0	0.5	100.0	0.0	0.0
TP 093	335.20	9.70	12	9	0	3	4	4	4	6.0	4.5	0.0	1.5	2.0	2.0	2.0	75.0	0.0	25.0
TP 089	328.40	9.72	5	5	0	0	1	1	3	2.5	2.5	0.0	0.0	0.5	0.5	1.5	100.0	0.0	0.0
TP 083	282.30	9.81	2	1	1	0	0	0	2	1.0	0.5	0.5	0.0	0.0	0.0	1.0	50.0	50.0	0.0
TP 082	252.00	9.94	7	3	4	0	1	2	4	3.5	1.5	2.0	0.0	0.5	1.0	2.0	42.9	57.1	0.0
TP 075	239.40	10.00	2	1	1	0	1	0	1	1.0	0.5	0.5	0.0	0.5	0.0	0.5	50.0	50.0	0.0
TP 073	235.90	10.01	6	4	2	0	0	3	3	3.0	2.0	1.0	0.0	0.0	1.5	1.5	66.7	33.3	0.0
TP 065	213.60	10.09	7	3	3	1	0	1	6	3.5	1.5	1.5	0.5	0.0	0.5	3.0	42.9	42.9	14.3
TP 059	202.90	10.12	6	1	1	4	6	0	0	3.0	0.5	0.5	2.0	3.0	0.0	0.0	16.7	16.7	66.7
TP 053	192.20	10.17	17	16	1	0	0	1	16	8.5	8.0	0.5	0.0	0.0	0.5	8.0	94.1	5.9	0.0
TP 050	176.80	10.24	13	5	7	1	0	6	7	6.5	2.5	3.5	0.5	0.0	3.0	3.5	38.5	53.8	7.7
TP 042	162.20	10.28	6	2	2	2	1	3	2	3.0	1.0	1.0	1.0	0.5	1.5	1.0	33.3	33.3	33.3
TP 033	144.70	10.32	46	45	1	0	0	8	38	23.0	22.5	0.5	0.0	0.0	4.0	19.0	97.8	2.2	0.0
TP 027	58.00	12.08	0	0	0	0	0	0	0	0.0	0.0	0.0	0.0	0.0	0.0	0.0	0.0	0.0	0.0
TP 025	54.50	12.13	31	14	5	12	8	7	16	15.5	7.0	2.5	6.0	4.0	3.5	8.0	45.2	16.1	38.7
TP 023	29.60	12.44	0	0	0	0	0	0	0	0.0	0.0	0.0	0.0	0.0	0.0	0.0	0.0	0.0	0.0
TP 019	20.60	12.47	30	27	1	2	3	2	25	15.0	13.5	0.5	1.0	1.5	1.0	12.5	90.0	3.3	6.7
TP 015	14.50	12.49	11	4	6	1	1	1	9	5.2	1.9	2.9	0.5	0.5	0.5	4.3	36.4	54.5	9.1
TP 011	10.10	12.63	5	4	0	1	0	2	3	2.0	1.6	0.0	0.4	0.0	0.8	1.2	80.0	0.0	20.0
TP 007	7.80	12.68	2	2	0	0	0	0	2	1.0	1.0	0.0	0.0	0.0	0.0	1.0	100.0	0.0	0.0
TP 001	0.50	12.86	6	3	1	2	4	1	1	4.0	2.0	0.7	1.3	2.7	0.7	0.7	50.0	16.7	33.3

Supplementary table 5.4 Charcoal counting and burned vegetation groups (Poaceae, Forbs and Wood).

(A2) Appendix to chapter 6: Hypersalinity accompanies tectonic restriction in the Messinian Eastern Mediterranean

George Kontakiotis, **Geanina A. Butiseacă**, Assimina Antonarakou, Konstantina Agiadi, Stergios D. Zarkogiannis, Emilija Krsnik, Evangelia Besiou, Willem Jan Zachariasse, Lucas Lourens, Danae Thivaiou, Efterpi Koskeridou, Pierre Moissette, Andreas Mulch, Vasileios Karakitsios, Iuliana Vasiliev

Supplementary figures

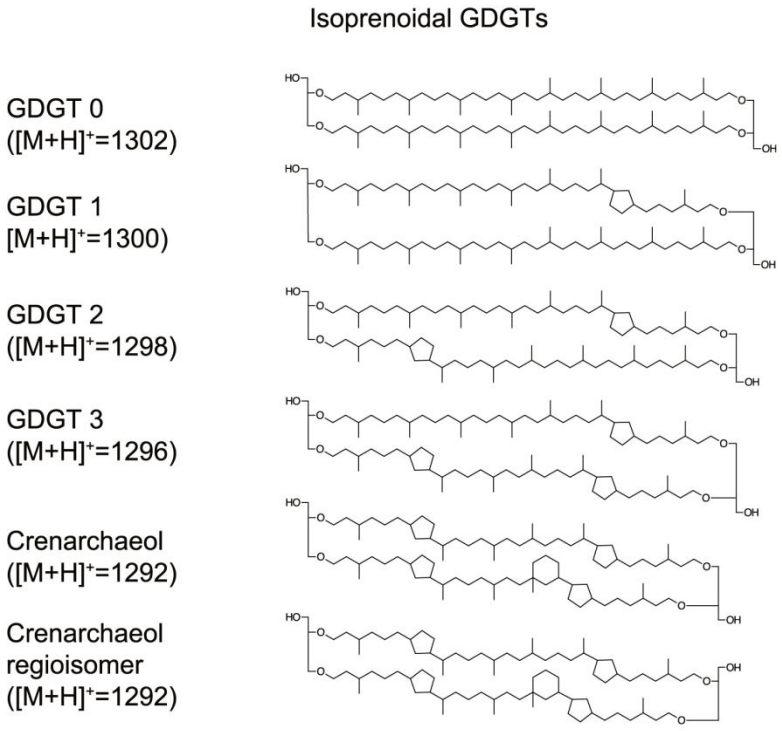

Supplementary figure 6.1 Chemical core structures of isoGDGTs, after Tierney (2012)

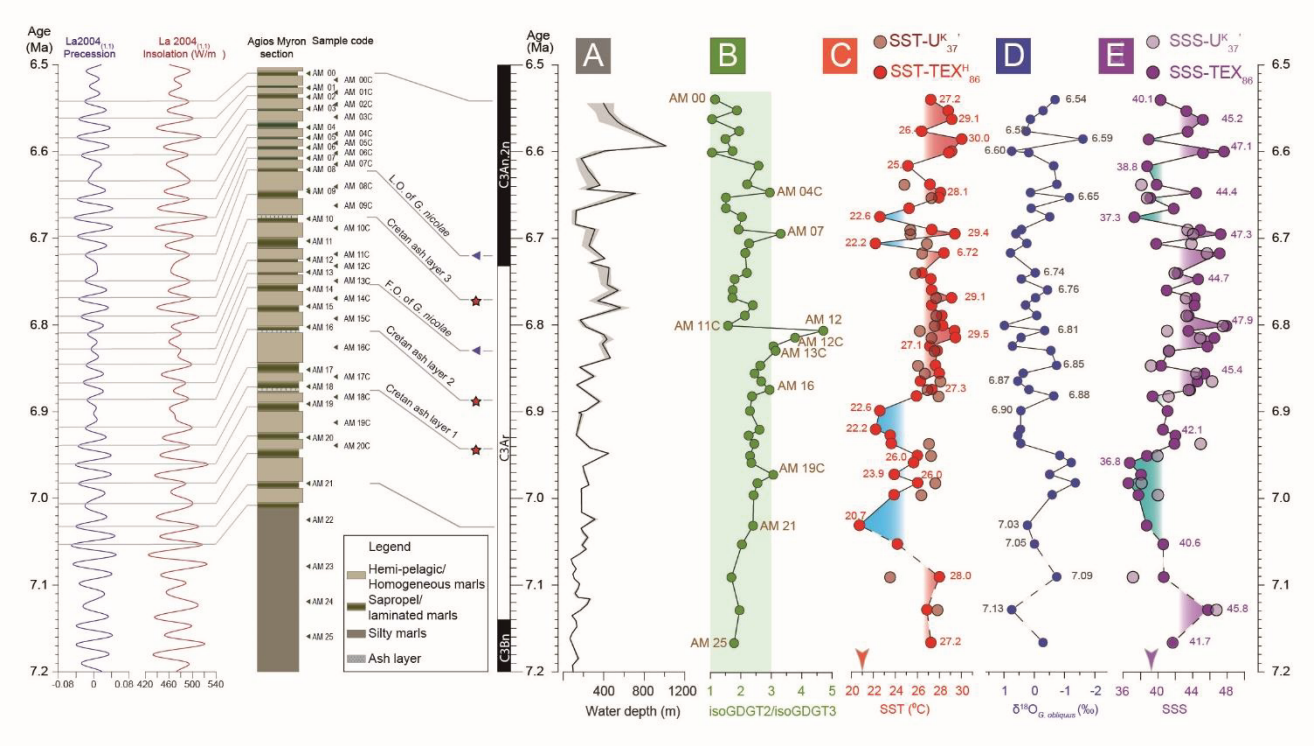

Supplementary figure 6.2 Agios Myron a) reconstructed depositional depth from Zachariasse et al. (2021); b) Large majority of the samples show GDGT2/GDGT3 index typical for isoGDGT input from the upper water column as reported in the present-day eastern Mediterranean, with values between 1 and 3 represented by the light green band (Kim et al., 2015); c) Sea surface temperature (SST) calculated based on TEX^{H}_{86} (SST-TEX^{H}_{86}) and on U^{K}_{37}' (SST-U^{K}_{37}'); d) $\delta^{18}O$ measured on *Globigerinoides obliquus* ($\delta^{18}O_{G.\ obliquus}$); e) sea surface salinities (SSS) based on SST-TEX^{H}_{86} and SST-U^{K}_{37}'. On the left-hand side is the astronomical precession and insolation summer curve of Laskar et al. (2004), the lithological column, samples names and position, bioevents and ash layers used for calibration to the APTS (Lourens et al., 2004). For clarity, the red numbers next to SST data are obtained temperature estimates based on TEX^{H}_{86}, the grey numbers next to $\delta^{18}O_{G.\ obliquus}$ points indicate ages in Ma, while the purple numbers next to SSS indicate calculated salinity based on SST-TEX^{H}_{86}. The arrows indicate the present-day values for SST and SSS.

Supplementary table

Sample code	Level (m)	Age (Ma)	SST-SST^H	$\delta^{18}O_{sw}$	$\delta^{18}O_{IVF-sw}$	SSS-SST-SST^H	SST-U^K_{37}	$\delta^{18}O_{sw}$	$\delta^{18}O_{IVF-sw}$	SSS-SST-U^K_{37}	$\delta^{18}O$	STD $\delta^{18}O$	GDGT2/GDGT3
AM 00	25.25	6.540	27.21	1.82	1.85	40.31	n.d.	n.d.	n.d.	n.d.	-0.69		1.15
AM 00C	24.90	6.553	28.80	2.54	2.60	43.30	n.d.	n.d.	n.d.	n.d.	-0.29		1.87
AM 01	24.65	6.563	29.13	3.03	3.07	45.21	n.d.	n.d.	n.d.	n.d.	0.13		1.06
AM 01C	24.40	6.577	26.39	2.60	2.63	43.45	n.d.	n.d.	n.d.	n.d.	0.27		1.95
AM 02	24.20	6.586	30.03	1.48	1.50	38.94	n.d.	n.d.	n.d.	n.d.	-1.61	0.67	1.50
AM 02C	23.80	6.600	29.11	3.65	3.68	47.66	n.d.	n.d.	n.d.	n.d.	0.75	0.87	1.73
AM 03	23.75	6.601	28.86	3.02	3.08	45.23	n.d.	n.d.	n.d.	n.d.	0.18		1.05
AM 03C	23.40	6.616	25.14	1.43	1.46	38.76	n.d.	n.d.	n.d.	n.d.	-0.64	1.09	2.58
AM 04	22.90	6.638	27.14	1.74	1.74	39.86	24.96	1.29	1.28	38.05	-0.75	0.65	2.21
AM 04C	22.65	6.647	28.11	2.81	2.87	44.42	n.d.	n.d.	n.d.	n.d.	0.12		2.95
AM 05	22.50	6.653	27.95	1.50	1.55	39.13	27.43	1.39	1.44	38.70	-1.16		1.51
AM 05C	22.25	6.665	25.24	2.19	2.23	41.84	n.d.	n.d.	n.d.	n.d.	0.10		1.51
AM 06	22.05	6.675	22.59	1.03	1.09	37.28	n.d.	n.d.	n.d.	n.d.	-0.51	0.37	2.03
AM 06C	21.75	6.690	27.31	2.95	2.99	44.90	25.51	2.57	2.62	43.40	0.42	0.63	1.93
AM 07	21.65	6.695	29.40	3.57	3.59	47.26	25.52	2.76	2.78	44.03	0.61		3.31
AM 07C	21.40	6.706	22.19	1.70	1.72	39.80	27.02	2.71	2.73	43.83	0.25	0.16	2.27
AM 08	21.15	6.717	28.41	3.54	3.56	47.15	26.59	3.16	3.18	45.64	0.78		2.15
AM 08C	20.40	6.740	26.42	2.30	2.34	42.27	25.97	2.21	2.25	41.90	-0.03		2.20
AM 09	20.15	6.747	27.23	2.93	2.93	44.66	n.d.	n.d.	n.d.	n.d.	0.43		1.80
AM 09C	19.60	6.760	27.30	2.08	2.02	41.01	n.d.	n.d.	n.d.	n.d.	-0.44		1.74
AM 10	19.20	6.769	29.11	2.86	2.84	44.28	27.84	2.59	2.58	43.22	-0.04	0.17	1.72
AM 10C	18.80	6.777	27.31	2.81	2.83	44.25	n.d.	n.d.	n.d.	n.d.	0.29		2.39
AM 11	18.20	6.789	28.21	2.63	2.66	43.57	27.87	2.56	2.59	43.29	-0.08		2.13
AM 11	17.70	6.801	28.29	3.71	3.75	47.93	27.73	3.60	3.64	47.47	0.99		1.58
AM 12	17.45	6.806	29.39	1.61	2.65	43.53	26.37	1.98	2.03	41.02	-0.34		4.71
AM 12C	17.20	6.814	29.45	3.40	3.40	46.54	27.43	2.98	2.98	44.86	0.43	0.73	3.78
AM 13	16.90	6.824	27.14	3.21	3.20	45.74	n.d.	n.d.	n.d.	n.d.	0.72		3.07
AM 13C	16.50	6.830	27.80	2.08	2.10	41.31	27.70	2.06	2.08	41.23	-0.55		3.14
AM 14	16.15	6.847	27.65	1.86	1.86	40.37	26.21	1.56	1.56	39.17	-0.74		2.64
AM 14C	15.80	6.856	27.99	3.03	3.11	45.38	26.83	2.79	2.87	44.41	0.37	0.17	2.45
AM 15	15.45	6.865	26.28	2.85	2.92	44.58	28.24	3.26	3.32	46.22	0.55	0.12	2.67
AM 15C	15.00	6.874	27.33	2.70	2.71	43.75	27.07	2..65	2.65	43.53	0.18		2.94
AM 16	14.65	6.882	25.92	1.59	1.62	39.39	28.08	2.04	2.07	41.19	-0.64	0.58	2.37
AM 16C	13.85	6.899	22.59	1.98	2.05	41.12	n.d.	n.d.	n.d.	n.d.	0.44	0.26	2.30
AM 17	12.80	6.920	22.21	1.91	1.92	40.59	n.d.	n.d.	n.d.	n.d.	0.46		2.61
AM 17C	12.55	6.927	23.53	2.28	2.28	42.03	n.d.	n.d.	n.d.	n.d.	0.54	0.05	2.26
AM 18	12.20	6.937	23.64	2.21	2.25	41.92	27.20	2.95	2.99	44.89	0.45	0.54	2.44
AM 18C	11.70	6.951	26.00	1.41	1.46	38.74	27.39	1.70	1.75	39.90	-0.84	0.94	2.30
AM 19	11.40	6.959	25.66	0.96	0.96	36.75	n.d.	n.d.	n.d.	n.d.	-1.22		2.35
AM 19C	10.65	6.972	23.90	1.30	1.28	38.06	n.d.	n.d.	n.d.	n.d.	-0.51	0.62	3.07
AM 20	10.10	6.982	26.03	0.90	0.92	36.60	27.78	1.26	1.28	38.06	-1.36		2.55
AM 20C	9.65	6.996	23.88	1.22	1.21	37.76	26.51	1.77	1.76	39.95	-0.59	0.14	2.42
AM 21	8.05	7.031	20.74	1.38	1.45	38.70	n.d.	n.d.	n.d.	n.d.	0.23		2.40
AM 22	7.10	7.053	24.18	1.86	1.93	40.62	n.d.	n.d.	n.d.	n.d.	-0.01	0.23	2.04
AM 23	5.50	7.090	28.00	1.93	1.94	40.68	23.67	1.02	1.04	37.08	-0.74		1.69
AM 24	3.90	7.128	26.87	3.18	3.22	45.80	27.98	3.41	3.45	46.73	0.75		1.96
AM 25	2.30	7.166	27.23	2.22	2.20	41.71	n.d.	n.d.	n.d.	n.d.	-0.29		1.78

Supplementary table 6.1 Agios Myron biomarker and oxygen isotope data.

(A3) Appendix to chapter 7: Multiple crises preceded the Mediterranean Salinity Crisis: Aridification and vegetation changes revealed by biomarkers and stable isotopes

Geanina A. Butiseacă, Marcel T.J. van der Meer, George Kontakiotis, Konstantina Agiadi, Danae Thivaiou, Evangelia Besiou, Assimina Antonarakou, Andreas Mulch, Iuliana Vasiliev

Supplementary figure

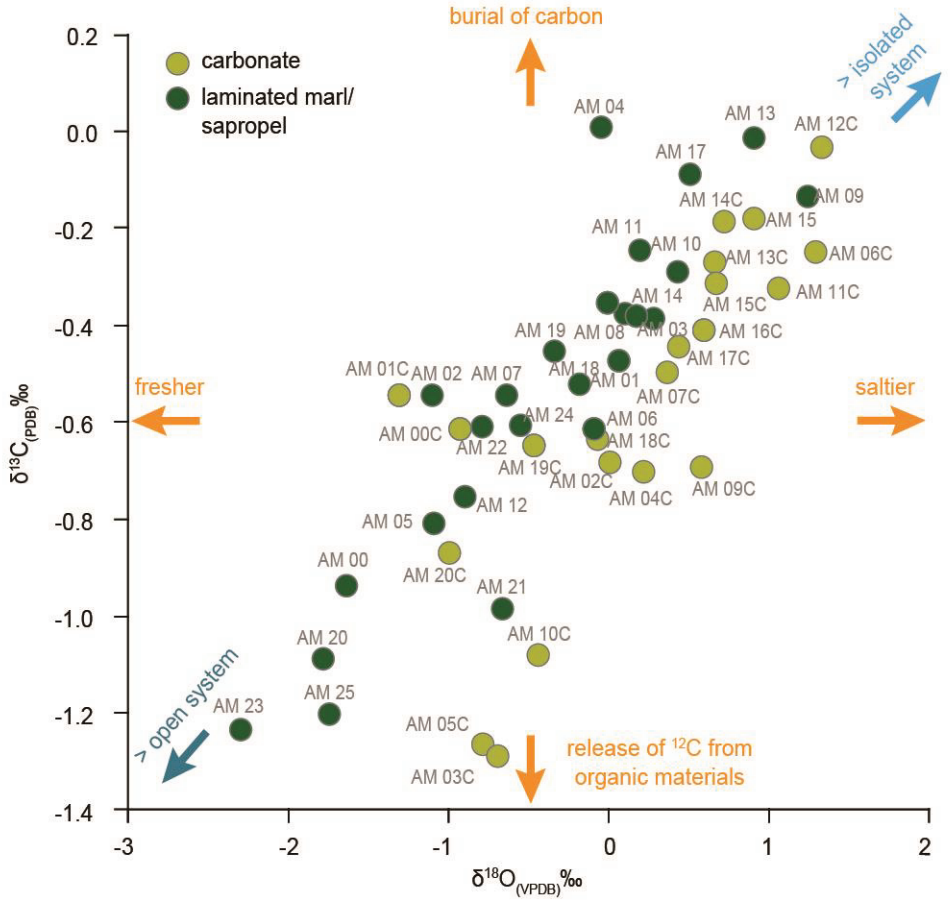

Supplementary figure 7.1 Diagram showing the distribution of $\delta^{13}C$ against $\delta^{18}C$ on bulk sediments.

Supplementary tables

Sample Name	Stratigraphic level (m)	Age (Ma)	δ^2H_{C37}	St. dev. δ^2H_{C37}	$N\delta^2H_{C37}$	δ^2H_{C38}	St. dev. δ^2H_{C38}	$N\delta^2H_{C38}$
AM 01C	24.40	6.58	n.d.	n.d.	n.d.	-165.4	8.7	2
AM 03	23.75	6.60	-156.8	2.3	2	-166.7	2.0	2
AM 05	22.50	6.65	-191.2	0.0	2	-192.3	0.8	2
AM 07	21.65	6.69	-194.3	0.5	2	-196.5	0.2	2
AM 10	19.20	6.77	-181.7	12.8	2	-199.0	0.0	2
AM 10C	18.80	6.78	-169.2	2.4	3	-164.9	2.1	2
AM 11	18.20	6.79	-199.4	0.7	2	-201.2	4.5	2
AM 11C	17.70	6.80	-167.9	11.1	2	-184.9	5.6	2
AM 13	16.90	6.82	-159.1	9.8	2	-169.0	5.4	2
AM 13C	16.50	6.83	-185.4	1.3	2	-188.4	3.6	2
AM 14	16.15	6.85	-198.9	3.0	2	-200.8	0.5	2
AM 15	15.45	6.86	-175.7	0.2	2	-178.9	2.1	2
AM 15C	15.00	6.87	-188.9	0.2	2	-193.9	1.0	2
AM 17C	12.55	6.93	-184.4	5.6	2	-185.2	4.7	2
AM 19C	10.65	6.97	-186.8	8.3	2	-194.8	1.3	2
AM 20	10.10	6.98	-159.1	2.3	2	-168.1	3.6	2
AM 20C	9.65	7.00	-155.0	7.0	3	-170.1	0.0	1
AM 21	8.05	7.03	-178.4	0.2	2	-187.0	2.8	2
AM 22	7.10	7.05	n.d.	n.d.	n.d.	-168.9	0.8	2
AM 23	5.50	7.09	-183.1	6.0	2	-177.6	3.9	2
AM 24	3.90	7.13	-181.5	0.2	2	-185.1	4.9	2

Supplementary table 7.1 δ^2H long chain alkenones (C_{37}–C_{38}) on samples from Agios Myron section.

Sample Name	Stratigraphic level (m)	Age (Ma)	$\delta^{13}C_{C29}$	St. dev. $\delta^{13}C_{C29}$	$N\delta^2C_{C29}$	$\delta^{13}C_{C31}$	St. dev. $\delta^{13}C_{C31}$	$N\delta^{13}C_{C31}$
AM 01	24.65	6.563	-28.6	0.2	2	n.d.	n.d.	n.d.
AM 05	22.50	6.653	-31.2	0.2	2	-32.1	0.3	2
AM 07	21.65	6.695	-31.1	0.4	3	-31.6	0.5	3
AM 10	19.20	6.769	-30.2	0.3	3	-29.9	0.3	3
AM 10C	18.80	6.777	-34.4	0.0	2	-35.3	0.1	2
AM 11	18.20	6.789	-33.1	0.5	2	-33.7	0.3	2
AM 13C	16.50	6.830	-30.6	0.3	2	-31.1	0.0	2
AM 14	16.15	6.847	-31.3	1.0	3	-31.6	0.7	3
AM 15C	15.00	6.874	-33.3	0.0	2	-32.6	1.2	2
AM 17	12.80	6.920	-33.6	0.0	2	-34.4	0.0	2
AM 19C	10.65	6.972	-32.9	0.2	2	-34.0	0.2	2
AM 20	10.10	6.982	-30.9	0.7	3	-31.9	1.1	3
AM 20C	9.65	6.996	-34.6	0.1	2	-35.2	0.0	2
AM 22	7.10	7.053	-33.0	0.4	2	-34.3	0.1	2
AM 23	5.50	7.090	-32.5	0.3	2	-32.4	0.5	2
AM 24	3.90	7.128	-32.6	0.1	2	-33.5	0.2	2
AM 25	2.30	7.166	-33.2	0.8	2	-34.4	0.6	2

Supplementary table 7.2 $\delta^{13}C$ on long chain *n*-alkanes (C_{29}–C_{31}).

Sample Name	Stratigraphic level (m)	Age (Ma)	MAT (°C)	pH	BIT Index
AM 00	25.25	6.54	13.9	7.7	0.88
AM 00C	24.90	6.55	13.8	7.3	0.79
AM 01	24.65	6.56	11.4	7.2	0.78
AM 01C	24.40	6.58	11.0	6.8	0.79
AM 02	24.20	6.59	13.0	7.9	0.76
AM 02C	23.80	6.60	15.4	7.7	0.73
AM 03	23.75	6.60	9.9	7.3	0.80
AM 03C	23.40	6.62	13.3	7.4	0.59
AM 04	22.90	6.64	12.0	6.6	0.67
AM 04C	22.65	6.65	10.5	7.0	0.67
AM 05	22.50	6.65	15.8	7.0	0.70
AM 05C	22.25	6.67	15.1	7.2	0.70
AM 06	22.05	6.68	13.9	7.7	0.84
AM 06C	21.75	6.69	9.2	6.4	0.69
AM 07	21.65	6.69	6.0	5.5	0.63
AM 07C	21.40	6.71	12.7	6.8	0.85
AM 08	21.15	6.72	9.6	6.1	0.79
AM 08C	20.40	6.74	19.2	7.1	0.74
AM 09	20.15	6.75	17.7	7.3	0.82
AM 09C	19.60	6.76	16.9	7.0	0.73
AM 10	19.20	6.77	12.1	6.6	0.70
AM 10C	18.80	6.78	15.4	7.2	0.83
AM 11	18.20	6.79	6.4	5.9	0.60
AM 11C	17.70	6.80	15.1	6.8	0.79
AM 12	17.45	6.81	10.5	6.9	0.47
AM 12C	17.20	6.81	11.0	6.5	0.52
AM 13	16.90	6.82	11.2	6.5	0.45
AM 13C	16.50	6.83	19.3	6.9	0.39
AM 14	16.15	6.85	15.1	6.4	0.26
AM 14C	15.80	6.86	7.7	5.9	0.47
AM 15	15.45	6.86	14.9	6.4	0.62
AM 15C	15.00	6.87	10.9	6.5	0.50
AM 16	14.65	6.88	10.5	6.3	0.86
AM 16C	13.85	6.90	9.9	7.2	0.73
AM 17	12.80	6.92	14.1	6.7	0.79
AM 17C	12.55	6.93	14.9	7.4	0.81
AM 18	12.20	6.94	12.9	6.7	0.66
AM 18C	11.70	6.95	11.3	6.1	0.79
AM 19	11.40	6.96	8.4	6.1	0.79
AM 19C	10.65	6.97	19.8	6.9	0.52
AM 20	10.10	6.98	20.8	6.9	0.64
AM 20C	9.65	7.00	14.7	7.1	0.56
AM 21	8.05	7.03	16.3	6.7	0.80
AM 22	7.10	7.05	21.2	7.1	0.75
AM 23	5.50	7.09	15.9	6.5	0.73
AM 24	3.90	7.13	16.0	6.8	0.77
AM 25	2.30	7.17	14.3	6.6	0.70

Supplementary table 7.3 MAT, BIT and paleo-pH data obtained from GDGTs.

Sample Name	Stratigraphic level (m)	Age (Ma)	$\delta^{13}C$ (PDB)	$\delta^{18}O$ (VPDB)	N
AM 00	25.25	6.54	-0.94	-1.64	3
AM 00C	24.90	6.55	-0.61	-0.93	4
AM 01	24.65	6.56	-0.48	0.06	3
AM 01C	24.40	6.58	-0.55	-1.31	4
AM 02	24.20	6.59	-0.54	-1.10	7
AM 02C	23.80	6.60	-0.68	0.01	7
AM 03	23.75	6.60	-0.38	0.17	4
AM 03C	23.40	6.62	-1.29	-0.69	7
AM 04	22.90	6.64	0.01	-0.05	7
AM 04C	22.65	6.65	-0.70	0.22	7
AM 05	22.50	6.65	-0.81	-1.09	4
AM 05C	22.25	6.67	-1.27	-0.79	7
AM 06	22.05	6.68	-0.61	-0.09	7
AM 06C	21.75	6.69	-0.25	1.30	7
AM 07	21.65	6.69	-0.55	-0.64	4
AM 07C	21.40	6.71	-0.50	0.36	7
AM 08	21.15	6.72	-0.38	0.10	3
AM 09	20.15	6.75	-0.14	1.24	4
AM 09C	19.60	6.76	-0.70	0.58	4
AM 10	19.20	6.77	-0.29	0.43	4
AM 10C	18.80	6.78	-1.08	-0.44	3
AM 11	18.20	6.79	-0.25	0.19	7
AM 11C	17.70	6.80	-0.32	1.06	4
AM 12	17.45	6.81	-0.76	-0.90	4
AM 12C	17.20	6.81	-0.04	1.34	7
AM 13	16.90	6.82	-0.01	0.91	4
AM 13C	16.50	6.83	-0.27	0.66	4
AM 14	16.15	6.85	-0.39	0.28	4
AM 14C	15.80	6.86	-0.19	0.72	7
AM 15	15.45	6.86	-0.18	0.91	4
AM 15C	15.00	6.87	-0.32	0.67	4
AM 16	14.65	6.88	-0.35	-0.01	7
AM 16C	13.85	6.90	-0.41	0.59	7
AM 17	12.80	6.92	-0.09	0.51	3
AM 17C	12.55	6.93	-0.44	0.44	7
AM 18	12.20	6.94	-0.52	-0.18	7
AM 18C	11.70	6.95	-0.64	-0.07	7
AM 19	11.40	6.96	-0.46	-0.34	3
AM 19C	10.65	6.97	-0.65	-0.47	3
AM 20	10.10	6.98	-1.09	-1.79	4
AM 20C	9.65	7.00	-0.87	-1.00	4
AM 21	8.05	7.03	-0.99	-0.66	4
AM 22	7.10	7.05	-0.61	-0.79	4
AM 23	5.50	7.09	-1.23	-2.30	3
AM 24	3.90	7.13	-0.61	-0.55	4
AM 25	2.30	7.17	-1.20	-1.75	4

Supplementary table 7.4 $\delta^{13}C$ and $\delta^{18}O$ data on bulk sediments.

Nr.	Site	Age (Ma)	MAT (°C)	SST (°C)	Method	Location	Reference
1	Taman, Panagia	7.6	17	14	TEX_{86}	E. Paratethys (Russia)	Butiseacă et al., 2021
2	Vidin-Montana	~7–6.7	14–17		Pollen	C. Paratethys (Bulgaria)	Ivanov et al., 2002
3	Kladovo	~7	13.8–15.4		Leaf physiology	C. Paratethys (Serbia)	Utesher et al., 2007
4	Crveni Breg	~7	13.8–16.6		Leaf physiology	C. Paratethys (Serbia)	Utesher et al., 2007
5	Beli Breg	Late Messinian	~15		Pollen	C. Paratethys (Bulgaria)	Ivanov et al., 2021
6	Taman, Zheleznyi Rog	~6.2–5.33	~6–25		TEX_{86}	E. Paratethys (Russia)	Vasiliev et al., 2020
7	380 Site	~6.2–5.33		~6–24	TEX_{86}	E. Paratethys (Black Sea)	Vasiliev et al., 2020
8	Vegora	6.4–6	10–13.5		Pollen & leaves	Paratethys/Med. (N. Greece)	Bouchal et al., 2020
9	Agios Myron	7.2–6.54		20.7–30	TEX_{86}	E. Mediterranean (C. Crete, Greece)	Kontakiotis, Butiseacă et al., 2022
				23.7–28.2	U^{K}_{37}	E. Mediterranean (C. Crete, Greece)	Kontakiotis, Butiseacă et al., 2022
10	Agios Myron	7.2–6.54	6–21.2		TEX_{86}	E. Mediterranean (C. Crete, Greece)	This study
11	Faneromeni	7.2–6.9		16–26	Sr/Ca	E. Mediterranean (E. Crete, Greece)	Kontakiotis et al., 2019
12	Pissouri	6.9–6.5	4.5–28	21.6–30.6	TEX_{86}	E. Mediterranean (Cyprus)	Mayser et al., 2017
13	Kalamaki	6.4–5.9		~20–26	TEX_{86}	E. Mediterranean (Zakynthos, Greece)	Vasiliev et al., 2019
14	Monte dei Corvi	7.2–6.4		19.5–27.6	U^{K}_{37}	W. Mediterranean (Italy)	Tzanova et al., 2015
15	Sorbas	6.2–5.9		~9.5–19	Mg/Ca; Ba/Ca	W. Mediterranean (Spain)	Mancini et al., 2020
16	Aïn Lorma (Saïs Basin)	~7.8–7	20–24		Pollen	Rifian Corridor (Morocco)	Targhi et al., 2021

Supplementary table 7.5 Synthesis of Messinian temperature records in Mediterranean and Paratethys.